# Ultrasonic Spray Coating for the Fabrication of Polymeric Organic Light-Emitting Diodes

Thomas James Routledge

Department of Physics and Astronomy

Faculty of Science

The University of Sheffield


The University Of Sheffield.

Thesis submitted for the degree of Doctor of Philosophy

October 2018

## Acknowledgements

There are many people without whom I would not have made it to this point, and I would like to take this opportunity to thank them. Firstly, I would like to thank my supervisor Alastair Buckley for giving me this opportunity and his continual support and guidance throughout. The members of the EPMM group, past and present, deserve a great deal of thanks for not only the brilliant academic help over the years but for the friendships and emotional support that they continue to give. A special mention to EPMM group technician Dr. Matthew Wright, without him none of the lab equipment would ever have been working. I would like to thank other friends and collaborators from across the university, Ossila Ltd and Power roll Ltd.

I would like to thank my family, Lindsey and Lindsey's family for their love, support and the sacrifices they have made that have allowed me to reach this point.

## Abstract

This thesis investigates the use of the large-area, roll-to-roll compatible deposition technique of ultrasonic spray coating for the fabrication of polymeric organic light-emitting diodes (OLEDs).

Firstly, in Chapter 4 a range of different materials are investigated as potential solution processable electron-injection layers, typically this layer is deposited via thermal evaporation in OLEDs but a solution based alternative is required for deposition via ultrasonic spray coating. Solution-processed electron-injection layers: caesium carbonate ($Cs_2CO_3$), 8-hydroxy-quinolinato lithium (Liq) and polyethylenimine-ethoxylated (PEIE), are spin cast to tune thickness for optimal device performance and investigated for compatibly with ultrasonic spray coating under ambient conditions. Caesium carbonate deposited in an inert atmosphere was found to improve device performance compared to thermally evaporated lithium fluoride references but when cast in an ambient atmosphere the device performance was very poor due to the hygroscopic nature of $Cs_2CO_3$. Devices fabricated with optimal thickness Liq electron-injection layer had low mean peak luminance of 1197

cd $m^{-2}$. Devices with PEIE layers of 2.7 ± 0.1 nm spin cast under ambient conditions have mean peak performance metrics of 3.18 cd $A^{-1}$, 1.14 Lm $W^{-1}$, and 10690 cd $m^{-2}$.

In Chapter 5 the wide parameter space of ultrasonic spray coating is probed in order to determine the processing window and optimisation process for depositing uniform polymer thin films. The parameter space for ultrasonic spray coating has been investigated and an optimisation process for spraying uniform thin polymer films has been developed using hole-transporting polymer poly[(9,9-dioctylfluorenyl-2,7-diyl)-co-(4,4'(N-(4-sec-butylphenyl))) diphenylamine] (TFB). The processing window for casting uniform films of TFB from a 4 mg $ml^{-1}$ toluene solution cast onto a substrate held at 25 °C with a fluid pressure of 50 mbar have been shown to be a pass height of 40 mm and a range of pass speeds from 125 – 200 mm $s^{-1}$ to fabricate films between 66 – 97 nm.

In Chapter 6 a study is undertaken to determine if there is a fundamental issues with films deposited via ultrasonic spray coating that could limit the electrical performance of devices containing these film compared to those deposited via spin coating. The influence of thin film processing technique and surface roughness on the electrical performance of unipolar polymer OLEDs are studied, and a negligible difference is found between low-roughness spray cast (Ra < 10 nm) and spin cast devices of equivalent thicknesses. However, above 10 nm roughness there is a reduction in injection efficiency, up to an 86 % loss in performance for roughnesses of the order of 40 % of the thickness of the film. As such a processing window of Ra < 10 nm for achieving comparable electrical performance between spin and spray cast devices is demonstrated.

Finally, in Chapter 7 the different layers of a White-emitting polymer OLED are deposited via ultrasonic spray coating in separate devices for optimisation, then the layers are sprayed subsequently in the same device and lastly large-area devices are fabricated to demonstrate the scalability of the process. White-emitting polymer OLEDs have been fabricated in which the hole-injection layer, emissive layer and electron-injection layer were deposited via ultrasonic spray coating.

Several different device studies have been conducted: Firstly, devices with PEDOT:PSS deposited via ultrasonic spray coating as a hole-injection layer were fabricated and show comparable device performance to those with spin-cast PEDOT:PSS.

Secondly, devices with a white-light-emitting polymer (LEP), deposited via ultrasonic spray coating, have mean peak current efficiency of 4.93 cd $A^{-1}$, 90 % of the value of the spin cast references 5.45 cd $A^{-1}$. The mean peak power efficiency of the spray cast devices was 2.42 Lm $W^{-1}$, 82 % of the spin cast references 2.97 Lm $W^{-1}$. The mean peak luminance of the spray cast devices was 8149 cd $m^{-2}$, 80% of the reference spin cast value 10189 cd $m^{-2}$. These results are equivalent to those in literature where devices fabricated by Gilissen et al. in which a yellow-light-emitting polymer was deposited via ultrasonic spray coating achieved 9.71 Lm $W^{-1}$, 81 % of the spin cast reference.

Thirdly, attempts were made to replace the electron-injection layer with an air-stable, non-ionic and non-conjugated polymer, polyethylenimine-ethoxylated (PEIE), layer deposited via ultrasonic spray coating. Devices in which PEIE was deposited via ultrasonic spray coating as an electron-injection layer showed poor device metrics and non-uniform emission.

Finally, white-light-emitting devices were then fabricated in which the hole-injection and emissive layers were sequentially deposited via ultrasonic spray coating, a first for polymer OLEDs. The mean peak current efficiency for the spray cast devices was 2.43 cd $A^{-1}$, 72 % of the value of the spin cast references 3.39 cd $A^{-1}$. The mean peak power efficiency of the spray cast devices was 0.83 Lm $W^{-1}$, 71 % of the spin cast references 1.17 Lm $W^{-1}$. The mean peak luminance of the spray cast devices was 7409 cd $m^{-2}$, 70 % of the reference spin cast value 10626 cd $m^{-2}$. The same layers were then spray cast to fabricate large-area devices to demonstrate the possibility of coating over large areas and the potential compatibility of this technique with roll-to-roll processing, a yield of working pixels of 95.8 % was achieved.

## Publications

[1] J.E. Bishop, T.J. Routledge, D.G. Lidzey, Advances in Spray-Cast Perovskite Solar Cells, J. Phys. Chem. Lett. 9 (2018) 1977–1984. doi:10.1021/acs.jpclett.8b00311.

[2] M. Wong-Stringer, O.S. Game, J.A. Smith, T.J. Routledge, B.A. Alqurashy, B.G. Freestone, A.J. Parnell, N. Vaenas, V. Kumar, M.O.A. Alawad, A. Iraqi, C. Rodenburg, D.G. Lidzey, High-Performance Multilayer Encapsulation for Perovskite Photovoltaics, Adv. Energy Mater. (2018). doi:10.1002/aenm.201801234.

[3] J.E. Bishop, J.A. Smith, C. Greenland, V. Kumar, N. Vaenas, O.S. Game, T.J. Routledge, M. Wong-Stringer, C. Rodenburg, D.G. Lidzey, High-Efficiency Spray-Coated Perovskite Solar Cells Utilizing Vacuum-Assisted Solution Processing, ACS Appl. Mater. Interfaces. 10 (2018) 39428–39434. doi:10.1021/acsami.8b14859.

[4] T.J. Routledge, D.G. Lidzey, A.R. Buckley, Ultrasonic spray coating as an approach for large-area polymer OLEDs: The influence of thin film processing and surface roughness on electrical performance, AIP Adv. 9 (2019). doi:10.1063/1.5082791.

[5] T.J. Routledge$^{\alpha}$, M. Wong-Stringer$^{\alpha}$, O.S. Game, J.A. Smith, J.E. Bishop, N. Vaenas, B.G. Freestone, D.M. Coles, T. McArdle, A.R. Buckley, D.G. Lidzey, Low-temperature, high-speed reactive deposition of metal oxides for perovskite solar cells, J. Mater. Chem. A. 7 (2019) 2283–2290. doi:10.1039/C8TA10827G.

[6] M. Wong-Stringer$^{\alpha}$, T.J. Routledge$^{\alpha}$, T. McArdle, C. Wood, O.S. Game, J.A. Smith, J.E. Bishop, N. Vaenas, D.M. Coles, A.R. Buckley, D.G. Lidzey, A flexible back-contact perovskite solar micro-module, *Accepted by Energy & Environmental Science but not published at time of submission.*

α – Authors contributed equally.

## Conference Presentations

UK Semiconductors (UKSC), Sheffield, UK, July 2016 – Poster presentation

UK Semiconductors (UKSC), Sheffield, UK, July 2017 – Oral presentation on behalf of James Bishop

University of Sheffield Physics and Astronomy departmental research day 30th month oral PhD presentations 2017 – 2nd prize

## Contents

# Chapter 1

# Introduction

Electric lighting is an absolute fundamental of modern life. If you are at home, work, inside or outdoors you'll almost certainly be illuminated by some form of electrical lighting. The first mass produced light bulb was the incandescent light bulb and it is still used today. In an incandescent bulb there is a resistive wire filament sealed within a partial vacuum or inert gas, a current is applied across the filament causing it to heat to a high enough temperature to emit light. Incandescent bulbs are limited to an maximum efficiency of around 17 Lm $W^{-1}$ as around 95 % of the energy put into the bulb is transferred into waste energy in the form of heat.[1,2]

The low efficiency of incandescent bulbs has driven research into more efficient, and therefore cheaper lighting. One popular higher efficiency alternative to incandescent bulbs are fluorescent tube lights. Fluorescent tube lights consist of a sealed, phosphor coated glass tube containing a mercury vapour/gas mixture. When a current is applied to the cathode within the tube electrons are emitted into the gas, these electrons collide with mercury atoms in the gas causing excitation of the outermost electron in the mercury atoms. The electron subsequently relaxes by emitting a UV photon which is absorbed by the phosphor coating and re-emitted as visible light in a similar process. Over the past 40 years fluorescent tube lights have been developed to have luminous efficiencies around 90 Lm $W^{-1}$, longer life times and less flickering issues.[1] Compact fluorescent bulbs are now available designed to fit light fittings previously used for incandescent bulbs. The price of fluorescent tube lights/compact fluorescent bulbs are typically higher than incandescent bulbs. However, the higher efficiency and longer lifetime make fluorescent lighting more

cost efficient overall, but the initial higher cost of such technologies is still a barrier for efficient lighting.[2] One downside to fluorescent lighting is the potential risk of mercury contamination of the area if the glass breaks as such special precautions must be taken when disposing of fluorescent lights.

One promising field of research for lighting is solid state lighting (SSL). Solid state lights are made up entirely of solid materials in which the charge carriers, electrons and holes, are confined within solid structure. This differs from incandescent and fluorescent lighting which contain either a vacuum or a gas. The two main forms of SSL are light-emitting diodes (LEDs) and organic light-emitting diodes (OLEDs). Both inorganic and organic light-emitting diodes use semiconducting materials to emit light through the process of electroluminescence, with LEDs using crystalline materials such as gallium arsenide and OLEDs using carbon based materials. The first LED to emit in the visible region was reported in 1962, with the efficiencies improving over time and with the publication of blue LEDs in the early 1990's the route to a white LED (WLED) was achieved in 1996.[3–6] The first commercial WLEDs had efficiencies comparable to incandescent bulbs but in only a couple of years WLED efficiency has increased massively so commercial devices with efficiency over 200 Lm $W^{-1}$ are now available.[6,7] The rapid improvement in device performance suggests that there is still potential to improve device efficiency in the near future.

Organic compounds were first shown to produce electroluminescence by Bernanose in 1955. Bernanose applied voltages up to 2000 V to 100-200 μm thick acridine derivatives.[8] In 1963 Pope and co-workers observed electroluminescence in single crystal anthracene. The 10-20 μm thick crystals were prepared by sublimation and from solution and began to emit light above 400 V.[9] Later in the 1960's similar devices with lower, but still not commercially viable, operating voltages were produced by Helfrich and Schneider in "recombination radiation in anthracene crystals" and by the Mehl and Bucher group.[10–12]. In the early 1980's a key development was made in the OLED field by Ching Tang's group at Kodak. The group were the first to add a hole-injection layer (HIL) into the device structure.[13]

This innovation led to operating voltages below 20V, brighter devices and higher quantum efficiencies.[11]

In 1990 Burroughes et al. used 100 nm thick films of poly(p-phenylene vinylene)(PPV) to make green emitting OLEDs.[14] This work using PPV was the first step in making an OLED from an emissive conjugated polymer thin film but much work was still needed in order to make displays or lighting using this technique meet commercial standards. Research that followed aimed to synthesise PPV derivatives that were soluble, higher purity and had improved structural regularity.[15] In 1991 Braun and Heeger used MEH-PPV, a PPV derivative with soluble side chains, dissolved in an organic solvent to spin coat an emissive conjugated polymer thin film as a layer in an OLED.[16] The ease in which OLEDs could now be fabricated, compared to previous techniques, and new soluble polymers led to improvements in OLED performance over the following years. The evolution of OLEDs in the 20 years following Burroughes work was due in part to the development of emissive conjugated polymers but also due to innovations in the device architecture, further development of small molecules and phosphorescent emitters and an increased understanding of the physics of charge transport in OLEDs leading to the multiple new interlayers.[17–23] The first white OLED (WOLED) was reported in 1994 by Kido et al. where host polymer poly(N-vinylcarbazole) (PVK) was doped with blue, green and orange emitting small molecules to combine to emit over a broad range with a luminance of 3400 cd $m^{-2}$ at 14 V, and an efficiency of 0.83 lm $W^{-1}$.[24] The field has advanced at a rapid rate since this point with improved device stability and efficiencies up to 130 Lm $W^{-1}$ for white phosphorescent devices.[25–29]

Large improvements in efficiency and luminance have been made for both LEDs and OLEDs, and these devices are now fabricated on an industrial scale for premium products such as televisions, displays and lighting (for inorganics). Inorganic LEDs are typically fabricated via epitaxial growth on expensive crystalline substrates using techniques such as metal-organic chemical vapour deposition. This is a slow process that involves high control and is limited to small-area depositions, leading to displays or lights requiring arrays of small LEDs.[30] Further to this inorganic

LEDs are point light sources as such require the light emitted to be scattered to produce diffuse light required for lighting, which leads to a reduction in efficiency and limits design.

The consumer price of solid state lighting (SSL) units could be reduced drastically if production cost could be lowered, this could be achieved by increasing the rate of production and increasing the size of the fabricated light sources. One such method of mass production, which could be used to fabricate SSL on an industrial scale for lighting is Roll-to-Roll (R2R) processing. Roll-to-Roll (R2R) processing uses a roll of flexible material which is unfurled at speed, coated or printed on then wound up into a roll which can then be cut to the desired dimensions. The rolls of flexible material used vary in size and can be up to Kilometres long and meters wide. The high throughput of R2R processing and wide nature of the substrates used require a rapid, large-area coating technique.

Organic LEDs, typically small molecules LEDs, can be deposited via thermal evaporation under high vacuum, this process is used to fabricate OLED televisions but the complexity of these devices lead to a slower process and consumer prices over £1500. Thermal evaporation of small molecules for the fabrication of large-area OLEDs is a process which is compatible with high throughput coating but the small molecule layers deposited may lack the mechanical robustness to undergo unravelling and re-reeling of flexible substrates required for a R2R process, as well as there being potential issues with interlayer diffusion during thermal cycling during fabrication.[31] This coupled with the high vacuums required for depositions use a large amount of energy, can be expensive to achieve, with cost rising with larger vacuum chambers required for higher output are challenging barriers for thermal evaporation of OLEDS as a route for low cost lighting.

Another route to fabricating OLEDs, typically polymer based OLEDs, is via solution processing. Small-scale processing of solution processed OLEDs in labs is typically achieved using spin coating but this process struggles to coat uniformly over large areas and is incompatible with R2R processing. However, some potential R2R compatible techniques have already demonstrated the coating of polymeric thin films from solution for electronic devices.[32–34] In this thesis ultrasonic spray

coating is investigated as a deposition technique for uniform, thin polymer films for the fabrication of OLEDs. Ultrasonic spray coating, a large-area R2R compatible coating technique, has already been used to successfully fabricate organic electronics such as solar cells and transistors, but the high sensitivity to thickness variations and the sequential deposition of layers required for OLED fabrication provides a stern test for the wide spread application of ultrasonic spray coating.

If OLEDs could be successfully deposited using a R2R compatible process like ultrasonic spray coating then not only could this potentially reduce the cost of efficient lighting but the way lighting is used could change. R2R fabricated OLEDs could be millimetre thick, large-area, flexible panels emitting across the device not requiring a diffuser unlike other sources. The thin and flexible nature could allow lighting to be integrated into building, vehicle or outside designs unlike any other form of lighting. OLEDs are already becoming popular for use in screens and displays such as phones and television due to their efficiency, high resolution and thin nature but these products are expensive due to the low fabrication rates. If OLEDs could be fabricated via R2R processing then these screens could be cheap to produce and flexible allowing for increased integration in design and use in clothing/wearable technology. Such cheap, flexible displays could also be potentially used for digital signage, pricing labels in retail, billboards or newspapers/magazines, all applications whereby the information displayed needs regularly updating but with cheap mass produced OLED displays this could be done digitally reducing waste.

## 1.1: Thesis Summary and Motivation

The focus of this thesis has been to investigate the feasibility of the novel deposition technique of ultrasonic spray coating to fabricate polymer light-emitting diodes. The motivation to investigate ultrasonic spray coating of WOLEDs is due to the high efficiency achievable by WOLEDs, the need for affordable efficient lighting and the compatibility of ultrasonic spray coating with roll-to-roll processing.

In Chapter 2, an overview of organic physics is given building to an understanding of the origin of the semiconducting nature of conjugated polymers, the photophysics of such materials and the operating principles of devices incorporating them. The

characterisation of devices and the origin of white emission from organic light-emitting diodes is discussed before a brief literature review of roll-to-roll coating techniques with the view of industrialising the fabrication of OLEDs. The techniques used for the preparation, fabrication and characterisation of OLEDs are described in Chapter 3.

In Chapter 4, caesium carbonate, 8-hydroxy-quinolinato lithium and polyethylenimine-ethoxylated (PEIE) are investigated as solution-processed electron-injection layers (EILs) for white-emissive polymer LEDs. The EILs are deposited via spin coating at a range of different thicknesses to optimise device performance, the effect of ambient processing on device performance is also investigated to probe the compatibility of these materials with a large-area ambient coating technique such as ultrasonic spray coating. It is found that under ambient processing conditions PEIE performed best with mean peak metrics of 3.18 cd $A^{-1}$, 1.14 Lm $W^{-1}$, and 10690 cd $m^{-2}$.

Chapter 5 describes the physics behind the key stages of depositing a thin film via ultrasonic spray coating; the formation of droplets of a solution, transferring the droplets onto the substrate, the spreading and merging of droplets to form a continuous wet film and the evaporation of the solvent to form a dry thin film. Thin films of poly[(9,9-dioctylfluorenyl-2,7-diyl)-co-(4,4'(N-(4-sec-butylphenyl))) (TFB) are cast via ultrasonic spray coating using a range of different deposition parameters and the morphology is characterised in order to demonstrate the parameter space and the optimisation process required to deposit uniform thin films. Issues with the USI Prism Ultra-coat 300 system are raised and how they are managed is discussed in order to maintain a good level of repeatability from device-to-device and run-to-run.

In Chapter 6, the influence of thin film processing technique and surface roughness on the electrical performance of unipolar polymer devices is studied. The injection efficiency of holes into films of poly[(9,9-dioctylfluorenyl-2,7-diyl)-co-(4,4'(N-(4-sec-butylphenyl))) diphenylamine], cast by ultrasonic spray coating is compared with those cast by spin coating. It is shown via statistical analysis, across a range of thicknesses typical of those used in OLEDs, that there is no intrinsic difference in the

injection efficiency between ultrasonic spray coating and spin coating. This reinforces the importance of spray coating as a potential route to high volume manufacturing of OLED based technology. The importance of controlling the roughness of films is also demonstrated and a threshold of 10 nm average roughness is determined, below which the effect of roughness on injection efficiency is negligible. As such a process window for achieving comparable spin and spray cast hole injection performance is wide with spray cast films with Ra < 10 nm being easily achieved by control of drying time through solvent choice, substrate temperature, formulation concentration and pass speed.

In Chapter 7, uniform PEDOT:PSS films, with a root-mean-square (rms) roughness of 2.14 nm, are successfully deposited via ultrasonic spray coating. OLEDs with spray cast PEDOT:PSS as the hole-injection layer have been demonstrated and have comparable luminance to spin cast references but the efficiency metrics are lower than the spin cast references. The lower efficiencies are due to additives to the spray cast ink increasing the conductivity of the layer leading to off pixel current contributions, it is demonstrated that if the devices are patterned more precisely the efficiency metrics of the spray cast PEDOT:PSS devices are comparable to the spin cast references.

Highly uniform white-light-emitting polymer (LEP) films are successfully deposited via ultrasonic spray coating with a rms roughness of 1.33 nm, an equivalent roughness to spin cast films. These films were incorporated into devices and compared with spin cast references. OLEDs with a spray cast emissive layer have a mean peak current efficiency, power efficiency and luminance of 90 %, 82 % and 80 % of the spin cast references respectively. In comparison Gilissen et al. fabricated devices with the emissive layer polymer (Merck Super Yellow) spray cast and achieved, with a champion device, a value for power efficiency 81% of the spin cast reference.[35] The comparable device performance between spin and spray cast devices, narrow spread of metrics and high yield demonstrate the potential for the use of the roll-to-roll compatible technique of ultrasonic spray coating for the deposition of the emissive layer in a polymer OLED.

Devices are fabricated with spray cast polyethylenimine-ethoxylated (PEIE) films as the electron-injection layer, these devices had comparable efficiency metrics to the spin cast references but the mean peak luminance was less than 50 % of the reference. Device performance has been shown in Chapter 4 to be highly sensitive to PEIE thickness with the optimum thickness 2.7 ± 0.1 nm and a very narrow thickness window for good device performance. Improving the uniformity of spray cast PEIE films and thus fabricating devices of comparable performance to spin cast references proved to be exceptionally challenging due to the inability to characterise the thin, transparent, colourless PEIE layers and optimise the spraying parameters accordingly during the fabrication process, this was reflected in the non-uniform electroluminescence of these devices.

OLEDs are then fabricated in which PEDOT:PSS and the white-light-emitting polymer were deposited sequentially via ultrasonic spray coating, after studying the literature as far as I am aware this is the first multilayer ultrasonic spray cast polymer OLED. These multilayer spray cast OLEDs have a mean peak current efficiency, power efficiency and luminance of 72 %, 71 % and 70 % of the spin cast references respectively. The high performance and comparable spread to spin cast reference devices demonstrates the potential for the use of the roll-to-roll compatible technique of ultrasonic spray-coating for the deposition of multilayer polymer OLEDs.

Attempts are then made to scale up to fabricate large-area (1875 $mm^2$) 24 pixel multilayer spray cast polymer OLEDs. A degraded batch of ethylene glycol in the PEDOT:PSS blend ink led to non-uniformity and holes in the spray-cast PEDOT:PSS films which resulted in poor devices metrics. Despite the issues with the PEDOT:PSS layer remarkably the yield was 95.8 % of 48 pixels across two devices this demonstrates the feasibility and robustness of using ultrasonic spray coating to process over large areas.

Finally, the results of this thesis are summarised in Chapter 8 with suggestions on how this work could be taken forward in the future.

## 1.2: References


[1] E.F. Schubert, J.K. Kim, Solid-state light sources getting smart., Science (80-. ). 308 (2005) 1274–8. doi:10.1126/science.1108712.

[2] C.J. Humphreys, Solid-state lighting, MRS Bull. 33 (2008) 459–470. doi:10.1557/mrs2008.91.

[3] N. Holonyak, S.F. Bevacqua, Coherent (visible) light emission from Ga(As1-xPx) junctions, Appl. Phys. Lett. 1 (1962) 82–83. doi:10.1063/1.1753706.

[4] F.A. Ponce, D.P. Bour, Nitride-based semiconductors for blue and green light-emitting devices, Nature. 386 (1997) 351–359. doi:10.1038/386351a0.

[5] S. Nakamura, T. Mukai, M. Senoh, High-brightness InGaN/AlGaN double-heterostructure blue-green-light-emitting diodes, J. Appl. Phys. 76 (1994) 8189–8191. doi:10.1063/1.357872.

[6] J. Cho, J.H. Park, J.K. Kim, E.F. Schubert, White light-emitting diodes: History, progress, and future, Laser Photon. Rev. 11 (2017) 1600147. doi:10.1002/lpor.201600147.

[7] K. Bando, K. Sakano, Y. Nohuchi, Y. Shimizu, Development of High-bright and Pure-white LED Lamps., J. Light Vis. Environ. 22 (1998) 2–5. doi:10.2150/jlve.22.1_2.

[8] A. Bernanose, Electroluminescence of organic compounds, 1955. http://iopscience.iop.org/article/10.1088/0508-3443/6/S4/319/pdf (accessed September 26, 2018).

[9] M. Pope, H.P. Kallmann, P. Magnante, Electroluminescence in organic crystals, J. Chem. Phys. 38 (1963) 2042–2043. doi:10.1063/1.1733929.

[10] W. Helfrich, W.G. Schneider, Recombination radiation in anthracene crystals, Phys. Rev. Lett. (1965). doi:10.1103/PhysRevLett.14.229.

[11] Y. Kim, C. Ha, Advances in Organic Light-Emitting Devices, Trans Tech Publications Ltd, 2008.

[12] A.R. Buckley, Organic light-emitting diodes (OLEDs): Materials, devices and applications, Elsevier, 2013.

[13] C. Tang, Organic electroluminescent cell, US Pat. 4,356,429. (1982). https://patents.google.com/patent/US4356429A/en (accessed September 26, 2018).

[14] J.H. Burroughes, D.D.C. Bradley, A.R. Brown, R.N. Marks, K. Mackay, R.H. Friend, P.L. Burns, A.B. Holmes, Light-emitting diodes based on conjugated polymers, Nature. 347 (1990) 539–541. doi:10.1038/347539a0.

[15] K. Müllen, U. Scherf, eds., Organic Light-Emitting Devices: Synthesis, Properties and Applications, Wiley-vch, Germany, 2006.

[16] D. Braun, A.J. Heeger, Visible light emission from semiconducting polymer diodes, Appl. Phys. Lett. 58 (1991) 1982–1984. doi:10.1063/1.105039.

[17] K.R. Choudhury, J. Lee, N. Chopra, A. Gupta, X. Jiang, F. Amy, F. So, Highly efficient hole injection using polymeric anode materials for small-molecule organic light-emitting diodes, Adv. Funct. Mater. 19 (2009) 491–496. doi:10.1002/adfm.200801368.

[18] Z.W. Liu, M.G. Helander, Z.B. Wang, Z.H. Lu, Efficient bilayer phosphorescent organic light-emitting diodes: Direct hole injection into triplet dopants, Appl. Phys. Lett. 94 (2009) 113305. doi:10.1063/1.3099903.

[19] G.E. Jabbour, Y. Kawabe, S.E. Shaheen, J.F. Wang, M.M. Morrell, B. Kippelen, N. Peyghambarian, Highly efficient and bright organic electroluminescent devices with an aluminum cathode, Org. Electroluminescent Diodes Appl. Phys. Lett. 71 (1997) 913. doi:10.1063/1.119392.

[20] G. He, M. Pfeiffer, K. Leo, M. Hofmann, J. Birnstock, R. Pudzich, J. Salbeck, High-efficiency and low-voltage p-i-n electrophosphorescent organic light-emitting diodes with double-emission layers, Appl. Phys. Lett. 85 (2004) 3911. doi:10.1063/1.1812378.

[21] M. Ikai, S. Tokito, Y. Sakamoto, T. Suzuki, Y. Taga, Highly efficient

phosphorescence from organic light-emitting devices with an exciton-block layer, Appl. Phys. Lett. 79 (2001) 156–158. doi:10.1063/1.1385182.

[22] V.I. Adamovich, S.R. Cordero, P.I. Djurovich, A. Tamayo, M.E. Thompson, B.W. D'Andrade, S.R. Forrest, New charge-carrier blocking materials for high efficiency OLEDs, Org. Electron. Physics, Mater. Appl. 4 (2003) 77–87. doi:10.1016/j.orgel.2003.08.003.

[23] M.A. Baldo, D.F. O'Brien, Y. You, A. Shoustikov, S. Sibley, M.E. Thompson, S.R. Forrest, Highly efficient phosphorescent emission from organic electroluminescent devices, Nature. 395 (1998) 151–154. doi:10.1038/25954.

[24] J. Kido, K. Hongawa, K. Okuyama, K. Nagai, White light-emitting organic electroluminescent devices using the poly(N-vinylcarbazole) emitter layer doped with three fluorescent dyes, Appl. Phys. Lett. 64 (1994) 815–817. doi:10.1063/1.111023.

[25] J. Liu, Q. Zhou, Y. Cheng, Y. Geng, L. Wang, D. Ma, X. Jing, F. Wang, The first single polymer with simultaneous blue, green, and red emission for white electroluminescence, Adv. Mater. 17 (2005) 2974–2978. doi:10.1002/adma.200501850.

[26] K. Kato, T. Iwasaki, T. Tsujimura, Over 130 lm/W All-Phosphorescent White OLEDs for Next-generation Lighting, J. Photopolym. Sci. Technol. 28 (2015) 335–340. doi:10.2494/photopolymer.28.335.

[27] C. Coburn, C. Jeong, S.R. Forrest, Reliable, All-Phosphorescent Stacked White Organic Light Emitting Devices with a High Color Rendering Index, ACS Photonics. 5 (2018) 630–635. doi:10.1021/acsphotonics.7b01213.

[28] S. Reineke, M. Thomschke, B. rn Lü ssem, K. Leo, White organic light-emitting diodes: Status and perspective, Rev. Mod. Phys. 85 (2013). doi:10.1103/RevModPhys.85.1245.

[29] F. Zhao, D. Ma, Approaches to high performance white organic light-emitting diodes for general lighting, Mater. Chem. Front. 1 (2017) 1933–1950.

doi:10.1039/C6QM00365F.

[30] L. Liu, J.H. Edgar, Substrates for gallium nitride epitaxy, Mater. Sci. Eng. R Reports. 37 (2002) 61–128. doi:10.1016/S0927-796X(02)00008-6.

[31] M. Caironi, Y.-Y. Noh, Large Area and Flexible Electronics, Wiley-VCH Verlag GmbH & Co. KGaA, Weinheim, Germany, 2015. doi:10.1002/9783527679973.

[32] T. Mäkelä, S. Jussila, H. Kosonen, T.G. Bäcklund, H.G.O. Sandberg, H. Stubb, Utilizing roll-to-roll techniques for manufacturing source-drain electrodes for all-polymer transistors, Synth. Met. 153 (2005) 285–288. doi:10.1016/j.synthmet.2005.07.140.

[33] F.C. Krebs, S.A. Gevorgyan, J. Alstrup, A roll-to-roll process to flexible polymer solar cells: Model studies, manufacture and operational stability studies, J. Mater. Chem. 19 (2009) 5442–5451. doi:10.1039/b823001c.

[34] R.R. Søndergaard, M. Hösel, F.C. Krebs, Roll-to-Roll fabrication of large area functional organic materials, J. Polym. Sci. Part B Polym. Phys. 51 (2013) 16–34. doi:10.1002/polb.23192.

[35] K. Gilissen, J. Stryckers, P. Verstappen, J. Drijkoningen, G.H.L. Heintges, L. Lutsen, J. Manca, W. Maes, W. Deferme, Ultrasonic spray coating as deposition technique for the light-emitting layer in polymer LEDs, Org. Electron. Physics, Mater. Appl. 20 (2015) 31–35. doi:10.1016/j.orgel.2015.01.015.

# Chapter 2

# Background Theory

## 2.1: Introduction

In this chapter a broad range of concepts are introduced and discussed to firstly, in Section 2.2, build an understanding of the semiconducting properties of conjugated polymers and the photophysics of these materials. These concepts are then built upon as the physics of charge injection into and transport through organic materials within device structures are discussed in Section 2.3. In Section 2.4 the concept of emitting white light from a polymer in an organic light-emitting device is discussed and the characterisation of these devices is explained. In Section 2.5 the solution processing of organic light-emitting devices via lab scale processing is introduced. Towards the end of this section a brief review of the potential routes toward the industrial fabrication of organic light-emitting devices is presented with a particular focus on spray coating as a route toward roll-to-roll fabrication of polymer based organic light-emitting diodes.

## 2.2: General Background

### 2.2.1: Atomic Orbitals

Electrons within an atom are described as being in orbitals of discrete energy levels around the nucleus. In contrast to the classical scenario of an orbiting object such as a satellite around a planet where the movement and position of the satellite is known, the quantised electron orbitals describe the probability of there being an electron within a certain region.[1]

The properties of the atomic orbitals, including shape and electron occupation, are determined by the combination of four quantum numbers: the principal quantum number ($n$) which denotes the potential energy of the electron, the azimuthal quantum number ($l$) which denotes the magnitude of the angular momentum of the electron, the magnetic quantum number ($m_l$) which gives the direction of angular momentum and the spin quantum number ($m_s$) gives the direction of spin of the electron. The electron is classed as a lepton thus has half integer spin $\left(\pm\frac{1}{2}\right)$, the other quantum numbers have integer values and the conditions which define these values are stated in table 2.1.[2]

| $n$ ($n \geq 1$) | $l$ ($(n\text{-}1) \geq l \geq 0$) | $m_l$ ($l \geq m_l \geq -l$) | $m_s$ ($s \geq m_s \geq -s$) | Orbital name | | Number of electrons |
|---|---|---|---|---|---|---|
| 1 | 0 | 0 | 1/2 | 1s | | 2 |
| | | | -1/2 | | | |
| 2 | 0 | 0 | 1/2 | 2s | | 8 |
| | | | -1/2 | | | |
| | 1 | -1 | 1/2 | 2p | $2p_x$ | |
| | | | -1/2 | | | |
| | | 0 | 1/2 | | $2p_y$ | |
| | | | -1/2 | | | |
| | | 1 | 1/2 | | $2p_z$ | |
| | | | -1/2 | | | |

*Table 2. 1: Quantum numbers, conditions which define the quantum numbers, orbital names and the number of electrons in each shell for the first 2 shells.*

Table 2.1 shows the values of the quantum numbers for the first two shells of electrons ($n$ =1 and $n$ =2). The Pauli exclusion principle states that no two electrons can have identical quantum numbers, as such the first shell can only contain two electrons and as the magnitude of the angular momentum is zero these electron are confined to an s orbital, in this case the 1s orbital.[3] The second higher energy shell, $n$ = 2, if full, contains eight electrons split between electron orbitals with angular moment of zero or one which relate to the 2s and 2p orbitals. Electrons fill the orbitals in the first few shells in order of increasing energy, 1s then 2s then 2p then 3s. As such there are two electrons in the 2s orbital and six in the 2p orbital. The 2p orbital subdivides into three sub-orbitals of equal energy where the direction of

angular momentum dictates the orientation of the $p_x$, $p_y$ and $p_z$ sub-orbitals as demonstrated in Figure 2.1. At higher energies, beyond the first few electron shells, the azimuthal quantum number can increase further to l = 2 (d-orbitals) and l = 3 (f-orbitals), these orbitals are complex and unlikely to be encountered in organic semiconductors as such are not discussed here.

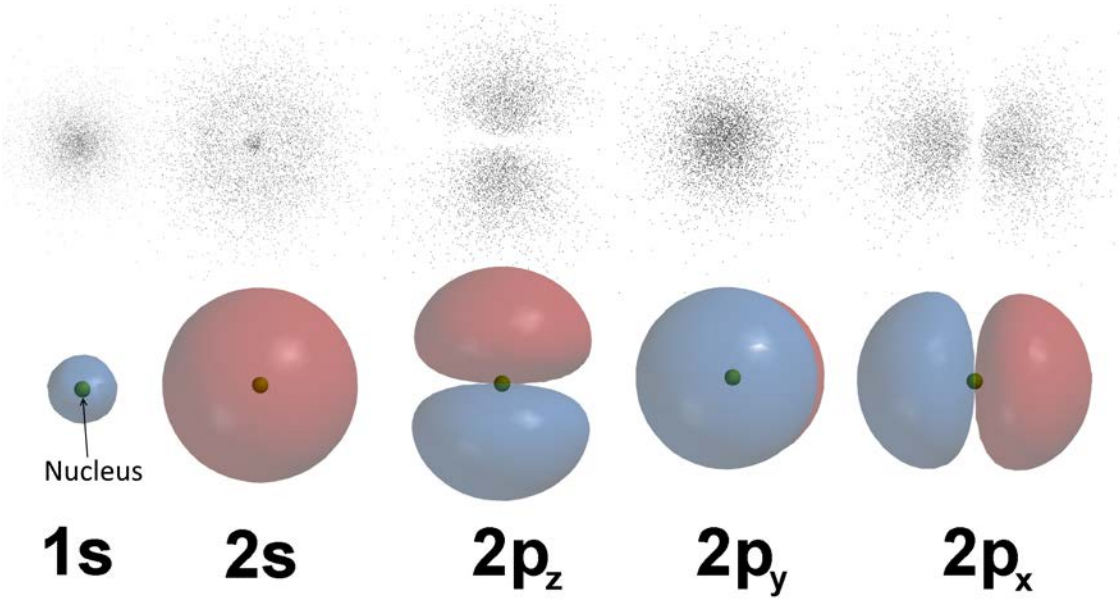


*Figure 2. 1: (Top) The 2D electron probability density distribution of the first and second s orbitals (1s, 2s) and the p orbitals ($p_x$, $p_y$ and $p_z$). (Bottom) The 3D electron probability density distribution diagrams illustrating the first and second atomic s orbitals and the p orbitals (x, y, z) around a nucleus.*

### 2.2.2: Molecular Orbitals

In order to build more complex organic materials atoms must be brought together and covalent bonds formed between them to make molecules. When two atoms are brought within a close vicinity their orbitals overlap to form molecular orbitals. The simplest example of this is given in Figure 2.2 where two atoms, each with a single electron in an s-orbital, are brought together and form a bonding orbital.

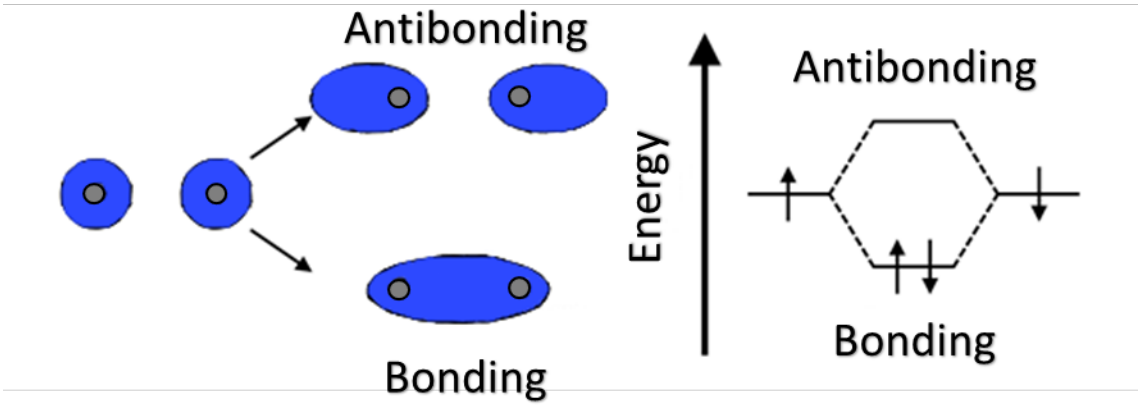


*Figure 2. 2: A diagram demonstrating the constructive and destructive interaction of electron orbitals when two atoms are brought together to form a molecule and molecular orbitals. Constructive interaction between atomic orbitals leads to a lower energy bonding molecular orbital. Destructive interaction between atomic orbitals leads to a higher energy antibonding molecular orbital.*

This occurs when there is a constructive interaction between the electron wavefunctions of the atomic orbitals, which form a single electron cloud in which the two electron reside between the two atoms. The increase in electron density between the two atoms acts to increase the shielding to coulombic repulsion, lowering the energy of the molecular orbital in relation to the individual atomic orbitals. Conversely, in the case where either one or both of the atoms have a full outer shell the additional electrons are excluded from the bonding orbital due to the Pauli exclusion principle and will occupy an antibonding orbital instead.[3] This destructive interaction between the electron wavefunctions leads to a lower electron density between the atoms, less coulombic shielding, a higher energy state and a less stable bond.

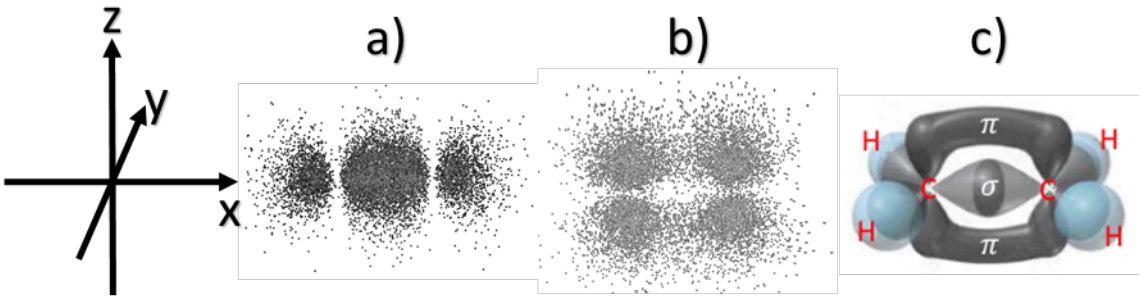


*Figure 2. 3: a) and b) are 2D electron probability density distributions of the bonds in ethene ($C_2H_4$) where a) are the σ-bonds (between nuclei) and b) are the π-bonds (away from the adjoining axis). c) is an illustration of all of the bonds.*

When two atoms are brought together to form a molecule the molecular orbitals, both bonding and anti-bonding, between the atoms that are symmetrical around the adjoining axis (e.g x-axis) are called $\sigma$-bonds.[4] The molecular orbitals that form from atomic orbitals that were perpendicular to the adjoining axis (those symmetrical around z axis in this example) form $\pi$-bonds. The orbitals formed due to $\pi$-bonding are further from the axis connecting the atoms as such the coulombic attraction to the nuclei is weaker and the $\pi$-bonds are less strongly bound.[5]

### 2.2.3: Orbital Hybridisation

The main class of materials of interest in this thesis are organic polymers, carbon is the main building block of organic molecules and forms the backbone of most polymers. As such the electronic configuration of carbon and how it interacts with other atoms is of great interest and importance. Elemental carbon has 6 electrons in the orbitals $1s^2$, $2s^2$, $2p_x^1$, $2p_y^1$. The two electrons in the outer 2p orbital suggest that carbon will only be able to form a maximum of two covalent bonds, this however is not the case as carbon can form four bonds as demonstrated by the existence of the molecule methane ($CH_4$). Carbon is allowed to form four covalent bonds due to the process of orbital hybridisation which results in carbon having an electronic configuration of $1s^2$, $2s^1$, $2p_x^1$, $2p_y^1$, $2p_z^1$. Firstly an electron from the 2s orbital is excited to the 2p orbital, the excitation energy is provided from the electromagnetic attraction between the carbon atom and another atom brought close to the carbon atom in the bonding process. The remaining 2s orbital can then combine with a

number of different 2p orbitals forming a new kind of hybrid atomic orbital, an sp orbital.[5] The number of 2p orbitals the 2s orbital merges with defines the level of hybridisation. $Sp^1$ hybridisation is the mixing of one p orbital with the s orbital resulting in two sp orbitals, $sp^2$ hybridisation is the mixing of two p orbitals with the s orbital resulting in three sp orbitals and $sp^3$ hybridisation is the mixing of three p orbitals with the s orbital leading to four sp orbitals.

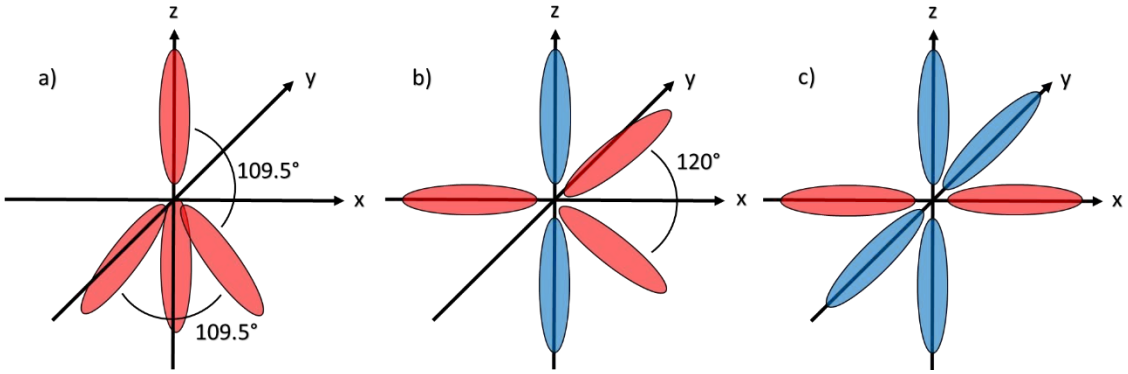


*Figure 2. 4: Diagrams visualising a) $sp^3$, b) $sp^2$ and c) $sp^1$ orbital hybridisation. The blue orbitals demonstrate un-hybridised p orbitals, the red orbitals demonstrate hybridised s and p orbitals. The hybridised sp orbitals in b) ($sp^2$ hybridisation) are all in the x-y plane.*

Figure 2.4 shows how in case of $sp^2$ hybridisation the sp orbitals are in the x-y plane, these will form $\sigma$-bonds when in a molecule which as mentioned in section 2.2 are strongly bound and spatially in the region between two bound nuclei. The un-hybridised p orbital in this situation extends perpendicularly to the plane of the sp orbitals and will form weakly bound $\pi$-bonds when forming a molecule which are key for the semiconducting property of organic molecules going forward. In the case of $sp^3$ hybridisation the sp orbitals will again form strongly bound $\sigma$-bonds but the lack of un-hybridised p orbitals will lead to molecules with this level of hybridisation to be insulators.

### 2.2.4: Conjugation and Band Formation

The concepts of atomic orbitals, molecular orbits and orbital hybridisation discussed so far in this chapter are important building blocks towards explaining the electronic properties of semiconducting organic materials. The $\sigma$-bond, formed

between two atoms in a molecule from the hybridised sp orbitals are referred to as a single bond. The $\pi$-bond, formed between un-hybridised p orbitals, in combination with a $\sigma$-bond is referred to as a double bond. The alternation between single and double bonds along a molecule or polymer is defined as conjugation, and it is conjugation that is responsible for the semiconducting properties of some organic materials. The single and double bond in polymer chains differ in length due to the Peierls instability leading to shorter double and longer single bonds.[6] This more energetically favourable conformation results in a higher electron density in the regions with double bonds. The widely used example to demonstrate conjugation is benzene. Benzene is a molecule that comprises of a hexagonal ring of six $sp^2$ hybridised carbon atoms bound with alternating single and double bounds with a single hydrogen atom bound to each carbon atom.[5]

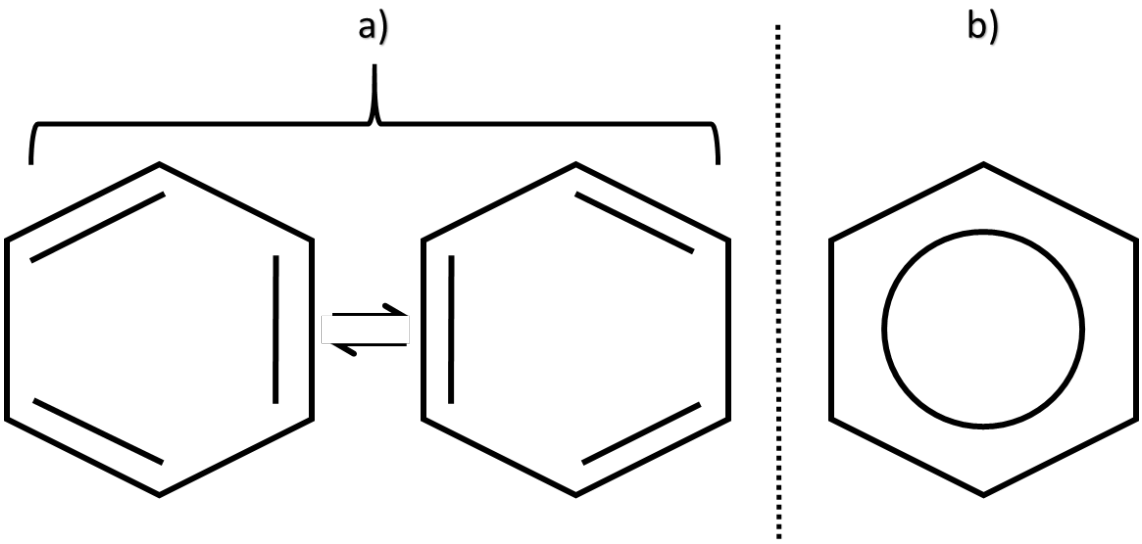


*Figure 2. 5: (a) The two possible orientations in which the double bonds can be positioned on a benzene ring, these are indistinguishable as such π-electrons are delocalised along the entirety of the benzene ring as illustrated by the third image (b).*

There are two potential positions in which the double bonds can be considered to be as shown in Figure 2.5. In both scenarios the $\pi$-orbitals of the carbon ring, are a combination of $\pi$-orbitals between the pairs of carbon atoms in the ring. This leads to a torus of delocalised charge above and below the plane of the benzene ring. As such the two configurations are indistinguishable as changing the position of the

double bonds doesn't change the molecule. The quantum mechanical nature of electron orbitals coupled with the indistinguishable nature of the benzene ring configuration allows the electrons within the $\pi$-orbitals to be in both places at once and thus the $\pi$-electrons are delocalised around the benzene ring.[4,5] In a conjugated polymer chain, like in a benzene ring, the $\pi$-electrons are delocalised along the conjugated backbone of the polymer chain. Now, if we picture a linear torsion-free defect-free polymer with alternating single and double bonds along the length of the polymer chain. If the single and double bonds in conjugated polymers such as this were of equal length the $\pi$-electrons would be delocalised along the full length of the polymer chain. In such a case the bonding and anti-bonding states would be indistinguishable, there would be no bandgap but instead a single half-filled energy band and the polymer would act as a one-dimensional metal.[7]

However, the variation in single and double bond lengths in combination with defects that can occur along the polymer, twisting/flexing of the chain, addition of substituents and interactions with the surroundings act to limit the delocalisation along the conjugated backbone leading to regions of delocalised $\pi$-electrons rather than delocalisation along the full length of the polymer. As such conjugated polymers are semiconductors rather than metallic-like conductors.[8]

As discussed in the molecular orbitals section the $\pi$-bond is weakly bound compared to the $\sigma$-bond as such the delocalised $\pi$-bonding orbital is weakly bound and is the highest energy state occupied by electrons. This orbital is then referred to as the highest occupied molecular orbital (HOMO). The higher energy $\pi$-antibonding orbital is referred to as the lowest unoccupied molecular orbital (LUMO). The HOMO and LUMO levels are similar to the valence and conduction bands respectively of inorganic semiconductors as such the difference in energy between the HOMO and LUMO levels is similarly called the bandgap. The size of the bandgap in conjugated polymers is derived from the delocalisation length of the $\pi$-electrons, the greater the delocalisation length the lower the bandgap and vice versa.[8,9]

### 2.2.5: Organic Photophysics

One of the key properties of conjugated polymers which make them of such interest to researchers is the fact they can absorb and emit photons across a range of

different wavelengths, these wavelengths can be engineered during the fabrication of the polymer. Figure 2.6 is an energy level diagram demonstrating the Franck-Condon principle in an ideal conjugated system.[10–12] The lower curve represents the ground electronic state of a molecule and the higher energy curve the excited electronic state of a molecule. Each level contains several quantised vibrational energy states (n). An electron can be excited from the HOMO (ground state) to the LUMO (excited state) when a photon with energy equal to or greater than the bandgap is absorbed. This electronic transition is represented on the energy level diagram by a vertical line as it is likely to occur without a change in position of the nuclei. If the electron is excited with a photon with energy greater than the band gap then the electron will be excited to one of the quantised vibrational states in the LUMO, the electron with then rapidly relax to the lowest vibrational state in the LUMO through non-radiative decay via the emission of a phonon.[13] A phonon is a quasiparticle or quantum of vibrational energy associated with lattice oscillations analogous to a photon as a quantum of electromagnetic energy.

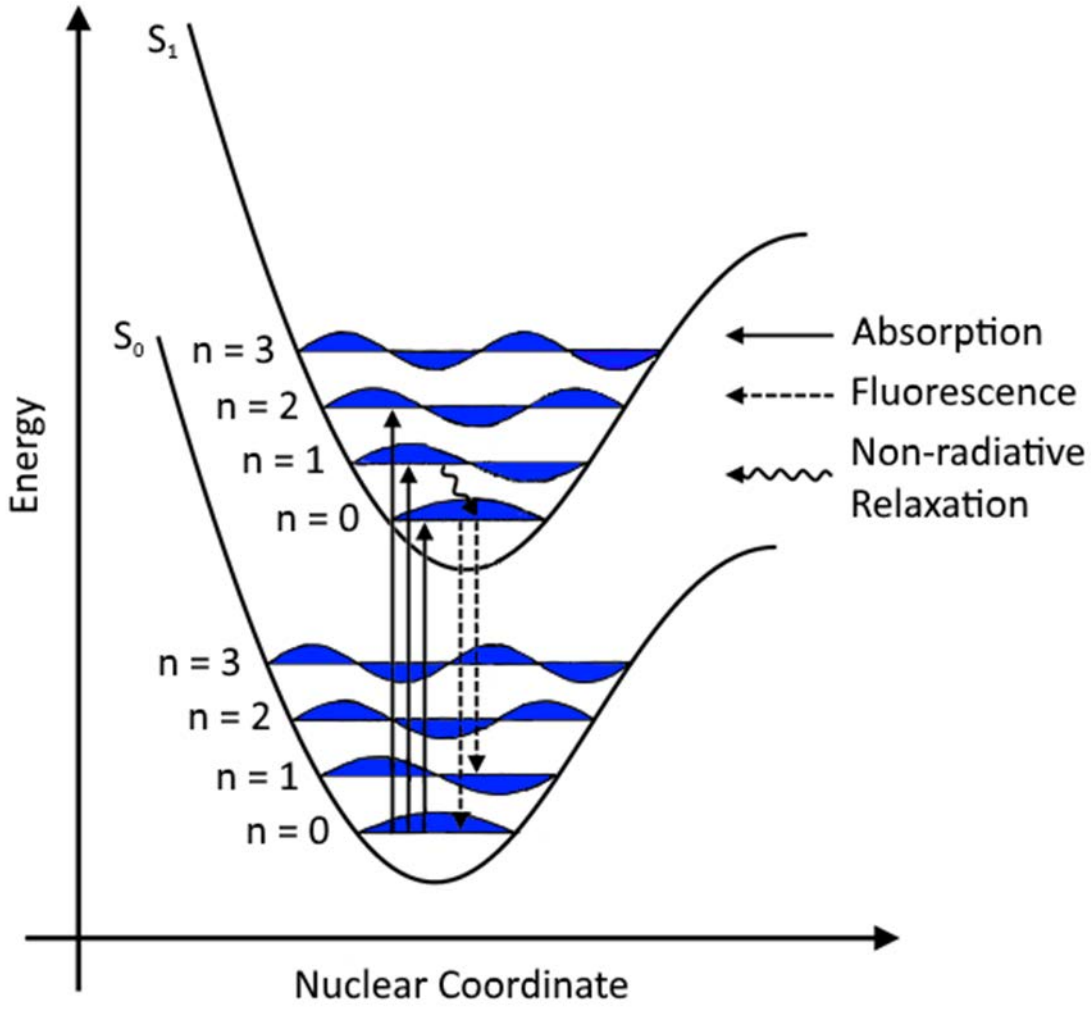


*Figure 2. 6: An energy level diagram demonstrating the Frank-Condon principle. The ground state, $S_0$, and the first excited state, $S_1$, are shown with the quantised vibrational states within the ground and excited states, n. The vertical solid arrows demonstrate the excitation of an electron from the ground to excited state via absorption of a photon. The curved line demonstrate the fast non-radiative relaxation of an electron from an excited vibrational state to the ground vibrational state in the excited state via emission of a phonon. The dashed lines demonstrate the radiative relaxation of electrons from the vibrational ground state in first excited state to the vibrational states in the ground state (fluorescence).*

The excitation of an electron to the LUMO leaves an absence of an electron in the HOMO, this is referred to as a hole. The hole is treated as a particle with equal but

opposite charge to the electron. Due to the equal and opposite charges of the hole and electron in the LUMO they are coulombically bound to form an electrically neutral quasiparticle called an exciton. The low relative dielectric constants of organics, typically around 3, result in a strong coulombic attraction between the paired electron and hole lead to the exciton being tightly bound ($E_{binding} > k_BT$) and localised, this form of exciton is known as a Frenkel exciton.[14,15] Further to this when an electron is promoted to an excited state it interacts with phonons and forms a quasiparticle, an electron-polaron, this interaction causes deformation in the surrounding area, relaxing the molecular bonds and reducing the energy of the LUMO level locally.[16] This effect is mirrored by the formation of a hole-polaron in the HOMO raising the energy of the HOMO level, the combination of the shifts in local LUMO and HOMO level reduce the separation of the electron and hole and aid in the tight binding of the Frenkel exciton that has been formed.

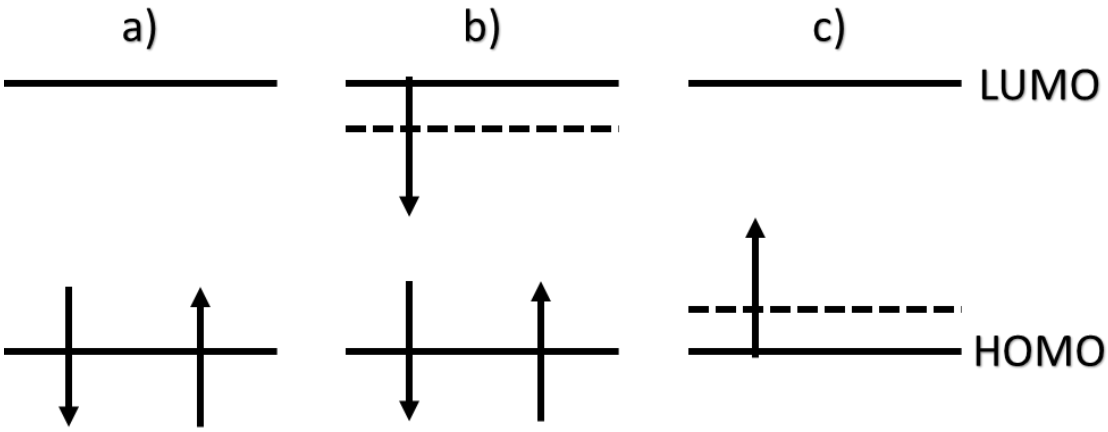


*Figure 2. 7: The interaction between excited electrons/holes and their surroundings via interactions with phonons form electron-polaron/hole-polaron quasiparticles. The formation of these quasiparticles cause shifts in the energy of the LUMO deeper for electron-polarons (b) and the HOMO shallower for hole-polarons (c), a) shows the ground state for comparison.*

The electron and hole which form the exciton can recombine via radiative relaxation of the electron from the LUMO to of one of the vibrational states of the HOMO, via

emission of a photon, in a process termed fluorescence. The radiative relaxation into different vibrational states in the HOMO will cause a slight change in the wavelength of the photons emitted, broadening the emission spectrum of the material. The process of non-radiative decay of the electron from higher vibrational states to the lowest vibrational state in the LUMO is a more rapid process than the radiative relaxation process of exciton recombination as such the electron bound in the exciton will relax to the lowest vibrational state of the LUMO prior to the radiative relaxation process.[17]

The energy level landscape and transitions laid out so far in this section so far have only included a single electron which is far from the case in conjugated polymers. To discuss a system with more than one electron we must consider the quantum numbers discussed in atomic orbitals section, and to simplify the discussion the states and transitions are expressed in the terms of electron wavefunctions. The combined wavefunctions of electron-electron or electron-hole can couple to have a total spin of the system, S, to be equal to zero or one, due to the different combination of the intrinsic ½ spin of the electrons. Those with the overall spin state of zero are classed as singlet states, which have antisymmetric wavefunctions, and those with the overall spin state of one are classed as triplet states, which have symmetric wavefunctions.

The wavefunctions of the ground and the excited singlet states are given by:

$$\Psi_{S_0} = (|\uparrow\downarrow\rangle), \qquad \Psi_{S_1} = \frac{1}{\sqrt{2}}(|\uparrow\downarrow\rangle - |\downarrow\uparrow\rangle) \tag{2.1}$$

Where the upwards arrow in the ket (|  ⟩) denotes the + ½ spin operator and the downwards arrow in the ket the – ½ spin operator. The triplet states can be expressed through three symmetric wavefunctions

$$\Psi_{T_1} = \frac{1}{\sqrt{2}}(|\uparrow\downarrow\rangle + |\downarrow\uparrow\rangle) \qquad \Psi_{T_1} = (|\uparrow\uparrow\rangle) \qquad \Psi_{T_1} = (|\downarrow\downarrow\rangle) \tag{2.2}$$

In the energy landscape the excited triplet states sit at a slightly lower energy than the excited singlet state as there is a lesser repulsion between electrons as they sit in separate orbitals.

For optical transitions between states to occur the spin (intrinsic angular momentum) must be conserved, $\Delta S = 0$, and the orbital angular momentum must be non-zero, $\Delta L \neq 0$.[3,18] In the case of the transition from the excited singlet state to the ground singlet state (fluorescence) the intrinsic angular momentum is conserved and the orbital angular momentum changes from one to zero, this due to the photon emitted having integer angular momentum. It can be seen that for a transition from the excited triplet state to the ground singlet state the spin would have to change from one to zero as such this transition is dipole-forbidden. However, this transition can occur via spin-orbit coupling. Spin-orbit coupling describes the interaction between the spin and orbital angular momentum of a particle which can flip the spin of the electron involved in the transition. The low probability of this transition leads to triplet states having a much longer lifetime than singlet states. The process of emitting a photon in the transition from a triplet to a lower energy singlet state is known as phosphorescence. Phosphorescence from emissive conjugated polymers is very unlikely as the atoms that make up conjugated polymers are typically lighter atoms with lower orbital quantum numbers, whereas heavier atoms have electrons in orbitals with higher angular momentum and as such will more readily be involved in spin-orbit interactions.[13] Further to this the 3:1 ratio of excited triplet states to excited singlet states combined with the lack of phosphorescence from typical polymers limits the theoretical maximum internal efficiency of fluorescent polymers to 25 %.[19]

## 2.3: Device Physics

### 2.3.1: Device Architecture

OLED device architectures most simply can be either ‘standard’ or ‘inverted’, as shown in Figure 2.8. The standard architecture employs a hole-injecting anode as the 1$^{st}$ layer on top of a substrate, the electron-injecting cathode being the ‘top’ layer and the emissive layer sandwiched in-between.[20,21] The inverted architecture is the inverse with the cathode being the first layer deposited onto the substrate and the ‘top’ layer being the anode.[22] Further to the ordering of the contacts defining the architecture of an OLED it is critical to consider the direction in which the device

will emit. Bottom-emitting OLEDs, the most commonly used, emit light from the emissive layer and out of the device through the substrate as such the 'bottom' contact must be a transparent conducting layer, such as indium-tin oxide (ITO), whilst the choice of top contact to be a reflective conductor such as aluminium can increase the emission through the bottom of the device. However, in a top-emitting device the top electrode must be transparent, in this design the substrate can be metallised plastic which offers a potential route to low cost, flexible and high throughput devices. However, it can be challenging to find and deposit effective transparent layers directly on top of the emissive layer without causing damage to the layer. In this thesis all devices fabricated are standard bottom-emission devices.

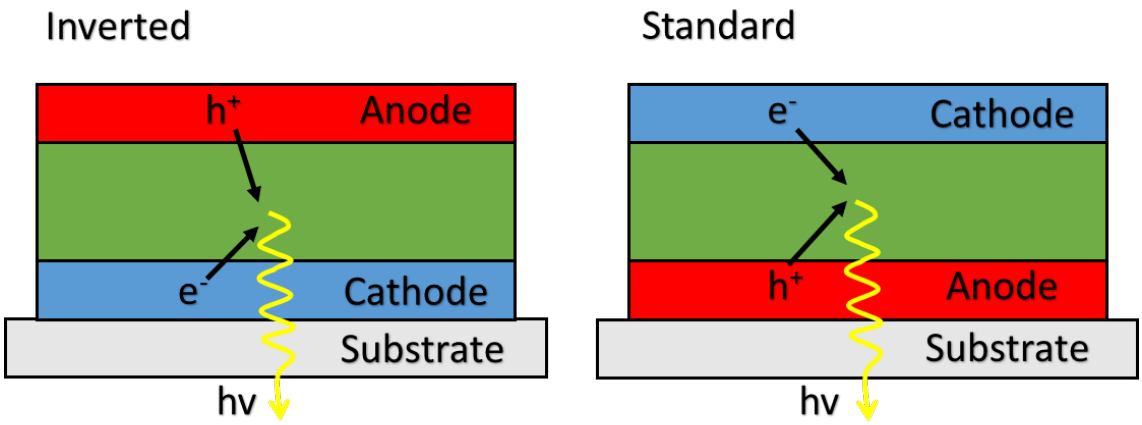


*Figure 2. 8: A schematic of a bottom emission standard OLED architecture and a bottom emission inverted OLED architecture.*

Expanding on the simplistic idea of device structure of an emissive layer sandwiched between two electrodes, in addition devices typically have charge-transport/blocking and injecting layers. The addition of transporting/blocking and injecting layers aid in the injection and balance of flow of charges into the emissive layer by providing intermediate energy steps between the electrodes and the emissive layer.[23,24] As well as this these layers can determine if a device is standard or inverted architecture as materials such as ITO and aluminium can be used as either an anode or cathode, so by inserting a layer above ITO that blocks electrons with a large energy barrier and transports holes ITO can act as an anode and vice versa. Figure 2.9 gives an example vacuum energy level diagram of a device

with intermediate energy steps to aid charge transport through the device and large energy barriers to define the polarity and confine charges in the emissive layer.

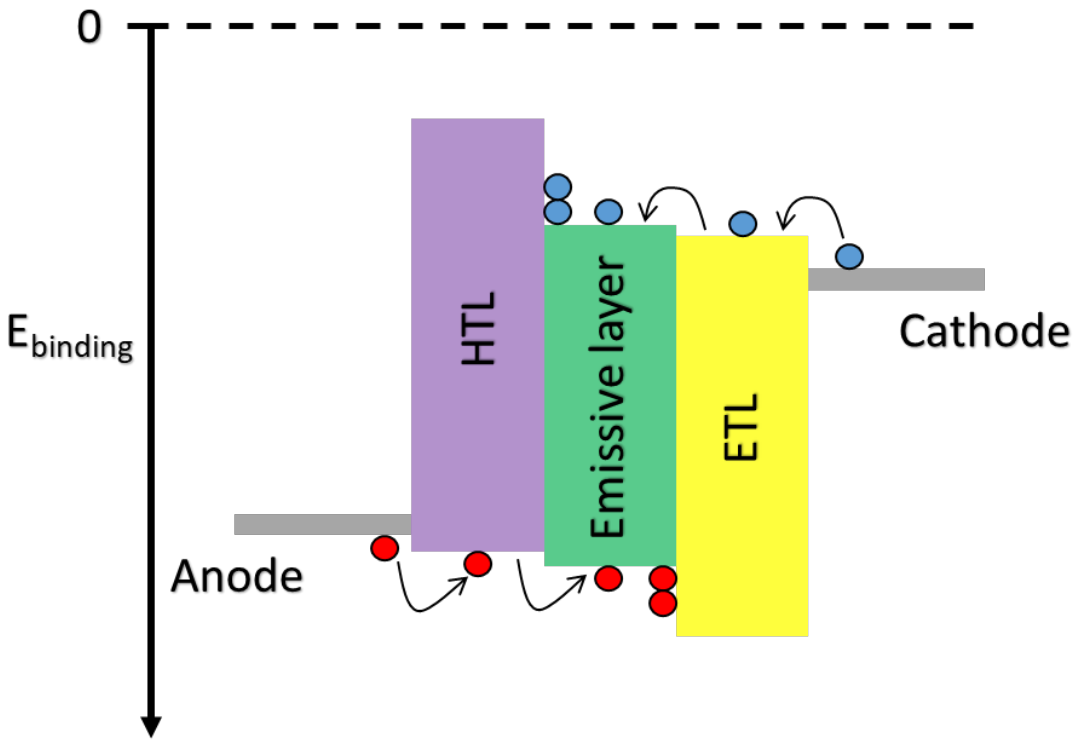


*Figure 2. 9: Vacuum energy level diagram of layers in a device showing the intermediate energy levels (HTL – hole-transporting layer, ETL – electron-transporting layer) between the emissive layer and the electrodes to aid transport of charges (red=holes, blue=electrons) into the emissive layer and large energy barriers to confine charges within the emissive layer improving emission efficiency.*

### 2.3.2: Charge Injection

To begin to use conjugated organics for emissive materials in devices first charges must be injected into the organic material. In this thesis the area of most interest in terms of charge injection is that of metal-organic interfaces. When fabricating a device the work function of the electrodes and HOMO/LUMO levels of semiconductors relative to the vacuum level are often compared in order to fabricate a device with an energy level cascade or to confine charges in a certain layer in order to maximise the performance of devices as illustrated in Figure 2.9.[25] The work function of a material is equal to the vacuum level, where an

electron is unaffected by the potential of the material, minus the fermi level inside the material. The fermi level of a material is the level of the highest energy state which is occupied by an electron, for a metal this is the minimum energy to eject an electron.[26] When two materials are brought into contact the fermi levels of these materials can shift via the formation of an interfacial dipole and the transfer of charges can occur.[27]

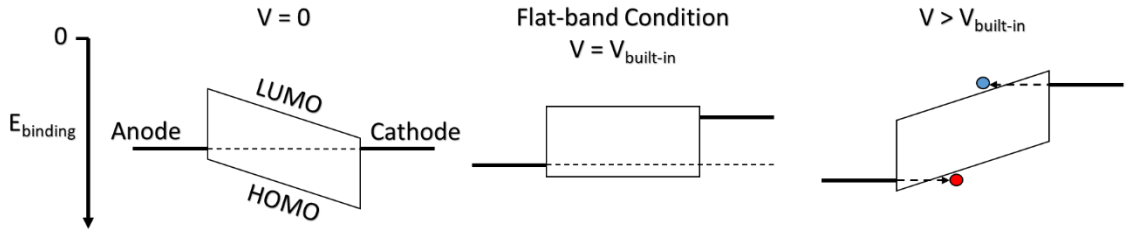


*Figure 2. 10: In the first image the anode and cathode have been connected to the organic layer, a common fermi level is formed across the device. In the second image a voltage is applied equal to the difference in work functions of the anode and cathode, the built-in voltage. The applied voltage tilts the bands of the organic and when the voltage applied is equal to the built-in voltage a flat-band condition is reached. In the third image a voltage larger than the built-in voltage is applied to the device, charges are injected through the triangular barriers, excitons can be formed and emission can occur.*

In the case of metal-organic contacts fermi level alignment occurs can occur if the work function of the metal is shallower than an upper critical Fermi level of the organic for the LUMO level to inject electrons. In order for the Fermi levels to align with the HOMO and inject holes the work function of the metal must be deeper than the lower critical Fermi level.[28] An Ohmic contact is said to have been formed when there is flow of charges across the interface with no injection barrier.[27] In reality however the energy levels at an interface are rarely this well aligned and small barriers (barrier < 0.3 eV) can still exist in quasi-ohmic contacts but these must be overcome to inject charges.[29–32] The first image in Figure 2.10 shows the effect of connecting the anode, cathode and organic material, the difference in work functions of the contacts creates flow of charges in order to equalise the Fermi levels

and a built-in voltage is established. When the voltage applied across the organic is equal to the built-in voltage the flat energy-band condition is returned (Figure 2.10 2nd image) but due to slight barriers at the interfaces charges aren't yet injected into the organic. As the applied voltage is further increased charges begin to get injected into the organic as the barriers are overcome via thermionic emission and through Fowler-Nordheim tunnelling through the triangular energy barrier (Figure 2.10 3rd image).[20,33–35]

### 2.3.3: Charge Transport

Once electrons have been injected into the LUMO of a polymer and holes into the HOMO these excited charges form polarons as described in the organic photophysics section.[36–38] These charges must be transported from near the electrodes along backbone of polymers and between polymer chains in order to form an exciton in the emissive polymer prior to radiatively relaxing.

As discussed in the conjugation and band formation section the semiconducting nature of conjugated polymers means that charges are only delocalised across a molecular segment rather than the entire conjugated chain, this is due to local small changes in the energy levels. The small perturbations in the energy levels can be caused by the surrounding environment for example in a crystalline organic molecule the structure is highly spatially ordered and there is little variation in the energy levels. In contrast, in an amorphous polymer there is essentially no structural order and the spread in energy levels within the bands are much larger.[16]

The process of charge transport across this varied energy landscape within either the HOMO or LUMO can be described as a phonon-assisted hopping process.[39] Where the charge hops between the different energy sub-states of the regions of delocalisation along or between polymer chains.

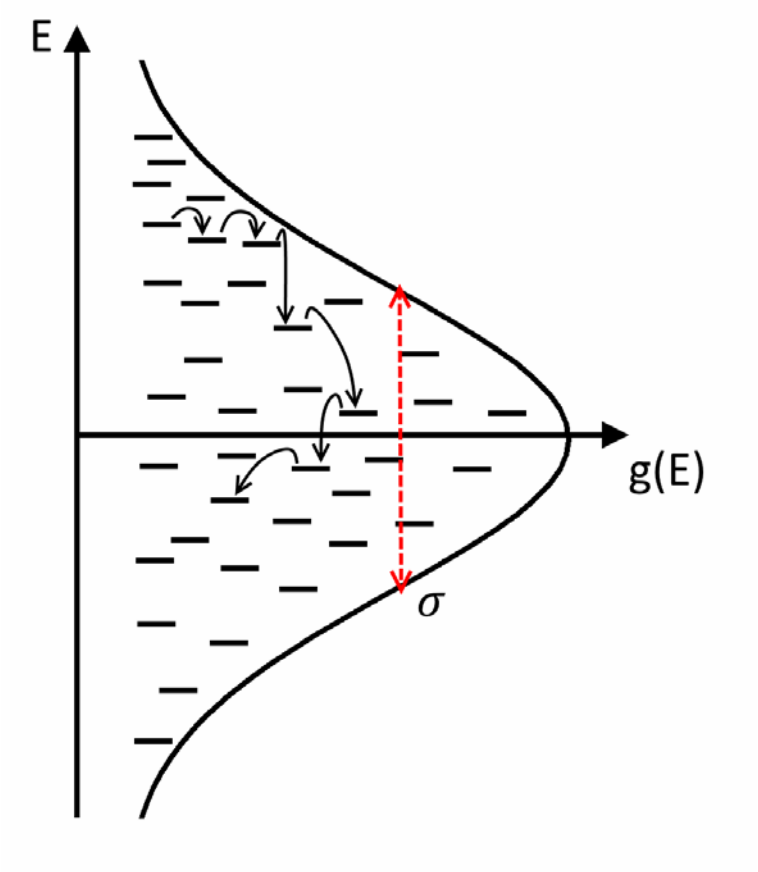


*Figure 2. 11: A visualisation of the Gaussian distribution of energy sub-states (g(E)) within the HOMO or LUMO of a disordered conjugated polymer. The solid arrows demonstrate the diffusion hopping process of a charge from higher to lower energy sub-states (when KT < σ). The dashed red arrow shows the width of the Gaussian distribution of transport states.*

The simplest model to describe this transport comes if the form of the Gaussian disorder model (GDM), where the transport states are modelled as a Gaussian distribution of the disordered energy sub-states with the distribution of states is given by $g(E)$:[40,41]

$$g(E) = \frac{1}{\sigma\sqrt{2\pi}} exp\left(-\frac{E^2}{2\sigma^2}\right) \quad (2.3)$$

Here, $\sigma$ is the width of the Gaussian distribution of transport states and is dependent on the level of disorder in the polymer chain. The spread of energy sub-states allows transport of charges to occur in the absence of an electric field via diffusion from

higher to lower energy sub-states. As such the lower energy tail of the density of states can become a trap states for charges. As the temperature of the system rises diffusion to higher energy sub-states becomes possible due to the assistance of phonons. The hopping rate can then be defined by the Miller-Abrahams equation, where by the probability of hopping occurring (thus rate of hopping ) is dependent not only upon the difference in energy between the two sub-states but also on the spatial separation of the two sites.[42] Under operation as a device the charges in the polymer will be aiding by an electric field across the device, this will not only cause charges to flow in a specific direction rather than random hopping between different energy sub-states but it will tilt the density of states, reducing energy barriers to transport.[20] In device physics the charge transport ability of a material is typically described using the charge carrier mobility, μ. Following on from the GDM Bässler derived the field-temperature dependent mobility via Monte-Carlo simulations to be:[43,44]

$$\mu(T,F) = \mu_0 exp\left[-\left(\frac{2\sigma}{3k_BT}\right)^2\right]\begin{cases} exp\left[C(\sigma^2 - \Sigma^2)E^{1/2}\right] & \Sigma \geq 1.5 \\ exp\left[C(\sigma^2 - 2.25)E^{1/2}\right] & \Sigma < 1.5 \end{cases} \quad (2.4)$$

Equation 2.4 incorporates both the energetic disorder, $\sigma$, and the positional disorder, $\sum$. $\mu_0$ is the zero-field mobility of the material and C is an empirical constant related to intermolecular spacing. As such it can be seen that the mobility of a material can be increased by reducing the energetic and spatial disorder such as by increasing the conjugation length of the polymer used or by increasing the crystallinity of the polymer layer.[45]

### 2.3.4: Unipolar Charge Transport

If a metal/organic contact is considered Ohmic then the current through a simple metal/organic/metal driven device is limited by the mobility of the organic. If the architecture of a device is designed such that the workfunctions of both electrodes match either the HOMO or LUMO of the organic material sandwiched in between them then Ohmic contacts can be formed, and only one type of charge can be injected or extracted. This device structure is known as a unipolar device and by only allowing for the injection and extraction of one type of charge the transport

properties of the organic material for that charge can be investigated. In unipolar devices at low applied fields (low driving voltage) the current is dependent on the density of charges intrinsically within the organic, with charges diffusing through the organic material (Ohmic regime).[46] As the applied voltage is increased further the number of charges injected into the organic increase such that there is a build-up of carriers and the electric field at the electrode is zero, this is the space charge regime. In this regime the current is no longer dependant on the density of charges but instead is dependent on the mobility of the organic and the applied electric field. The space-charge-limited current, $j_{SCL}$, can be calculated using the Mott-Gurney relationship:[47]

$$j_{SCL} = \frac{9}{8}\varepsilon_0\varepsilon_r\mu\frac{E^2}{L} \tag{2.5}$$

Where $\varepsilon_0$ is the permittivity of free space, $\varepsilon_r$ is the relative permittivity, $\mu$ is the mobility of the organic, E is the applied electric field and L is the thickness of the layer. However, it has been shown that the mobility increases with applied field as such a Poole-Frenkel field dependence can be used to modify the Mott-Gurney relationship to account for this as shown in Equation 2.6:[48–52]

$$j_{SCL} = \frac{9}{8}\varepsilon_0\varepsilon_r\mu_0\frac{E^2}{L}\exp(\gamma\sqrt{E}) \tag{2.6}$$

Here $\gamma$ is the field dependent factor and $\mu_0$ is the zero-field charge mobility of the organic. This equation allows for the modelling of j-V curves of materials of known properties or the extraction of mobility from the gradient of the space-charge-limited current. However, when testing devices it is challenging to deconvolute the Ohmicity of a contact and the mobility of the material being studied. The mobility of a material can be measured using the time of flight (TOF) method where a laser pulse generates charges via photoexcitation near one electrode and the mean time of arrival is recorded at the far electrode, from this and knowledge of the electric field and thickness of the sample the mobility can be calculated. The TOF technique requires amongst other conditions the studied material is of high purity, of low disorder (as disorder broadens the measured times) and crucially that the material thickness must be much larger than the penetration depth of the excitation light.[16,53] This leads to a thickness requirement on micron scale which is

challenging to uniformly deposit for polymers and not representative of a typical device structure. A method that can be used to investigate the transport of a material within the structure of a unipolar device is the injection efficiency. The injection efficiency ($\eta$) is determined by calculating the theoretical space-charge-limited current ($J_{SCL}$) for a thickness of the material being investigated and comparing it to the measured current ($J_{measured}$) in the space-charge-limited regime:[54,55]

$$\eta = \frac{J_{measured}}{J_{SCL}} \tag{2.7}$$

The injection efficiency can be used to probe the Ohmicity of a contact with a specific material.[56] Comparing the injection efficiency, at the same applied electric field, of identical material systems but differing thickness of the studied material or identical structure where the studied layer has been deposited using a different technique allows for comments to be made on the charge transport of the bulk studied material as the Ohmicity of the contact should be equivalent.[57,58]

### 2.3.5: Exciton Diffusion

Upon making contact between the electrodes and a polymer, applying a driving voltage high enough to inject electrons into the LUMO and holes into the HOMO of the polymer which are then swept along and between the polymer chains towards the alternate electrodes, the next step towards light emission is the binding of these charges to form excitons. When an excited electron hops with the aid of the applied electric field onto a molecule in which a hole is present in the HOMO the previously described tightly bound quasiparticle, an exciton, can form between the two charges.

Although the exciton is a relatively short-lived quasiparticle it can still travel along or between polymer chains prior to the components undergoing radiative recombination. The neutral quasiparticle is unaffected by the applied electric field but can travel through a diffusion process allowing the exciton to 'hop' from one delocalised region to another. The average distance an exciton can diffuse ($L_D$) prior to recombining is defined by a combination of the lifetime of the exciton ($\tau$), and the diffusion coefficient (D) which is dependent on the properties of the polymer.[59]

$$L_D = \sqrt{D\tau} \tag{2.8}$$

In conjugated polymers the average diffusion length is typically sub-ten nanometres.[60] There are two energy transfer mechanisms which drive the diffusion of excitons in organics; Förster resonance energy transfer (FRET) and Dexter energy transfer.[61–63] FRET, summarised pictorially in Figure 2.12a, occurs when the exciton on a molecule couples via a non-radiative dipole-dipole interaction with an electron in the ground state of the molecule the exciton is transferring to. The electron in the exciton then relaxes non-radiatively, transferring the energy to the electron in the ground state of the molecule being transferred to, promoting this electron to the excited state thus forming an exciton in this secondary molecule. The efficiency of this process decreases rapidly with spatial separation ($r^{-6}$) between the molecules involved in the transfer.[40,61] Dexter energy transfer involves the direct transfer of the excited electron from the LUMO of one molecule to another and the direct transfer of an electron in the HOMO in the inverse direction. This process relies on wavefunction overlap and as such decreases in efficiency exponentially with spatial separation, as such Dexter energy transfer occurs over shorter distances than FRET.[64,65]

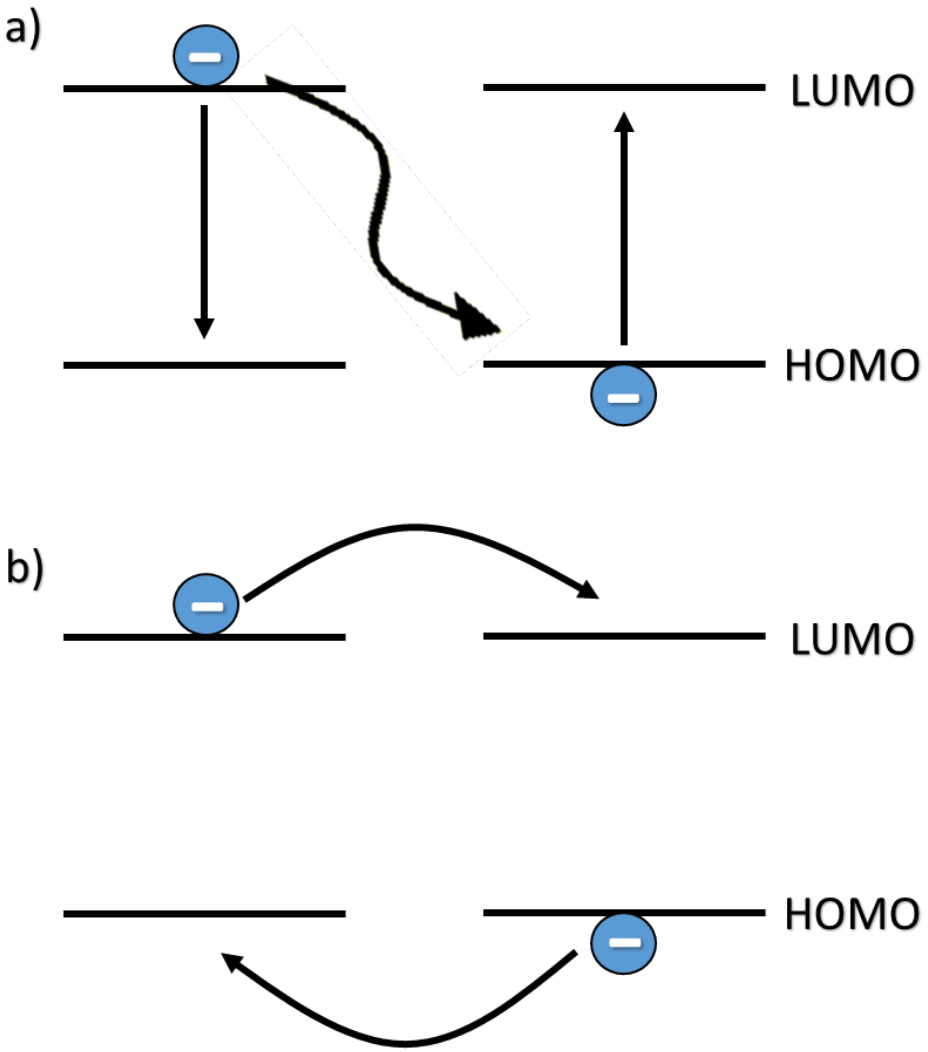


*Figure 2. 12: a) A schematic diagram of the process of exciton diffusion via Förster resonance energy transfer (FRET). The energy of the excited electron in the exciton is transferred to the ground state electron in a neighbouring site via a non-radiative dipole-dipole interaction, exciting the neighbouring electron and forming an exciton in the neighbouring site. b) A schematic diagram of the process of exciton diffusion via Dexter energy transfer whereby an excited electron is transferred directly to the LUMO of another molecule and an electron is the HOMO is transferred in the inverse direction.*

## 2.4: Lighting Standards, Concepts and Characterisation of Devices

### 2.4.1: The Human Eye

An understanding of how the human eye detects light is of great importance when considering the description and characterisation of organic light-emitting devices. The eye much like other optical detectors has a wavelength dependant spectral response. As light passes into the eye UV-light (below around 400 nm) is filtered out and the sensitivity to wavelengths beyond 600 nm drops rapidly to negligible by 700 nm. This occurs as human eyes uses three types of cones to detect light, each sensitive to different wavelength regions, the combination of these wavelength dependent sensitivities for an average person can be described by the photopic response curve, Figure 2.13.[20]

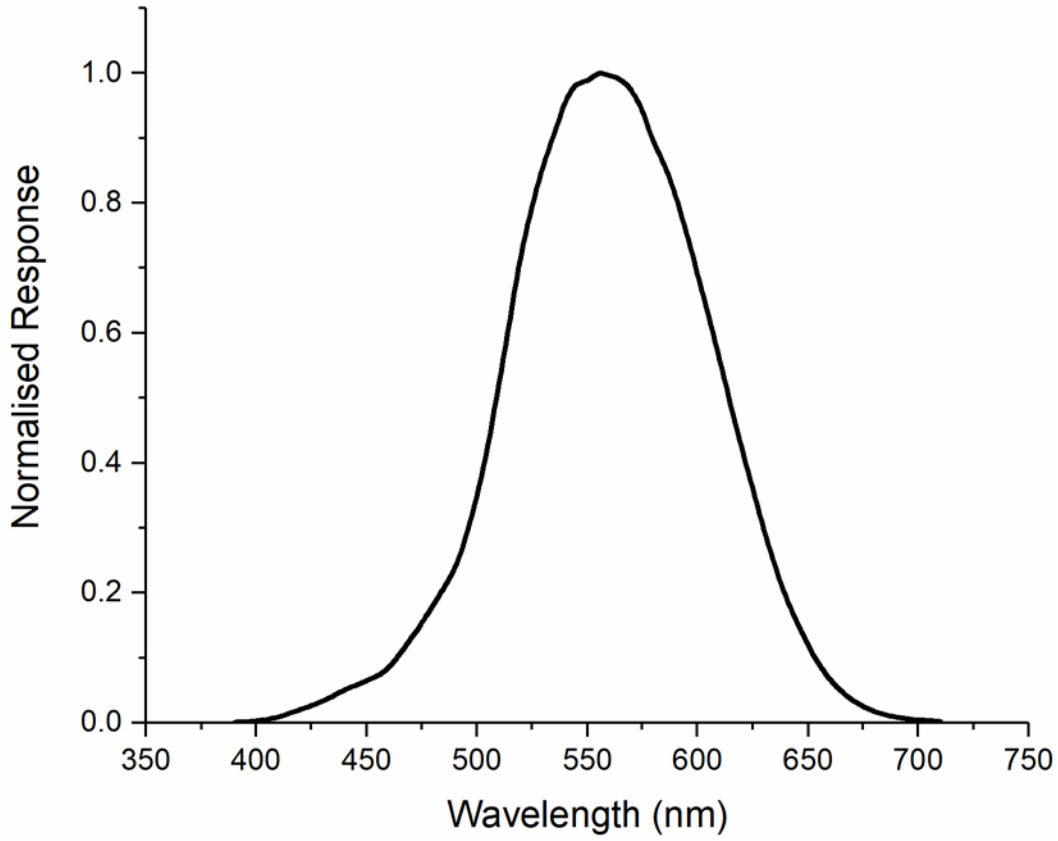


*Figure 2. 13: The normalised Photopic response curve, demonstrating how the sensitivity of the average human eye varies with the wavelength of light.*

It can be seen from the photopic response of the eye that the peak sensitivity is at 555 nm, which is green light and the maximum theoretical efficiency is 683 lm $W^{-1}$. This increased sensitivity to certain wavelength regions and diminished sensitivity at the visible wavelength extremes must be considered when fabricating OLEDs in order to achieve the desired colour but also when testing devices and performance.[66]

### 2.4.2: Quantifying Colour

When discussing OLEDs and lighting it is important to define the colour of the emitter being discussed in a parametric manner. There are a number of approaches in which to do this which summarise the full emission spectrum into one or more characteristics numbers. Correlated colour temperature (CCT) describes the temperature of a blackbody which has a colour which most closely represents the colour emitted by the non-blackbody emitter being described. However, describing the emission of a device using a CCT alone does not precisely quantify the emission. A more comprehensive technique for characterising the colour of a light source is the 1931 Commission Internationale de l'Eclairage (CIE) colour coordinates.[67] The CIE colour space is a plot of all possible visible colours on which an emission spectrum can be mapped using the CIE xy co-ordinates. The CIE xy mapping coordinates are calculated to take into account the components that make up the photopic response curve and therefore the perceived intensity of different colours. A CIE 1931 chromaticity diagram is shown in Figure 2.14 with a Planckian Blackbody locus superimposed.

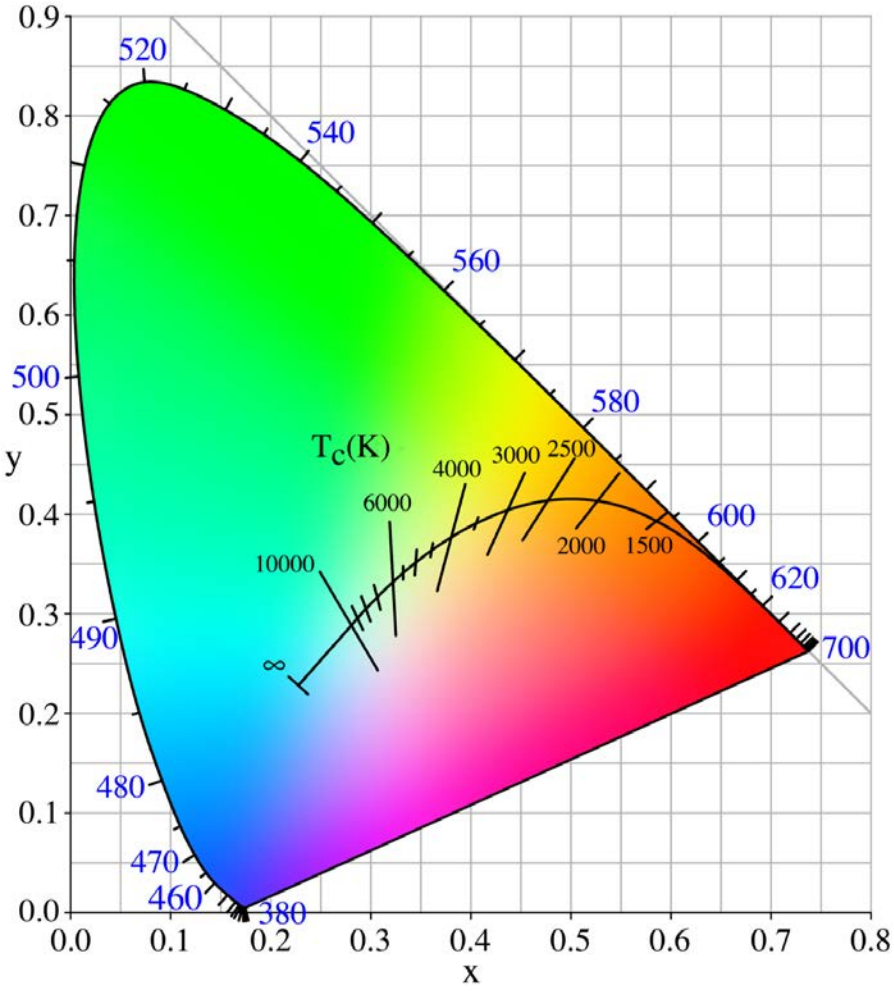


*Figure 2. 14: CIE 1931 xy chromaticity space in which the coordinates are used to characterise the colour of emission from LEDs. The Planckian locus, which shows the temperature a blackbody would have to be to emit at the colour it is superimposed onto in the colour map, across a range of temperatures.*

### 2.4.3: White-Light-Emitting Polymer

The focus of this thesis is to demonstrate the possibility to deposit the multiple layers require for an OLED via ultrasonic spray coating as the initial step towards large area coating and industrialising of the process to reduce the cost of fabrication with the view of using polymer OLEDs for lighting. To aid in the demonstration of ultrasonic spray-coating as a route to affordable lighting from OLEDs the emissive polymer used in this thesis emits broadly over the visible spectrum to appear white. In Section 2.2.4 (conjugation and band formation section) it was explained how

delocalisation length in polymer chains dictates the bandgap of the polymer, and in Section 2.25 it was explained how the size of the bandgap coupled with the range of vibrational states that can be radiatively relaxed into dictate the wavelengths of the emitted photons. As such in order for the emission of a polymer to be perceived to be white the polymer must emit at a range of different wavelengths such that when combined, and taking into account the photopic response of the eye at different wavelengths, the emission appears white. There are three main emissive layer architectures, demonstrated in Figure 2.15, in which OLEDs can be fabricated to produce white light: Multiple emissive layers, a blend in a single layer or copolymer emissive layer.

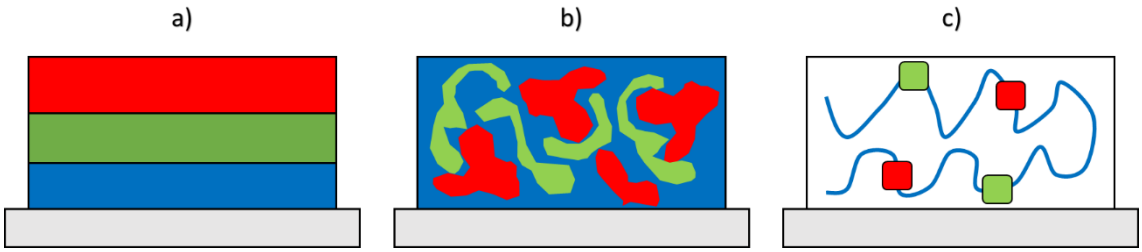


*Figure 2. 15: Three routes to white light emission for OLEDs: a) A multilayer structure where separately emitting green, blue and red layers are combined to produce a broad white emission. b) A blend of polymers in a single layer which emit different colours to combine for white emission. c) A single copolymer layer in which a blue emitting polymer backbone is combined with red or red and green chromophores in a specific ratio to emit a broad spectrum that appears white.*

White light can be emitted from a multilayer emissive structure where a combination of different layers that separately emit blue and red in a dual layer system or blue, red and green in a triple layer system. This route is typically used for evaporated small molecule devices as depositing multiple emissive layers sequentially can be challenging via solution processing required for polymers as orthogonal solvents must be used for the sequential layers limiting the possible polymers that can be cast to those that are soluble in such solvents.[68,69] To overcome the challenges of solution processing sequential emissive layers an alternate route of casting a blend of different colour emitting polymers in one layer

to emit white light can be used.[70–73] This approach comes with many challenges: a common solvent for the blend components must be used, limiting polymer choice; the use of different solvents and deposition processes can affect the morphology of the cast polymer blend film.[74–76] Devices incorporating polymer blends require fastidious control over the morphology as different sized phase domains / level of phase separation effect the charge and exciton dynamics within the layer which effects the device performance.[77]

A third route involves the use of a copolymer, in which red or red and green chromophores are copolymerised with an energetically deep blue emitting host polymer backbone.[78,79] Charges can be transferred along the backbone, between the polymers chains and from the host into the narrower bandgap red or red and green emitting units with excitons formed in the different sections of the polymer and radiatively recombine and emit photons of the wavelengths related to the units emitting. As such by controlling the ratio of host polymer units and the other emitting units during the copolymerisation process the colour of emission can be tuned. In this thesis a single emissive layer structure is employed where a white-light-emitting copolymer containing red and blue emitting chromophores is used to fabricate devices. Any further details of the properties of the white-light-emitting copolymer used in this thesis such as structure or molecular weight are not disclosed due to the commercially sensitive nature of the product.

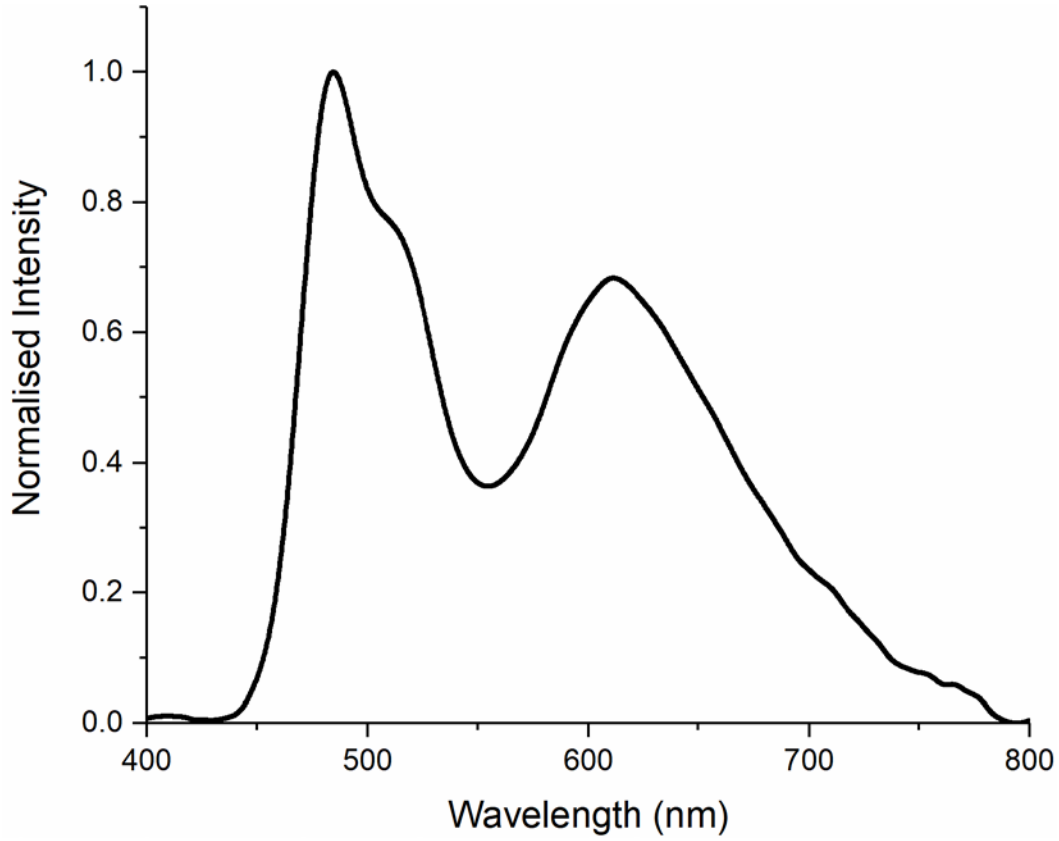


*Figure 2. 16: The electroluminescent spectrum of a device driven at 10 V with the emissive layer being the white-light-emitting copolymer used in this thesis.*

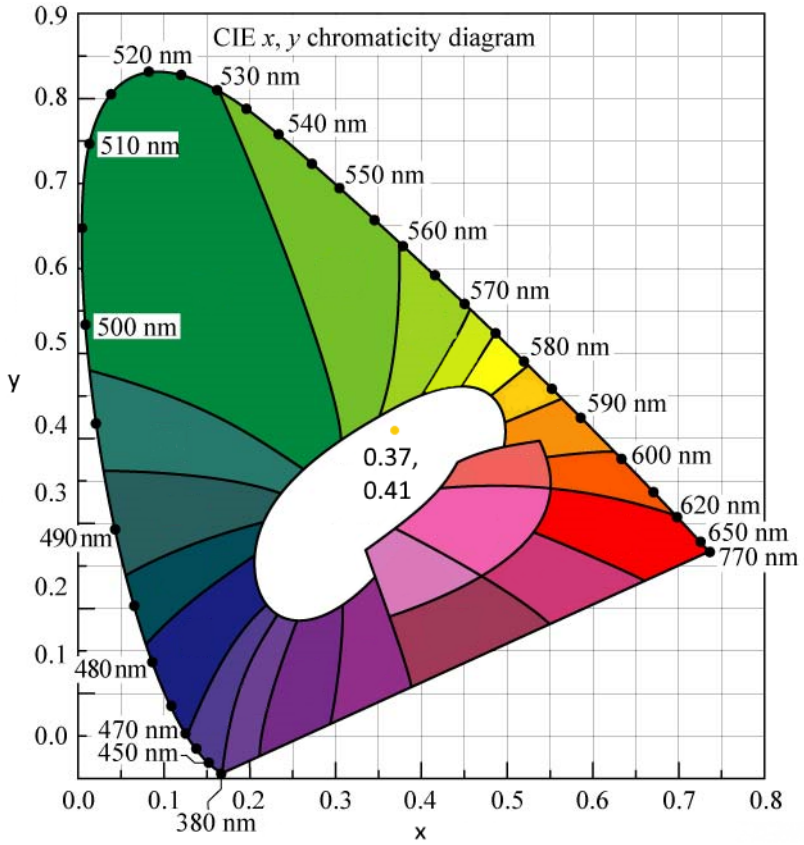


*Figure 2. 17: CIE 1931 xy chromaticity space on which the white are coloured region are split. The colour coordinates of 0.37, 0.41 are marked which have been calculated from the spectrum in Figure 2.16 which shows the electroluminescent spectrum of a device containing the white-light-emitting copolymer used in this thesis. The correlated colour temperature of this polymer is 4455 K.*

The devices in this thesis incorporate a white-light-emitting copolymer with a CIE xy coordinate of 0.37, 0.41 and correlated colour temperature of 4455 K when driven at 10 V (9022 cd $m^{-2}$).

### 2.4.4: Device Characterisation

In order to test and characterise an OLED a voltage must be applied in order to inject and drive the flow of charges through the device to allow excitons to be formed in the emissive layer, radiative recombination to occur and light to be emitted. As such devices are tested by applying a voltage sweep, measuring the current across the device and measuring the light emitted. As discussed above the photosensitivity of the 'average' human eye should be taken into account when described the

performance of an OLED as such photometric metrics should be used to quantify the emission. The luminance flux, lumens (lm), is the rate of flow of radiant energy taking into account the photopic response of the eye. Candela (cd) (or luminous intensity) is defined as the luminous flux per solid angle.[20,80] An OLED can be considered to be a Lambertian emitter if the emission is isotropic, emitting with equal radiance across any point of the forward hemisphere, if this is the case then the luminance can be defined as the luminous intensity divided by a small area over which the light in emitted given by the units, cd $m^{-2}$.[81]

The luminance is measured as the voltage sweep is applied to a device, the luminance-voltage and current-voltage curves can then be used to characterise the devices. The luminous efficiency (Current efficiency), cd $A^{-1}$, can be calculated by the ratio of luminance to the current density (current divided by pixel area). The luminous power efficiency (power efficiency), lm $W^{-1}$, can be calculated by dividing the luminance by the combination of current density times the voltage, then multiplying the final result by $\pi$ as for a Lambertian source 1 lm = $\pi$ cd.[66] As such the current efficiency allows the analysis of the influence of current and power efficiency the influence of applied voltage.

The current-voltage and luminance-voltage curves can also provide important information about the device being tested. Figure 2.18 shows example curves which demonstrate the effect of varying energy level alignment in devices and varying the thickness of the emissive layer in a device.

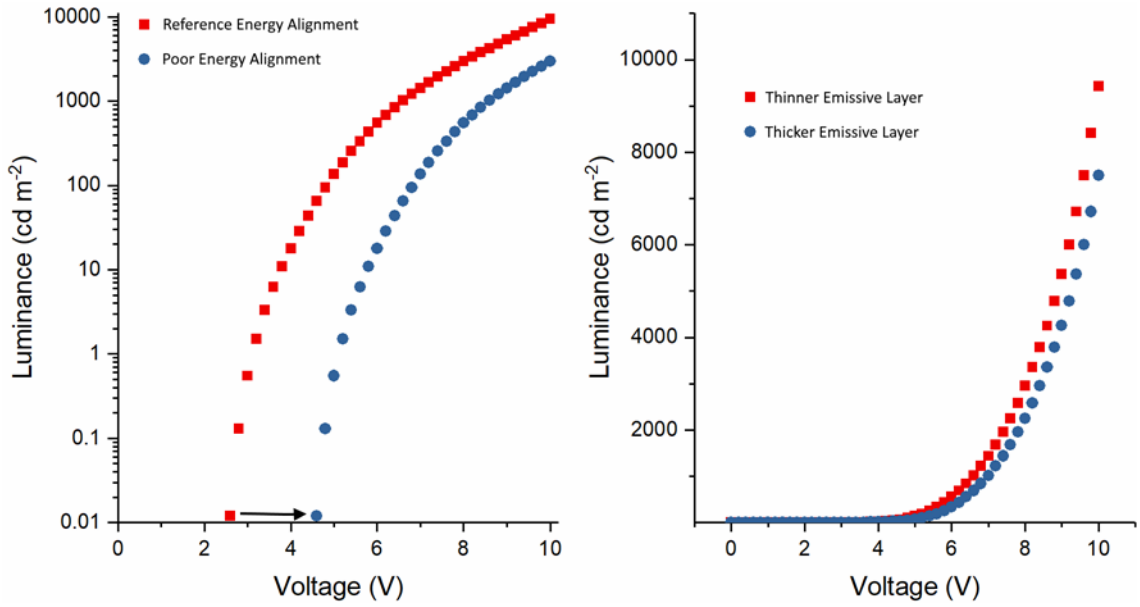


*Figure 2. 18: The left-hand graph demonstrates the increase in turn-on voltage when the energy levels of a devices are poorly aligned. The right-hand graph demonstrates the effect of increasing the thickness of the emissive layer on the L-V curve.*

As discussed in the charge injection section an ideal OLED would have a perfect Ohmic contact between the electrodes and the hole- and electron- transporting layers. The HOMO of the hole-transporting layer and the emissive layer would be energetically aligned, the LUMO of the electron-transporting layer and the emissive layer would be perfectly aligned. In this scenario as the voltage applied to the device increases the field across the device would increase tilting the bands in the device until the flat-band condition was achieved and at this point there would be no barriers for injection from the electrodes all the way into the emissive layer and after initial injection emission would begin to occur. The voltage required for emission to begin to be detected is defined as the turn-on voltage and in this ideal case would be equal to the built-in voltage of the device. However, as discussed earlier the perfect alignment between metal electrodes and organic transport layers is difficult as such this increases the barrier to injection and thus increases the turn-on voltage. Further to this, it is likely the HOMOs of the transport and emissive layer and LUMOs of the transport and emissive layer will not be perfectly aligned, for example the wide bandgap polymers required as a component for white emission have very deep HOMO levels, as such these can potentially add barriers to injection

also contributing to the increase in turn-on voltage from the ideal scenario.[82,83] The left-hand graph in Figure 2.18 demonstrates the increase in turn-on voltage on the luminance-voltage curves for a device with worse energy alignment. Current and luminance-voltage curves can vary when changing the thickness of the emissive layer in devices this is reflected in changes in the efficiency and gives a route for finding the optimum thickness of the emissive layer. If the energy levels of a device are well aligned and the contacts with the electrodes are Ohmic then the typically low mobility of organics will be the limiting factor for the current. The luminance of OLEDs scales with the current as the greater population of charges injected into the emissive layer the more excitons can form and the more photons can be emitted. As such as the emissive layer is thinned in an OLED the current and luminance for the same voltage will typically increase. However, as the emissive layer is thinned further the luminance will not increase proportionally with current as some charges may be swept through the emissive layer and out through the rest of the device before an exciton can formed, increasing the leakage current. Also Excitons formed within 30 nm of the electrodes can be quenched further limiting the increase of luminance with current thus the efficiency will be lower.[84,85]

Another issue with thinning the emissive layer is the current across the device is higher for the same voltage and the thermal stress on the thin emissive layer is higher, this can create 'hot spots' and the probability of thermal / electrochemical degradation during a sweep of same voltage range is increased which leads to delamination of the layers.[86,87] Also if there are any impurities that have contaminated the device, the thinner the device the more likely the impurity is to have spanned from one electrode to another thus electrically shorting the device. If a thicker emissive layer is deposited within a device the current for the equivalent voltage will decrease as will the luminance, as shown in the right-hand graph of Figure 2.18, but typically the peak efficiency will increase. As with the luminance not increasing proportionally with current for thinner emissive layers the inverse is applicable here as there will be less charges being swept through the entire emissive layer without forming an exciton and emitting, also thicker emissive layer will minimise exciton quenching as such the efficiency can increase as the emissive layer thickness is increased. However, as the emissive layer is made thicker less charges

are injected into the emissive layer for the same voltage as such the probability of forming an exciton in the emissive layer prior to the injected polaron undergoing non-radiative relaxation decreases. Secondly, with a thicker emissive layer the chance of reabsorption of the emitted photon within a layer of the device is increased as the photon has a longer path to escape the device.[85] As such the optimisation of the thickness of the emissive layer in an OLED is a compromise between efficiency and luminance.

## 2.5: Solution Processing

Organic semiconducting materials such as small molecules and polymers can be used to efficiently convert electricity to light in organic light-emitting diodes (OLEDs). Polymer LEDs have several advantages over inorganic LEDs including low-temperature processing, ambient processing, ability to tune physical properties by tuning chemical structure, greater mechanical flexibility and critically the ability to process from solution. The combination of these advantages when processing polymer layers allows for the rapid optimisation of new materials on lab scale and opens up the possibility to coat over large areas and onto delicate flexible substrates.

### 2.5.1: Wetting

There are a number of different coating techniques used for the fabrication of OLEDs. The main aim of the various different coating techniques is to repeatedly fabricate thin films of uniform thickness, no gaps or flaws, with smooth surface morphology. There are a number of factors that can affect the quality of films fabricated depending on the coating method but one universal issue is the wetting of the solution to the substrate.

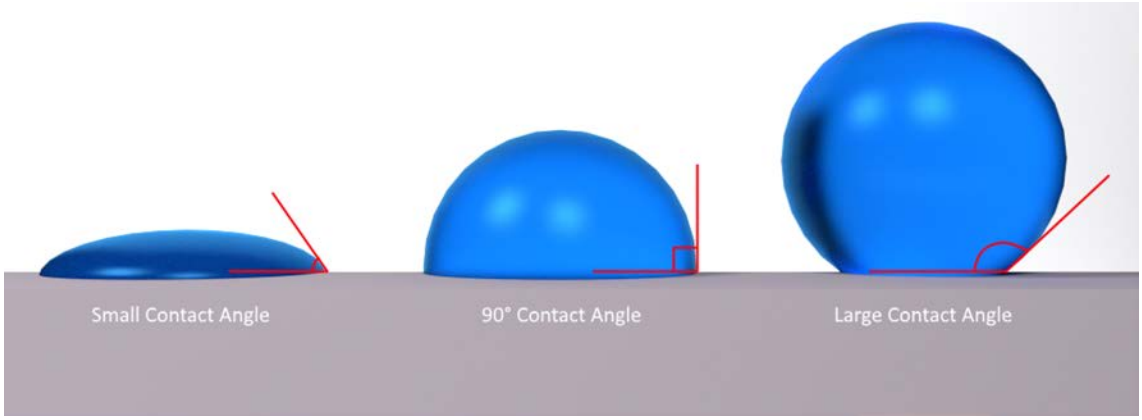


*Figure 2. 19: Three droplets on a substrate demonstrating: firstly, good wetting with a small contact angle. Secondly, poor wetting with a 90° contact angle and thirdly, the droplet de-wetting from the substrate shown by a contact angle over 90°.*

Wetting is the degree to which a liquid can maintain contact with a solid surface. It is determined by the combination of interfacial energies between the solution, the substrate and the air. Surface energy of a liquid results from the greater attraction of the liquids molecules to themselves than the attraction of the liquid molecules to the substrate. The greater the interfacial energy difference between the solution/substrate ($\gamma_{SL}$) and substrate/air ($\gamma_{SA}$) the larger the contact angle ($\theta_e$) (where is the $\gamma_{LA}$ liquid/air interfacial energy).[88]

$$\cos(\theta_e) = \frac{(\gamma_{SA} - \gamma_{SL})}{\gamma_{LA}} \quad (2.9)$$

The smaller the contact angle the more the solution spreads out across the substrate forming a more uniform film. If the contact angle is greater than or equal to 90° beads of the solution are formed as the solution does spread and it de-wets from the surface.

### 2.5.2: Spin Coating

Spin coating, a form of wet processing, is a commonly used lab technique of producing both solar cells and OLEDs. To spin coat a thin film the solution is deposited onto a rotating substrate. The solution is spread out across the substrate due to the centrifugal (centripetal) force. The substrate is spun until excess solution is ejected, the solvent evaporates and the thin film is dry. The thickness of films ($h_f$)

is dependent on the concentration of the solution (C) as well as the angular velocity of the substrate (Ω), as shown in Equation 2.10.[89]

$$h_f \propto \frac{C}{\Omega^2} \qquad (2.10)$$

Spin coating is used widely for small area devices due to the high level of control over film thickness, morphology and surface topography allows for the repeatable fabrication of thin films. Spin coating can be used to scale up to larger area devices, to a certain extent, but it is highly wasteful and not easily adapted for industrial processing.[90]

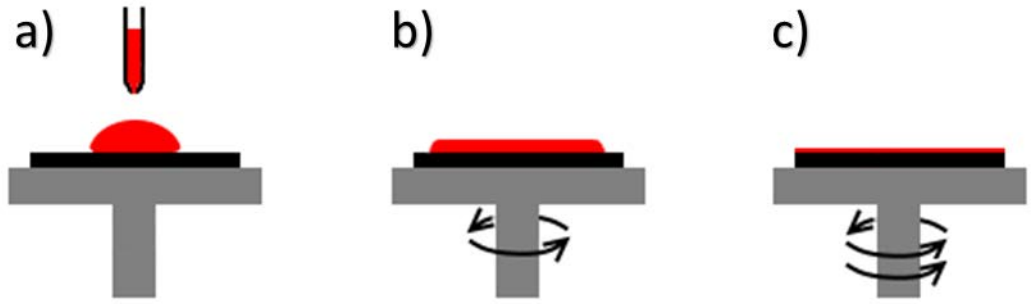


*Figure 2. 20: A schematic of the stages involved in fabricating a thin film via spin coating. a) Depositing the solution onto a static substrate from a pipette, for dynamic spin coating the substrate would be rotating at this stage. b) and c) demonstrate a slower and quicker spin speed of the substrate respectively showing the relationship between spin speed and film thickness described in Equation 2.10.*

### 2.5.3: Roll-to-Roll Compatible Deposition Techniques

The possibility of processing polymer thin films from solution at low temperatures is a possible route towards industrialising the fabrication process of large area OLEDs. In the field of electronics the route to industrialised fabrication of devices is thought to be via roll-to-roll processing. Roll-to-roll processing (R2R) requires a flexible plastic substrate which is stored wound on a reel, unravelled at high speed, coated before being re-wound onto a storage reel in a similar process to the printing of newspapers.[91] In order to industrialise the fabrication process of OLEDs a large

area, high-throughput coating technique must be established which is compatible with roll-to-roll processing.[92]

### 2.5.4: Ink-jet Printing

Ink-jet printing is used widely in homes and offices as a way of producing hard copies of electronic images and text. Over the past decade researchers have adapted the technology successfully printing transistors, nano-sized silver colloids, OLEDs and other electronics.[93–98]

The printing head contains a reservoir of ink (deposition solution) with an open nozzle at the bottom, the narrow diameter of the nozzle combined with the surface tension of the ink stops it from flowing from the printing head. The solution is expelled from the printing head in individual droplets which are formed from one of two methods; thermally or piezoelectrically. In thermal ink-jet printing (often referred to as bubble jet) a small area within the head is rapidly heated causing an increase in pressure. The increase in pressure allows the ink to overcome the surface tension forcing a droplet out of the nozzle.[53] In a Piezoelectric ink-jet printer a current is applied to a piezoelectric material within the printing head which causes it to rapidly expand in volume, increasing the pressure within the printing head, leading to the formation of an ink droplet in the same method as thermal ink-jet printing.[53] Some ink-jet printers accelerate droplets towards the substrate using an electric field, and deflect excess droplets, but this limits the possible deposition solutions to those which are charged. The printing head sweeps back and forth perpendicular to the motion of the substrate as the droplets are ejected, coating the substrate.

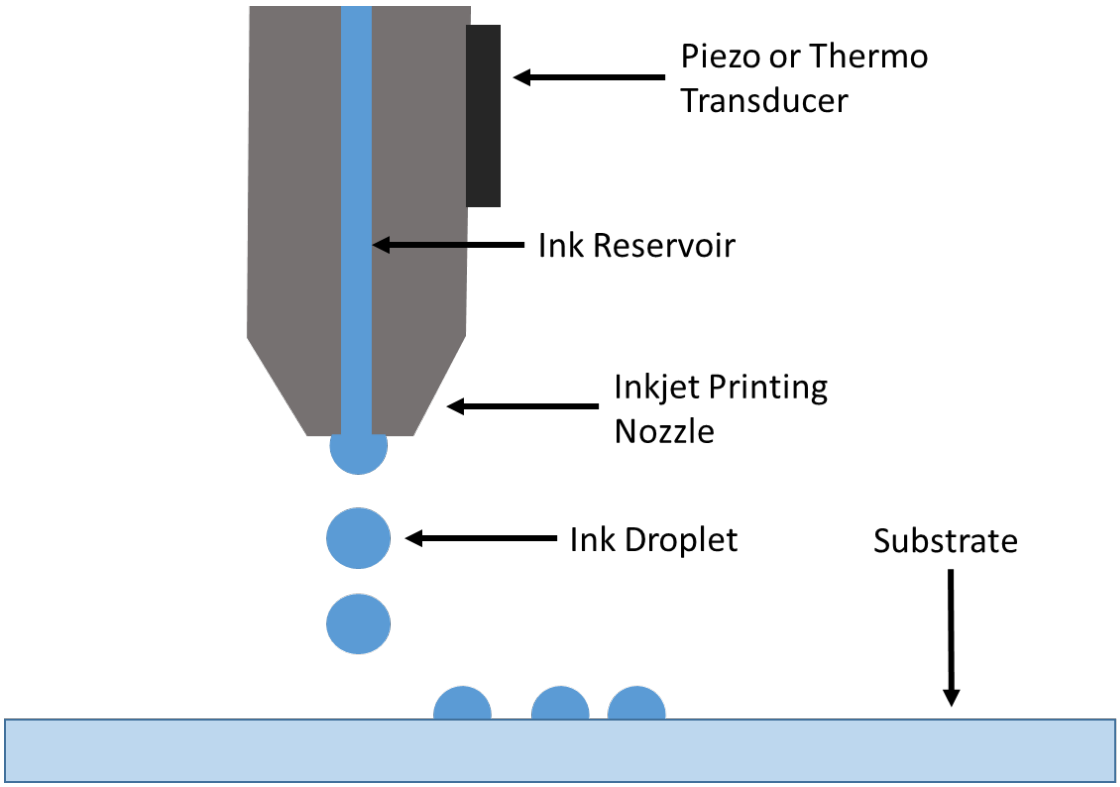


*Figure 2. 21: A schematic of an ink-jet printer.*

The deposition by individual drops gives high control over the thickness of cast films via the relationship shown in Equation 2.11.[99]

$$h_f = N_d V_d \frac{c}{\rho} \tag{2.11}$$

Where $N_d$ is the number of droplets per unit area, $V_d$ is the volume of the droplets, $c$ is the concentration of solution and $\rho$ is the density of material in the final film.

Ink-jet can be used to print or coat organic materials and has the potential to scale up to fabricate large-area OLEDs. Ink-jet printers for electronics have been developed and are now commercially available but there are still some doubts over the adaptability of the technology for mass production of OLEDs. The complexity of drop by drop deposition limits the speed at which a substrate can be coated such that the technique could be adapted for R2R processing but the throughput would be lower compared to other possible coating techniques.

### 2.5.5: Blade Coating and Slot-Die Coating

Blade (Knife) coating is a technique which has already been adapted for use in R2R processing of OLEDs.[100] Blade coating consists of a moving flexible substrate with a knife just above it at one point which can be fixed at different heights varying the size of the gap between the knife edge and substrate. The ink is fed continuously onto the substrate in front of the blade, as the substrate moves below the blade only ink of height less than the gap between the knife edge and substrate is coated onto the substrate, the remaining ink is held back.[101]

Blade coating is a simplistic technique and as such it doesn't allow for much customisation, the width of the film can only be changed between batches and patterned deposition isn't possible. A benefit of blade coating is that very smooth films can be obtained even on rough surfaces and the thickness of the film is proportional to the distance between knife edge and substrate ($g$) as shown in Equation 2.12, although the velocity of the substrate can cause small variations.[99]

$$h_f = \frac{g}{2}\left(\frac{c}{\rho}\right) \tag{2.12}$$

Slot-die coating is a similar technique which is already used for R2R processing of solar cells and OLEDs.[99,102,103] In Slot-die coating the ink is pumped into a coating head which is fixed just above the moving substrate like the blade in blade coating. As the ink flows from the head onto the substrate a standing meniscus is formed due to the narrow gap and a continuous film is deposited as the substrate moves on.

The volume of ink pumped through the head can be varied to match the speed of substrate so all the ink supplied to the coating head is coated with no loss. Equation 2.13 shows the thickness of deposited films is dependent on the flow rate of the ink ($f$), the speed of the substrate ($S$), the width of film deposited ($w$), the solution concentration ($c$) and the density of material in the final film ($\rho$).[99]

$$h_f = \frac{f}{Sw}\left(\frac{c}{\rho}\right) \tag{2.13}$$

Blade and slot-die coating can be used with a wide range of ink viscosities and due to the way the ink is deposited dewetting is much less of an issue compared to techniques such as ultrasonic spray and ink-jet coating.

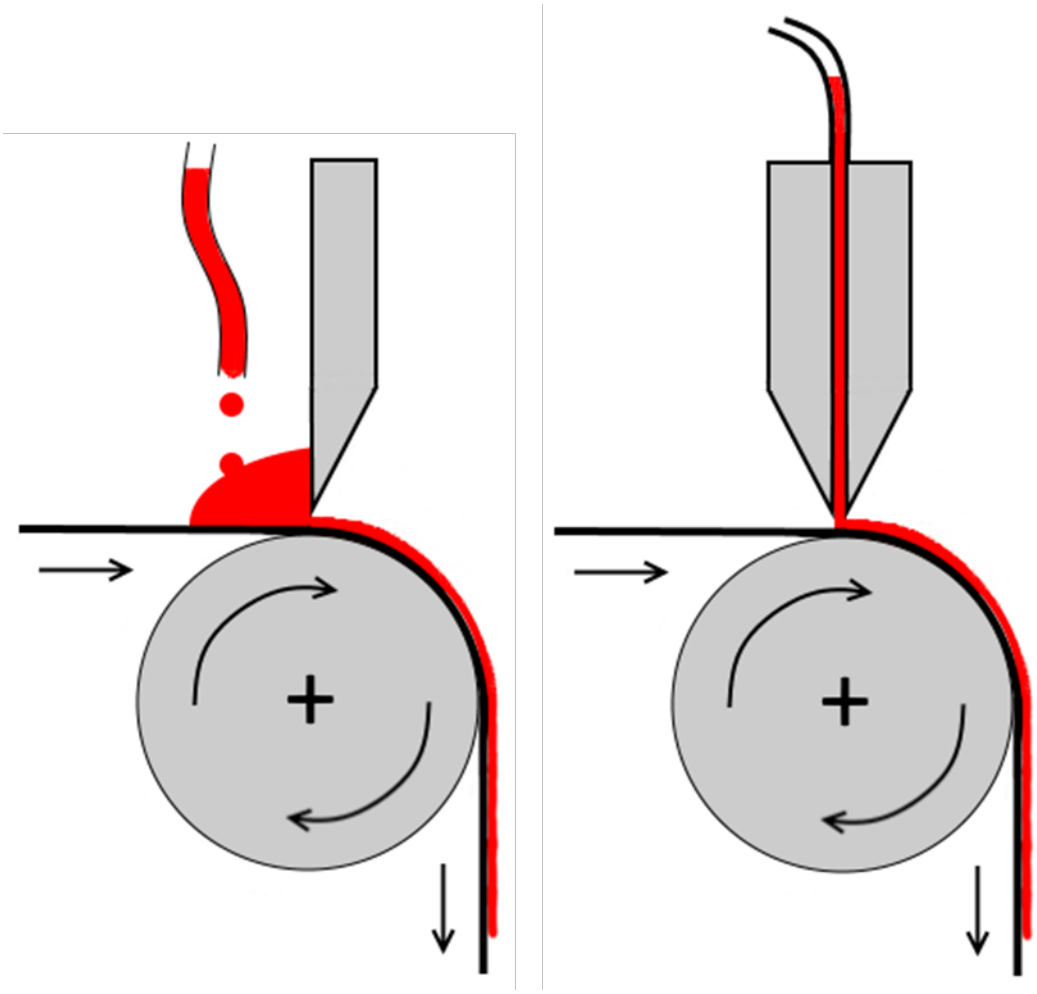

*Figure 2. 22: A schematic of a) Blade coating, b) Slot-die coating.*

### 2.5.6: Flexographic and Gravure coating

Gravure and Flexographic printing are two very similar R2R processing techniques which have been used for printing newspapers and leaflets and have now been adapted for electronics.[104–109] Gravure printing has a patterned cylinder which is rotated through an ink bath, continuously refilling the cavities of the pattern. Wastage of ink is minimised as the cylinder rotates by a doctor blade removing excess ink before the cylinder is pressed against the substrate. A second cylinder on

the reverse side of the substrate ensures good contact and transfer of the ink onto the substrate.

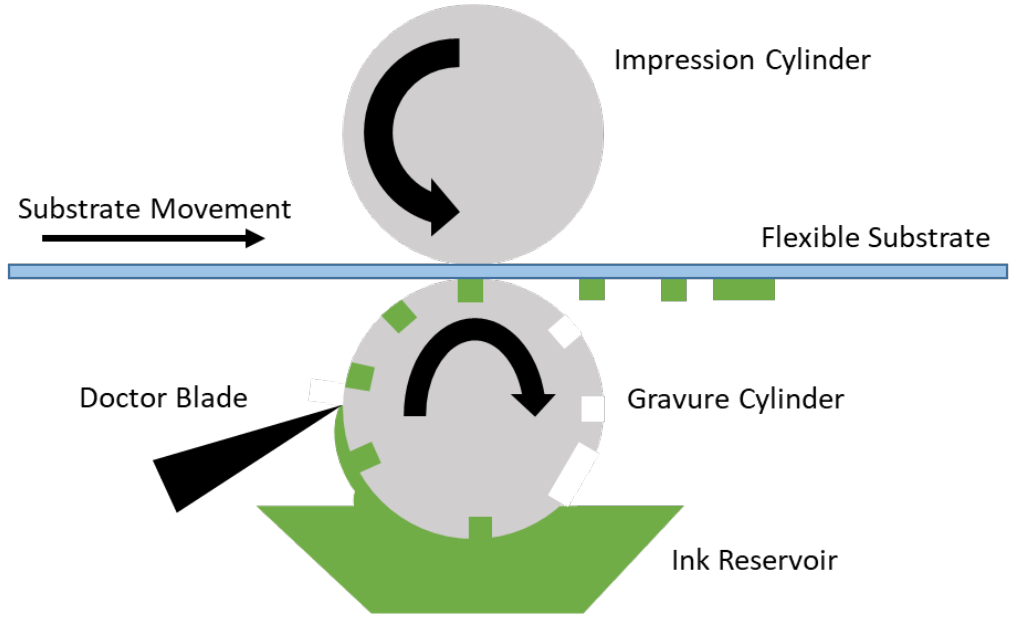


*Figure 2. 23: A schematic of the gravure printing process.*

Flexographic printing uses an extra cylinder to transfer the ink compared to Gravure printing. The Anilox roller is partially submerged in an ink bath and as it rotates a doctor blade controls the volume of ink transferred to the printing plate cylinder. The printing plate cylinder is patterned in a similar manner to the Gravure cylinder but instead of transferring the ink into the cavities the ink is transferred to the raised areas. The printing plate cylinder then presses against the substrate as it passes between it and the impression cylinder, transferring the ink via direct contact like a traditional stamp.

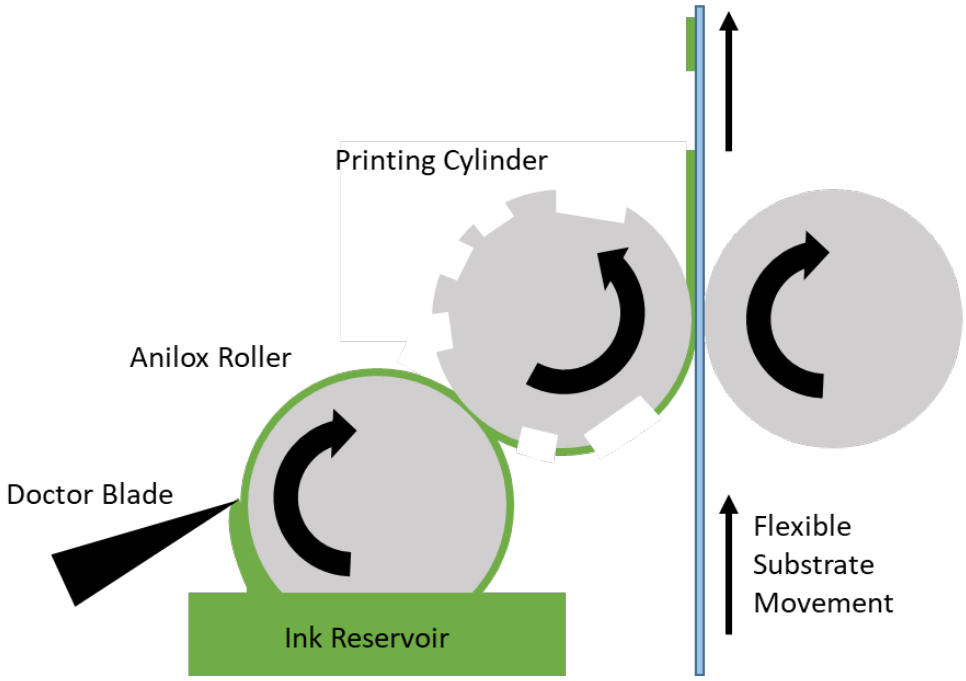


*Figure 2. 24: A schematic of a flexographic printing process.*

Gravure and Flexographic printing have the potential to have very high throughput, using low viscosity inks these techniques could potentially reach printing speeds of 15 m $s^{-1}$.[101]

There are some issues which could limit the use of the techniques for fabricating OLEDs, one such issue is the lack of customisation. To change the pattern which is printed requires new roller which has the desired pattern engraved, this would slow the manufacturing process and would have a large cost to have multiple engraved cylinders. Solutions must be viscous and use low volatility solvents to ensure wetting of the rollers and to stop rapid evaporation of the deposition solution, only polymers that are soluble in such solvents can be being coated.

### 2.5.7: Spray Coating

Spray coating has the potential to be compatible with high-throughput processing such as R2R processing as it enables the rapid coating of large areas with low material wastage. Although some spray heads are able to deposit narrow spray widths, typically to pattern via spray coating involves the use of a mask which would increase the wastage of solution. There are two main sub-technologies within the

spray coating bracket: airbrush (pneumatic) and ultrasonic. In an airbrush spray head the solution is sheared into droplets via the use of pressurised nitrogen or air forcing the solution through an orifice. In recent years a number of polymer based electronic devices have been fabricated using airbrush spray coating.[110–115] However, the flow rate of the solution, the droplet size and velocity of ejected droplets are coupled to the pressure of the air (or nitrogen), these can all effect the uniformity of the final cast film. Ultrasonic spray coating, the main focus of this thesis, atomises the casting solution into droplets via high frequency vibrations, the droplets are then guided to the substrate below via a shaping gas. Ultrasonic spray coating is a highly customisable process in which air pressure, solution pressure, height, speed, substrate temperature, spray width and spray time can all be varied. The range of settings allows for precise control over thickness and deposition area, minimising waste solution and giving the potential to scale up to large area OLEDs. Ultrasonic spray coating has been used to deposit a range of different materials and layers in electronic devices.[116–123] One paper of particular interest consists of work by Gilissen et al. where a yellow emitting polymer was spray cast with the other layers deposited via spin coating and thermal evaporation.[124] Another example of ultrasonic spray coating for OLEDs in literature includes the deposition of F8BT on top of a spin cast TFB layer as part of an emissive bi-layer using.[125] Liu et al. have contributed greatly to the area with four publications included depositing a small molecule hole-transporting layer, an inorganic hole-transporting layer, a small molecule emissive layer and a device in which both a polymer hole-transporting layer and an emissive small molecule layer were spray cast.[126–129] However, in these works the solutions are often highly dilute and require a multi-pass raster spraying pattern which is incompatible with a R2R process unlike the single spray pass technique used in all spray coating in this thesis. Further details on ultrasonic spray coating and the specifics of the system used in this thesis are provided in Chapter 3 and in Chapter 5.

## 2.6: References


[1] W. Heisenberg, Quantum Theory and Measurement (ed JA Wheeler and WH Zurek), Princeton, NJ: Princeton University Press, 1983.

[2] R.M. Eisberg, R. Resnick, Quantum physics of atoms, molecules, solids, nuclei, and Particles. second edition, John Wiley & Sons, 1985.

[3] W. Pauli, Über den Zusammenhang des Abschlusses der Elektronengruppen im Atom mit der Komplexstruktur der Spektren, Zeitschrift Für Phys. 31 (1925) 765–783. doi:10.1007/BF02980631.

[4] P. Atkins, J. De Paula, Elements of Physical Chemistry, 6th Editio, Oxford University Press, 2013.

[5] J. Clayden, N. Greeves, S. Warren, P. Wothers, Organic Chemistry, Oxford University Press, Oxford, 2001.

[6] R.E. Peierls, Quantum theory of solids, Oxford University Press, 1955.

[7] A.O. Patil, A.J. Heeger, F. Wudl, Optical Properties of Conducting Polymers, Chem. Rev. 88 (1988) 183–200. doi:10.1021/cr00083a009.

[8] J. Roncali, Molecular engineering of the band gap of π-conjugated systems: Facing technological applications, Macromol. Rapid Commun. 28 (2007) 1761–1775. doi:10.1002/marc.200700345.

[9] J.L. Brédas, R. Silbey, D.S. Boudreaux, R.R. Chance, Chain-length dependence of electronic and electrochemical properties of conjugated systems: polyacetylene, polyphenylene, polythiophene, and polypyrrole, J. Am. Chem. Soc. 105 (1983) 6555–6559. doi:10.1021/ja00360a004.

[10] J. Franck, Elementary processes, Trans. Faraday Soc. (1924) 536. doi:10.1039/TF9262100536.

[11] E.U. Condon, Nuclear motions associated with electron transitions in diatomic molecules, Phys. Rev. 32 (1928) 858–872. doi:10.1103/PhysRev.32.858.

[12] E.U. Condon, The Franck-Condon Principle and Related Topics, Am. J. Phys. 15

(1947) 365–374. doi:10.1119/1.1990977.

[13] M. Pope, C.E. Swenberg, Electronic processes in organic crystals and polymers, Oxford University Press, 1999.

[14] J. van der Horst, P. Bobbert, P. de Jong, M. Michels, G. Brocks, P. Kelly, Ab initio prediction of the electronic and optical excitations in polythiophene: Isolated chains versus bulk polymer, Phys. Rev. B - Condens. Matter Mater. Phys. 61 (2000) 15817–15826. doi:10.1103/PhysRevB.61.15817.

[15] J.L. Brédas, D. Beljonne, V. Coropceanu, J. Cornil, Charge-transfer and energy-transfer processes in π-conjugated oligomers and polymers: A molecular picture, Chem. Rev. 104 (2004) 4971–5003. doi:10.1021/cr040084k.

[16] V. Coropceanu, J. Cornil, D.A. Da, S. Filho, Y. Olivier, R. Silbey, J.-L. Brédas, Charge Transport in Organic Semiconductors, Chem. Rev. 107 (2007) 926–952. doi:10.1021/cr050140x.

[17] T.M. Clarke, J.R. Durrant, Charge photogeneration in organic solar cells, Chem. Rev. 110 (2010) 6736–6767. doi:10.1021/cr900271s.

[18] R. Evans, The Atomic Nucleus, McGraw-Hill Book Company, INC, New York, 1955.

[19] R.H. Friend, R.W. Gymer, A.B. Holmes, J.H. Burroughes, R.N. Marks, C. Taliani, D.D.C. Bradley, D.A. Dos Santos, J.L. Brédas, M. Lögdlund, W.R. Salaneck, Electroluminescence in conjugated polymers, Nature. 397 (1999) 121–128. doi:10.1038/16393.

[20] K. Müllen, U. Scherf, eds., Organic Light-Emitting Devices: Synthesis, Properties and Applications, Wiley-vch, Germany, 2006.

[21] Y. Kim, C. Ha, Advances in Organic Light-Emitting Devices, Trans Tech Publications Ltd, 2008.

[22] S. Ciná, D. Vaufrey, C. Fery, B. Racine, H. Doyeux, A. Bettinelli, J.-C. Martinez, P-135: Efficient Electron Injection from PEDOT-PSS into a Graded-n-doped Electron Transporting Layer in an Inverted OLED Structure, SID Symp. Dig.

Tech. Pap. 36 (2005) 819. doi:10.1889/1.2036571.

[23] C.W. Tang, S.A. Vanslyke, Organic electroluminescent diodes, Appl. Phys. Lett. 51 (1987) 913–915. doi:10.1063/1.98799.

[24] S. Aratani, C. Zhang, K. Pakbaz, S. Höger, F. Wudl, A.J. Heeger, Improved efficiency in polymer light-emitting diodes using air-stable electrodes, J. Electron. Mater. 22 (1993) 745–749. doi:10.1007/BF02817349.

[25] H. Ishii, K. Sugiyama, E. Ito, K. Seki, Energy Level Alignment and Interfacial Electronic Structures at Organic/Metal and Organic/Organic Interfaces, Adv. Mater. 11 (1999) 605–625. doi:10.1002/(SICI)1521-4095(199906)11:8<605::AID-ADMA605>3.0.CO;2-Q.

[26] C. Kittel, H.Y. Fan, Introduction to Solid State Physics, 8th ed., 1957. doi:10.1119/1.1934457.

[27] M.N. Rudden, J. Wilson, Elements of solid state physics (2nd edition), Wiley, 1993.

[28] S. Braun, W.R. Salaneck, M. Fahlman, Energy-level alignment at organic/metal and organic/organic interfaces, Adv. Mater. 21 (2009) 1450–1472. doi:10.1002/adma.200802893.

[29] P.W.M. Blom, M.C.J.M. Vissenberg, Charge transport in poly(p-phenylene vinylene) light-emitting diodes, Mater. Sci. Eng. R Reports. 27 (2000).

[30] I.H. Campbell, D.L. Smith, Physics of organic electronic devices, Solid State Phys. 55 (2001) 1–117. doi:10.1016/S0081-1947(01)80003-5.

[31] G.G. Malliaras, J.C. Scott, The roles of injection and mobility in organic light emitting diodes, J. Appl. Phys. 83 (1998) 5399–5403. doi:doi:10.1063/1.367369.

[32] Z. Liu, M. Kobayashi, B.C. Paul, Z. Bao, Y. Nishi, Contact engineering for organic semiconductor devices via Fermi level depinning at the metal-organic interface, Phys. Rev. B - Condens. Matter Mater. Phys. 82 (2010). doi:10.1103/PhysRevB.82.035311.

[33] I.D. Parker, Carrier tunneling and device characteristics in polymer light-emitting diodes, J. Appl. Phys. 75 (1994) 1656–1666. doi:10.1063/1.356350.

[34] R.H. Fowler, L. Nordheim, Electron Emission in Intense Electric Fields, 1928.

[35] J.C. Scott, Metal-organic interface and charge injection in organic electronic devices, Cit. J. Vac. Sci. Technol. A. 21 (2003) 521. doi:10.1116/1.1559919.

[36] H. Zhao, Y. Yao, Z. An, C.Q. Wu, Dynamics of polarons in conjugated polymers: An adaptive time-dependent density-matrix renormalization-group study, Phys. Rev. B - Condens. Matter Mater. Phys. 78 (2008) 1–6. doi:10.1103/PhysRevB.78.035209.

[37] N. Zhao, Y.Y. Noh, J.F. Chang, M. Heeney, I. McCulloch, H. Sirringhaus, Polaron localization at interfaces in high-mobility microcrystalline conjugated polymers, Adv. Mater. 21 (2009) 3759–3763. doi:10.1002/adma.200900326.

[38] Y. Meng, X.J. Liu, B. Di, Z. An, Recombination of polaron and exciton in conjugated polymers, Org. Electroluminescent Diodes Appl. Phys. Lett. 131 (2009) 913. doi:10.1063/1.3274680.

[39] P.W. Anderson, Absence of diffusion in certain random lattices, Phys. Rev. 109 (1958) 1492–1505. doi:10.1103/PhysRev.109.1492.

[40] H. Bässler, Localized states and electronic transport in single component organic solids with diagonal disorder, Phys. Status Solidi. 107 (1981) 9–54. doi:10.1002/pssb.2221070102.

[41] S. Nespurek, E.A. Silinsh, Space - Charge -Limited Current Theory for Molecular Crystals with Gaussian Distribution of Local Trapping States, Phys. Status Solidi A. 34 (1976) 747–759. doi:10.1002/pssa.2210340240.

[42] A. Miller, E. Abrahams, Impurity conduction at low concentrations, Phys. Rev. 120 (1960) 745–755. doi:10.1103/PhysRev.120.745.

[43] D. Hertel, H. Bässler, Photoconduction in amorphous organic solids, ChemPhysChem. 9 (2008) 666–688. doi:10.1002/cphc.200700575.

[44] H. Bässler, Charge Transport in Disordered Organic Photoconductors a Monte Carlo Simulation Study, Phys. Status Solidi. 175 (1993) 15–56. doi:10.1002/pssb.2221750102.

[45] R. Noriega, J. Rivnay, K. Vandewal, F.P. V Koch, N. Stingelin, P. Smith, M.F. Toney, A. Salleo, A general relationship between disorder, aggregation and charge transport in conjugated polymers, Nat. Mater. 12 (2013) 1038–1044. doi:10.1038/nmat3722.

[46] G.T. Wright, Mechanisms of space-charge-limited current in solids, Solid. State. Electron. 2 (1961) 165–189. doi:10.1016/0038-1101(61)90034-X.

[47] N.F. Mott, R.W. Gurney, Electronic processes in ionic crystals, Clarendon Press, Oxford, 1940. http://cds.cern.ch/record/2144379.

[48] P. Blom, M. de Jong, M. van Munster, Electric-field and temperature dependence of the hole mobility in poly(p-phenylene vinylene), Phys. Rev. B - Condens. Matter Mater. Phys. 55 (1997) R656–R659. doi:10.1103/PhysRevB.55.R656.

[49] D.M. Pai, Transient Photoconductivity in Poly(N-vinylcarbazole), J. Chem. Phys. 52 (1970) 2285–2291. doi:10.1063/1.1673300.

[50] M. Van der Auweraer, F.C. De Schryver, P.M. Borsenberger, H. Bässler, Disorder in Charge Transport in doped polymers, Adv. Mater. 6 (1994) 199–213. doi:10.1002/adma.19940060304.

[51] J. Frenkel, On Pre-Breakdown Phenomena in Insulators and Electronic Semi-Conductors, Phys. Rev. 54 (1938) 647–648. doi:10.1103/PhysRev.54.647.

[52] E.H. Sondheimer, The mean free path of electrons in metals, Adv. Phys. 1 (1952) 1–42.

[53] A.R. Buckley, Organic light-emitting diodes (OLEDs): Materials, devices and applications, Elsevier, 2013.

[54] M. Abkowitz, J.S. Facci, J. Rehm, Direct evaluation of contact injection efficiency into small molecule based transport layers: Influence of extrinsic

factors, J. Appl. Phys. 83 (1998) 2670–2676. doi:10.1063/1.367030.

[55] A. Ioannidis, J.S. Facci, M.A. Abkowitz, Evolution in the charge injection efficiency of evaporated Au contacts on a molecularly doped polymer, J. Appl. Phys. 84 (1998) 1439–1444. doi:10.1063/1.368179.

[56] Y. Shen, A.R. Hosseini, M.H. Wong, G.G. Malliaras, How to make ohmic contacts to organic semiconductors, ChemPhysChem. 5 (2004) 16–25. doi:10.1002/cphc.200300942.

[57] H.H. Fong, A. Papadimitratos, J. Hwang, A. Kahn, G.G. Malliaras, Hole injection in a model fluorene-triarylamine copolymer, Adv. Funct. Mater. 19 (2009) 304–310. doi:10.1002/adfm.200800738.

[58] A. Buckley, D. Pickup, C. Yates, Y. Zhao, D. Lidzey, Hole injection in tri-arylamine containing polyfluorene co-polymer devices with molybdenum oxide contacts, J. Appl. Phys. 109 (2011) 1–7. doi:10.1063/1.3562184.

[59] L.A.A. Pettersson, L.S. Roman, O. Inganäs, Modeling photocurrent action spectra of photovoltaic devices based on organic thin films, Junction Sol. Cells J. Appl. Phys. 86 (1999) 183. doi:10.1063/1.370757.

[60] Y. Tamai, H. Ohkita, H. Benten, S. Ito, Exciton Diffusion in Conjugated Polymers: From Fundamental Understanding to Improvement in Photovoltaic Conversion Efficiency, J. Phys. Chem. Lett. 6 (2015) 3417–3428. doi:10.1021/acs.jpclett.5b01147.

[61] T. Förster, Energiewanderung und Fluoreszenz, Naturwissenschaften. 33 (1946) 166–175. doi:10.1007/BF00585226.

[62] D.L. Dexter, A theory of sensitized luminescence in solids, J. Chem. Phys. 21 (1953) 836–850. doi:10.1063/1.1699044.

[63] O. V Mikhnenko, P.W.M. Blom, T.-Q. Nguyen, Exciton diffusion in organic semiconductors, Energy Environ. Sci. 8 (2015) 1867. doi:10.1039/c5ee00925a.

[64] W.A. Luhman, R.J. Holmes, Investigation of energy transfer in organic

photovoltaic cells and impact on exciton diffusion length measurements, Adv. Funct. Mater. 21 (2011) 764–771. doi:10.1002/adfm.201001928.

[65] A. Köhler, H. Bässler, Triplet states in organic semiconductors, Mater. Sci. Eng. R Reports. 66 (2009) 71–109. doi:10.1016/j.mser.2009.09.001.

[66] S.R. Forrest, D.D.C. Bradley, M.E. Thompson, Measuring the efficiency of organic light-emitting devices, Adv. Mater. 15 (2003) 1043–1048. doi:10.1002/adma.200302151.

[67] T. Smith, J. Guild, The CIE colorimetric standards and their use, Trans. Opt. Soc. 33 (1931) 73.

[68] J. Kido, M. Kimura, K. Nagai, Multilayer white light-emitting organic electroluminescent device., Science (80-. ). 267 (1995) 1332–4. doi:10.1126/science.267.5202.1332.

[69] P.E. Burrows, S.R. Forrest, S.P. Sibley, M.E. Thompson, Color-tunable organic light-emitting devices, Appl. Phys. Lett. 69 (1998) 2959. doi:10.1063/1.117743.

[70] M. Berggren, O. Inganäs, G. Gustafsson, J. Rasmusson, M.R. Andersson, T. Hjertberg, O. Wennerström, Light-emitting diodes with variable colours from polymer blends, Nature. 372 (1994) 444–446. doi:10.1038/372444a0.

[71] S. Tasch, E.J.W. List, O. Ekström, W. Graupner, G. Leising, P. Schlichting, U. Rohr, Y. Geerts, U. Scherf, K. Müllen, Efficient white light-emitting diodes realized with new processable blends of conjugated polymers, Appl. Phys. Lett. 71 (1998) 2883. doi:10.1063/1.120205.

[72] M. Granström, O. Inganäs, White light emission from a polymer blend light emitting diode, Appl. Phys. Lett. 68 (1998) 147. doi:10.1063/1.116129.

[73] J. Huang, G. Li, E. Wu, Q. Xu, Y. Yang, Achieving high-efficiency polymer white-light-emitting devices, Adv. Mater. 18 (2006) 114–117. doi:10.1002/adma.200501105.

[74] X. Liu, S. Huettner, Z. Rong, M. Sommer, R.H. Friend, Solvent additive control

of morphology and crystallization in semiconducting polymer blends, Adv. Mater. 24 (2012) 669–674. doi:10.1002/adma.201103097.

[75] N. Corcoran, A.C. Arias, J.S. Kim, J.D. MacKenzie, R.H. Friend, Increased efficiency in vertically segregated thin-film conjugated polymer blends for light-emitting diodes, Appl. Phys. Lett. 82 (2003) 299–301. doi:10.1063/1.1537049.

[76] Y. Liu, J. Zhao, Z. Li, C. Mu, W. Ma, H. Hu, K. Jiang, H. Lin, H. Ade, H. Yan, Aggregation and morphology control enables multiple cases of high-efficiency polymer solar cells, Nat. Commun. 5 (2014) 5293. doi:10.1038/ncomms6293.

[77] E. Moons, Conjugated polymer blends: linking film morphology to performance of light emitting diodes and photodiodes, J. Phys. Condens. Matter. 14 (2002) 12235. http://iopscience.iop.org/article/10.1088/0953-8984/14/47/301/pdf (accessed September 23, 2018).

[78] G. Tu, Q. Zhou, Y. Cheng, L. Wang, D. Ma, X. Jing, F. Wang, White electroluminescence from polyfluorene chemically doped with 1,8-napthalimide moieties, Appl. Phys. Lett. 85 (2004) 2172–2174. doi:10.1063/1.1793356.

[79] J. Liu, Z.Y. Xie, Y.X. Cheng, Y.H. Geng, L.X. Wang, X.B. Jing, F.S. Wang, Molecular Design on Highly Efficient White Electroluminescence from a Single-Polymer System with Simultaneous Blue, Green, and Red Emission, Adv. Mater. 19 (2007) 531–535. doi:10.1002/adma.200601580.

[80] J.G. Holmes, The Nature and Measurement of Light, in: Light Meas. Ind., International Society for Optics and Photonics, 1979: pp. 2–6.

[81] N.C. Greenham, R.H. Friend, D.D.C. Bradley, Angular Dependence of the Emission from a Conjugated Polymer Light-Emitting Diode: Implications for efficiency calculations, Adv. Mater. 6 (1994) 491–494. doi:10.1002/adma.19940060612.

[82] W. Li, L. Yao, H. Liu, Z. Wang, S. Zhang, R. Xiao, H. Zhang, P. Lu, B. Yang, Y. Ma, Highly efficient deep-blue OLED with an extraordinarily narrow FHWM of 35

nm and a y coordinate <0.05 based on a fully twisting donor–acceptor molecule, J. Mater. Chem. C. 2 (2014) 4733–4736. doi:10.1039/C4TC00487F.

[83] H. Park, J. Lee, I. Kang, H.Y. Chu, J.-I. Lee, S.-K. Kwon, Y.-H. Kim, Highly rigid and twisted anthracene derivatives: a strategy for deep blue OLED materials with theoretical limit efficiency, J. Mater. Chem. 22 (2012) 2695–2700. doi:10.1039/C2JM16056K.

[84] N.C. Greenham, I.D.W. Samuel, G.R. Hayes, R.T. Phillips, Y.A.R.R. Kessener, S.C. Moratti, A.B. Holmes, R.H. Friend, Measurement of absolute photoluminescence quantum efficiencies in conjugated polymers, Chem. Phys. Lett. 241 (1995) 89–96. doi:10.1016/0009-2614(95)00584-Q.

[85] Y. Cao, I.D. Parker, G. Yu, C. Zhang, A.J. Heeger, Improved quantum efficiency for electroluminescence in semiconducting polymers, Nature. 397 (1999) 414–415. doi:10.1038/17087.

[86] P.E. Burrows, V. Bulovic, S.R. Forrest, L.S. Sapochak, D.M. McCarty, M.E. Thompson, Reliability and degradation of organic light emitting devices, Appl. Phys. Lett. 65 (1994) 2922–2924. doi:10.1063/1.112532.

[87] S. Scholz, D. Kondakov, B. Lüssem, K. Leo, Degradation mechanisms and reactions in organic light-emitting devices, Chem. Rev. 115 (2015) 8449–8503. doi:10.1021/cr400704v.

[88] P.G. De Gennes, Wetting: Statics and dynamics, Rev. Mod. Phys. 57 (1985) 827–863. doi:10.1103/RevModPhys.57.827.

[89] C.J. Lawrence, The mechanics of spin coating of polymer films, Phys. Fluids. 31 (1988) 2786–2795. doi:10.1063/1.866986.

[90] S. Han, J. Derksen, J.H. Chun, Extrusion Spin Coating: An Efficient and Deterministic Photoresist Coating Method in Microlithography, IEEE Trans. Semicond. Manuf. 17 (2004) 12–21. doi:10.1109/TSM.2003.822734.

[91] D.R. Gamota, K. Brazis, Paul Kalyanasundaram, J. Zhang, Printed Organic and Molecular Electronics, Springer science & business media, 2013.

[92] W.S. Wong, A. Salleo, Flexible Electronics: Materials and Applications, 2009. doi:10.1007/978-0-387-74363-9.

[93] H. Sirringhaus, T. Kawase, R.H. Friend, T. Shimoda, M. Inbasekaran, W. Wu, E.P. Woo, High-resolution Inkjet Printing of All- Transistor Circuits, Science (80-. ). 290 (2000) 2123–2126. doi:10.1126/science.290.5499.2123.

[94] H.-H. Lee, K.-S. Chou, K.-C. Huang, Inkjet printing of nanosized silver colloids, Nanotechnology. 16 (2005) 2436–2441. doi:10.1088/0957-4484/16/10/074.

[95] C.N. Hoth, S.A. Choulis, P. Schilinsky, C.J. Brabec, High photovoltaic performance of inkjet printed polymer:Fullerene blends, Adv. Mater. 19 (2007) 3973–3978. doi:10.1002/adma.200700911.

[96] F. Villani, P. Vacca, G. Nenna, O. Valentino, G. Burrasca, T. Fasolino, C. Minarini, D. Della Sala, Inkjet Printed Polymer Layer on Flexible Substrate for OLED Applications, J. Phys. Chem. C. (2009). doi:10.1021/jp8095538.

[97] C.F. Madigan, C.R. Hauf, L.D. Barkley, N. Harjee, E. Vronsky, S.A. Van Slyke, Advancements in inkjet printing for OLED mass production, Dig. Tech. Pap. - SID Int. Symp. 45 (2014) 399–402. doi:10.1002/j.2168-0159.2014.tb00108.x.

[98] S.-H. Lee, J.Y. Hwang, K. Kang, H. Kang, Fabrication of organic light emitting display using inkjet printing technology, 2009 Int. Symp. Optomechatronic Technol. (2009) 71–76. doi:10.1109/ISOT.2009.5326101.

[99] F.C. Krebs, Fabrication and processing of polymer solar cells: A review of printing and coating techniques, Sol. Energy Mater. Sol. Cells. 93 (2009) 394–412. doi:10.1016/j.solmat.2008.10.004.

[100] H. Youn, K. Jeon, S. Shin, M. Yang, All-solution blade-slit coated polymer light-emitting diodes, Org. Electron. Physics, Mater. Appl. 13 (2012) 1470–1478. doi:10.1016/j.orgel.2012.04.008.

[101] R.R. Søndergaard, M. Hösel, F.C. Krebs, Roll-to-Roll fabrication of large area functional organic materials, J. Polym. Sci. Part B Polym. Phys. 51 (2013) 16–

34. doi:10.1002/polb.23192.

[102] K.-J. Choi, J.-Y. Lee, J. Park, Y.-S. Seo, Multilayer slot-die coating of large-area organic light-emitting diodes, Org. Electron. 26 (2015) 66–74. doi:10.1016/J.ORGEL.2015.07.025.

[103] B. Park, O.E. Kwon, S.H. Yun, H.G. Jeon, Y.H. Huh, Organic semiconducting layers fabricated by self-metered slot-die coating for solution-processable organic light-emitting devices, J. Mater. Chem. C. 2 (2014) 8614–8621. doi:10.1039/C4TC00817K.

[104] H. Yan, Z. Chen, Y. Zheng, C. Newman, J.R. Quinn, F. Dötz, M. Kastler, A. Facchetti, A high-mobility electron-transporting polymer for printed transistors, Nature. 457 (2009) 679–686. doi:10.1038/nature07727.

[105] A. de la Fuente Vornbrock, D. Sung, H. Kang, R. Kitsomboonloha, V. Subramanian, Fully gravure and ink-jet printed high speed pBTTT organic thin film transistors, Org. Electron. 11 (2010) 2037–2044. doi:10.1016/J.ORGEL.2010.09.003.

[106] S. Tekoglu, G. Hernandez-Sosa, E. Kluge, U. Lemmer, N. Mechau, Gravure printed flexible small-molecule organic light emitting diodes, Org. Electron. 14 (2013) 3493–3499. doi:10.1016/J.ORGEL.2013.09.027.

[107] G. Grau, J. Cen, H. Kang, R. Kitsomboonloha, W.J. Scheideler, V. Subramanian, Gravure-printed electronics: recent progress in tooling development, understanding of printing physics, and realization of printed devices, Flex. Print. Electron. 1 (2016) 023002. doi:10.1088/2058-8585/1/2/023002.

[108] P. Kopola, M. Tuomikoski, R. Suhonen, A. Maaninen, Gravure printed organic light emitting diodes for lighting applications, Thin Solid Films. 517 (2009) 5757–5762. doi:10.1016/j.tsf.2009.03.209.

[109] D.Y. Chung, J. Huang, D.D.C. Bradley, A.J. Campbell, High performance, flexible polymer light-emitting diodes (PLEDs) with gravure contact printed hole injection and light emitting layers, Org. Electron. Physics, Mater. Appl. 11 (2010) 1088–1095. doi:10.1016/j.orgel.2010.03.010.

[110] M.P. Aleksandrova, Improvement of the electrical characteristics of polymer electroluminescent structures by using spray-coating technology, J. Coatings Technol. Res. 9 (2012) 157–161. doi:10.1007/s11998-009-9220-2.

[111] A. Asadpoordarvish, A. Sandström, C. Larsen, R. Bollström, M. Toivakka, R. Österbacka, L. Edman, Light-emitting paper, Adv. Funct. Mater. 25 (2015) 3238–3245. doi:10.1002/adfm.201500528.

[112] A. Sandström, A. Asadpoordarvish, J. Enevold, L. Edman, Spraying light: Ambient-air fabrication of large-area emissive devices on complex-shaped surfaces, Adv. Mater. 26 (2014) 4975–4980. doi:10.1002/adma.201401286.

[113] A. Abdellah, D. Baierl, B. Fabel, P. Lugli, G. Scarpa, Spray-coating deposition for large area organic thin-film devices, Tech. Proc. 2009 NSTI Nanotechnol. Conf. Expo, NSTI-Nanotech 2009. 2 (2009) 447–450. http://hdl.handle.net/10863/4216.

[114] Y. Zheng, R. Wu, W. Shi, Z. Guan, J. Yu, Effect of in situ annealing on the performance of spray coated polymer solar cells, Sol. Energy Mater. Sol. Cells. 111 (2013) 200–205. doi:10.1016/j.solmat.2013.01.011.

[115] A. Abdellah, B. Fabel, P. Lugli, G. Scarpa, Spray deposition of organic semiconducting thin-films: Towards the fabrication of arbitrary shaped organic electronic devices, Org. Electron. Physics, Mater. Appl. 11 (2010) 1031–1038. doi:10.1016/j.orgel.2010.02.018.

[116] Y. Zhang, N.W. Scarratt, T. Wang, D.G. Lidzey, Fabricating high performance conventional and inverted polymer solar cells by spray coating in air, Vacuum. 139 (2017) 154–158. doi:10.1016/j.vacuum.2016.09.017.

[117] N.W. Scarratt, J. Griffin, T. Wang, Y. Zhang, H. Yi, A. Iraqi, D.G. Lidzey, Polymer-based solar cells having an active area of 1.6 cm2 fabricated via spray coating, APL Mater. 3 (2015) 126108. doi:10.1063/1.4937553.

[118] Y. Zhang, J. Griffin, N.W. Scarratt, T. Wang, D.G. Lidzey, High efficiency arrays of polymer solar cells fabricated by spray-coating in air, Prog. Photovolt Res. Appl. 24 (2016) 275–282. doi:10.1002/pip.2665.

[119] A. Colsmann, M. Reinhard, T.H. Kwon, C. Kayser, F. Nickel, J. Czolk, U. Lemmer, N. Clark, J. Jasieniak, A.B. Holmes, D. Jones, Inverted semi-transparent organic solar cells with spray coated, surfactant free polymer top-electrodes, Sol. Energy Mater. Sol. Cells. 98 (2012) 118–123. doi:10.1016/j.solmat.2011.10.016.

[120] M. Majumder, C. Rendall, M. Li, N. Behabtu, J.A. Eukel, R.H. Hauge, H.K. Schmidt, M. Pasquali, Insights into the physics of spray coating of SWNT films, Chem. Eng. Sci. 65 (2010) 2000–2008. doi:10.1016/j.ces.2009.11.042.

[121] M. Shao, S. Das, K. Xiao, J. Chen, J.K. Keum, I.N. Ivanov, G. Gu, W. Durant, D. Li, D.B. Geohegan, High-performance organic field-effect transistors with dielectric and active layers printed sequentially by ultrasonic spraying, J. Mater. Chem. C. 1 (2013) 4384–4390. doi:10.1039/c3tc30535j.

[122] C. Girotto, D. Moia, B.P. Rand, P. Heremans, High-performance organic solar cells with spray-coated hole-transport and active layers, Adv. Funct. Mater. 21 (2011) 64–72. doi:10.1002/adfm.201001562.

[123] J.E. Bishop, D.K. Mohamad, M. Wong-Stringer, A. Smith, D.G. Lidzey, Spray-cast multilayer perovskite solar cells with an active-area of 1.5 cm2, Sci. Rep. 7 (2017) 7962. doi:10.1038/s41598-017-08642-2.

[124] K. Gilissen, J. Stryckers, P. Verstappen, J. Drijkoningen, G.H.L. Heintges, L. Lutsen, J. Manca, W. Maes, W. Deferme, Ultrasonic spray coating as deposition technique for the light-emitting layer in polymer LEDs, Org. Electron. Physics, Mater. Appl. 20 (2015) 31–35. doi:10.1016/j.orgel.2015.01.015.

[125] T. Fukuda, A. Sato, Fluorene bilayer for polymer organic light-emitting diode using efficient ionization method for atomized droplet, Org. Electron. Physics, Mater. Appl. 26 (2015) 1–7. doi:10.1016/j.orgel.2015.07.008.

[126] S. Liu, X. Zhang, M. Yin, H. Feng, J. Zhang, L. Zhang, W. Xie, Coffee-Ring-Free Ultrasonic Spray Coating Single-Emission Layers for White Organic Light-Emitting Devices and Their Energy-Transfer Mechanism, ACS Appl. Energy Mater. 1 (2018) 103–112. doi:10.1021/acsaem.7b00011.

[127] S. Liu, X. Zhang, H. Feng, J. Zhang, L. Zhang, W. Xie, Two-dimensional-growth small molecular hole-transporting layer by ultrasonic spray coating for organic light-emitting devices, Org. Electron. Physics, Mater. Appl. 47 (2017) 181–188. doi:10.1016/j.orgel.2017.05.024.

[128] S. Liu, X. Zhang, S. Wang, H. Feng, J. Zhang, H. Yang, L. Zhang, W. Xie, Hybrid organic light-emitting device based on ultrasonic spray-coating molybdenum trioxide transport layer with low turn-on voltage, improved efficiency & stability, Org. Electron. 52 (2018) 264–271. doi:10.1016/j.orgel.2017.10.041.

[129] S. Liu, X. Zhang, L. Zhang, W. Xie, Ultrasonic spray coating polymer and small molecular organic film for organic light-emitting devices, Sci. Rep. 6 (2016) 1–10. doi:10.1038/srep37042.

# Chapter 3

# Experimental Methods

## 3.1: Introduction

In this chapter, the procedures are laid out for the preparation, fabrication and characterisation of organic light-emitting diodes (OLEDs) in this thesis. In Section 3.2 the methods followed for the preparation of solutions are described, in Section 3.3 the fabrication techniques used for producing devices in this thesis are reviewed. In Section 3.4 the device architecture and the fabrication of devices layer-by-layer is described. The procedures used for characterising the performance and emission of OLEDs and single-carrier devices are presented in Section 3.5, and the techniques used to characterise thin films are shown in Section 3.6.

## 3.2: Solution Preparation

All solutions in this thesis were prepared within a clean room environment. Amber glass vials (chosen to minimise possibility of photodegradation of solutions) and the vial lids were blasted with nitrogen to remove particulates, these vials were then rinsed with isopropyl alcohol before drying with nitrogen. The vial, without lid, was placed onto a microbalance to zero the scales before carefully depositing materials into the vials using a disposable spatula to the desired weight. Whilst under a fume hood the appropriate solvent is then added to the vial using a micropipette to prepare the desired concentration. Solutions of hygroscopic/air-unstable materials were prepared by cleaning the vial as discussed above prior to moving the empty vial into the dry nitrogen atmosphere glove box. The vial was then opened, blown with nitrogen and sealed before removing from the glovebox and zeroing the microbalance to the weight of the sealed vial. The vial was then returned to the

glovebox where an amount of material is transferred to the vial using a disposable spatula, the vial is then resealed and weighed on the microbalance in air. This process is repeated until the mass of material is enough for the desired concentration of solution to be prepared, at which point the vial is returned to the glovebox and anhydrous solvent is added to the solvent via micropipette to prepare the solution of desired concertation. Solutions were then placed on a hotplate till the solute is fully solubilised with occasional aggravation using a vortex mixer to aid this process. If particulates still remain in solution prior to use they were filtered using either 0.45 μm PTFE or PVDF depending on the solvent properties.

## 3.3: Fabrication Techniques

### 3.3.1: Spin Coating

Spin coating is the ubiquitous technique for solution processing thin films on a laboratory scale. Thin films are formed by depositing a volume of solution onto substrate which is coupled to a rotating chuck, the solution is spread uniformly across the surface of the substrate by the centrifugal (centripetal) force, with excess solution being ejected. As the substrate continues to spin the solvent then evaporates leaving a uniform dry film. The final film thickness, as discussed in Section 2.5.2, is dependent on the solution concentration, viscosity, solvent diffusivity and has an inverse relationship to spin speed.[1] The repeatable thickness of thin films cast via spin coating combined with the known thickness relationship allows for the rapid optimisation of materials as once a film is cast and measured the spin speed for the casting same solution required for a desired film thickness can be estimated, or the required solution concentration for a specific thickness can be estimated if cast at the same spin speed.

Two models of spin coaters were used to deposit thin films in this thesis: A Laurell spin coater and an Ossila spin coater. The Laurell systems, uses a vacuum chuck, whereby the substrate is held in place during rotation by a vacuum. The Ossila system uses a recessed chuck in which the substrate sits.

### 3.3.2: Ultrasonic Spray Coating

A PRISM Ultra-coat 300 system made by Ultrasonic Systems Inc. is used to deposit thin films in Chapters 5, 6 and 7 of this thesis. In this system the casting solution is fed onto a vibrating tip driven by a rapidly contracting and expanding piezoelectric crystal to resonate at 35 KHz. The solution is atomised into a fine mist of droplets as it contacts the tip, the mist is shaped and directed by a nitrogen flow towards the substrate placed on a hotplate below. The spray head is mounted on a computer controlled gantry which controls the motion of the spray head for each deposition allowing for high precision and repeatability. The deposition parameters that can be varied include: pass length, pass height, pass speed, shaping gas pressure, solution flow rate, deposition time and substrate temperature. Further to these parameters the properties of the casting solvent and solution concentration all contribute to the vast parameter space that affects the uniformity and thickness of cast films. In Chapter 5 this parameter space is probed and a guide to fabricating uniform thin polymer films is laid out.

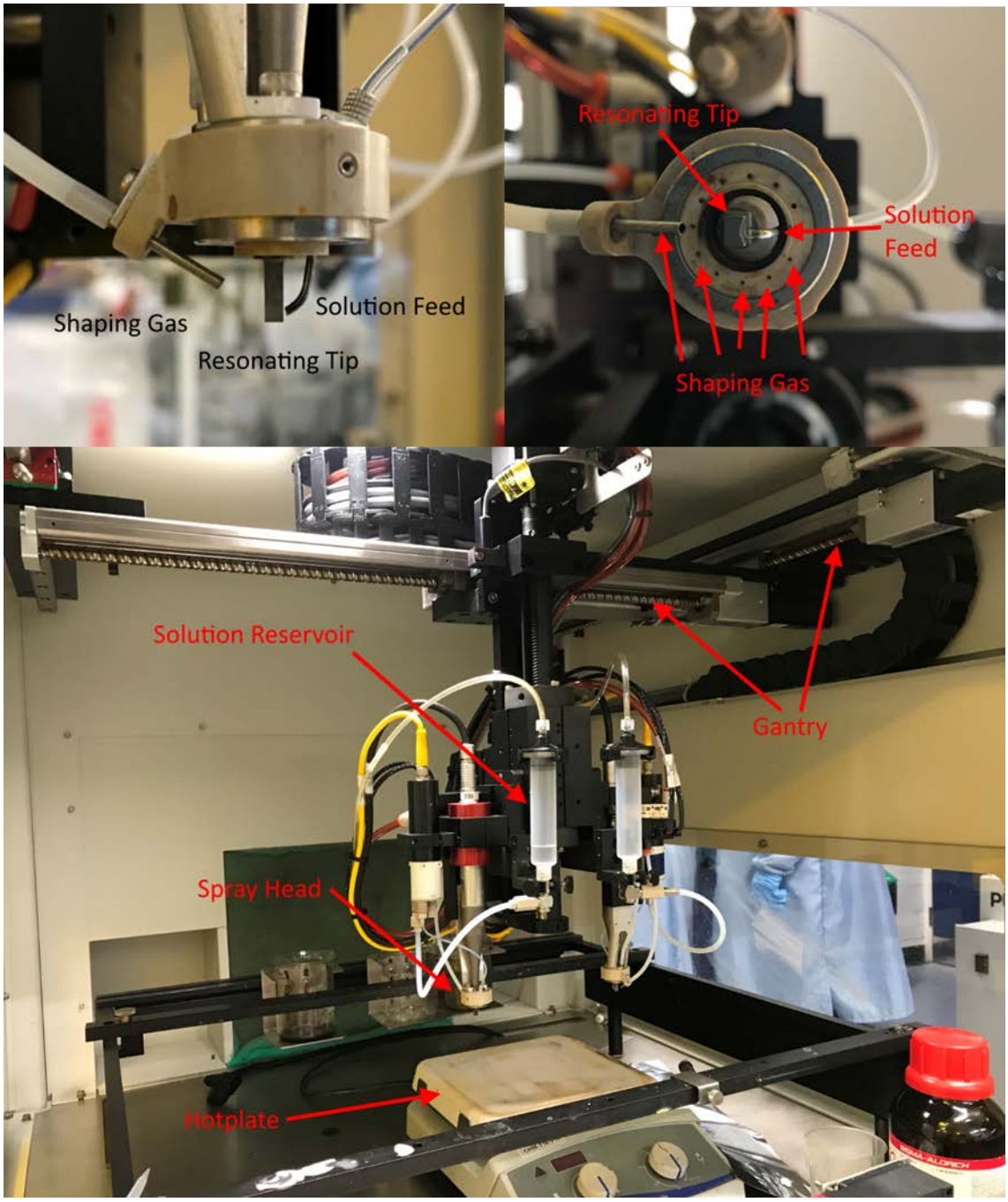


*Figure 3. 1: Top left – A side on picture of the spray head showing the solution feed onto the piezoelectric tip and the shaping gas tube from which nitrogen flows and guides the spray mist down onto a substrate below. Top right – A view from below the spray head showing again the solution feed, piezoelectric tip and the main shaping gas tube. The ring of holes around the resonating tip are another source of pressurised nitrogen which helps shape and define the width of the spray pattern. Bottom – A picture of the spray coating system showing the computerised gantry on which the spray head is*

*mounted, the reservoir in which the casting solution is stored, the spray head and a hotplate below on which the substrate is placed during deposition.*

### 3.3.3: Thermal Evaporation

Thermal evaporations are undertaken under a high vacuum (Pressures lower than $4x10^{-6}$ mbar) this acts to reduce the evaporation temperature of the desired material and reduce contaminants. When at ambient pressure the material to be deposited is placed on a resistive source or within a crucible which is stable above the evaporation temperature of the material, the crucible is then placed within a resistive tungsten wire basket. The evaporation chamber is then sealed and the evacuation process begins with first the use of a roughing pump to achieve a low vacuum prior to a cryopump lowering the pressure to a high vacuum. Once at high vacuum a current is passed through the resistive source or the resistive wire basket, the temperature of the source/crucible rises and the material heats up begins evaporating above a certain temperature dependent on the specific material and pressure in the chamber. The rate of deposition and thickness deposited are measured using a quartz crystal monitor. The quartz crystal, when new, oscillates at 6 MHz, as material is deposited and begins to build up on the monitor the frequency at which it oscillates decreases, which with knowledge of the density and z-ratio (acoustic impedance of the deposition material) of the material allows for the mass and thickness of the material deposited on the crystal monitor to be calculated. This coupled with a geometric tooling factor, which accounts for the positional difference between the crystal monitor and the substrate being deposited upon, allows for the calculation of thickness deposited on the substrate and rate of deposition. The tooling factor for each evaporation source was calculated by evaporating thick films, estimated to be a few hundred nanometres, with an initial tooling factor. The thickness of these films are then measured via surface profilometry, spectroscopic ellipsometry or atomic force microscopy depending on the material properties and the tooling factor corrected for differences between the predicted thickness and measured thickness. Lithium fluoride and Molybdenum (VI) oxide layers used in devices in this thesis were deposited at 0.2 Å $s^{-1}$, Aluminium cathodes were

deposited at 1 Å $s^{-1}$. Evaporated layers in this thesis are patterned via the use of a shadow mask.

## 3.4: Device Architecture and Fabrication

In this thesis both organic light-emitting devices (OLEDs) and hole-only devices are fabricated on the same 15 x 20 mm glass substrates with a pre-patterned 100 nm indium-tin oxide (ITO) layer. A schematic of device architectures used in this thesis is laid out in Figure 3.2.

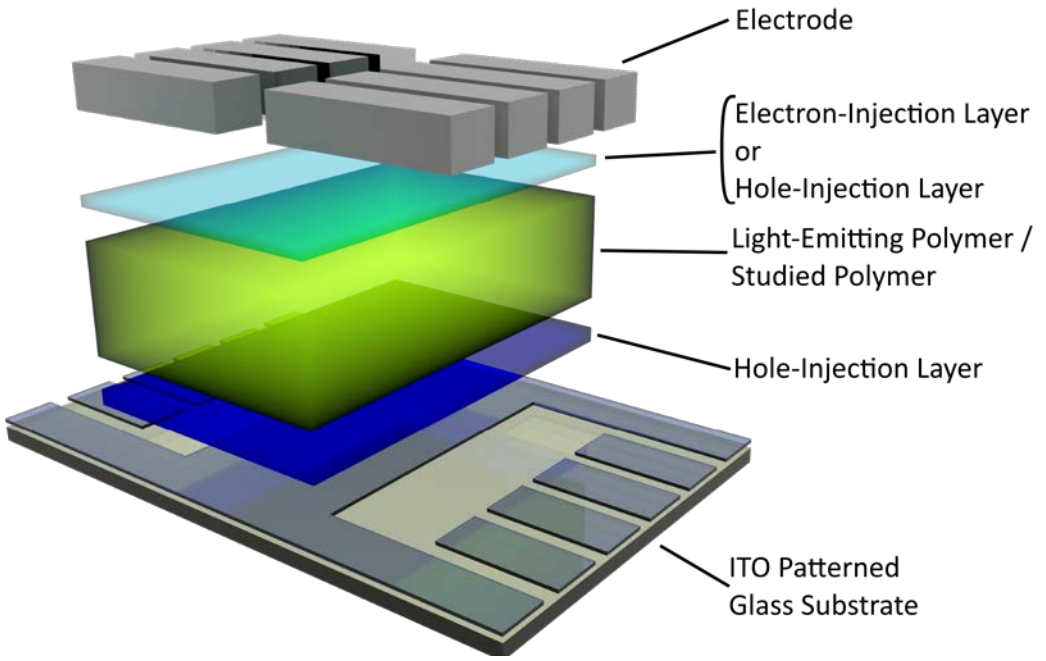


*Figure 3. 2: Schematic of the device architecture used in this thesis on 8-pixel ITO patterned substrate. This image shows a solution deposited layer below the electrode, in a device with thermally evaporated hole- or electron-injection layer this layer would be patterned like the top electrode.*

The OLEDs in this thesis take advantage of the transparent nature of ITO and are standard architecture bottom emitting devices, with ITO acting as the anode and the reflective top metal contacts acting as the cathode. On top of the ITO anode the next layer is a hole-injection layer (HIL), the following layer is the white-light-emitting polymer (LEP). Between the LEP and the cathode is an electron-injection layer (EIL), Figure 3.2 depicts a solution cast EIL as investigated in Chapter 4 in reference

thermally evaporated EIL devices this layer would have the same pattern as the cathode rather than a continuous layer. The hole-only devices in this thesis vary from the OLED structure by having the studied hole-transporting polymer instead of the LEP, and have a thermally evaporated hole-injection layer rather than an EIL.

Prior to device fabrication the substrates were cleaned to remove surface contaminants and aid in the wetting of the subsequently deposited solutions to the substrate. The substrates were loaded into a PET rack, submerged in a solution of Hellmanex (III) mixed with boiling deionised water (DI) and sonicated for 10 minutes. This was followed by the rinsing of the substrates in boiling DI prior to sonicating the substrates for 10 minutes in boiling DI. A further rinse in boiling DI is followed by a 10 minutes of sonication in isopropyl alcohol (IPA). The substrates were then dried using a nitrogen gun before being exposed to a UV-Ozone treatment for 15 minutes.

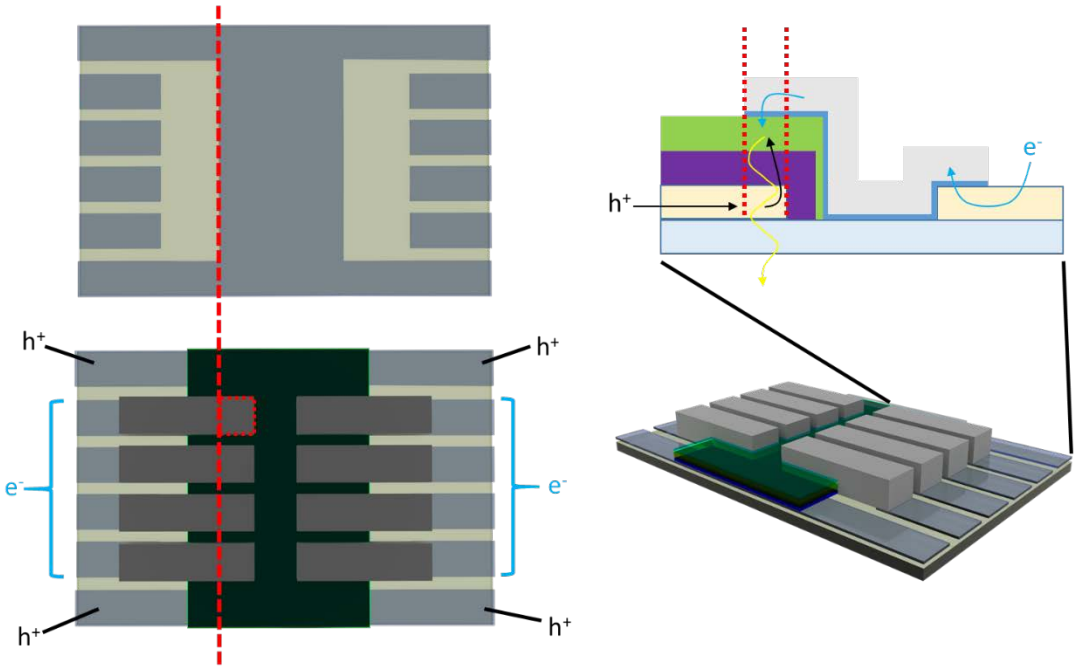


*Figure 3. 3: The top left image shows a top-down view of an 8-pixel ITO substrate. The bottom left image shows a top-down view of a completed 8-pixel device demonstrating how regions of layers have been removed over the ITO fingers to pattern the device. The dashed red line shows the edge of the central ITO pad and the dashed red square shows the area in which all layers are present which defines the pixel of 4 mm², this*

*occurs eight times over the substrate as such this is an eight pixel device. The ITO corners of the substrates are connected to the central ITO pad which allows charges to be transported to the bottom of the pixels, as shown for hole injection in OLEDs in the top right image. In OLEDs the electrons are transported through the ITO fingers, into the evaporated metal contacts, along the metal layer to the top of the pixel area and down into the other layers of the device within the pixel area at which point the opposite charges may radiatively recombine in the emissive layer to emit a photon. The bottom right image depicts a side on image of a completed device prior to any encapsulation, in which a glass slide will cover the full width of the substrate and to a length where only the ITO is exposed to air.*

Once the cleaning process has been completed the HIL can be deposited. Poly(3,4-ethylenedioxythiophene):poly(styrenesulfonate), PEDOT:PSS, is used as the bottom hole-injection layer for all devices in this thesis. PEDOT:PSS is a combination of the conjugated polymer PEDOT and non-conjugated polymer PSS which has a negatively charged $SO_3^-$ group. The addition of PSS is to solubilise the PEDOT allowing for PEDOT:PSS to be spin cast from an aqueous solution.[2] The ratio of PEDOT to PSS can be varied to change the depth of the HOMO and to vary the conductivity of the final PEDOT:PSS film. The conductive, highly transparent and smooth films cast from PEDOT:PSS are favourable properties for both organic photovoltaics and OLEDs.[3] The specific PEDOT:PSS used in this thesis is AL4083 with a PEDOT to PSS ratio of 1:6 and a work function around 5.2 eV. The aqueous PEDOT:PSS was filtered through a 0.45 μm PVDF filter prior to use for spin coating or for the preparation of the spray coating solution as described in Chapter 7. The spin cast PEDOT:PSS layer in deposited under a fume hood in a clean room via dynamic spin coating at 5000 rpm to form a continuous 40 ± 3 nm thick layer. The layer is then removed over the ITO fingers using a DI water soaked cotton bud, leaving the layer coated over the central ITO pad and onto the glass but crucially not on the ITO fingers. Following the swabbing process the PEDOT:PSS coated substrate is then placed on a 120 °C hotplate for 15 minutes to remove any remnant water in the film. The spray cast deposition of PEDOT:PSS is discussed in detail in Chapter 7.

The emissive layer of the OLEDs in this thesis is a white-light-emitting copolymer (LEP) as described in Chapter 2. The LEP was deposited dynamically from a 12 mg $ml^{-1}$ in p-Xylene at a spin speed of 2400 rpm for spin cast devices to form a layer 63 ± 3 nm thick. The deposition of the LEP via spray coating is described in detail in Chapter 7. After depositing the film it was patterned in the same positions as the HIL below using a cotton bud soaked with p-Xylene. In the hole-only devices the studied polymer, TFB, is deposited via spin coating at a range of different spin speeds from a range of different concentrations in toluene. The film is removed over ITO fingers via swabbing with a toluene soaked cotton bud.

In reference OLEDs in this thesis Lithium Fluoride (LiF) is thermally evaporated through a shadow mask at 0.2 Å $s^{-1}$ to form a 3 nm EIL prior to the deposition of a 100 nm Aluminium cathode at 1 Å $s^{-1}$ under the same vacuum.

In the hole-only devices in this thesis the layer above the studied polymer is a further HIL of thermally evaporated Molybdenum (VI) oxide, deposited at a rate of 0.2 Å $s^{-1}$ to form a 10 nm layer prior to the deposition of a 100 nm Aluminium cathode at 1 Å $s^{-1}$ under the same vacuum.

The evaporation of the top contact through a shadow mask defines the area of the pixels on the substrate as the regions where there is a complete stack of all the layers, as such the architecture used in this thesis leads to eight 4 $mm^2$ pixels on each device.

Once all layers are deposited the devices are removed from the vacuum chamber directly into the dry nitrogen atmosphere of the glovebox where they are encapsulated by applying a drop of UV-curable epoxy resin on top of the device stack, placing a glass slide down to cover all the deposited layers and exposing the devices to 30 minutes of UV light to cure the resin. UV light has the potential to cause degradation in the polymer layers within a device, to test if this was occurring during curing of the epoxy air-stable devices were fabricated, half of which were encapsulated as described above and half had no UV exposure, no difference in device performance was observed between the two splits as such the epoxy protects

the rest of the device stack from UV induced photodegradation during the curing process.

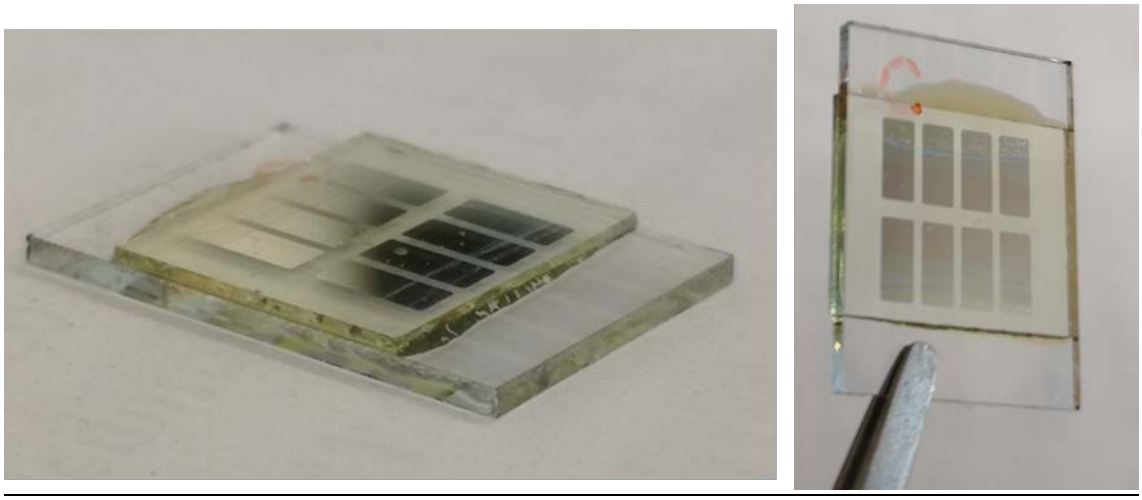

*Figure 3. 4: Photographs of a completely fabricated and encapsulated OLED.*

In Chapter 7 large area devices were fabricated using 25 x 75 mm glass substrates pre-patterned with 100 nm of ITO. These substrates pictured in Figure 3.5 have a similar design to 8 pixel but larger to fit 24 pixels of 9 $mm^2$. A slight but important difference in layout between large-area and 8 pixel substrates is that between each ITO finger which connects to the pixel there is an ITO strip that is connected to the central pad, this attempts to minimise the path length of charges in ITO which is known to cause resistive losses when scaling up devices.[4–6]

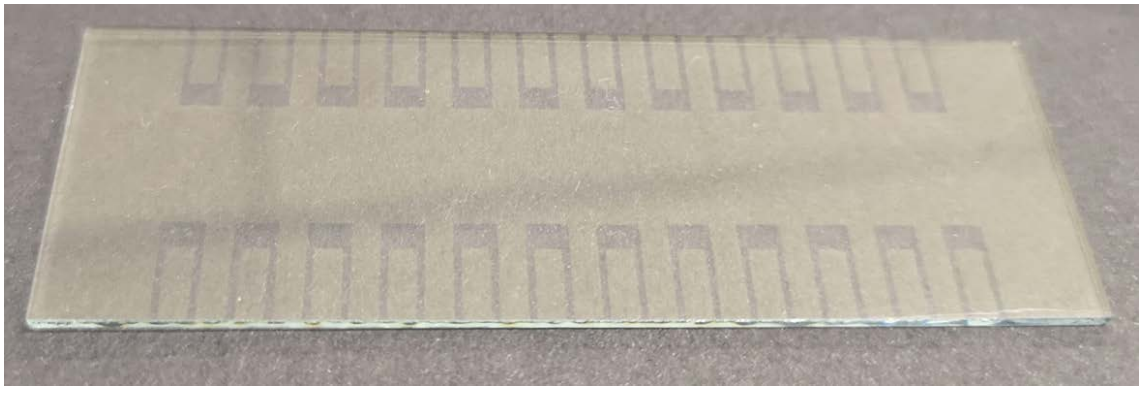

*Figure 3. 5: A photograph of a large area/scale-up substrate used to fabricate 9 $mm^2$ 24 pixel devices.*

The cleaning procedure for large-area substrate was identical to that of 8 pixel substrates but only three large-area substrates could be cleaned in each batch through this process unlike the twenty 8 pixel substrate that can be cleaned in one run.

The layers cast on the large area substrates were patterned in the same manner as with the 8 pixel substrates, the electron-injection layer and top electrodes were evaporated in the same method using a larger evaporation mask in which only four devices could be deposited on per run and devices were encapsulated in the same manner as the 8 pixel substrates but using a larger glass encapsulation slide.

## 3.5: Device Characterisation Techniques

### 3.5.1: Current-Voltage-Luminance Measurements (I-V-L)

To characterise the output from fabricated OLEDs, devices are mounted into an Ossila push-fit testing board, where spring-load gold pins contact the ITO fingers and main pad such that electrical contact can be made to each pixel individually via turning a switch. The testing board is mounted in a magnetised stand on an optical bench with a Konica Minolta LS-110 luminance meter aligned at a normal incidence to the bottom of the substrate. The luminance meter is fitted with a No° 110 close-up lens and is aligned such that the silicon photodiode within the luminance meter is 21 cm from the bottom of the substrate. The measuring distance can be tuned by small margins by twisting the lens so that the measurement-area ring in the in-built viewfinder is in focus within the area of the pixel, as the pixel is in focus. The LS-110 has a 1/3° acceptance angle of light this coupled with the normal alignment of the luminance meter justifies the assumption that the devices tested in this thesis can be treated as Lambertian emitters. As light passes through the luminance meter it passes through a filter before being measured by the photodiode, this filter coupled with a colour-correction factor of 1.050 alters the spectra such that the photodiode response closely replicates the Commission Internationale de l'Eclairage (CIE) relative photopic luminosity response. A Keithley 2602 source measure unit or an Ossila Xtralien X100 source measure unit were used to sweep voltage for each pixel separately from 0 to 10 V, in 0.2 V steps whilst measuring the current at each voltage

step. The Luminance is measured, in cd $m^{-2}$, after the current at each voltage step. Device metrics such as current efficiency, power efficiency and peak luminance can then be calculated after the data from sweeps has been recorded. After a pixel has be swept the testing board and optical stand it is mounted on are adjusted to align the next pixel to the luminance meter, the tested pixel is switched off and the newly aligned pixel is switched on.

Single-carrier devices were tested in the same testing set-up, minus the use of the luminance meter. The maximum voltage swept to was dependant on the thickness of the studied polymer layer in each pixel, with the voltage swept such that the electric field would pass 1 MV $cm^{-1}$ based on the relationship:

$$E = \frac{V}{d_{polymer}}$$

Where d is the thickness of the studied polymer layer.

### 3.5.2: Electroluminescence Spectroscopy

The electroluminescent spectra from devices fabricated in this thesis were recorded using an Andor Shamrock 303i spectrometer. An optical fibre coupled into the spectrometer with a cross-sectional area smaller than the pixel area was placed on the bottom of a device within the region of a pixel. A background measurement was taken in this setup within a dark room, the pixel was then swept from 0 to 10 V in 0.2 V steps as with I-V-L measurements with the spectra being recorded continuously, and this was repeated for multiple pixels and devices with no noticeable variation in emission recorded.

## 3.6: Film Characterisation Techniques

### 3.6.1: Surface Profilometry

A Bruker DextakXT has been used to measure the thickness, roughness and to produce 3D maps scans of layers in this thesis. To measure the thickness of a layer a razor blade was used to remove an area of the film from the substrate with any remnant film debris removed from the surface using a nitrogen gun to avoid any issues during measurements. The substrate is placed on the motorised dektak stage

and the 12.5 μm radius diamond tipped stylus is lowered onto the surface of the sample with a stylus force of 29 μN. The length of a line scan and time taken is set in the Vision64 program which controls the Dektak, with a typical thickness measurement taken in this thesis taken over 750 μm in 15 seconds, leading to a resolution of 167 nm per point. This resolution is less than that obtained from measurement techniques such as atomic force microscopy (AFM), leading to smoothing of smaller features of films studied but allowing for larger regions of the films to be analysed. As the line scan runs the stylus remains in the same xy position, the stage with the substrate upon it moves as such the tip of the stylus effectively passes along the cleared area of the substrate before being dragged over the edge and onto the layers being measured, with the stylus raising to continue the scan on the top surface of the material of interest. The stylus is linked to a linear variable differential transformer which translates physical motion of the stylus to electrical signals which can be interpreted by the software and then the difference in stylus height on the substrate and on the layer can be compared and the thickness can be calculated. All thickness stated in this thesis that are taken via surface profilometery are based on an average of a minimum of three measurements to ensure a representative thickness, errors stated from such thicknesses demonstrate the spread of values measured.

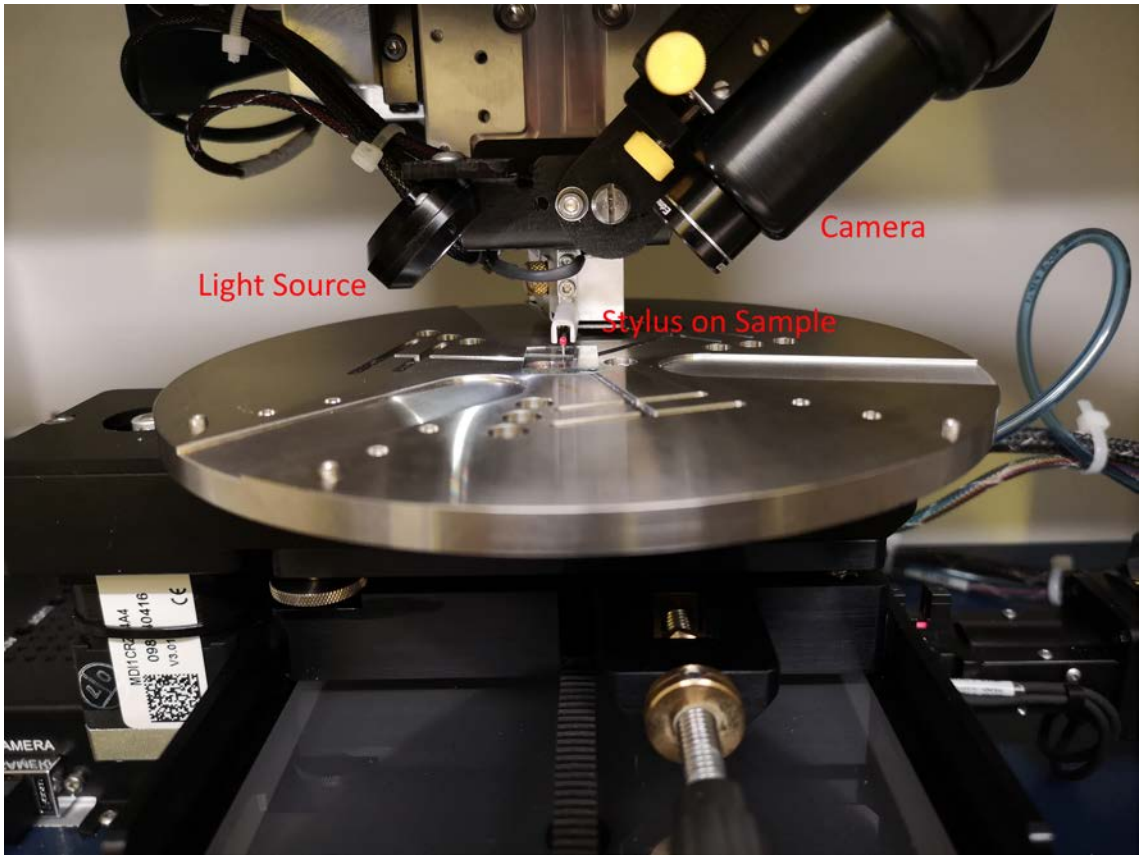


*Figure 3. 6: A photograph of the motorised stage of the Bruker DektakXT showing the stylus down on a substrate with the 10x optical camera and light source labelled.*

The roughness average (Ra) and root-mean-square (rms) roughness are also calculated by the Vision64 software for line scan but the roughness measurements in this thesis are based upon 3D maps scans as this is more accurate representation of the surface of the entire film.

Map scans were set up by determining the scan length, desired width of the final map scan, time per scan and number of scans the combination of these factors determined the resolution of the final map scan. 3D maps scans were constructed by the Vision64 software from a number of individual line scans stitched together, after the previous line scan is complete the tip returns to a point next to the start point of the previous line before beginning the next line scan. The final topographical map scans are exported and processed in Gwyddion software to produce the final figures in this thesis, the roughness values stated for map scans are taken calculated in this software.

### 3.6.2: Spectroscopic Ellipsometry

Spectroscopic ellipsometry involves the probing of a layer by light with the changes in polarisation and intensity of light reflected from the sample measured and used to calculate the thickness of the layer as well as the optical properties: refractive index (n) and extinction coefficient (k). Figure 3.7 shows a photograph of the Woollam M-2000V ellipsometer used in this thesis. Light of wavelengths from 370 – 1000 nm is emitted from a Xenon lamp then passed through a monochromator, which only allows a single wavelength to pass through. The light then passes through a polariser such that it is linearly polarised with known polarised components. The light then falls on the sample where it passes through the thin film and is reflected off the silicon substrate, this process causes a change in the phase and intensity of the light leading to elliptically polarised light. The light then passes through an analyser, a rotating polariser, the angle of the analyser is varied and coupled with the CCD this allows for the polarisation and intensity of the reflected light to be measured. These values are then compared with the initial output light to determine the change in phase ($\Delta$) and change in the intensity of polarisation ($\Psi$).[7]

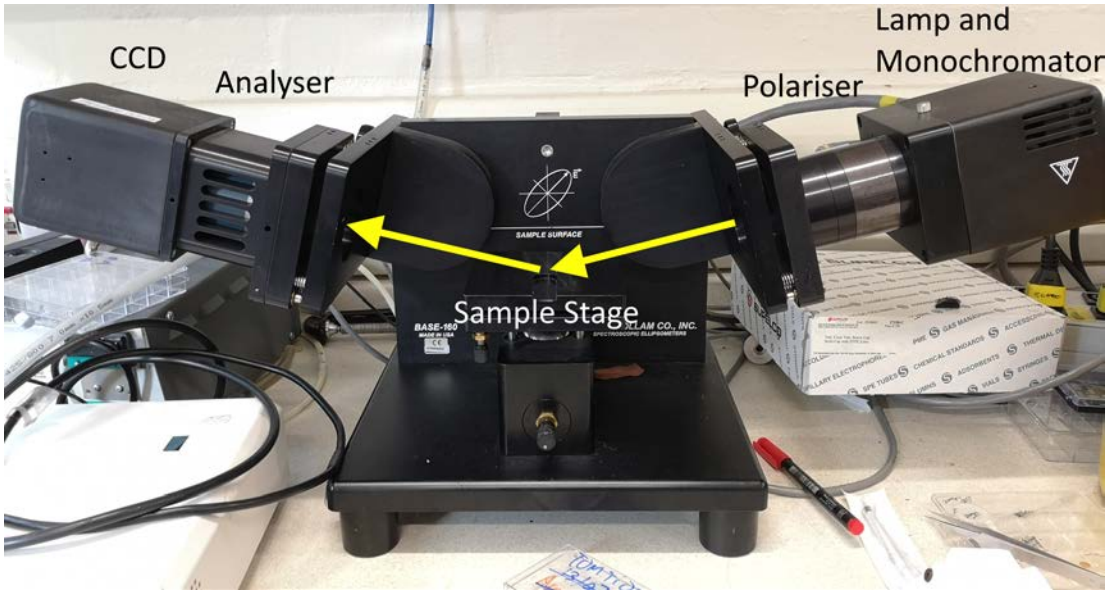


*Figure 3. 7: A photograph of the Woollam M-2000V ellipsometer with the key components labelled. The light source arm and detector arm are at 30° to avoid high losses due to reflections at the interface.*

A model that approximates the structure being measured is developed based on the optical constants, thickness and roughness of the material to produce $\Delta$ and $\Psi$ values for comparison with the experimentally determined values. In this thesis a Cauchy model (Equation 3.1) has been used for comparison in order to estimate the thickness and refractive index of the layer being studied.

$$n(\lambda) = A + \frac{B}{\lambda^2} + \frac{C}{\lambda^4} \ldots \quad (3.1)$$

The Cauchy model relies on variables A, B and C as well as the wavelength ($\lambda$) but does not include the extinction coefficient as such it can only be applied to wavelength ranges where the modelled material displays high transmittance. Once a model has been generated it is compared to the experimental data and the parameters are tuned in an iterative process to minimise the mean-square error (MSE) between the measured and modelled data. When the MSE has been minimised the estimated thickness of the studied layer can be extracted. The data processing and modelling for ellipsometry was performed using CompleteEASE software.

### 3.6.3: Contact Angle

The contact angle of solutions on ITO substrates were probed using an Attension Theta optical tenisometer as pictured in Figure 3.8. The tensiometer uses a setup where an adjustable stage is positioned between a monochromatic LED with smooth lighting integration sphere and a high-resolution, high-speed camera.

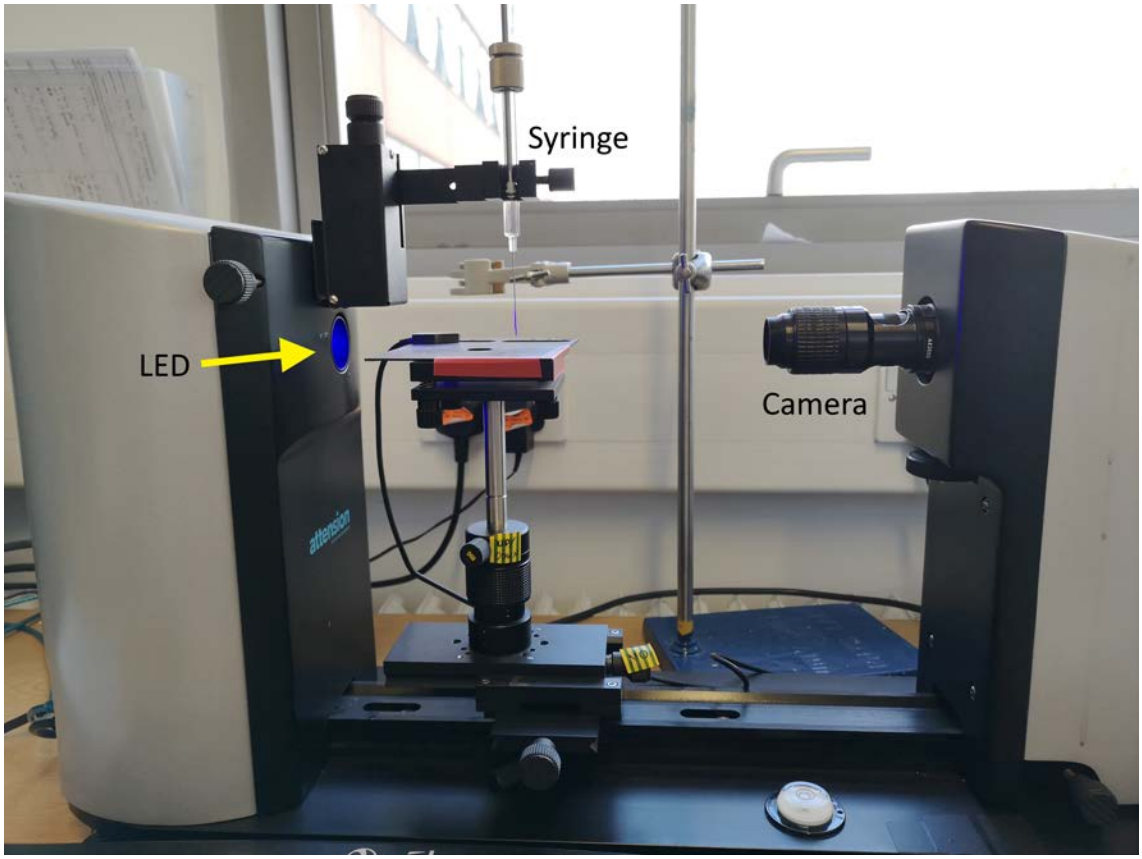


*Figure 3. 8: A labelled photograph of the Attension Theta tensiometer used to measure contact angles of droplets on ITO substrates in this thesis.*

To calibrate the system a ball bearing of known diameter is placed on the stage and the camera is focussed on the ball bearing. An image is then taken using the camera and a circle is fitted to the edges of the ball bearing and the diameter of the ball bearing is inputted into the software. An un-patterned ITO substrate then replaced the ball bearing and the focus on the substrate is checked. The solution of interest is loaded into a syringe with a fine needle, the syringe is then held in a clamp such that the tip of the needle is above the centre of the substrate. The camera is set running, taking an image every 16 ms for the desired time period, a small droplet of solution is deposited from the syringe onto the substrate below. After images of the droplet spreading on the substrate have been recorded the user looks through the images to find the first image of the droplet settled on the substrate, inputs the location of the substrate surface (baseline) making sure the point of contact between the edges of the droplet and the substrate sit on this line. The image processing software then

attempts to fit an ellipse extending below the substrate to the droplet to each frame. The software then for each frame calculates the angle between the baseline and the ellipse at the points they intersect giving the contact angle at both edges of the droplet, also an average of the two is calculated for all frames.

### 3.6.4: Laser-Beam-Induced Current Mapping

Laser-beam-induced current (LBIC) mapping is a device measurement technique that can spatially resolve current generation within and between pixels. A laser beam focused to a point on the active layer of a device generates a photocurrent at that position which is measured, the laser point is raster scanned in steps across the device and the measurement is repeated at each point building a spatial map of the distribution of current generation. The absorption and thus current generated is dependent upon the thickness of the layers within the device as such LBIC mapping allows for a route to probe the uniformity of thickness within a pixel and across the pixels of a device.

A picture of the LBIC mapping experimental setup is shown in Figure 3.9, the key components of the system are labelled.

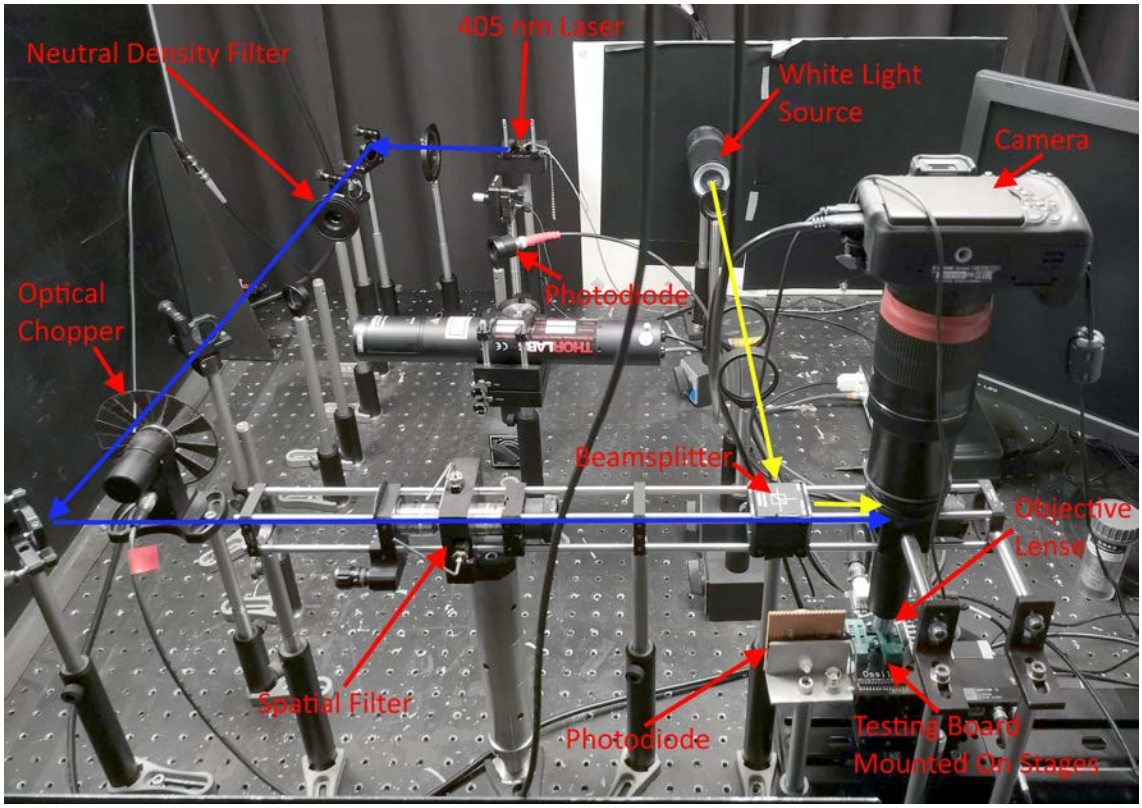


*Figure 3. 9: A photograph of the LBIC setup with key components labelled. The beam path of the 405 nm laser is marked with blue arrows. The beam path of the white light source used for alignment is shown using yellow arrows.*

The beam from a 405 nm, 3 mW laser was passed through a variable neutral density filter with a fraction of the beam being reflected onto a photodiode to record and account for fluctuations in laser power. The beam then passes through an optical chopper and a spatial filter which help collimate the beam and minimise effects such as airy rings of the beam or Newton's rings on the device. After exciting the spatial filter the beam is incident on a beam splitter where a fraction of the beam is split onto a secondary photodiode to further check for fluctuations in power and the main beam path continues on through a 10x microscope objective and onto the device. The device is mounted in an electrical testing board and the board is mounted on a computer controlled xy stage and a manual z stage. A Stanford Research Systems SR830 lock-in amplifier was used to maximise the signal and measure the current generated.

A white light source is directed via the beam splitter, through the microscope objective to illuminate the device, this allows for the position of the laser spot on the device to be seen as to align in the xy plane and the z stage allows the laser spot to be focussed on the device.

A device is mounted and levelled in the testing board before moving the stage such that the device sits under the objective. After aligning and focussing the laser spot on the device with the optical chopper switched off, the dimensions of scan and step size are inputted by the user into a LabVIEW script. The LBIC maps presented in Chapter 7 required 130 by 230 steps with a step size of 50 μm to cover all 8 pixels on a device and the surrounding regions. The optical chopper is switched on and all other light sources other than the laser are switched off and the script is started. At each point of the scan five current measurements are taken, with a one second settle time between each measurement, and an average of these measurements is written to a txt file. The stage then shifts 50 μm after completing the measurement of the first point and the next measurement begins, this is repeated as the laser raster scans across the device to construct the map, for maps of 130 by 230 steps with 50 μm steps this takes in the region of 40 hours to complete.

## 3.7: Summary

The experimental techniques and procedures used in this thesis have been introduced and discussed in this chapter. Spin coating and thermal evaporation are used in all experimental chapters, ultrasonic spray coating is used in Chapters 5, 6 and 7. The device architecture and fabrication described in this chapter is used across all experimental chapters. Current-Voltage measurements as used in Chapter 6 to investigate single-carrier devices, Current-Voltage-Luminance measurements are taken in Chapters 4 and 7. Spectroscopic ellipsometry is used in Chapter 4 to determine the thicknesses of thin-film spin cast electron-injection layers. In Chapter 7 contact angle measurements are used to investigate the use of solvent blends on the wetting of a solution to a surface and LBIC mapping is used to probe the uniformity of spin cast and spray cast layers in an OLED.

## 3.8: References


[1] C.J. Lawrence, The mechanics of spin coating of polymer films, Phys. Fluids. 31 (1988) 2786–2795. doi:10.1063/1.866986.

[2] A.M. Nardes, M. Kemerink, M.M. de Kok, E. Vinken, K. Maturova, R.A.J. Janssen, Conductivity, work function, and environmental stability of PEDOT:PSS thin films treated with sorbitol, Org. Electron. 9 (2008) 727–734. doi:10.1016/J.ORGEL.2008.05.006.

[3] C.H. Jonda, A.B.R. Mayer, U. Stolz, Surface roughness effects and their influence on the degradation of organic light emitting devices, J. Mater. Sci. 35 (2000) 5645–5651. doi:10.1023/A:1004842004640.

[4] J.E. Bishop, D.K. Mohamad, M. Wong-Stringer, A. Smith, D.G. Lidzey, Spray-cast multilayer perovskite solar cells with an active-area of 1.5 cm2, Sci. Rep. 7 (2017) 7962. doi:10.1038/s41598-017-08642-2.

[5] Y. Galagan, E.W.C. Coenen, W.J.H. Verhees, R. Andriessen, Towards the scaling up of perovskite solar cells and modules, J. Mater. Chem. A. 4 (2016) 5700–5705. doi:10.1039/c6ta01134a.

[6] R. Clark, K. Tapily, K. Yu, T. Hakamata, S. Consiglio, C. Wajda, J. Smith, G. Leusink, Perspective: New process technologies required for future devices and scaling, APL Mater. 6 (2018). doi:10.1063/1.5026805.

[7] J.A. Woollam Co, CompleteEASE™ Data Analysis Manual, 2004. http://www.jawoollam.com (accessed September 17, 2018).

# Chapter 4

# Solution-Processed Electron-Injection Layers for Polymer Light-Emitting Diodes

## 4.1: Introduction

The performance of OLEDs has improved over time with a key development being the introduction of multilayer device architectures.[1–4] Introducing layers such as electron-injection layers (EILs), hole-injection layers (HILs), electron-transporting layers (ETLs) and hole-transporting layers (HTLs) between the emissive layer and the electrodes have been demonstrated to increase device luminance and efficiency by reducing energy barriers to charge injection, improving the balance of injected charges, confining charges within the emissive layer, reducing exciton quenching and tuning the recombination location to improve light out-coupling.[5–7]

Typically multilayer devices are fabricated via thermal evaporation under a high vacuum although it is possible to scalably deposit under vacuum, high vacuums in large chambers which are required for large area deposition of such thin reactive layers are challenging to achieve and very expensive. Scalable solution-processed multilayer devices are often viewed as a potential route for low-cost fabrication due to room-temperature high-vacuum-free processing.[8,9] The main challenge of fabricating multilayer solution-processed devices is the need for alternate layers to be cast from orthogonal solvents to avoid the layer below being dissolved during the deposition. Commonly used thermally deposited EILs such as lithium fluoride (LiF) and calcium are insoluble in alcohol type solvents which could be cast on conjugated polymer emissive layers as such alternate solution-processable EILs must be used.

In this chapter caesium carbonate, 8-hydroxy-quinolinato lithium and polyethylenimine-ethoxylated are investigated as solution-processed spin cast electron-injection layers for white-light-emitting polymer LEDs. The dependence of device performance on the thickness of these different electron-injecting layers is investigated in order to optimise device performance. This work is undertaken with the future aim of depositing this material via ultrasonic spray coating under ambient conditions to complete a fully spray cast polymer LED.

## 4.2: Device Fabrication

Devices in this chapter were fabricated using pre-patterned 8 pixel ITO TEC 20 substrates purchased from Ossila Ltd. The substrates were cleaned following the protocol laid out in Chapter 3. Al 4083 grade PEDOT:PSS was filtered using a 0.45 µm PVDF mircodisc filter prior to spin coating at 5000 rpm to yield a 40 ± 3 nm film. The PEDOT:PSS films were annealed on a hotplate, in air at 120 °C for 15 mins and then cooled to room temperature prior to deposition of the emissive layer. The white-light-emitting polymer (LEP) was spin cast in ambient conditions from a 12 mg $ml^{-1}$ p-Xylene solution at 2400 rpm to form a 63 ± 3 nm film. Devices were then coated by the electron-injection materials discussed in the following sections via spin coating. The layers over the ITO contacts were wiped away using a solvent soaked cotton bud. The solvent used for each layer was deionised water for PEDOT:PSS, p-Xylene for the LEP and the respective solvent used to deposit the EILs. A 100 nm Aluminium electrode capped the devices deposited through a shadow mask via thermal evaporation under a minimum vacuum of 4 x $10^{-6}$ mbar to define a pixel area of 4 $mm^2$. Devices were encapsulated using a UV-curable epoxy and a glass slide in an inert atmosphere prior to being tested.

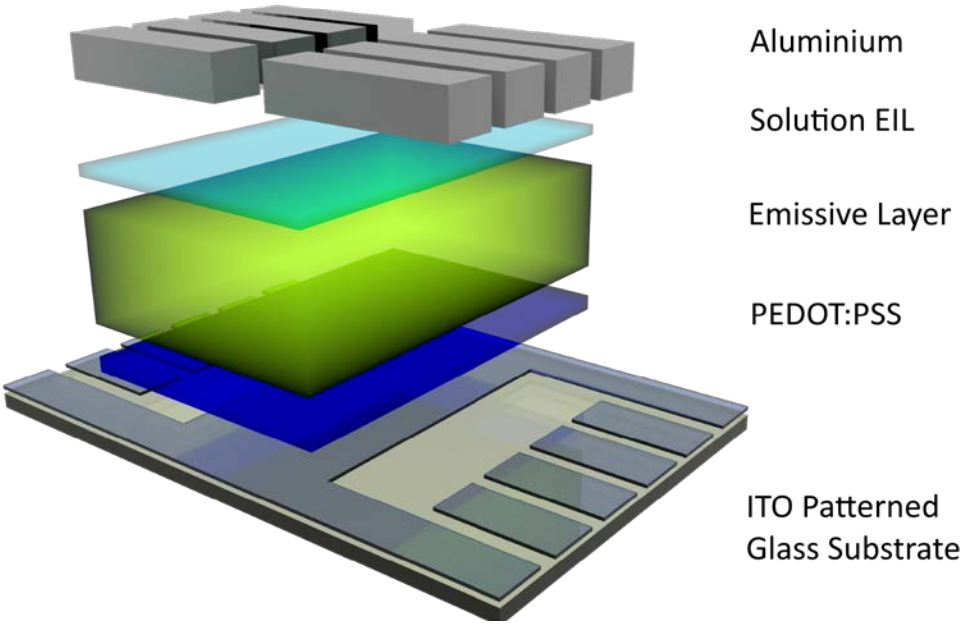


*Figure 4. 1: A 3D rendering of the device architecture used in this chapter. A pre-patterned ITO coated glass substrate coated by a 40 ± 3 nm PEDOT:PSS layer, a 63 ± 3 nm emissive layer, varying thicknesses of spin cast electron-injection layers and a 100 nm Aluminium cathode.*

The thickness of the PEDOT:PSS, emissive layer and electrode were confirmed using a Bruker DektakXT surface profilometer. Thicknesses of the various solution-processed electron-injection layers which produced the best device metrics were measured via ellipsometry. Ellipsometry was performed using a spectroscopic ellipsometer (M2000v, J. A. Woollam Co., USA). The different EILs were deposited from the same concentrations and spin speeds used for devices onto silicon substrates. Ψ, the ratio of the amplitude of incident and reflected light, and Δ, the ratio of the phase lag between incident and reflected light, were recorded over a wavelength range of 370 to 1000 nm. A Cauchy model was used to fit to this data in the optically transparent region, 370 – 800 nm, of the thin film, (where the extinction coefficient, $k \approx 0$) and determine the thicknesses of the EILs. The thickness of the non-optimal performance EILs were calculated based on the thicknesses measured via the ellipsometer then applying the thickness-spin-coating relationship discussed in Section 2.5.2.[10]

## 4.3: Caesium Carbonate as a Solution-Processed Electron-Injection Layer

In this section caesium carbonate, $Cs_2CO_3$, is investigated as a potential solution-processed electron-injection layer for devices using the white-light-emitting polymer (LEP) used in this thesis. An alkali metal salt, $Cs_2CO_3$ has been used extensively as an EIL when deposited via thermal evaporation and more recently as a spin cast EIL.[11–15] Spin cast $Cs_2CO_3$ reacts with the thermally evaporated aluminium cathode to form an Al-O-Cs complex at the interface between the aluminium and $Cs_2CO_3$ which reduces the work function of the aluminium decreasing the barrier for electron injection. Further to this $Cs_2CO_3$ acts as a hole-blocking layer, confining holes within the emissive layer to help to balance the density of charges and increase efficiency.[12]

$Cs_2CO_3$ was spin cast in a dry nitrogen atmosphere at a range of spin speeds (2000 – 5000 rpm) from anhydrous 2-ethoxyethanol at a range of concentrations (0.5 – 8 mg $ml^{-1}$) in order to find an optimal thickness for this device structure.

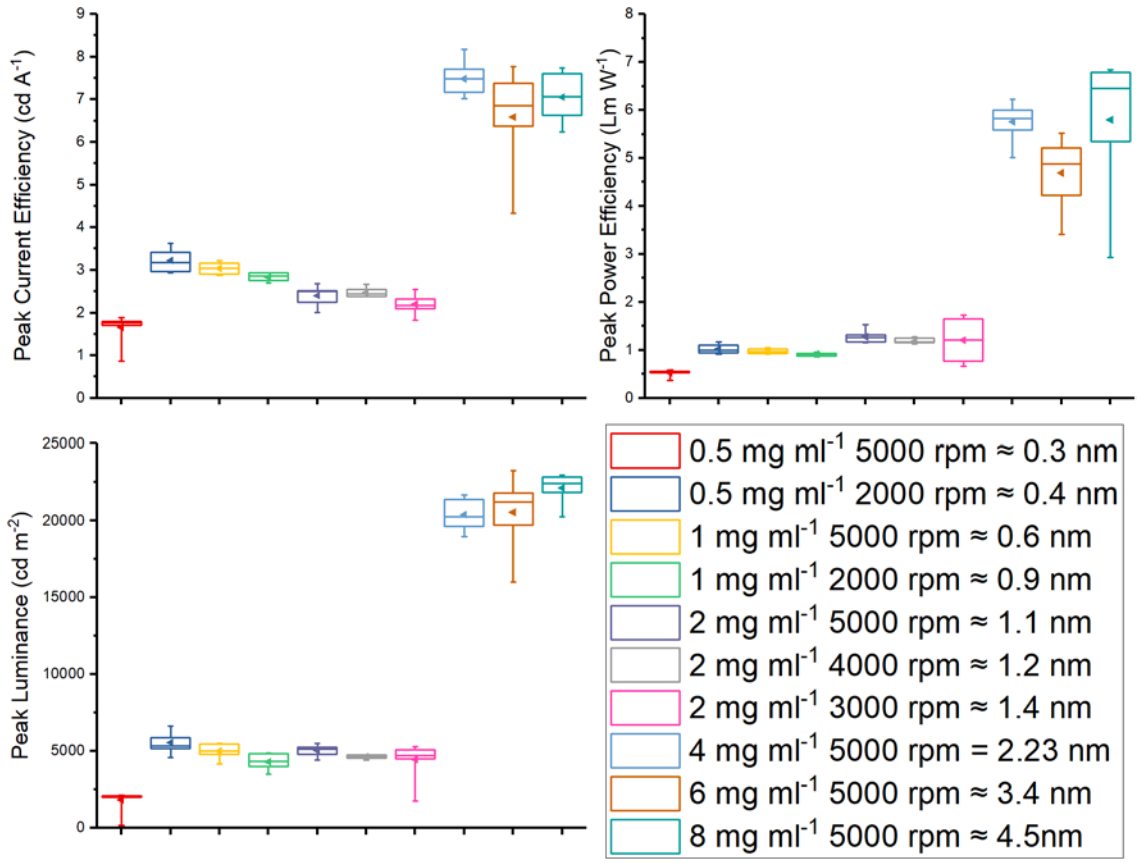


*Figure 4. 2: The key device performance metrics a) peak current efficiency, b) peak power efficiency and c) peak luminance of devices with spin cast $Cs_2CO_3$ as the electron-injection layer. $Cs_2CO_3$ was deposited from a range of different concentrations, 0.5 – 8 mg ml$^{-1}$, and a range of spin speeds, 2000 – 5000 rpm, to vary the thickness of the layer.*

The devices with $Cs_2CO_3$ cast from a 0.5 mg ml$^{-1}$ solution at 5000 rpm have the lowest mean device metrics of 1.66 cd A$^{-1}$, 0.52 Lm W$^{-1}$ and 1811 cd m$^{-2}$. Devices with $Cs_2CO_3$ cast from 0.5 mg ml$^{-1}$ at 2000 rpm through to those cast from 2 mg ml$^{-1}$ at 3000 rpm had very similar metrics, all a slight improvement on the thinnest $Cs_2CO_3$ layer with the mean metrics 2.20 - 3.23 cd A$^{-1}$, 0.91 – 1.27 Lm W$^{-1}$ and 4309 - 5545 cd m$^{-2}$. The estimated thicknesses of these cast films are 1.4 nm or less, the root-mean-square roughness of the LEP deposited via spin coating is measured in Chapter 7 to be 1.4 nm as such the low concentration spin cast $Cs_2CO_3$ layers are unlikely to uniformly coat the LEP layer resulting in an incomplete film or a conformal coating of varying thickness leading to poor device performance. There is a large jump in the performance metrics to the films cast from 4 – 8 mg ml$^{-1}$ which

have similar metrics, the range of mean metrics 6.59 – 7.49 cd $A^{-1}$, 4.69 – 5.80 Lm $W^{-1}$ and 20403 - 22130 cd $m^{-2}$. The devices with the $Cs_2CO_3$ cast from 4 mg $ml^{-1}$ have narrowest spread of data for the peak current efficiency and peak power efficiency with standard deviations of 0.38 cd $A^{-1}$ and 0.38 Lm $W^{-1}$ respectively. However, the devices with $Cs_2CO_3$ cast from 4 mg $ml^{-1}$ have a fractionally larger spread in mean peak luminance than those cast from 8 mg $ml^{-1}$, standard deviations of 1001 cd $m^{-2}$ and 996 cd $m^{-2}$ respectively. Due to the slightly higher performance metrics and narrower distribution across two of the three metrics the $Cs_2CO_3$ film cast from a 4 mg $ml^{-1}$ solution was chosen as the optimum deposition thickness. Ellipsometry performed on a $Cs_2CO_3$ film spin cast at 5000 rpm from a 4 mg $ml^{-1}$ solution onto a silicon substrate confirmed the thickness to be 2.2 ± 0.1 nm. This optimal thickness is in agreement with work done by Huang et al. where the peak device efficiency was achieved with solution-processed $Cs_2CO_3$ of a thickness between 2.0 – 2.4 nm based on comparison with thermally evaporated data and estimated from X-ray photon spectroscopy absorption data.[12]

The performance of devices with $Cs_2CO_3$ cast from a 4 mg $ml^{-1}$ solution is in fact higher than the equivalent reference devices from the same run with a 3 nm thermally evaporated lithium fluoride EIL which had mean peak luminance, current efficiency and power efficiency of 9022 cd $m^{-2}$, 5.01 cd $A^{-1}$ and 2.54 Lm $W^{-1}$ respectively.

The deposition of solution based EILs via spray coating under a dry nitrogen atmosphere for proof of concept lab scale fabrication is acceptable but if this is to be viewed in the context of an industrial roll-to-roll process then there are a number of issues. To scale up such a process would require a very large glovebox and a near constant purging of fresh nitrogen through the box as to remove evaporated solvent from the atmosphere, both these factors would raise the costs significantly and reduce the financial viability of the process. Further to this having multiple spray heads rapidly depositing within the same glovebox and the continuous flow of nitrogen required would lead to a turbulent atmosphere which would affect the directionality of the mist of droplets being deposited and the uniformity and repeatability of the deposited films. As such potential EILs for ultrasonic spray

coating must be stable under ambient processing. Devices with the same optimal thickness of $Cs_2CO_3$ were fabricated under ambient conditions as the next step towards depositing this layer via ultrasonic spray coating. The current efficiency and luminance against voltage of a representative pixel from ambient processed and glovebox processed devices are compared below.

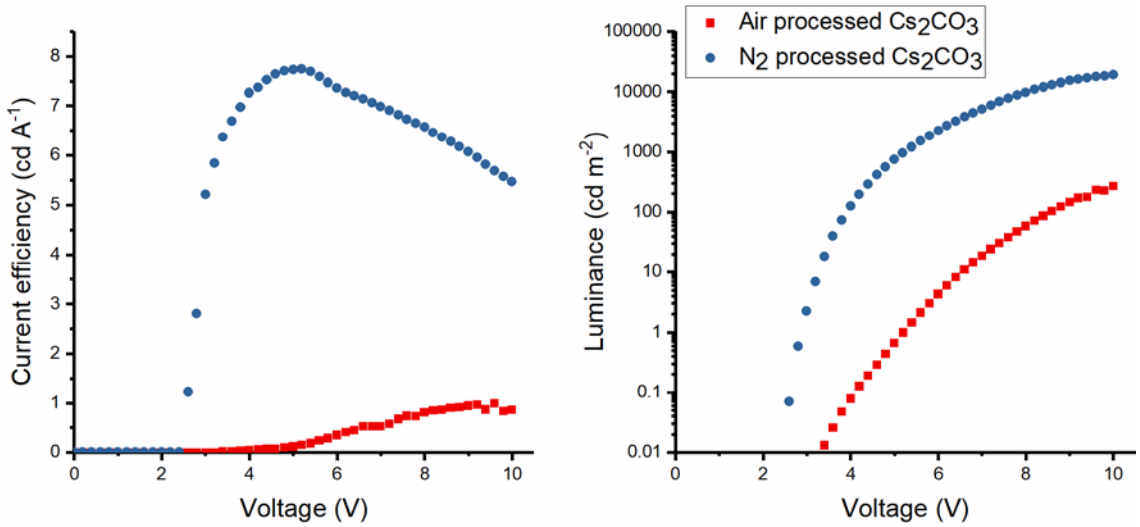


*Figure 4. 3: The current efficiency against voltage and Luminance against voltage of devices with $Cs_2CO_3$ EILs spin cast to the same thickness in a nitrogen atmosphere (blue) and in ambient conditions (red).*

Figure 4.3 shows that the device in which $Cs_2CO_3$ is cast in air is drastically worse than the devices with the EIL cast under nitrogen. The peak current efficiency decreases nearly eight-fold and there is a decrease in peak luminance of around two orders of magnitude. A similar effect on device performance in which $Cs_2CO_3$ films have been exposed to ambient conditions has been shown in literate with a 30 minute exposure enough to reduce the $Cs_2CO_3$ EIL device performance drastically.[16]

Despite the impressive performance metrics of devices in which $Cs_2CO_3$ is cast in the glovebox the poor performance of devices in which the film was cast in air means that $Cs_2CO_3$ is not a viable option for deposition in the ambient ultrasonic spray coating system.

## 4.4: 8-Hydroxy-Quinolinato Lithium as a Solution-Processed Electron-Injection Layer

In this section 8-hydroxy-quinolinato lithium, Liq, is investigated as a potential solution-processable electron-injection layer for devices using the white-light-emitting polymer (LEP) used in this thesis. After initial promising results with $Cs_2CO_3$ the inability to process it under ambient conditions lead to Liq as a potential solution as it has been demonstrated to be resistant to ambient exposure.[16] Liq, an alkali metal complex, is far less hygroscopic than $Cs_2CO_3$ and is highly soluble in a range of alcohols allowing for smooth thin films to be cast via spin coating.[17] The interaction of Liq with the evaporated aluminium electrode leads to and interfacial dipole which reduces the barrier to electron injection into the emissive layer from the cathode.[18,19]

Liq is spin cast in a dry nitrogen atmosphere at a range of spin speeds (2000 – 4000 rpm) from anhydrous 2-ethoxyethanol at a range of concentrations (0.2 – 2 mg $ml^{-1}$) in order to find an optimal thickness for this device structure.

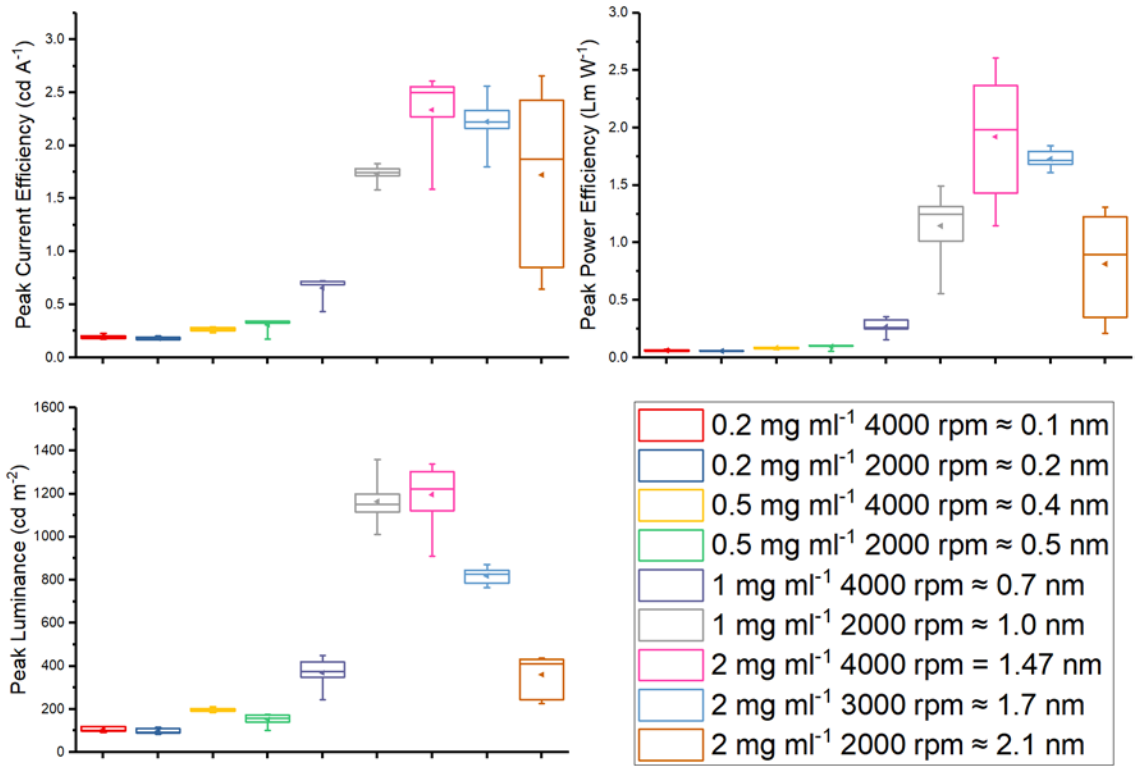


*Figure 4. 4: The key device performance metrics a) peak current efficiency, b) peak power efficiency and c) peak luminance of devices with spin cast Liq as the electron-*

*injection layer. Liq was deposited from a range of different concentrations, 0.2 – 2 mg ml$^{-1}$, and a range of spin speeds, 2000 – 4000 rpm, to investigate the device performance on the thickness of the layer.*

The devices with Liq cast from a 0.2 and 0.5 mg ml$^{-1}$ solutions at various deposition speeds have the lowest mean device metrics ranging from 0.18 – 0.31 cd A$^{-1}$, 0.06 – 0.1 Lm W$^{-1}$ and 98 - 198 cd m$^{-2}$. These solutions are highly dilute as such it is possible that complete films weren't formed or equally it is possible these films were complete but too thin to allow for reasonable device performance.

Devices with Liq cast from 1 mg ml$^{-1}$ at 4000 and 2000 rpm show a measurable improvement with an increase In the three mean performance metrics to 0.66 cd A$^{-1}$, 0.27 Lm W$^{-1}$ and 368 cd m$^{-2}$ for the 4000 rpm devices and 1.73 cd A$^{-1}$, 1.15 Lm W$^{-1}$ and 1164 cd m$^{-2}$. The peak performance devices were those with Liq cast from a 2 mg ml$^{-1}$ solution at 4000 rpm, the peak mean metrics were 2.34 cd A$^{-1}$, 1.92 Lm W$^{-1}$ and 1197 cd m$^{-2}$. The performance of devices then drastically decreased with slight increases in thickness as the devices with films cast from the same 2 mg ml$^{-1}$ solution but at slower spin speeds of 3000 and 2000 rpm had mean peak performance metrics of 2.22 and 1.72 cd A$^{-1}$, 1.73 and 0.81 Lm W$^{-1}$ and 818 and 360 cd m$^{-2}$ respectively. This demonstrates there is a very narrow optimum thickness window for Liq as an EIL, the layers must be thick enough to form a continuous layer but as the thickness of the layer increases, the performance decreases due to the poor electron mobility.[17,20] A Liq film cast from a 2 mg ml$^{-1}$ solution at 4000 rpm, equivalent to those in the highest performance devices, was cast onto a silicon substrate in order to perform ellipsometry to confirm the optimum thickness to be 1.5 ± 0.1 nm. The optimum thickness found in this device structure tends to agree with Liq used in small molecule and polymer LEDs in literature of between 0.5 – 2 nm.[16,18,21]

The mean peak power efficiency of devices with a 1.5 ± 0.1 nm Liq EIL are only slightly lower than the reference devices with a 3 nm thermally evaporated Lithium Fluoride EIL, 1.92 Lm W$^{-1}$ to 2.54 Lm W$^{-1}$. However the mean peak current efficiency, 2.34 cd A$^{-1}$ compared to 5.01 cd A$^{-1}$, and to a further extent the mean peak luminance,

1197 cd $m^{-2}$ compared to 9022 cd $m^{-2}$, of the devices with spin cast Liq are significantly lower than the thermally evaporated LiF reference. The disappointing performance metrics, particularly the low luminance, coupled with the fact that although being significantly less hygroscopic than $Cs_2CO_3$ the device performance will still drop when these films are fabricated in ambient, as required for spray deposition, shows that Liq is not a viable material for investigation as and ambient ultrasonic spray cast electron-injection layer.[16]

## 4.5: Polyethylenimine-Ethoxylated as a Solution-Processed Electron-Injection Layer

Following the disappointing performance metrics of spin cast Liq and the inability to process $Cs_2CO_3$ in air the decision was made to move away from alkali metal-containing compounds to primarily focus on materials which are air stable. In 2012 Zhou et al. demonstrated the potential of air-stable non-ionic and non-conjugated polymer polyethylenimine-ethoxylated, PEIE, to reduce the work function of electrodes for organic electronics. This work function shift, which reduces the barrier for electron injection, is due to a combination of the intermolecular dipole moments from the amine groups in the PEIE and the induction of interfacial dipoles with the aluminium electrode.[17,22,23]

In this section PEIE is investigated as a potential solution-processed electron-injection layer for devices using the white-light-emitting polymer (LEP) used in this thesis. PEIE is spin cast in ambient conditions from environmentally friendly isopropyl alcohol (IPA) at a range of dilute concentrations (0.01 wt.% – 0.4 wt.%) at 5000 rpm in order to find an optimal thickness for this device structure. Thin PEIE films are annealed for 10 minutes in ambient at 100 °C prior to the deposition of the Aluminium electrode following the method laid out by Zhou et al.[23]

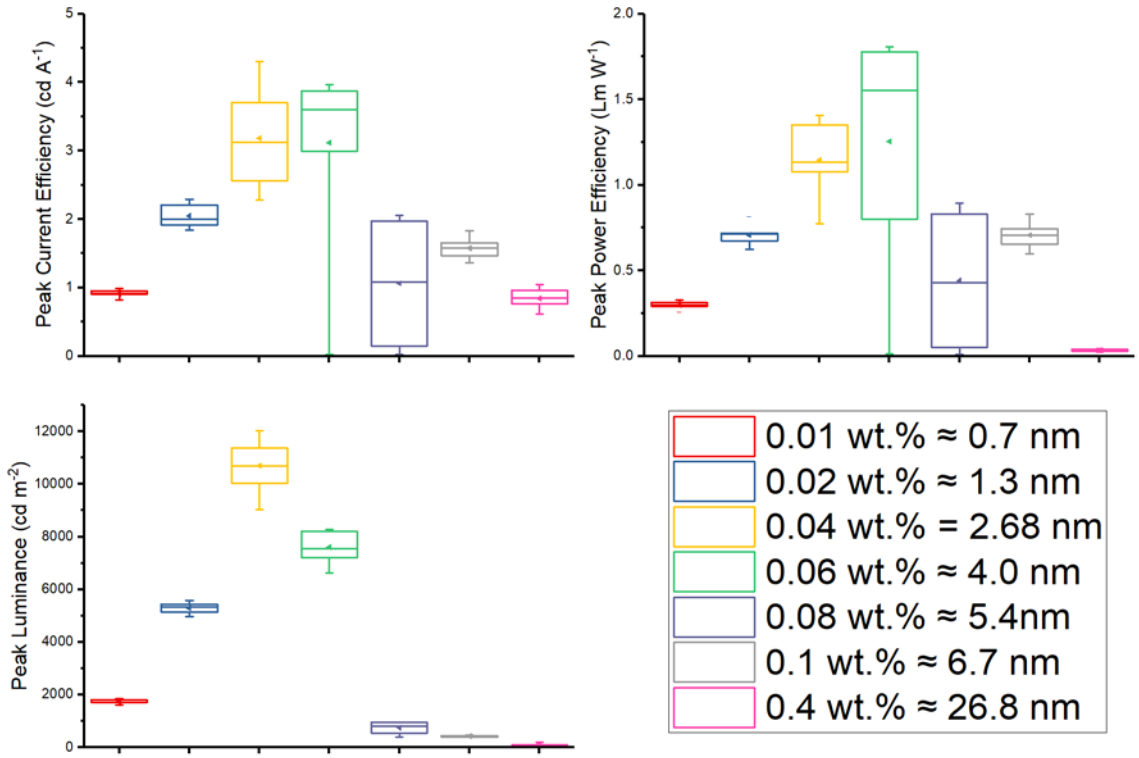


*Figure 4. 5: The key device performance metrics a) peak current efficiency, b) peak power efficiency and c) peak luminance of devices with spin cast PEIE as the electron-injection layer. PEIE was deposited from a range of different concentrations, 0.01 – 0.4 wt.%, at 5000 rpm to investigate the influence of the layer thickness on the device performance..*

Initial thickness investigations were based around the work done by Zhou et al. where the PEIE was deposited from a 0.4 wt.% solution to form a 10 nm layer. In this device structure those with PEIE cast from a 0.4 wt.% solution perform very poorly with mean peak current efficiency, power efficiency and luminance of 0.84 cd $A^{-1}$, 0.03 Lm $W^{-1}$ and 113 cd $m^{-2}$ respectively, similar luminance, 75 cd $m^{-2}$, to a reference device with no EIL (ITO / PEDOT:PSS / LEP / Aluminium). The insulating nature of PEIE dictates that when this layer is too thick the device performance will drop as such I began to probe lower concentration solutions.

Devices with thinner films cast from 0.08 and 0.1 wt.% show and improvement from cast from 0.4 wt.% but are still very poor with mean peak device metrics of 1.06 and 1.57 cd $A^{-1}$, 0.44 and 0.70 Lm $W^{-1}$ and 745 and 421 cd $m^{-2}$ respectively.

A significant increase in mean peak device metrics occurs for devices with films cast from 0.04 and 0.06 wt.% solutions. The mean peak current efficiency, 3.18 (0.65) and 3.12 (1.34) cd $A^{-1}$, and mean peak power efficiency, 1.14 (0.21) and 1.25 (0.62) Lm $W^{-1}$, are similar for 0.04 wt.% and 0.06 wt.% respectively but with a lower standard deviation for the more dilute solution as indicated by the values in brackets. The mean peak luminance of the devices with PEIE cast from 0.04 wt.% solution is higher than the mean of the devices with 0.06 wt.% EIL, 10690 cd $m^{-2}$ in comparison to cd 7600 $m^{-2}$.

As the PEIE film is cast from more dilute solutions, 0.02 and 0.01 wt.%, the mean peak luminance metrics decrease sharply to 2.05 and 0.92 cd $A^{-1}$, 0.71 and 0.30 Lm $W^{-1}$ and 5286 and 1762 cd $m^{-2}$ respectively. The decrease in performance metrics of the devices with PEIE films cast from these lower concentration solutions may be due to the film being too thin to shift the work function of the aluminium cathode the optimum amount leading to a high barrier for electron injection or due to incomplete surface coverage as the calculated thickness of these layers are less than the root-mean-squared roughness of the emissive layer (measured to be 1.4 nm using a dektak map scan in Chapter 7).

A PEIE film cast from a 0.04 wt.% IPA solution at 5000 rpm, equivalent to those in the highest performance devices, was cast onto a silicon substrate to measure the thickness via ellipsometry. The thickness was modelled to be 2.7 ± 0.1 nm.

The optimum thickness found in this device structure is slightly thinner than the optimum thickness estimated via XPS of 3.7 nm cast from 0.06 wt.% found for a blue-emitting polymer LED by Stolz et al.[22] In that work the electrode chosen was silver and as the thickness of PEIE deposited on the silver was increased the work function decreased to a minimum point at 4 nm of PEIE. In this chapter the electrode used is aluminium which has a lower work function than silver, as such it would require a lesser reduction in work function for a good alignment with the LUMO of the polymer thus a thinner layer of PEIE is required.

As a further test to confirm the thin layer of PEIE is performing as an EIL and the improvement in device performance is not due to a phenomenon caused by spin

rinsing the emissive layer with IPA and annealing the film, control devices were fabricated in which this process was performed which showed identical performance to those without an EIL.

The optimal thickness of PEIE devices have lower mean peak efficiency metrics than the LiF references 3.18 cd $A^{-1}$ compared to 5.01 cd $A^{-1}$, and 1.14 Lm $W^{-1}$ compared to 2.54 Lm $W^{-1}$. Although these metrics are lower than the references they are still an acceptable level and importantly unlike devices with Liq as the EIL the mean peak luminance is very good, in fact slightly higher than the LiF references at 10690 cd $m^{-2}$ compared to 9022 cd $m^{-2}$.

The high luminance and reasonable efficiency metrics of devices with PEIE EILs coupled with the fact these devices were fabricated under ambient conditions shows that PEIE is a viable material for investigation as and ambient ultrasonic spray cast electron-injection layer.

## 4.6: Conclusions

In this chapter caesium carbonate, 8-hydroxy-quinolinato lithium and polyethylenimine-ethoxylated have been investigated as solution-processed spin cast electron-injection layers for white-emissive polymer LEDs, with the future aim of depositing these materials via ultrasonic spray coating in ambient. The dependence of the device performance on the thickness of these different electron-injecting layers was investigated and the optimum thickness for this structure were found to be 2.2 ± 0.1 nm, 1.5 ± 0.1 nm, 2.7 ± 0.1 nm for caesium carbonate, 8-hydroxy-quinolinato lithium and polyethylenimine-ethoxylated respectively.

| | Liq ($N_2$ processed) | $Cs_2CO_3$ ($N_2$ processed) | $Cs_2CO_3$ (Ambient processed) | PEIE (Ambient processed) |
|---|---|---|---|---|
| **Mean peak current efficiency (cd $A^{-1}$)** | 2.34 | 7.49 | 0.96 | 3.18 |
| **Mean peak power efficiency (Lm $W^{-1}$)** | 1.92 | 5.76 | 0.32 | 1.14 |
| **Mean Peak Luminance (cd $m^{-2}$)** | 1197 | 20403 | 269 | 10690 |

*Table 4. 1: A table comparing the mean peak performance metrics of the different spin cast EILs and the atmosphere they were processed in.*

The devices fabricated under nitrogen with optimum $Cs_2CO_3$ thickness outperformed all other EILs with mean peak metrics of 7.49 cd $A^{-1}$, 5.76 Lm $W^{-1}$ and 20403 cd $m^{-2}$ but as discussed in Section 4.3 ambient processing is a requirement for the future use of ultrasonic spray coating as an industrial process, when equivalent devices were fabricated in ambient conditions the performance metrics were very poor as such $Cs_2CO_3$ was deemed not viable for ambient spray deposition.

Liq was investigated as a solution-processed EIL due to its less hygroscopic nature in comparison to $Cs_2CO_3$. Devices fabricated with optimum Liq thickness had mean peak performance metrics of 2.34 cd $A^{-1}$, 1.92 Lm $W^{-1}$ and 1197 cd $m^{-2}$, the metrics particularly the luminance were too low in comparison to the LiF reference devices as such Liq was deemed a non-viable option for an ambient spray cast EIL.

PEIE was investigated as a solution-processed EIL due to its stability in air, devices fabricated with optimum PEIE thickness under ambient conditions had mean peak metrics of 3.18 cd $A^{-1}$, 1.14 Lm $W^{-1}$, and 10690 cd $m^{-2}$. Although the efficiency metrics were lower than the thermally evaporated LiF EIL reference devices and all metrics

were lower than those of glovebox processed $Cs_2CO_3$ devices the still impressive luminance, ability to cast from environmentally friendly solvents and to be cast under ambient conditions led to the decision that PEIE would be a viable material for deposition via ultrasonic spray coating looking toward a fully spray cast ambient processed polymer LED.

## 4.7: References


[1] G. Malliaras, J. Salem, P. Brock, C. Scott, Electrical characteristics and efficiency of single-layer organic light-emitting diodes, Phys. Rev. B - Condens. Matter Mater. Phys. 58 (1998) R13411–R13414. doi:10.1103/PhysRevB.58.R13411.

[2] G.G. Malliaras, J.C. Scott, The roles of injection and mobility in organic light emitting diodes, J. Appl. Phys. 83 (1998) 5399–5403. doi:doi:10.1063/1.367369.

[3] C.W. Tang, S.A. Vanslyke, Organic electroluminescent diodes, Appl. Phys. Lett. 51 (1987) 913–915. doi:10.1063/1.98799.

[4] J.H. Burroughes, D.D.C. Bradley, A.R. Brown, R.N. Marks, K. Mackay, R.H. Friend, P.L. Burns, A.B. Holmes, Light-emitting diodes based on conjugated polymers, Nature. 347 (1990) 539–541. doi:10.1038/347539a0.

[5] R.H. Friend, R.W. Gymer, A.B. Holmes, J.H. Burroughes, R.N. Marks, C. Taliani, D.D.C. Bradley, D.A. Dos Santos, J.L. Brédas, M. Lögdlund, W.R. Salaneck, Electroluminescence in conjugated polymers, Nature. 397 (1999) 121–128. doi:10.1038/16393.

[6] S. Reineke, M. Thomschke, B. rn Lü ssem, K. Leo, White organic light-emitting diodes: Status and perspective, Rev. Mod. Phys. 85 (2013). doi:10.1103/RevModPhys.85.1245.

[7] N. Thejokalyani, S.J. Dhoble, Novel approaches for energy efficient solid state lighting by RGB organic light emitting diodes – A review, Renew. Sustain. Energy Rev. 32 (2014) 448–467. doi:10.1016/j.rser.2014.01.013.

[8] P.L. Burn, S.C. Lo, I.D.W. Samuel, The development of light-emitting dendrimers for displays, Adv. Mater. 19 (2007) 1675–1688. doi:10.1002/adma.200601592.

[9] F.C. Krebs, Fabrication and processing of polymer solar cells: A review of printing and coating techniques, Sol. Energy Mater. Sol. Cells. 93 (2009) 394–412. doi:10.1016/j.solmat.2008.10.004.

[10] C.J. Lawrence, The mechanics of spin coating of polymer films, Phys. Fluids. 31 (1988) 2786–2795. doi:10.1063/1.866986.

[11] J. Huang, G. Li, E. Wu, Q. Xu, Y. Yang, Achieving high-efficiency polymer white-light-emitting devices, Adv. Mater. 18 (2006) 114–117. doi:10.1002/adma.200501105.

[12] J. Huang, Z. Xu, Y. Yang, Low-work-function surface formed by solution-processed and thermally deposited nanoscale layers of cesium carbonate, Adv. Funct. Mater. 17 (2007) 1966–1973. doi:10.1002/adfm.200700051.

[13] J. Liu, X. Wu, X. Shi, J. Wang, Z. Min, Y. Wang, M. Yang, G. He, Highly Efficient and Stable Electron Injection Layer for Inverted Organic Light-Emitting Diodes, ACS Appl. Mater. Interfaces. 7 (2015) 6438–6443. doi:10.1021/am506300c.

[14] M.H. Chen, C.I. Wu, The roles of thermally evaporated cesium carbonate to enhance the electron injection in organic light emitting devices, J. Appl. Phys. 104 (2008) 1–5. doi:10.1063/1.3033501.

[15] Y. Li, D.Q. Zhang, L. Duan, R. Zhang, L.D. Wang, Y. Qiu, Elucidation of the electron injection mechanism of evaporated cesium carbonate cathode interlayer for organic light-emitting diodes, Appl. Phys. Lett. 90 (2007) 1–4. doi:10.1063/1.2429920.

[16] T. Chiba, Y.J. Pu, M. Hirasawa, A. Masuhara, H. Sasabe, J. Kido, Solution-processed inorganic-organic hybrid electron injection layer for polymer light-emitting devices, ACS Appl. Mater. Interfaces. 4 (2012) 6104–6108. doi:10.1021/am301732m.

[17] T. Chiba, Y.-J. Pu, J. Kido, Solution-processable electron injection materials for organic light-emitting devices, J. Mater. Chem. C. 3 (2015) 11567–11576. doi:10.1039/C5TC02421H.

[18] X. Zheng, Y. Wu, R. Sun, W. Zhu, X. Jiang, Z. Zhang, S. Xu, Efficiency improvement of organic light-emitting diodes using 8-hydroxy-quinolinato lithium as an electron injection layer, Thin Solid Films. 478 (2005) 252–255.

doi:10.1016/j.tsf.2004.08.020.

[19] W. Lee, J.W. Jung, High performance polymer solar cells employing a low-temperature solution-processed organic–inorganic hybrid electron transport layer, J. Mater. Chem. A. 4 (2016) 16612–16618. doi:10.1039/C6TA06911H.

[20] H. Xu, Y. Yue, H. Wang, L. Chen, Y. Hao, B. Xu, Single-crystal structure, photophysical characteristics and electroluminescent properties of bis(2-(4-trifluoromethyl-2-hydroxyphenyl) benzothiazolate)zinc, J. Lumin. 132 (2012) 919–923. doi:10.1016/j.jlumin.2011.12.016.

[21] Z. Liu, O. V. Salata, N. Male, Improved electron injection in organic LED with lithium quinolate/aluminium cathode, Synth. Met. 128 (2002) 211–214. doi:10.1016/S0379-6779(02)00011-5.

[22] S. Stolz, M. Scherer, E. Mankel, R. Lovrinčić, J. Schinke, W. Kowalsky, W. Jaegermann, U. Lemmer, N. Mechau, G. Hernandez-Sosa, Investigation of solution-processed Ultrathin electron injection layers for organic light-emitting diodes, ACS Appl. Mater. Interfaces. 6 (2014) 6616–6622. doi:10.1021/am500287y.

[23] Y. Zhou, C. Fuentes-hernandez, J. Shim, J. Meyer, A.J. Giordano, H. Li, P. Winget, T. Papadopoulos, H. Cheun, J. Kim, M. Fenoll, A. Dindar, W. Haske, E. Najafabadi, T.M. Khan, H. Sojoudi, S. Barlow, S. Graham, J. Brédas, S.R. Marder, A. Kahn, B. Kippelen, A Universal Method to Produce Low–Work Function Electrodes for Organic Electronics, Science (80-. ). 873 (2012) 327–332. doi:10.1126/science.1218829.

# Chapter 5

# Optimisation of Ultrasonic Spray Coating for Polymer OLED Layer Processing

## 5.1: Introduction

Currently the incumbent approach to fabricate lab-scale polymer OLEDs is via spin coating. While deposition via spin coating has many advantages such as excellent repeatability and it's simple to process high-quality films of a range of thicknesses, as such allowing for efficient optimisation of new materials, it is a time consuming process in which the majority of solution that is deposited is wasted and has limited scalability. In order for polymer OLEDs to evolve from lab fabricated devices for use purely in research to a feasible future alternative for displays and solid state lighting it must be demonstrated that devices can be fabricated via scalable techniques. Polymer films has been deposited by a range of potential scalable techniques for the fabrication of devices such as gravure,[1,2] slot-die[3] and ink-jet.[4] One such technique that has gained significant interest is spray-coating. This due to compatibility with roll-to-roll production, high material utilisation and prior use in industry (spray painting vehicles).

There are a number of sub-categories of spray coating, the most commonly reported in literature for the spray coating of polymers is airbrush this is due to the simple, robust and cheap nature of the setup required.[5–10] In this thesis I focus on the use of ultrasonic spray coating rather than airbrush as the ultrasonic system allows the finer control and repeatability of the spray mist and automated control increases the pass-to-pass repeatability and more closely replicates how the technique would

work in an industrial process. Ultrasonic spray coating has been shown to be an effect deposition technique for thin polymer films in solar cells[11–16] and transistors.[17] In papers such as these the focus is on presenting the device data, typically of champion devices and the parameters used to fabricate the device but there are very few examples of how the deposition parameters were optimised to achieve the uniform films required for champion devices. The lack of information on parameter tuning coupled with variations between different spray coating systems leads to problems replicating the work of others or using their learning to deposit other materials.

In this chapter I describe the stages involved in the deposition of a thin film via the ultrasonic spray coating process. Commonly used hole transporting polymer poly[(9,9-dioctylfluorenyl-2,7-diyl)-co-(4,4'(N-(4-sec-butylphenyl)))
diphenylamine] (TFB) is spray cast from a range of pass heights, pass speeds, solution concentrations and substrate temperatures to show the typical film morphologies achieved when these parameters are varied, in order to demonstrate the parameter optimisation process required to deposit uniform polymer films.

## 5.2: Ultrasonic Spray Coating: The Process of Spraying a Film

Fabrication via spray coating can typically be divided into four key stages; the formation of droplets of a solution, the deposition of the droplets onto a surface, the spreading and merging of droplets to from a wet film and the drying of the wet film. Each of these stages contribute to the uniformity of the final film as such controlling each stage is important. In this thesis ultrasonic spray coating is performed using an Ultrasonic Systems Inc. Prism ultra-coat 300 system using a single pass method. In this method the spray head passes over the substrate once at a constant velocity whilst depositing the solution, a wet film is formed on the substrate before drying. Some other works involve the use of a multi-pass technique whereby the single pass technique is repeated and the dry film is re-dissolved by the following pass of droplets to build up a layer, or an alternate multi-pass technique where the droplets evaporate prior to reaching the substrate/as they reach the substrate and a dry film is built up but this has been shown to form rougher films.[12,18,19] Others have

used long stationary depositions but this is not a feasible step toward high-throughput fabrication.[20]

In the Prism ultra-coat 300 system the solution is stored in a sealed reservoir (Figure 5.8), the solution is forced through piping in the bottom of the reservoir towards the spray head with the flow rate dictated by the pressure of nitrogen flowing into the reservoir acting on the solution surface. A piezoelectric crystal has a rapidly switching voltage applied across it causing it to expand and contract rapidly, the crystal is attached to a tip which resonates at 35 KHz. As the solution flows from the piping onto the tip the high frequency vibrations are transferred to the solution causing the solution to shear, ejecting a fine mist of micron-sized droplets from the apex of the standing wave. In contrast a simple pneumatic/airbrush spray deposition system shears the solution by passing it through an orifice within the spray gun whilst propelled by a pressurised gas. The mean size of droplets formed by the atomisation of the solution by the ultrasonic tip are smaller and have a narrower spread than droplets formed via airbrush deposition leading to higher film uniformity and repeatability.[21–24] The mist of droplets produced when spray coating for this chapter was visible but individual droplets couldn't be resolved by eye, indicating all wavelengths of light were scattered by the droplets as such they must be larger than the wavelength of light so of the order of microns to tens of microns in diameter. The mean droplet diameter in microns ($D_{0.5}$) has been shown to be dependent on the solution properties as well as the frequency of vibrations using the relationship introduced Mujumder et al. based on work by Lang and Berger.[22,25,26]

$$D_{0.5} = 0.34\left(\frac{8\pi\sigma}{\rho f^2}\right)^{1/3} \tag{5.1}$$

Where $\sigma$ (dyn cm$^{-1}$) is the surface tension of the solution, $\rho$ (g cm$^{-3}$) is the solution density and $f$ (Hz) is the frequency of tip vibration.

As the fine mist of droplets is formed a nitrogen gas flow widens and planarises the mist of droplets as they fall towards the substrate below, this with Equation 5.1 demonstrate the separation of deposition rate, droplet size and energy when using

ultrasonic spray coating.[25] In contrast increasing the flow rate using an airbrush nozzle results in an increase in droplet energy which may cause droplets to deflect back off the substrate and lead to non-uniformities in the final film.

As the droplets of solution land onto the substrate the third stage of this technique of spray coating begins. In an ideal scenario the individual droplets will wet well to the substrate, spread and merge to form a continuous wet film. In reality this is dependent on the droplet diameter, density, viscosity, surface tension as well as the substrate roughness and wettability.[19] The use of low roughness (1.8 nm rms) ITO substrates decreases the chance of droplets bouncing off the surface, the cleaning procedure described in Chapter 3 improves the wettability of the substrates. The low concentrations used for spray coating aid in lowering the solution density and viscosity of the droplets. However, as the mist of droplets descends from the spray head towards the substrate the solvent can begin to evaporate, increasing the solution density and viscosity of the droplets as such it is important to consider the volatility of the solvent when applying the spray coating technique described in this thesis. Another key solvent parameter to consider is the surface tension, if the surface tension of the deposited solution is too large the droplets will form a large contact angle with the surface and the droplets will not spread well and fully merge into a wet film before drying leaving an incomplete or highly uneven film.

There are a few techniques that can be employed to aid the wetting of droplets during the spray coating process. The addition of additives to the solution have been shown to change the viscosity or boiling point of the deposition solution which can aid in the wettability, but these additives may have a negative effect on device performance if they remain in the dry film.[27,28] A second widely used technique to improve the wetting of a spray cast solution is to increase the temperature of the substrate the solution is cast upon. Increasing the substrate temperature reduces the surface tension of the solution, reducing the droplet contact angle and increasing the probability of forming a continuous wet film.[29,30] However if the substrate temperature is raised too high it is possible for the droplets to dry before fully spreading and merging, forming a non-uniform film or for the droplets to evaporate prior to reaching the substrate. Another route to improve the wetting of a spray cast

solution is to use an alternate solvent with a lower surface tension. When looking for a lower surface tension solvent the other properties of the solvent must also be considered, as if the boiling point is much lower this will have an analogous effect to raising the substrate temperature too high, if the viscosity is much higher the droplets may not spread and form a uniform wet film, the density of the solvent changes the droplet size which could affect the film quality formed and most importantly the solute that is being sprayed may have lower solubility or even be insoluble in alternate solvents. Another potential route to improve the wetting of droplets and film formation is to use a solvent blend where a miscible secondary solvent with a lower boiling point and lower surface tension is added to the solution. Initially the addition of the lower surface tension secondary solvent aids wet film formation by decreasing the contact angle of the droplets to the surface, additionally as the secondary solvent evaporates localised surface tension gradients are formed causing the solution to flow onto the uncoated areas, this is the Marangoni effect.[12]

Once the droplets have spread, merged and a continuous film has been formed the wet film continues to flow as evaporation of the solvent begins to dominate and the film dries. In an ideal scenario these flows will help level the wet film as it dries leading to a uniform dry film. However if the substrate temperature, spray parameters and solvent properties are not correctly chosen then the wet film can pool, shrink or dewet resulting in a non-uniform dry film.

## 5.3: Optimisation of Spray Cast Polymer Films

As mentioned in the previous section of this chapter the uniformity of spray cast films is dependent on a wide parameter space. In this section the deposition parameters of spray speed, spray height, substrate temperature and solution concentration will be explored. The effect of changing these deposition parameters on the morphology of the dry film will be demonstrated followed by a discussion on how to optimise these parameters to deposit uniform films.

The well-studied conjugated polymer poly[(9,9-dioctylfluorenyl-2,7-diyl)-co-(4,4'(N-(4-sec-butylphenyl))) diphenylamine] (TFB), often used as a hole-

transporting layer in solar cells and OLEDs, has been spray cast from a range of pass heights (40 - 100 mm), pass speeds (20 - 400 mm $s^{-1}$), solution concentrations (4 and 8 mg $ml^{-1}$ in toluene) and substrate temperatures (25 – 60 °C) onto PEDOT:PSS coated ITO substrates. The resultant films were imaged using an Epson Perfection V370 scanner and thickness measurements were taken using a Bruker DektakXT.

### 5.3.1: Varying Spray Speed and Solution Concentration

The pass speed of the spray head has a large effect not only on the uniformity of the films formed but also on the thickness of the films. If other parameters such as flow rate and pass height remain the same then by decreasing the pass speed the volume of solution deposited on the substrate increases, leaving more material and thus a thicker film when the solvent evaporates and vice versa. Figure 5.1 displays TFB films spray cast at a range of pass speeds (20 - 300 mm $s^{-1}$) from a 4 mg $ml^{-1}$ toluene solution all at a spray height of 40 mm, with a fluid pressure of 50 mbar onto 8 pixel substrates (15 x 20 mm) held at 25 °C.

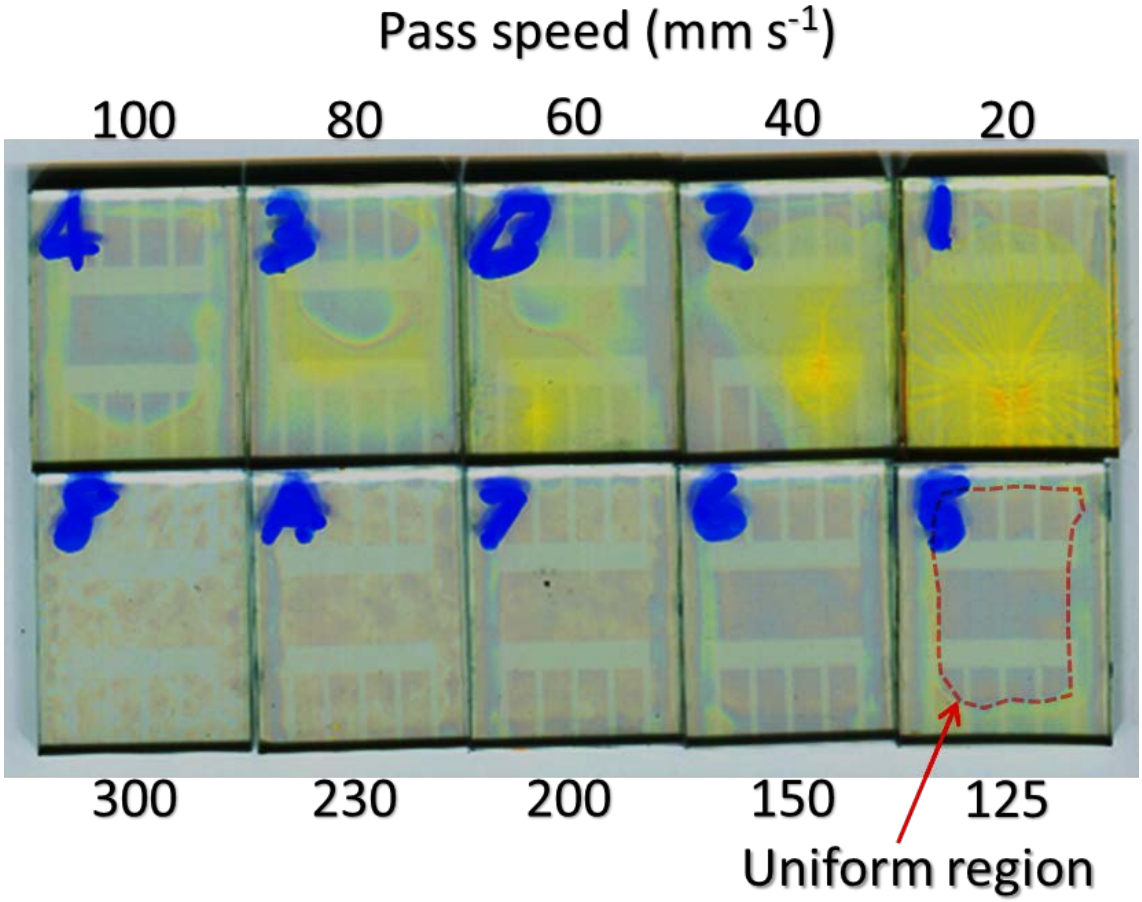


*Figure 5. 1: Images of TFB films deposited at a range of spray speeds, from 20 – 300 mm $s^{-1}$, onto PEDOT:PSS coated 8 pixel ITO substrates. The spray head passed over the substrates from bottom to top. All other parameters were kept constant during deposition. The yellow/orange regions are thick with the blue and more transparent regions being thinner areas of the films. The contrast and brightness of the images was altered to make the film features easier to see.*

It can be seen in Figure 5.1 that for this set of parameters films cast over 200 mm $s^{-1}$ form incomplete films and that films cast from 125 mm $s^{-1}$ or slower speeds have increasing thickness variation which appears to encroach from the edge of the substrate towards the centre the slower the pass speed.

If we focus initially on films cast 125 mm $s^{-1}$ or slower, as the volume deposited on the substrate is increased whilst the temperature remains constant the drying time

for the film will increase and this can have a marked effect on the morphology of the dry film.

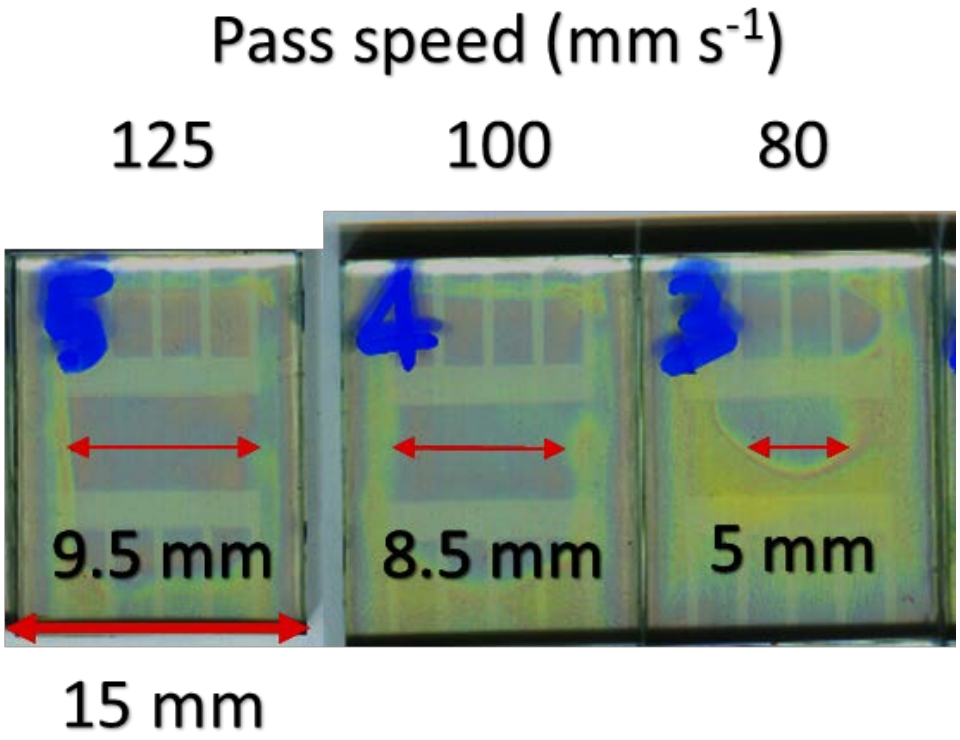


*Figure 5. 2: Images of TFB films deposited at pass speeds of 125, 100 and 80 mm $s^{-1}$, onto PEDOT:PSS coated 8 pixel ITO substrates.. The spray head passed over the substrates from bottom to top. All other parameters were kept constant during deposition. The yellow regions are thick with the blue and more transparent regions being thinner areas of the films. The contrast and brightness of the images was altered to make the encroaching picture framing effect easier to see.*

Films sprayed at 125 mm $s^{-1}$ or slower, as pictured in Figure 5.2, have drying times of over 20 seconds during the drying process the edges of substrate have lower solvent vapour saturation as not surrounded by wet film this increases the evaporation rate at the edge. Once the edge of the wet film in contact with the substrate dries the edge of the film is pinned as such the film cannot shrink as it dries, in order to maintain this fixed contact line fluxes of solution towards the edge of the film occur leading to an accumulation of polymer towards the edges of the

substrate reminiscent of a picture frame, with a larger ingress from the bottom of the substrate as this edge dried first due to the spray pass direction.[31,32]

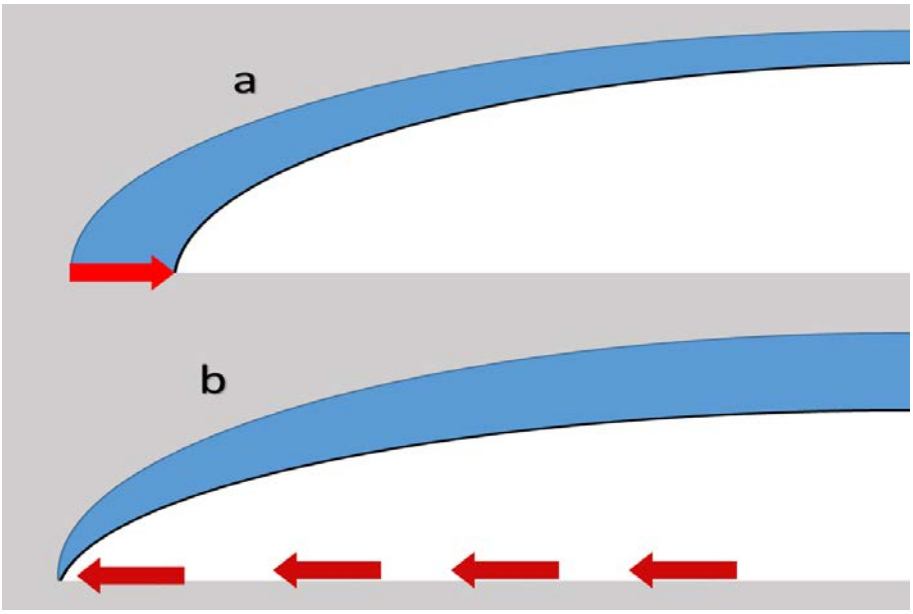


*Figure 5. 3: Images a) and b) demonstrate the incremental evaporation at the edge of a wet film, the blue region is the initial film and the white region is the film after an incremental drying time. Part a shows the result of evaporation prior to the edge of the film drying to form a contact line as such the wet film shrinks as it dries, demonstrated by the red arrow. Part b demonstrates the drying of a wet film when the contact line has been formed, the red arrows show the flux of solution to maintain the position of the contact line.*

As the drying time increases the flux of polymer towards the edge of the substrate continues over a longer period of time bringing larger amounts of polymer towards the wet/dry boarder line, the drying front retracts towards the centre of the substrate during this process as such the 'picture frame' encroaches further into the centre of the substrate. As a greater volume of solution is deposited on the substrate not only is the drying time much longer there is also an increase in the mass of polymer as such as the solvent evaporates the remaining solution is a much higher concentration. As the concentration of the remaining wet film increases so does the viscosity. Thin viscous films can suffer from convective instabilities when drying which induce thickness variations and roughness in the dry film surface, as notably

seen in the films sprayed at 20 and 40 mm $s^{-1}$ in Figure 5.1.[33,34] The further the rough, thick picture frame ingresses into the central area of the substrate the greater effect this will have on the performance of the device fabricated from this film as this is the region in which the pixels will be fabricated. To counteract the issues with the picture framing effect and get a uniform film across the substrate the drying time must be reduced, this can be achieved by reducing the deposited volume by increasing the pass speed. However, if the pass speed is increased too much then drying times will be too short leading to non-uniform or even incomplete films. Films cast at 400, 300 and 230 mm $s^{-1}$ are pictured in Figure 5.4 had drying times of less than 10 s, this fast drying time leads to a mottled surface with small regions of thick material surrounded by thin or uncovered regions, as the film dries before the droplets can spread, merge and form a continuous film.

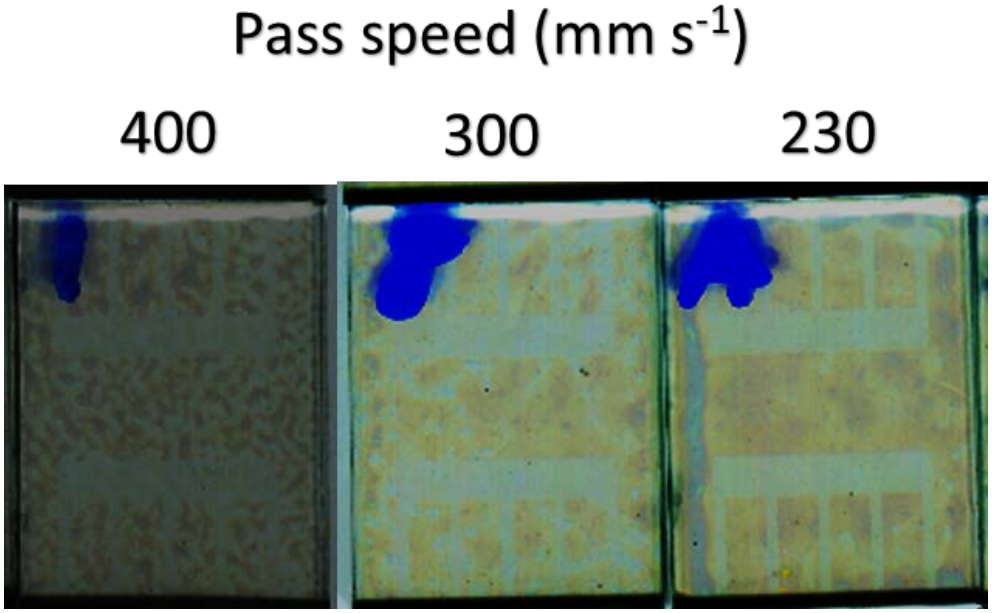


*Figure 5. 4: Images of TFB films deposited at pass speeds of 400, 300 and 230 mm $s^{-1}$, onto PEDOT:PSS coated 8 pixel ITO substrates. The spray head passed over the substrates from bottom to top. All other parameters were kept constant during deposition. The lighter/blue-grey regions on the ITO areas of the substrates are thinner or incomplete regions of the film. The contrast and brightness of the images was altered to make the film features easier to see.*

Figures 5.2 and 5.4 show the extremes of deposition pass speed and thus the importance of drying time on the quality of the final film. To form uniform dry films the pass speed must be slow enough to increase the drying time to allow droplets to spread, merge and level prior to the solvent evaporating but not so slow that a picture frame forms and starts encroaching toward the centre of the substrate before the solvent evaporates. There appears to be a window for uniform films cast at speeds between 125 – 200 mm $s^{-1}$ for this solution under the parameters previously stated, as shown by the films in Figure 5.5. Pass speeds between 125 – 200 mm $s^{-1}$ (7 – 12 m $min^{-1}$) would translate to acceptable web speeds in a R2R process, the web speeds could be further increased if spray heads were to move relative to the web.[35]

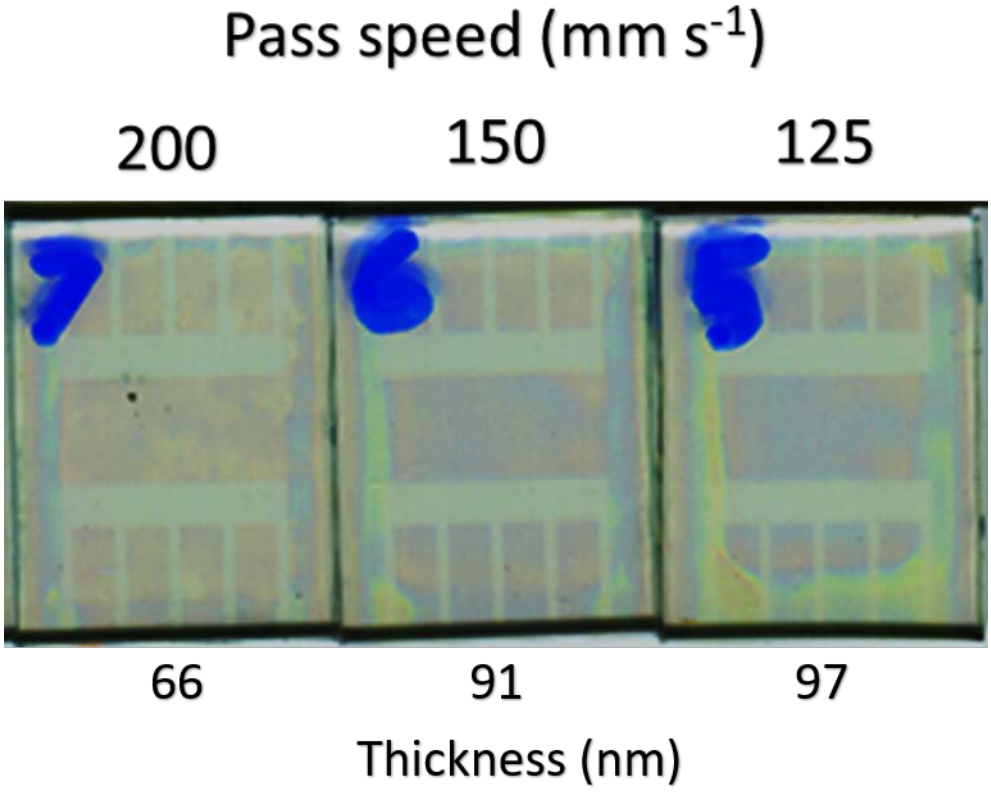


*Figure 5. 5: Images of TFB films deposited at pass speeds of 200, 150 and 125 mm $s^{-1}$, onto PEDOT:PSS coated 8 pixel ITO substrates. The spray head passed over the substrates from bottom to top. All other parameters were kept constant during deposition. The yellow/orange regions are thick with the blue and more transparent*

*regions being thinner areas of the films. The contrast and brightness of the images was altered to make the film features easier to see.*

The films cast from 200 – 125 mm $s^{-1}$ had a drying time between 10 – 20 s and have a thickness range from 66 – 97 nm respectively for the central region. To obtain films of a similar thickness range formed via spin coating requires solutions between 15 – 20 mg $ml^{-1}$ as such spray coating requires less polymer. Further to this there is minimal wastage in spray coating, only the volume that is not sprayed directly onto the substrate which can be greatly limited by narrowing and shortening the spray pass, whereas up to 90 % of the deposited solution is wasted when spin casting, this shows the potential for spray coating to be a more economical deposition technique.[36] Further to this the low concentrations required for spray coating potentially allow the use of solvents in which the solute has low solubility, broadening the choice of solvents available. If the desired film thickness is outside of this range cast from 4 mg $ml^{-1}$ between 200 – 125 mm $s^{-1}$ then the simplest way of increasing or decreasing the thickness whilst maintaining the film uniformity is the varying the concentration of the solution. If the concentration of the casting solution is increased but the volume kept constant then the mass of solute has increased by the drying time should be very similar as such the uniformity of the dry film should be consistent but thicker when the solvent evaporates. Films were cast under identical parameters as described previously with the single change of the solution concentration has been increased from 4 to 8 mg $ml^{-1}$ in toluene. Films cast at 125 – 200 mm $s^{-1}$ from 8 mg $ml^{-1}$ were measured to have thicknesses from 133 – 90 nm respectively. Finer changes in concentration and spray speed will allow for greater tuning of the thickness of the spray cast layer.

However, changing the concentration of the casting solution is not a universal solution to cast films of any thickness. As the concentration of the solution is changed the viscosity and thus how the solution flows on the substrate will change effecting the time taken for droplets to spread and merge as well as the drying time for the formation of a uniform film.

When optimising the spraying process for a polymer film I have shown that the thickness of films can be tuned by varying the pass speed within a certain processing window to form uniform thin films, films outside of this window, either cast at too fast or too slow speeds, have been demonstrated and discussed. It is possible to increase the range of thicknesses sprayed further by varying the solution concentration. In order to cast films uniformly across a larger range of thicknesses the other spray coating parameters need to be probed and optimised.

### 5.3.2: Varying Pass Height

The effect on film quality and thickness when varying spray pass speed and solution concentration was discussed in the previous section, it was demonstrated that there is a processing window in which uniform films can be cast by varying the spray speed and that varying concentration is another possible route to vary thickness but both have their limitations. Another possible route to further tune film uniformity and thickness is to vary the spray pass height. The thickness and uniformity of spray cast films are in fact more sensitive to pass height than the pass speed. If other parameters such as flow rate and pass speed remain constant then by increasing the pass height the volume of solution deposited is constant but the volume deposited on the substrate decreases, leaving less material and thus a thinner film when the solvent evaporates and vice versa. Figure 5.6 displays TFB films spray cast at a range of pass heights (40 - 100 mm) from a 4 mg $ml^{-1}$ toluene solution, all cast at a spray speed of 100 mm $s^{-1}$, with a fluid pressure of 50 mbar onto substrates held at 25 °C.

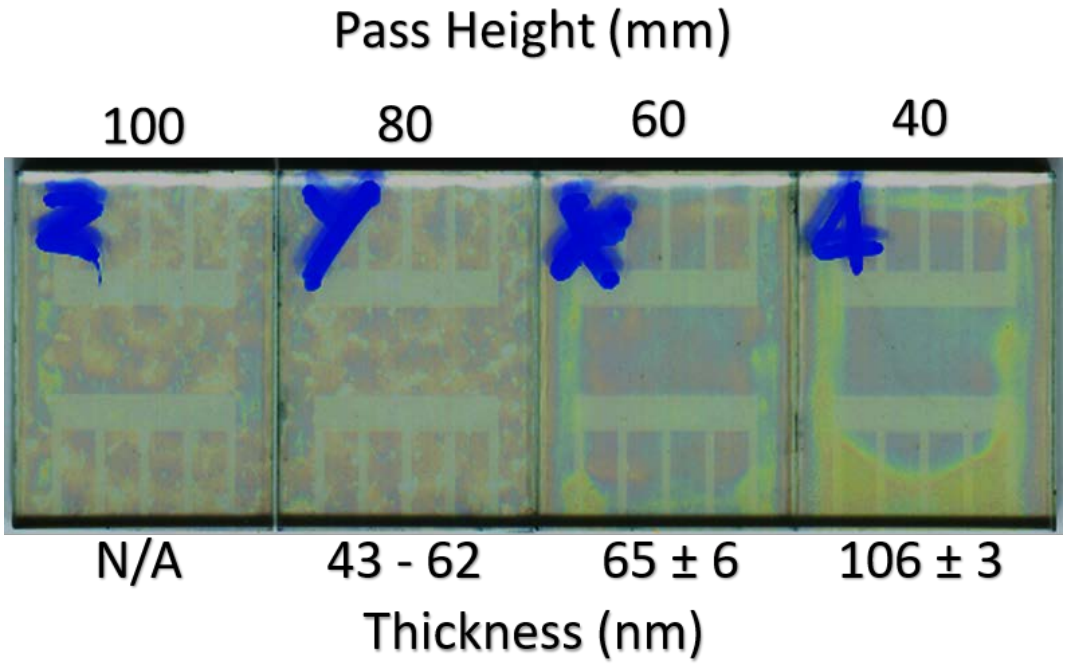


*Figure 5. 6: Images of TFB films deposited at pass heights of 100, 80, 60 and 40 mm, onto PEDOT:PSS coated 8 pixel ITO substrates. The spray head passed over the substrates from bottom to top. All other parameters were kept constant during deposition (pass speed = 100 mm $s^{-1}$, substrate temperature = 25 °C, solution concentration = 4 mg $ml^{-1}$ in toluene). The yellow/orange regions of the films are thick, the blue regions are thinner and the more grey/transparent regions being even thinner. The contrast and brightness on the images was altered to make the film features easier to see.*

At an initial pass height the shaping gas will cause the spray mist width to be a certain width when reaching the substrate and as such at a fixed flow rate and pass speed a certain density of droplets over that area. If the spray height is increased with all other parameters remaining constant then the spray mist width will be wider when passing over the substrate but the same volume of solution will be deposited over this spray area as such the number of droplets deposited onto the substrate will decrease, firstly this will lead to lesser volume of solution on the substrate and thinner films. Secondly, with less droplets falling onto the substrate they will have to spread further prior to merging and levelling to form a uniform wet

film before drying, this will take a longer period of time but with a lesser volume being deposited as the height increases the drying time decreases thus the likelihood of forming non-uniform dry films increases.

A film cast at a pass height of 40 mm, pictured in Figure 5.6, was measured to have a thickness of 106 nm with a variation of ±3 nm across the central region. The film cast at a pass height of 60 mm shows less ingress of the picture frame effect due to a shorter drying time, similar to a film cast at a faster pass speed, and is measured to have a thickness of 65 nm with a variation in thickness ±6 nm across the central region. The film cast at a pass height of 80 mm shows no picture framing but shows regions of varying thickness (measured by dektak) suggesting that the film dried prior to the droplets fully spreading, merging and levelling. The film was measured to have an average thickness of 52 nm with a max thickness measurement of 62 nm and a min of 43 nm. The film cast at a pass height of 100 mm shows further mottling and regions of incomplete film as such an accurate thickness measurement could not be obtained.

When optimising the spraying process for a polymer film I have shown that although the thickness of films can be tuned by varying the pass height the uniformity of the dry film is highly sensitive to this variation as such it is recommended that when attempting to spray a film that the spray height is chosen such that the width of the mist when reaching the substrate is slightly larger than the width of the substrate to fully coat the substrate but to minimise the morphological effects of changing the spray height. If the pass height necessary for this is quite high then the spray speeds used will need to be significantly lowered or the flow rate significantly raised or a combination of the two to increase the volume of solution deposited onto the substrate to allow the droplets to spread merge and level prior to the casting solvent evaporating.

### 5.3.3: Varying Substrate Temperature and the Importance of Solvent Properties

The effect on film quality and thickness when varying spray pass speed, pass height and solution concentration have been discussed, the importance of controlling the drying time has been a consistent theme when discussing the morphological effects

of varying these parameters. In this section the substrate temperature is varied when casting the solution to investigate the effect on film morphology and further to this the properties of the casting solvent are discussed.

Increasing the substrate temperature has two potential benefits to film morphology when spray casting a solution. Firstly, as discussed in Section 5.2, increasing the substrate temperature when depositing via spray coating can reduce the surface tension of the solution aiding in the wetting of the droplets and increasing the likelihood of forming a continuous film prior to the evaporation of the solvent.[29]

Secondly, increasing the substrate temperature will drive the evaporation of the solvent cast onto the substrate decreasing the drying time of the film. As discussed in the previous sections in this chapter if the drying time is too long then a flux of polymer toward the pinned edges of the film occurs causing thickness variations, the formation of the picture frame effect. As such by tuning the substrate temperature the uniformity of films can be improved, it is even possible to broaden the thickness range in which uniform films can be cast. If at a certain temperature and spray parameters a film is formed with a broad picture frame, covering part of the central region of the substrate then by increasing the substrate temperature and keeping the other spray parameters constant the drying time can be reduced, the width of the picture frame reduced and a thicker uniform central region formed. Conversely if the cast droplets are drying too quickly to merge and level to a continuous uniform wet film before drying, then by reducing the substrate temperature the drying time can be increased allowing the film to level before the solvent evaporates.

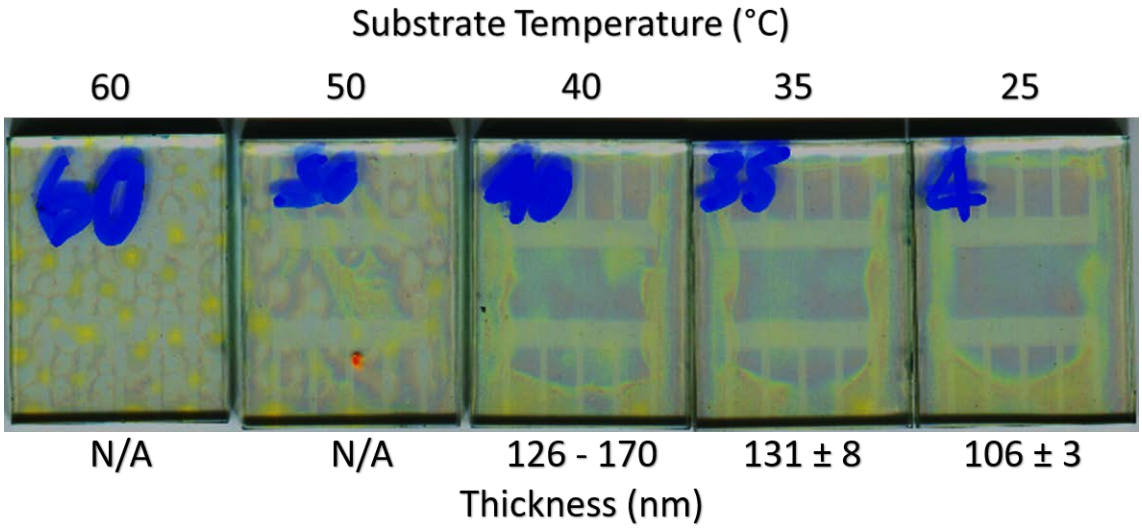


*Figure 5. 7: Images of TFB films deposited via ultrasonic spray coating onto PEDOT:PSS coated 8 pixel ITO substrates held at a range of temperatures from 25 – 60 °C. The spray head passed over the substrates from bottom to top. All other parameters were kept constant during deposition (pass speed = 100 mm $s^{-1}$, pass height = 40 mm, solution concentration = 4 mg $ml^{-1}$ in toluene). The yellow/orange regions are thick with the blue and then more grey/transparent regions being thinner areas of the films. The contrast and brightness of the images was altered to make the film features easier to see.*

Figure 5.7 displays TFB films spray cast at pass speed 100 mm $s^{-1}$ from a 4 mg $ml^{-1}$ toluene solution all at a spray height of 40 mm, with a fluid pressure of 50 mbar onto substrates held at a range of temperatures from 25 - 60 °C. It can be seen that as the substrate temperature is increased from 25 °C to 35 °C and 40 °C the thick picture frame is incomplete, encroaches less and the average thickness of the central region increases from 106 nm for 25 °C substrate to 131 nm for the 35 °C substrate and 146 nm for the 40 °C substrate. Although the average thickness of the central region increases as the substrate temperature is increased from 25 °C to 35 °C through to 40 °C there is also a decrease in uniformity across this area with a variation in thickness from the mean of ±3 nm for the 25 °C substrate temperature, ±8 nm for the 35 °C substrate temperature and maximum of 170 nm and a minimum of 126 nm for the film cast onto a substrate held at 40 °C. The large increase in variation in

thickness from the mean for the film cast at 35 °C to the film cast at 40 °C is mainly due to a region top right of the central area which is much thicker, this is due to the film drying too quickly for that region to spread and level across the active region, this becomes far more obvious when looking at the films cast on to substrates held at 50 °C and 60 °C.

For spray deposition onto substrates held at 50 °C the droplets likely partially evaporate and increase in concentration prior to reaching the substrate where they then dry rapidly leading to minimal merging of droplets and many small thick regions of polymer across the substrate. As the substrate temperature is further increased to 60 °C the film follow a similar trend with many small dots of thick polymer across the surface with very thin regions separating them in a leopard-print-like pattern.

When discussing the effect of the substrate temperature on the morphology of a spray cast film the boiling point of the solvent being used must be involved as the two are inexorably linked. As mentioned earlier in this section the solvent used for spraying these films is toluene, which has a boiling point of 110.6 °C. Based on the parameters used for spray coating in this chapter to spray uniform polymer films from toluene the substrate temperature must be kept below 50 °C.

In this chapter the processing window for casting uniform films of TFB from a 4 mg $ml^{-1}$ toluene solution cast onto a substrate held at 25 °C with a fluid pressure of 50 mbar have been shown to be a pass height of 40 mm and a range of pass speeds from 125 – 200 mm $s^{-1}$ to fabricate films between 66 – 97 nm. In summary when optimising a new material for spray coating there are many parameters to consider. Firstly, the properties of the solvents in which the material is soluble must be investigated, with the aim of finding a low surface tension solvent with a boiling point high enough to allow a uniform film to be sprayed onto a substrate held at a range of different temperatures to allow for control over drying time. Various dilute concentrations of casting solution should be fabricated for initial spray coating trials, for reference in this chapter uniform films of TFB were spray cast from solution between a third and a fifth of the concentration required to spin films of equivalent thicknesses. The spray pass height should be set so that the width of the

mist of droplets deposited completely coats the width of the substrate. At this point a range of spray pass speeds, flow rates (fluid pressure) and base plate temperatures should be probed and optimised to control the drying time to minimise the picture frame effect seen with longer drying times, and leopard print films seen with drying times which are too short.

## 5.4: Issues with the USI System

In this chapter I have laid out the physics of depositing thin films via ultrasonic spray coating and demonstrated the optimisation of spraying a thin polymer film. In this section I will discuss a few challenges I overcame with the spray coating system used in my work, USI Prism Ultra-coat 300, which could have affected the uniformity of cast films, the device-to-device and run-to-run repeatability.

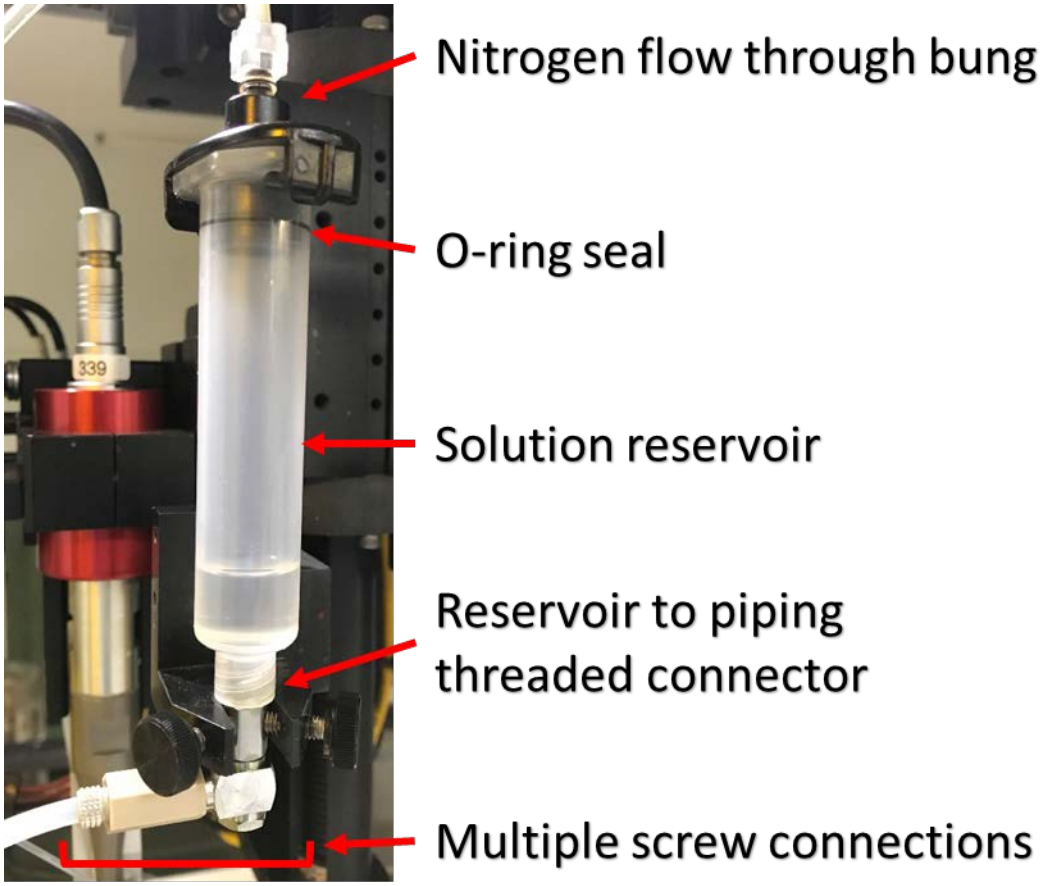


*Figure 5. 8: Labelled image of the solution reservoir and surrounding piping from the USI Prism Ultra-coat 300 system. A nitrogen flow passes through a pipe into the top of the solution reservoir through the black bung this then acts to drive the solution from*

*the reservoir through the tubing at the bottom of the image which eventually leads to the spray head.*

As discussed in Section 5.3 the volume deposited on the substrate when spray coating effects both the thickness and uniformity of the final film, this was tuned by varying the pass speed and pass height whilst keeping the flow rate constant. Another possible route for changing the volume deposited when spray coating is to vary the flow rate whilst keeping the other parameters constant. Typically on coating systems such as spray coaters or slot-die coaters a syringe pump is used to control the flow rate, the pump moves a certain distance over a certain period of time with the dimensions of the syringe know this defines the flow rate of solution passed to the deposition head. This system is simple but highly effective with the flow rate only varying from what has been set if the solution can leak out somewhere between the syringe pump and the deposition head. The USI Prism ultra-coat 300 system doesn't use a syringe pump to define a flow rate instead the fluid is driven by a flow of nitrogen applied to the solution reservoir as pictured in Figure 5.8. A flow of nitrogen is passed into the sealed solution reservoir through a bung at the top of the reservoir, the nitrogen then increases the pressure in the reservoir on the casting solution this then dictates the flow rate when the valve to the spray head is opened for deposition. The pressure of the incoming flow of nitrogen is measured and this is defined as the fluid pressure and is analogous to flow rate on this system, the fluid pressure is controlled by varying a manual dial with a range from 0 – 600 mbar which essentially increases the flow of nitrogen into the reservoir. For the polymer solutions used in this thesis the optimised fluid pressure was in the region of 50 mbar, due to the large range and thus lack of precision of the dial at comparatively low pressures it is not possible to precisely replicate the desired fluid pressure from one device run to another. This potential variation in fluid pressure and thus flow rate from one device run to another can lead to variation in solution volume deposited on a substrate, a variation in film thickness and uniformity and as such a variation in device performance for what appear to be the same parameters as a previous run.

In order to manage this issue the first film in a device run is cast with the previously optimised parameters, the film is observed as it dries and the thickness of the dry film is measured. The measured thickness is then compared with the thickness that was achieved previously from these parameters, if the thickness is different the fluid pressure dial is tweaked slightly and the process repeated until the thickness of the cast films matches that of the previous optimised device run, typically within 1 or 2 attempts.

Further to the run-to-run variation that can be caused by the lack of precision of the fluid pressure dial this can also cause issues with device-to-device repeatability within a single device run. During a spray coating run the fluid pressure dial can drift slightly due to small variations in the flow of nitrogen passing through the valve controlled by the dial. These variations are very small compared to the large range of the dial but due to the low fluid pressures required for the work in this thesis these variations cause a noticeable effect on the flow rate, as such the position of the fluid pressure dial is checked and attempts made to correct it between each spray pass. To confirm the fluid pressure is not drifting throughout the run the thickness of at least every other film cast is measured.

A further problem with the design of the solution reservoir in the USI Prism ultra-coat 300 system which causes issues with repeatability when spraying films is the quality of the seals of the solution reservoir. Every time in which the solution needs to be changed in the reservoir, be it for cleaning the reservoir or for spray deposition of a different solution the bung needs to be removed, the solution pipetted into the solution reservoir and the bung inserted back into the reservoir. The O-ring is on the bung and it is the O-ring that creates the seal which allows the fluid pressure to be increased when the bung is in the reservoir, as such the quality of the seal made by the O-ring affects the flow rate. Typically when O-rings are used they are placed to improve the seal quality in parts which rarely move as such the quality of the seal is consistent, whereas in this system the O-ring is removed and refitted each run as such it may sit slightly differently each time and the reservoir wall it is in contact with may have solvent on it as such the quality of the seal can change. As well as the O-ring at the top of the solution reservoir the seal at the bottom of the reservoir can

lead to similar issues. The solution reservoir is changed for each solution to avoid contamination, the reservoir has a threaded connection and screws into place. Multiple removals and reattachments of the reservoir can loosen the multiple screw connections shown at the bottom of Figure 5.8 this can cause solution leaks which will lower the flow rate and reduce the volume cast onto substrates and affect the thickness and uniformity of cast films.

These seal based issues for the reservoir are managed by drying the O-ring and the walls of the reservoir where it will contact between each replacement of the bung/O-ring and visually inspecting the positioning of the O-ring to confirm a proper seal has been achieved. Upon changing the solution reservoir all the screw connections below the reservoir are tightened to stop any solution leaks.

## 5.5: Conclusions

In this chapter I have discussed the physics behind the key stages of depositing a film via ultrasonic spray coating; the formation of droplets of a solution, transferring the droplets onto the substrate, the spreading and merging of droplets to form a continuous wet film and the evaporation of the solvent to form a dry thin film. I have demonstrated, characterised and discussed the effect of varying key spray deposition parameters—spray pass height, spray pass speed, solution concentration and substrate temperature—on the morphology of thin TFB films in order to demonstrate the parameter space and the optimisation process required to deposit uniform thin films. Finally I have raised some issues with the USI Prism ultra-coat 300 system and discussed how these are managed in order to maintain a good level of repeatability from device-to-device and run-to-run.

## 5.6: References

[1] P. Kopola, M. Tuomikoski, R. Suhonen, A. Maaninen, Gravure printed organic light emitting diodes for lighting applications, Thin Solid Films. 517 (2009) 5757–5762. doi:10.1016/j.tsf.2009.03.209.

[2] D.Y. Chung, D.S. Leem, D.D.C. Bradley, A.J. Campbell, Flexible multilayer inverted polymer light-emitting diodes with a gravure contact printed Cs2

CO3 electron injection layer, Appl. Phys. Lett. 98 (2011) 2009–2012. doi:10.1063/1.3560484.

[3] A. Sandström, H.F. Dam, F.C. Krebs, L. Edman, Ambient fabrication of flexible and large-area organic light-emitting devices using slot-die coating, Nat. Commun. 3 (2012). doi:10.1038/ncomms2002.

[4] F. Villani, P. Vacca, G. Nenna, O. Valentino, G. Burrasca, T. Fasolino, C. Minarini, D. Della Sala, Inkjet printed polymer layer on flexible substrate for OLED applications, J. Phys. Chem. C. 113 (2009) 13398–13402. doi:10.1021/jp8095538.

[5] D. Vak, S.-S. Kim, J. Jo, S.-H. Oh, S.-I. Na, J. Kim, D.-Y. Kim, Fabrication of organic bulk heterojunction solar cells by a spray deposition method for low-cost power generation, Appl. Phys. Lett. 91 (2007) 081102. doi:10.1063/1.2772766.

[6] C.N. Hoth, R. Steim, P. Schilinsky, S.A. Choulis, S.F. Tedde, O. Hayden, C.J. Brabec, Topographical and morphological aspects of spray coated organic photovoltaics, Org. Electron. Physics, Mater. Appl. 10 (2009) 587–593. doi:10.1016/j.orgel.2009.02.010.

[7] S.I. Na, B.K. Yu, S.S. Kim, D. Vak, T.S. Kim, J.S. Yeo, D.Y. Kim, Fully spray-coated ITO-free organic solar cells for low-cost power generation, Sol. Energy Mater. Sol. Cells. 94 (2010) 1333–1337. doi:10.1016/j.solmat.2010.01.003.

[8] M.P. Aleksandrova, Improvement of the electrical characteristics of polymer electroluminescent structures by using spray-coating technology, J. Coatings Technol. Res. 9 (2012) 157–161. doi:10.1007/s11998-009-9220-2.

[9] C.K. Chan, L.J. Richter, B. Dinardo, C. Jaye, B.R. Conrad, H.W. Ro, D.S. Germack, D.A. Fischer, D.M. Delongchamp, D.J. Gundlach, High performance airbrushed organic thin film transistors, Appl. Phys. Lett. 96 (2010) 94–97. doi:10.1063/1.3360230.

[10] N.A. Azarova, J.W. Owen, C.A. McLellan, M.A. Grimminger, E.K. Chapman, J.E. Anthony, O.D. Jurchescu, Fabrication of organic thin-film transistors by spray-

deposition for low-cost, large-area electronics, Org. Electron. Physics, Mater. Appl. 11 (2010) 1960–1965. doi:10.1016/j.orgel.2010.09.008.

[11] K.X. Steirer, M.O. Reese, B.L. Rupert, N. Kopidakis, D.C. Olson, R.T. Collins, D.S. Ginley, Ultrasonic spray deposition for production of organic solar cells, Sol. Energy Mater. Sol. Cells. 93 (2009) 447–453. doi:10.1016/j.solmat.2008.10.026.

[12] C. Girotto, D. Moia, B.P. Rand, P. Heremans, High-performance organic solar cells with spray-coated hole-transport and active layers, Adv. Funct. Mater. 21 (2011) 64–72. doi:10.1002/adfm.201001562.

[13] T. Wang, N.W. Scarratt, H. Yi, A.D.F. Dunbar, A.J. Pearson, D.C. Watters, T.S. Glen, A.C. Brook, J. Kingsley, A.R. Buckley, M.W.A. Skoda, A.M. Donald, R.A.L. Jones, A. Iraqi, D.G. Lidzey, Fabricating high performance, donor-acceptor copolymer solar cells by spray-coating in air, Adv. Energy Mater. 3 (2013) 505–512. doi:10.1002/aenm.201200713.

[14] Y. Zhang, J. Griffin, N.W. Scarratt, T. Wang, D.G. Lidzey, High efficiency arrays of polymer solar cells fabricated by spray-coating in air, Prog. Photovolt Res. Appl. 24 (2016) 275–282. doi:10.1002/pip.2665.

[15] N.W. Scarratt, J. Griffin, T. Wang, Y. Zhang, H. Yi, A. Iraqi, D.G. Lidzey, Polymer-based solar cells having an active area of 1.6 cm2 fabricated via spray coating, APL Mater. 3 (2015) 126108. doi:10.1063/1.4937553.

[16] Y. Zhang, N.W. Scarratt, T. Wang, D.G. Lidzey, Fabricating high performance conventional and inverted polymer solar cells by spray coating in air, Vacuum. 139 (2017) 154–158. doi:10.1016/j.vacuum.2016.09.017.

[17] M. Shao, S. Das, K. Xiao, J. Chen, J.K. Keum, I.N. Ivanov, G. Gu, W. Durant, D. Li, D.B. Geohegan, High-performance organic field-effect transistors with dielectric and active layers printed sequentially by ultrasonic spraying, J. Mater. Chem. C. 1 (2013) 4384–4390. doi:10.1039/c3tc30535j.

[18] C. Girotto, B.P. Rand, J. Genoe, P. Heremans, Exploring spray coating as a deposition technique for the fabrication of solution-processed solar cells, Sol.

Energy Mater. Sol. Cells. 93 (2009) 454–458. doi:10.1016/j.solmat.2008.11.052.

[19] M. Eslamian, Spray-on Thin Film PV Solar Cells: Advances, Potentials and Challenges, Coatings. 4 (2014) 60–84. doi:10.3390/coatings4010060.

[20] J.H. Heo, M.H. Lee, M.H. Jang, S.H. Im, Highly efficient $CH_3NH_3PbI_{3-x}Cl_x$ mixed halide perovskite solar cells prepared by re-dissolution and crystal grain growth via spray coating, J. Mater. Chem. A. 4 (2016) 17636–17642. doi:10.1039/C6TA06718B.

[21] S. Bose, S.S. Keller, T.S. Alstrøm, A. Boisen, K. Almdal, Process optimization of ultrasonic spray coating of polymer films, Langmuir. 29 (2013) 6911–6919. doi:10.1021/la4010246.

[22] R.J. Lang, Ultrasonic Atomization of Liquids, J. Acoust. Soc. Am. 34 (1962) 6–8. doi:10.1121/1.1909020.

[23] N.P. Pham, E. Boellaard, J.N. Burghartz, P.M. Sarro, Photoresist coating methods for the integration of novel 3-D RF microstructures, J. Microelectromechanical Syst. 13 (2004) 491–499. doi:10.1109/JMEMS.2004.828728.

[24] N.P. Pham, J.N. Burghartz, P.M. Sarro, Spray coating of photoresist for pattern transfer on high topography surfaces, J. Micromechanics Microengineering. 15 (2005) 691–697. doi:10.1088/0960-1317/15/4/003.

[25] M. Majumder, C. Rendall, M. Li, N. Behabtu, J.A. Eukel, R.H. Hauge, H.K. Schmidt, M. Pasquali, Insights into the physics of spray coating of SWNT films, Chem. Eng. Sci. 65 (2010) 2000–2008. doi:10.1016/j.ces.2009.11.042.

[26] H.L. Berger, Ultrasonic Liquid Atomization, Theory and Application, Partridge Hill Publishers, Hyde park, NY, 1998.

[27] J. Peet, M.L. Senatore, A.J. Heeger, G.C. Bazan, The role of processing in the fabrication and optimization of plastic solar cells, Adv. Mater. 21 (2009) 1521–1527. doi:10.1002/adma.200802559.

[28] D.K. Mohamad, J. Griffin, C. Bracher, A.T. Barrows, D.G. Lidzey, Spray-Cast Multilayer Organometal Perovskite Solar Cells Fabricated in Air, Adv. Energy Mater. 6 (2016). doi:10.1002/aenm.201600994.

[29] G.. Gittens, Variation of surface tension of water with temperature, J. Colloid Interface Sci. 30 (1969) 406–412. doi:10.1016/0021-9797(69)90409-3.

[30] J.E. Bishop, T.J. Routledge, D.G. Lidzey, Advances in Spray-Cast Perovskite Solar Cells, J. Phys. Chem. Lett. 9 (2018) 1977–1984. doi:10.1021/acs.jpclett.8b00311.

[31] R.D. Deegan, O. Bakajin, T.F. Dupont, G. Huber, S.R. Nagel, T.A. Witten, Capillary flow as the causes of ring stains from dried liquid drops, Nature, London. 389 (1997) 827–829.

[32] R.D. Deegan, O. Bakajin, T.F. Dupont, G. Huber, S.R. Nagel, T.A. Witten, Contact line deposits in an evaporating drop, Phys. Rev. E - Stat. Physics, Plasmas, Fluids, Relat. Interdiscip. Top. 62 (2000) 756–765. doi:10.1103/PhysRevE.62.756.

[33] C. Poulard, P. Damman, Control of spreading and drying of a polymer solution from Marangoni flows, Epl. 80 (2007). doi:10.1209/0295-5075/80/64001.

[34] K.A. Smith, On convective instability induced by surface-tension gradients J, Fluid Mech. 24 (1966) 401.

[35] J. Park, K. Shin, C. Lee, Roll-to-Roll Coating Technology and Its Applications: A Review, Int. J. Precis. Eng. Manuf. 17 (2016) 537–550. doi:10.1007/s12541-016-0067-z.

[36] S. Han, J. Derksen, J.H. Chun, Extrusion Spin Coating: An Efficient and Deterministic Photoresist Coating Method in Microlithography, IEEE Trans. Semicond. Manuf. 17 (2004) 12–21. doi:10.1109/TSM.2003.822734.

# Chapter 6

# Ultrasonic Spray Coating as an Approach for Large-Area Polymer OLEDs: The Influence of Thin Film Processing and Surface Roughness on Electrical Performance

In this chapter a detailed comparison of ultrasonic spray coating and spin coating for the fabrication of polymer organic light-emitting diodes (OLEDs) is demonstrated. Single-carrier devices of hole-transporting polymer poly[(9,9-dioctylfluorenyl-2,7-diyl)-co-(4,4'(N-(4-sec-butylphenyl))) diphenylamine] (TFB) are fabricated by ultrasonic spray coating. Uniform reference devices using spin coating are also made. It is shown, across a range of device thicknesses from 37 nm to 138 nm, typical of those used in OLED hole-transporting layers, that there is no statistical difference in the hole-injection efficiency between ultrasonic spray coating and spin coating (spin cast fit gradient: (9.4 ± 0.8) $x10^{-6}$, spin cast fit intercept: (- 1.2 ± 0.6) $x10^{-4}$, spray cast fit gradient: (9.4 ± 1.0) $x10^{-6}$, spray cast fit intercept: (- 1.9 ± 0.8) $x10^{-4}$). The importance of controlling the roughness of the films is demonstrated and a threshold of 10 nm average roughness (Ra) below which injection efficiency is not controlled by roughness is determined. However, above 10 nm roughness a reduction in injection efficiency up to an 86 % loss in performance for roughnesses of the order of 40 % of the thickness of the film. By optimising the deposition parameters, in order to allow the wet films to start to equilibrate, a wide processing window for smooth uniform films with excellent injection efficiency is found. This work reinforces the importance of ultrasonic spray

coating as a potential route to high-volume manufacturing of OLED based technology.

## 6.1: Introduction

Spray coating is a promising candidate for the low-cost and large scale processing of polymer semiconductors for use in optoelectronic devices such as area lighting,[1] solar cells,[2,3] electrochromic devices[4,5] and transistors.[6] Ultrasonic spray coating has the benefit over other spray coating techniques, such as airbrush spraying, of increased uniformity of droplet size, leading to increased spray and film uniformity.[7,8] Ultrasonic spray coating has been used widely in polymer organic photovoltaics (OPVs), spraying single[9–11] and multilayer devices[12–15] but the use for polymer organic light-emitting diodes (OLEDs) it has so far been limited.[16,17] Gilissen et al. deposited the emissive layer (Merck Super Yellow) of a polymer OLED via ultrasonic spray coating and achieved a power efficacy of 9.71 Lm $W^{-1}$ compared to 12 Lm $W^{-1}$ via spin coating.[17]

While these studies highlight the overall promise of ultrasonic spray deposition they do not elucidate potential issues or difficulties at a device structure level. In this chapter a detailed comparison of the performance of spray versus spin coating in an exemplar device is presented.

In ultrasonic spray coating a low concentration solution is fed onto an ultrasonic tip that vibrates at frequencies up to 35 KHz. The ultrasonic tip atomizes the solution into a fine mist of micrometre sized droplets which are then shaped and directed by a jet of gas as the spray head passes over the substrate. The individual solution droplets wet to the substrate, then spread and merge to form a complete fluid film. The film continues to flow and over time (a few seconds or more) increases in uniformity. Finally, the solvent within the film evaporates and a dry film is formed. The properties of the final film are dependent upon numerous process parameters, such as the physical properties of the solvent—including vapour pressure, viscosity and surface energy—, solution concentration, spray head height and speed, and the substrate temperature.[8,12,18–20]

In this chapter, I compare the electrical device performance of spin and spray cast films to determine the relationship between film properties and electrical properties. In order to understand spray coating the hole-injection efficiency (η) into spin cast and spray cast TFB layers of varying roughnesses was investigated across the thickness range 37-138 nm by normalizing the J-V curves for different devices via a mean-field approximation and calculating the space-charge-limited current ($J_{SCL}$).

$$\eta = \frac{J_{measured}}{J_{SCL}} \quad (1)$$

It is concluded that the surface roughness plays an important role in controlling injection efficiency but that for devices fabricated using spray or spin coating, that have comparable surface roughness, no difference in charge-injection efficiency can be measured. These results suggest that there is nothing intrinsic in spray coating that limits the overall device performance. The morphology of the as-formed layer does not limit the injection efficiency and transport in our experimental devices.

## 6.2: Device Fabrication

Hole only devices were fabricated using pre-patterned 8 pixel ITO substrates with a sheet resistance of 20 Ω square$^{-1}$ and an rms roughness of 1.8 nm (determined by a 10 x 10 μm AFM scan) purchased from Ossila Ltd. The ITO substrates were cleaned by sonication in Hellmanex III solution, deionized water and isopropyl alcohol. Once sonicated in isopropyl alcohol the substrates were dried with nitrogen and treated with UV-Ozone for 15 minutes. Al 4083 grade PEDOT:PSS was purchased from Ossila Ltd and was filtered using a 0.45 μm PVDF mircodisc filter prior to spin coating at 5000 rpm to yield a 40 nm film. The PEDOT:PSS films were annealed on a hotplate, in air at 120 °C for 15 mins and then cooled to room temperature prior to deposition of further layers. Poly[(9,9-dioctylfluorenyl-2,7-diyl)-co-(4,4'(N-(4-sec-butylphenyl))) diphenylamine] (TFB) was purchased from Ossila Ltd with a purity of >99 % and a molecular weight of 31,206 KDa. The spin coated TFB was cast from a toluene solution at varying concentrations in ambient conditions, from 10-30 mg ml$^{-1}$, and at a number of different spin speeds to obtain a range of thicknesses.

Ultrasonic spray cast TFB poly[(9,9-dioctylfluorenyl-2,7-diyl)-co-(4,4'(N-(4-sec-butylphenyl))) diphenylamine] films were deposited in ambient conditions from toluene solutions of varying concentrations (4, 6 and 8 mg $ml^{-1}$) using a PRISM Ultra-coat 300 system supplied by Ultrasonic systems, Inc. to give layer thicknesses of between 40 nm and 120 nm. The spray height (40 mm), base plate temperature (25 °C) and fluid pressure (50 mbar) were kept constant for each spray cast solution with the spray speed varied from 180-250 mm $s^{-1}$ to vary the thickness of the spray cast layer. TFB has a relatively high and non-dispersive mobility as measured by time of flight technique of 0.01 $cm^2$ $V^{-1}$ $s^{-1}$ [21,22] and along with a deep HOMO of –5.3 eV,[23] excellent photochemical and thermal stability[23] makes a good test case for device process investigations. It is widely used as a copolymer constituent in light-emitting and hole transporting layers.[24–29] It is highly soluble in aromatic solvents such as toluene, xylenes and chlorobenzene, and can be spray deposited from a range of these solvents. Toluene was the chosen solvent for this work as its relatively low boiling point for spray coating aids the formation of films with a range of uniformities and roughnesses.

The contacts were swabbed using toluene to pattern the device and the films were annealed at 100 °C for 10 minutes to remove any residual solvent. A bilayer top electrode of 10 nm Molybdenum(VI) oxide ($MoO_3$) and 100 nm Aluminium was thermally evaporated at a vacuum pressure of $6x10^{-6}$ mbar through a mask to define a pixel area of 4 $mm^2$. After the deposition of the top electrode the devices were encapsulated in an inert atmosphere (<1 ppm $H_2O$ and <1 ppm $O_2$) using UV-curable epoxy and a glass slide. External electrical connection to the devices were gained via friction contacts attached to the ITO glass substrate. The top electrode being evaporated over cleared ITO tracks on the underlying substrate.

## 6.3: Device Characterisation

Current-voltage sweeps were performed using a Keithley 2602 source measure unit. Thickness measurements, roughness measurements and topographical map scans were performed using a Bruker DektakXT. Map scans were replotted using Gwyddion 2.50 and statistical analysis of the data was performed using SAS Institute Inc JMP pro 13.

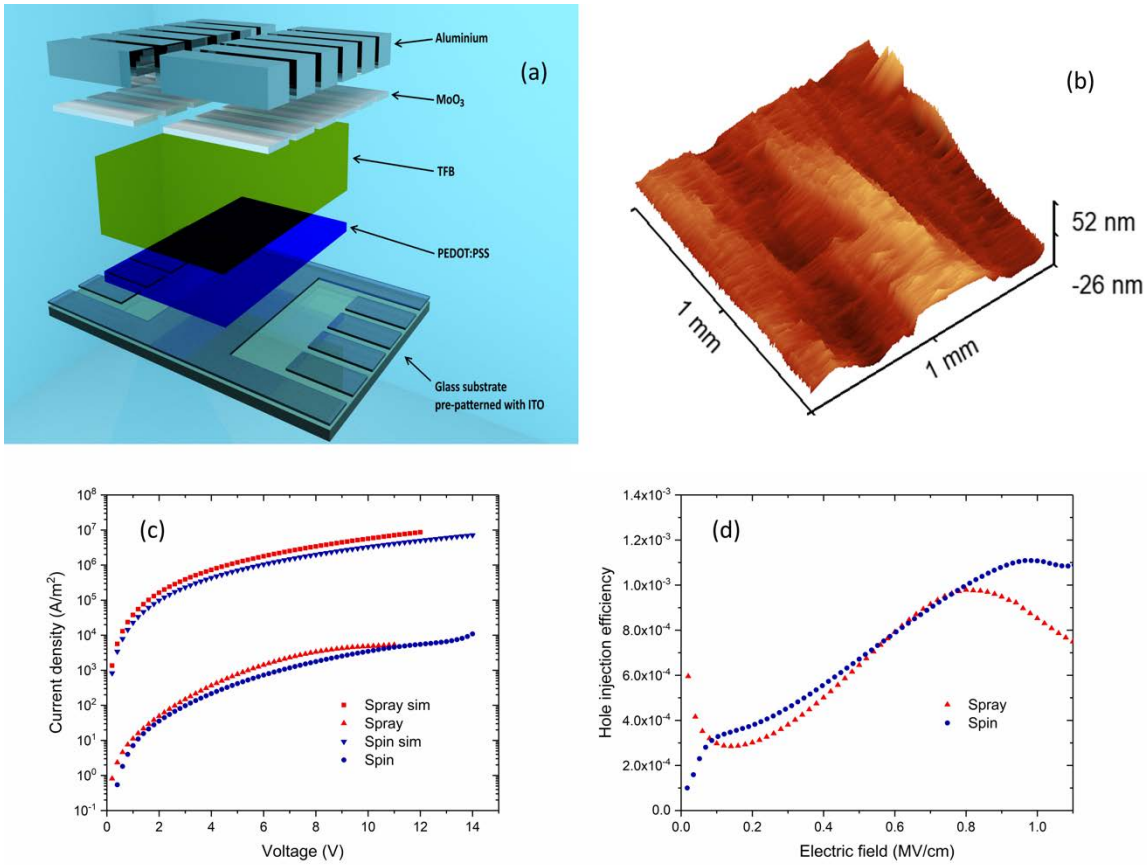


*Figure 6.1: (a) A 3D model of the device structure. (b) A topographical map scan of a spray cast TFB pixel (6 mg/ml S200 P4) with the mean thickness set to the measured thickness, 100 nm. (c) The current density against voltage of the space-charge-limited current simulated using (b), the measured data from the same pixel and the simulated space charge limited current for a uniform 116 nm thick device and the measured data from a spin cast device of the same thickness. (d) The hole-injection efficiency against electric field of the spin and spray cast pixels.*

Thin films of TFB were deposited via both spin coating and spray coating. Thickness measurements and surface height map scans (Figure 6.1b) were taken of the spray cast pixels prior to the evaporation of $MoO_3$ and Aluminium using a Bruker DektakXT. The 1 mm by 1 mm maps are constructed from 50 line scans with resolution of 220 nm along of the line scan direction and resolution of 20000 nm in the direction orthogonal to the lines. The roughness average, $R_a$, is the sum of the magnitude of deviation in thickness from the mean thickness divided by the number of samples taken across the map scan. This represents the finer random

irregularities of a surface rather than the larger scale thickness variations. The thickness of both spin and spray cast films as also measured by Dektak by scratching the surface of the film to the underlying substrate and scanning across the scratch. The roughness of the spin cast films was routinely measured to be <2 nm as such they are assumed to be perfectly uniform for space-charge-limited current calculations.

## 6.4: Results and Discussion

In order to compare quantitatively the measured current-voltage characteristics of devices fabricated using spray coating and spin coating the variation in thickness between the two different processing methods needs to be normalised. In addition, the variation of thickness within pixels and the surface roughness in the spray cast devices also needs to be corrected in order that a fair comparison be made. The approach chosen follows that of Abkowitz et al.[30] and Ioannidis et al.[31] in that a charge-injection efficiency of the device is calculated by comparing the measured current to a theoretical space-charge-limited current for the thickness and material being tested. The injection efficiency has been used to probe a range of contacts as well as the ability of such contacts to inject holes into TFB.[22,32] Following Abkowitz et al.[30] a theoretical space-charge-limited current is calculated for the non-uniform devices by dividing the device into an array of parallel elements of discrete thickness and calculating a theoretical bulk space-charge-limited current contribution from each element of the array. The below histogram, Figure 6.2, of height differences between neighbouring array elements (Δh) shows (for a 100 nm average thickness film) the mean and median differences are less than 1 nm. Furthermore, 95 % of the differences are less than 2 nm. The error in thickness between array elements is 2 %, which, by propagating through to a current via the Mott-Gurney relationship, leads to a 2 % error in current density. Both the error in current density due to the mean-field approximation, and the device-to-device variation is significantly larger, and as such, treating each array element as discrete is found to be valid with insignificant contributions to the overall device current from lateral conduction, as such the films are locally smooth but globally rough across the device.

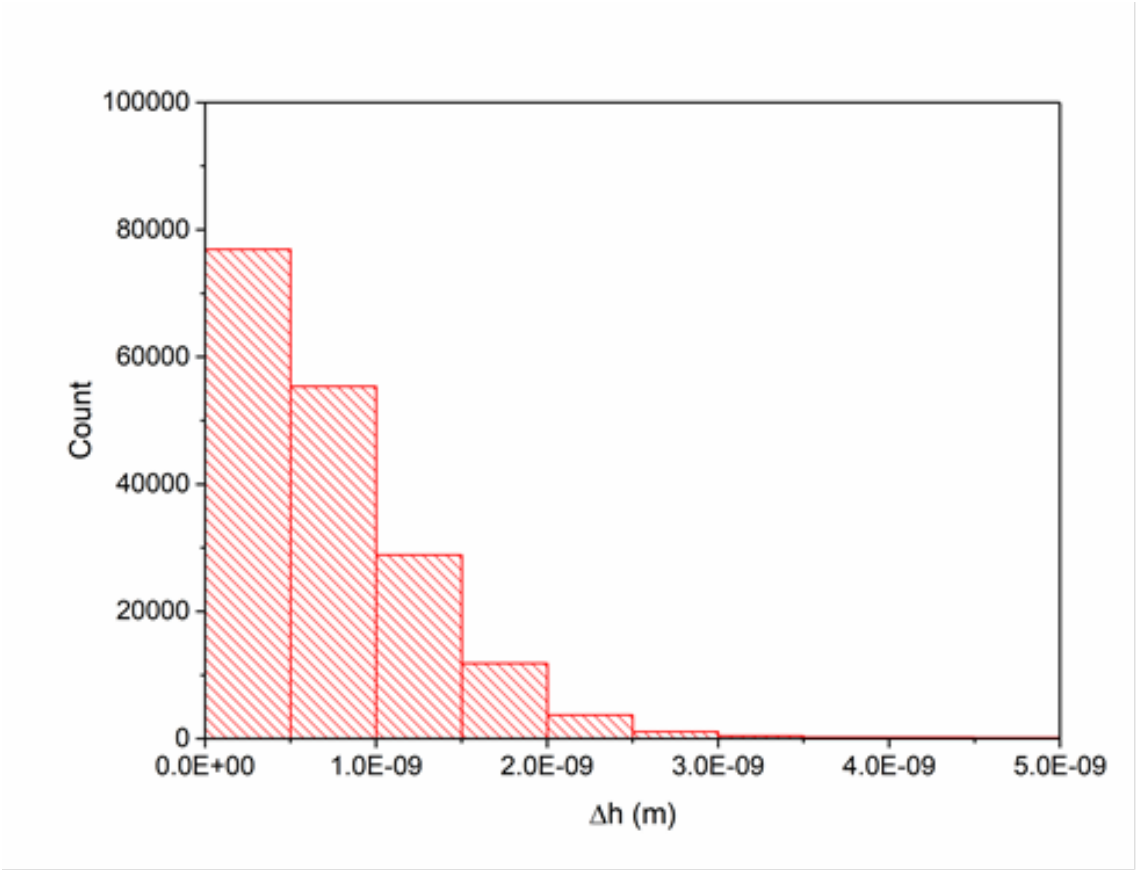


*Figure 6. 2: A histogram of the difference in height between neighbouring array elements from the map scan of a typical spray cast pixel (6 mg ml$^{-1}$ S200 P4). The mean Δh is 0.77 nm, the median is 0.60 nm.*

The theoretical space-charge-limited current is calculated using a modified Mott-Gurney relationship[33] with a Poole-Frenkel field dependent mobility,[34] $j = \frac{9}{8}\varepsilon_0\varepsilon_r\mu\frac{\bar{E}^2}{L}exp\left(\gamma\sqrt{\bar{E}}\right)$. Where $\varepsilon_r$ is the relative permittivity, μ is the bulk mobility, L is the layer thickness, γ is the field dependent factor and $\bar{E}$ is the mean electric field. A mean-field approximation is used to simplify the calculation for different thickness elements in the intra-device array. This approximation is shown to be valid[35–38] and leads to typical under estimation in zero-field mobility and the γ factor of 2 % and 15 % respectively[39] and an error in calculated $j$ of 10 %. For TFB the bulk mobility is taken as 0.01 cm$^2$ V$^{-1}$ s$^{-1}$,[21] the relative permittivity $\varepsilon_r \sim 3$[40] and field dependent factor $\gamma = 5.86 \times 10^{-4}$ (cm V$^{-1}$)$^{0.5}$. [22]

The theoretical space-charge-limited current values were compared to the measured current density values of the same pixels (Figure 6.1c) to show the variation of hole-injection efficiency against electric field (Figure 6.1d). The hole-injection efficiency at a fixed electric field (1 MV $cm^{-1}$) was used for direct comparison of pixels of different thicknesses and deposition techniques. In this chapter electrical measurements, topographical map scans and theoretical models are combined to determine the hole-injection efficiency of $MoO_3$ into TFB films. The hole-injection efficiency is used to probe the charge transport in TFB films across a range of thickness equivalent to those optimal for OLEDs, allowing us to compare the deposition techniques of ultrasonic spray coating and spin coating for the fabrication of OLEDs.

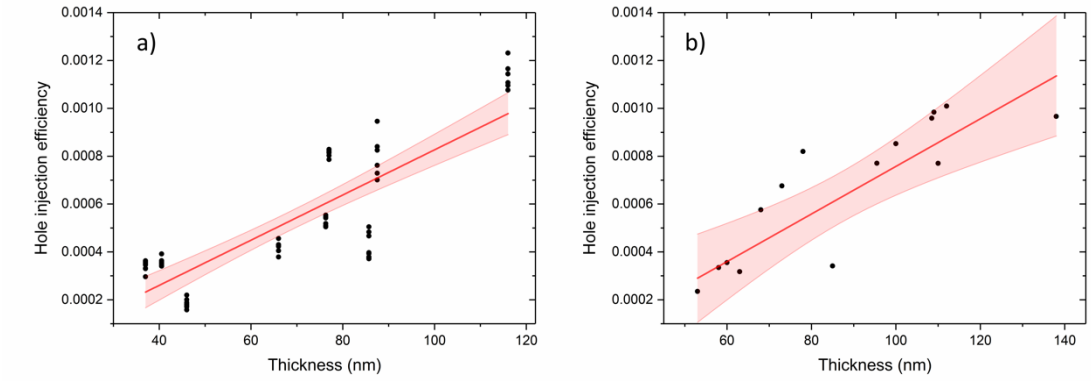


*Figure 6. 3: (a) The injection efficiency at 1 MV $cm^{-1}$ against thickness for the spin cast pixels, a liner regression has been fitted and the shaded region demonstrates the 95 % confidence interval. The linear regression fit has a P-value of <0.0001 and an R-squared adjusted value of 0.66 (b) The injection efficiency at 1 MV $cm^{-1}$ against thickness for the spray cast pixels, a linear regression has been fitted and the shaded region demonstrates the 95 % confidence interval. The linear regression fit has a P-value of 0.0003 and an R-squared adjusted value of 0.59.*

Figure 6.3 shows the variation of injection efficiency from $MoO_3$ into a range of different thicknesses of TFB deposited via spin coating and ultrasonic spray coating. Figure 6.1a shows a schematic of the device structure, consisting of ITO / PEDOT:PSS / TFB / $MoO_3$ / Aluminium. The thickness and deposition method of the

PEDOT:PSS (40 nm), $MoO_3$ (10 nm) and Aluminium (100 nm) are consistent for all devices. The thickness ranges covered by the two deposition techniques of TFB overlap allowing for the direct comparison of injection efficiency and thus the performance of spin and spray cast devices.

Looking first at the spin cast TFB devices (Figure 6.3a) it can be seen that the injection efficiency increases with thickness (within this range). The injection efficiency has been shown to vary due to the material used for injection,[22] the thickness of that layer[41] and the applied electric field.[22] In this work the injection material and thickness have been kept constant and the injection efficiencies were all measured at the same electric field strength. The mobility of materials with similar properties to TFB have been studied in literature; Ji et al. measured the mobility of pi-conjugated polymer P3HT in organic thin film transistors and demonstrated that mobility increases with thickness within the device thickness region (0-200 nm),[42] Chu et al.[35,43] demonstrated the mobility of hole-transporting small molecule NPB increases with thickness in an similar range as did Xu et al. who also demonstrated the same trend for hole-transporting small molecule TPD.[44] It can then be inferred that the increase in injection efficiency is due to an increase in the effective mobility of the TFB film toward the bulk mobility.[45]

To understand the microscopic structure and the effect on the charge injection and transport within a film it is often assumed that a film is made up of the substrate interface, the surface interface and the bulk of the film.[44,46–49] In this work two regions are focussed upon; the interfacial region at the surface of the TFB where the holes are injected from the $MoO_3$, and the bulk of the TFB. In a uniform thick film the interfacial region will be small compared to the film thickness and the charge dynamics of the film will be dominated by that of the bulk TFB, in thinner films the interfacial region thickness will be a larger proportion of the thickness of the film as a whole and such will play a larger part in charge dynamics of the film. This concept is analogous to variation of glass transition temperature ($T_g$) in polymer films as the thickness of the film is changed, Keddie et al. demonstrated as the thickness of a polymer film is increased the $T_g$ increases almost linearly for thin films then

becomes constant above a certain thickness as the thermal properties of the bulk dominate that of the film, as such we expect to see a similar trend in hole injection efficiency at greater thicknesses than studied here.[50] The influence of the interfacial regions on the charge dynamics of the film has been studied by Baldo et al.[49] for electron transport in $Alq_3$, by Chu et al[35,43] for hole transport in NPB, Xu et al[44] for hole transport in TPD and by Harding et al. for interlayers of TFB.[51] These works suggest that there are trap states in the injection interfacial region which result from dipole interactions between $MoO_3$ and TFB, changes in the polymer chain conformation or a combination of both. The disorder in the local dipole fields in the interfacial region cause a broadening of the manifold of states involved in hopping transport as such lowering the effective mobility. Changes in the conformation of polymer chains can also increase the intersite hopping distance for holes, reducing the hopping rate and thus lowering the effective mobility.

Figure 6.3b shows the injection efficiency of spray cast TFB devices increases with thickness like that of spin cast devices. A linear regression fit was applied to the spin cast and spray cast data, the gradients and intercepts of the spin cast and spray cast models agree within errors (Table 6.1), thus suggesting that device performance of spray cast devices is statistically equivalent to spin cast devices.

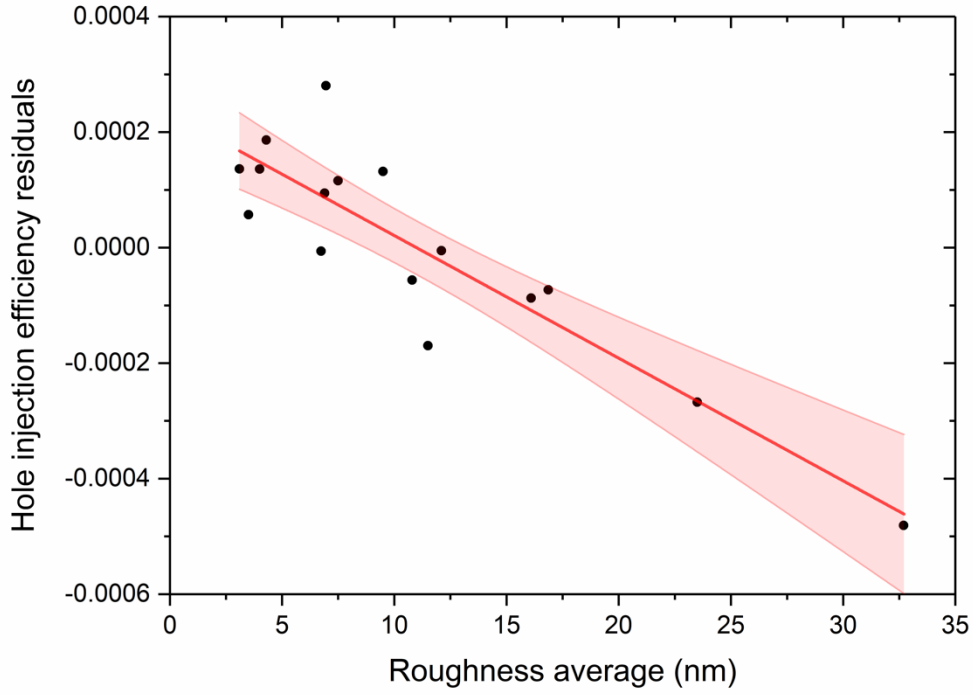


*Figure 6. 4: The injection efficiency residual, the calculated hole-injection efficiency minus the hole-injection efficiency predicted by the initial spray cast linear regression fit, at 1 MV cm$^{-1}$ against the roughness average (Ra) of the spray cast device pixels. The linear regression fit has a P-value <0.0001 and R-squared adjusted 0.79, the shaded region demonstrates the 95 % confidence interval.*

Since the roughness of the surface of spin cast TFB is too low to be reliably measured by the technique used in this experiment (< 2 nm) the spin cast pixels were assumed to be uniform with no significant roughness. The process of forming a film via spray coating can lead to non-uniform thickness, up to 52 nm from the mean (Figure 6.1b). Using map scans the thickness variation between array elements across spray cast devices were measured and taken into account in the initial spray cast linear regression fit, but the roughness of these devices were not accounted for. Figure 6.4 shows the injection efficiency residuals from spray cast linear regression fit verses thickness, plotted against the roughness average. The residual in this case is the difference between the measured value of injection efficiency and the predicted value of injection efficiency from the linear regression fit based on thickness

variation. The injection efficiency residuals decrease with increasing roughness, and above a Ra of around 10 nm the residuals become negative. The R-square adjusted value for this fit is 0.79 thus roughness has a significant effect on the injection efficiency. Rougher films, as-prepared by higher concentration formulations and faster pass speeds, lead to lower overall charge-injection efficiency. These films dry faster on the substrate, and within the film, the surface dries fastest of all. The consequence is that the surfaces of these rough films have less time to equilibrate in terms of molecular conformation and mixing. It is suggested that this leads to a lock-in of a non-equilibrium conformation within the film surface with a higher dispersion in the distribution of energy states that form the hole-transport manifold. This in turn leads to lower effective mobility and a lower hole-injection efficiency for the rougher films.

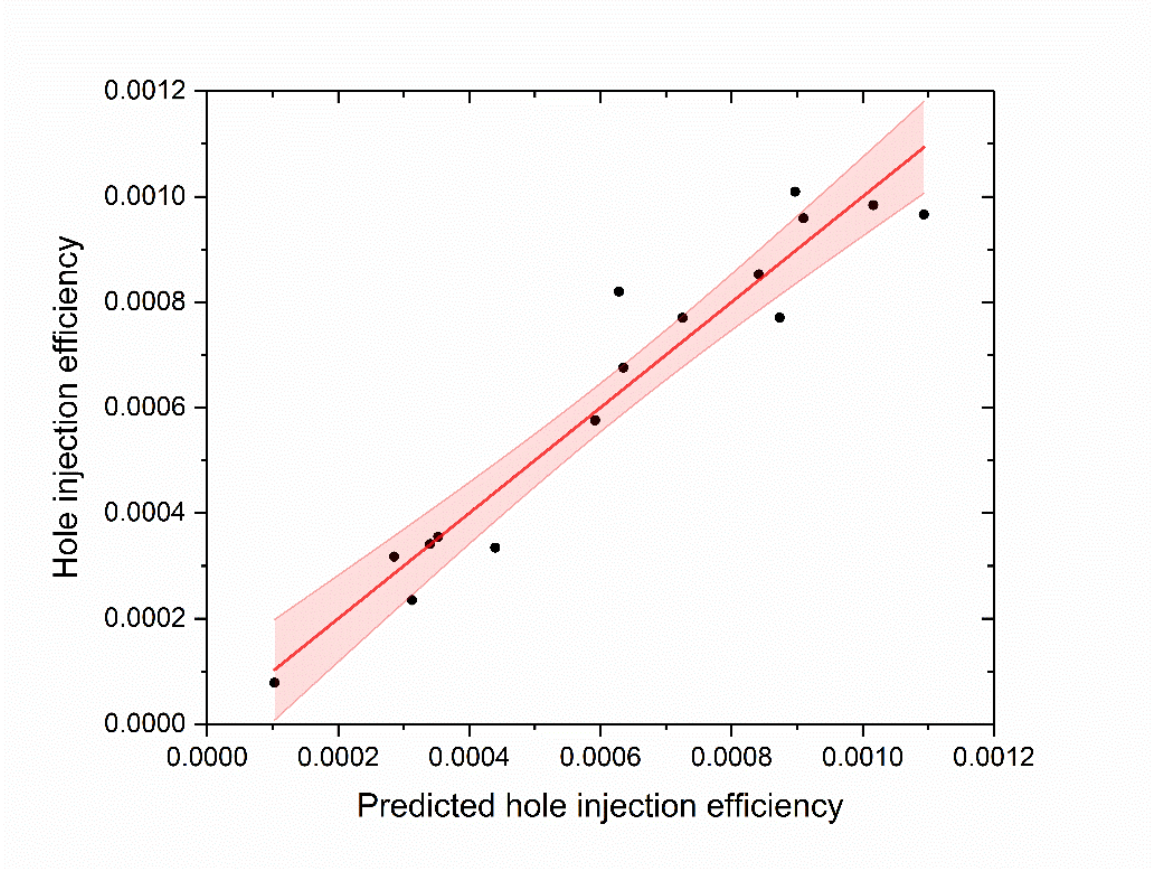


*Figure 6. 5: The calculated injection efficiency against the predicted injection efficiency by the linear regression fit based on the variation due to thickness and the roughness*

*of the spray-cast TFB layer (at 1 MV cm$^{-1}$)(Spray cast two parameter fit). The shaded region demonstrates the 95 % confidence interval from the fit.*

Figure 6.5 shows the measured hole-injection efficiency of the spray cast devices plotted against the injection efficiency predicted by the linear regression fit incorporating thickness and roughness. The measured and predicted data are strongly correlated and the confidence interval is very narrow.

| | **Spin cast fit** | **Spray cast single parameter fit** | **Spray cast two parameter fit** |
|---|---|---|---|
| **R-sq adjusted** | 0.66 | 0.59 | 0.91 |
| **Fit Gradient** | (9.4 ± 0.8) x10$^{-6}$ | (9.9 ± 2.1) x10$^{-6}$ | (9.4 ± 1.0) x10$^{-6}$ |
| **Fit intercept** | (- 1.2 ± 0.6) x10$^{-4}$ | (- 2.4 ± 1.9) x10$^{-4}$ | (- 1.9 ± 0.8) x10$^{-4}$ |
| **Model P value** | <0.0001* | 0.0003 | <0.0001* |

*Table 6. 1: Comparing the key fit parameters; fit gradient, fit intercept, P value and R-square adjusted for the spin cast and spray cast models dependent on thickness, and the spray cast model dependent on thickness and roughness.*

Table 6.1 compares the spin cast, single parameter spray cast and two parameter spray cast linear regression fits for hole-injection efficiency plotted against thickness. The errors in the gradient and intercept are reduced when going from the single to the two parameter spray-cast models. The gradient and intercept values of the two parameter spray cast model are closer to the values of the spin cast model than those of the single parameter spray cast model and they agree within errors. The p value of the two parameter spray-cast model compared to the single parameter model has decreased from 0.0003 to <0.0001 as such the two parameter spray-cast model p value is highly significant as is found in the spin cast model. This suggests that if the ultrasonic spray coating process is optimised to minimize roughness then overall device performance of OLEDs deposited via ultrasonic spray coating can equal those fabricated by spin coating.

## 6.5: Conclusions

The injection efficiency of holes into films of poly[(9,9-dioctylfluorenyl-2,7-diyl)-co-(4,4'(N-(4-sec-butylphenyl))) diphenylamine] cast by ultrasonic spray coating and those cast by spin coating have been compared. It is shown that across a range of thicknesses, typical of those used in OLEDs, that there is no intrinsic difference in the injection efficiency between ultrasonic spray coating and spin coating. This reinforces the importance of spray coating as a potential route to high volume manufacturing of OLED based technology. The importance of controlling the roughness of the films has been demonstrated and a threshold of 10 nm average roughness below which injection efficiency is not controlled by roughness has been determined. However, above 10 nm roughness there is a reduction in injection efficiency up to an 86 % loss in performance for roughnesses of the order of 40 % of the thickness of the film. However, the process window for achieving comparable spin and spray cast hole-injection performance is wide with spray cast films, with Ra < 10 nm being achieved by control of drying time through solvent choice, substrate temperature, formulation concentration and pass speed.

## 6.6: References


[1] A. Sandström, A. Asadpoordarvish, J. Enevold, L. Edman, Spraying light: Ambient-air fabrication of large-area emissive devices on complex-shaped surfaces, Adv. Mater. 26 (2014) 4975–4980. doi:10.1002/adma.201401286.

[2] C.N. Hoth, R. Steim, P. Schilinsky, S.A. Choulis, S.F. Tedde, O. Hayden, C.J. Brabec, Topographical and morphological aspects of spray coated organic photovoltaics, Org. Electron. Physics, Mater. Appl. 10 (2009) 587–593. doi:10.1016/j.orgel.2009.02.010.

[3] J.W. Kang, Y.J. Kang, S. Jung, M. Song, D.G. Kim, C.S. Kim, S.H. Kim, Fully spray-coated inverted organic solar cells, Sol. Energy Mater. Sol. Cells. 103 (2012) 76–79. doi:10.1016/j.solmat.2012.04.027.

[4] P. Shi, C.M. Amb, E.P. Knott, E.J. Thompson, D.Y. Liu, J. Mei, A.L. Dyer, J.R. Reynolds, Broadly absorbing black to transmissive switching electrochromic polymers, Adv. Mater. 22 (2010) 4949–4953. doi:10.1002/adma.201002234.

[5] C.M. Amb, P.M. Beaujuge, J.R. Reynolds, Spray-processable blue-to-highly transmissive switching polymer electrochromes via the donor-acceptor approach, Adv. Mater. 22 (2010) 724–728. doi:10.1002/adma.200902917.

[6] B.S. Hunter, J.W. Ward, M.M. Payne, J.E. Anthony, O.D. Jurchescu, D. Thomas, Low-voltage polymer / small-molecule blend organic thin-film transistors and circuits fabricated via spray deposition Low-voltage polymer / small-molecule blend organic thin-film transistors and circuits fabricated via spray deposition, 223304 (2015) 1–5. doi:10.1063/1.4922194.

[7] R. Engle, Advantages of ultrasonic spray coatings of biomaterials onto devices and implantables., Sono-Tek Present. 15th Int. Coat. Sci. Technol. Symp. (2010). http://www.sono-tek.com/wp-content/uploads/2012/01/Sono-Tek-ISCST-Symposium.pdf.

[8] M. Majumder, C. Rendall, M. Li, N. Behabtu, J.A. Eukel, R.H. Hauge, H.K. Schmidt, M. Pasquali, Insights into the physics of spray coating of SWNT films, Chem. Eng. Sci. 65 (2010) 2000–2008. doi:10.1016/j.ces.2009.11.042.

[9] K.X. Steirer, M.O. Reese, B.L. Rupert, N. Kopidakis, D.C. Olson, R.T. Collins, D.S. Ginley, Ultrasonic spray deposition for production of organic solar cells, Sol. Energy Mater. Sol. Cells. 93 (2009) 447–453. doi:10.1016/j.solmat.2008.10.026.

[10] J.G. Tait, B.P. Rand, P. Heremans, Concurrently pumped ultrasonic spray coating for donor:acceptor and thickness optimization of organic solar cells, Org. Electron. Physics, Mater. Appl. 14 (2013) 1002–1008. doi:10.1016/j.orgel.2013.01.023.

[11] T. Wang, N.W. Scarratt, H. Yi, A.D.F. Dunbar, A.J. Pearson, D.C. Watters, T.S. Glen, A.C. Brook, J. Kingsley, A.R. Buckley, M.W.A. Skoda, A.M. Donald, R.A.L. Jones, A. Iraqi, D.G. Lidzey, Fabricating high performance, donor-acceptor copolymer solar cells by spray-coating in air, Adv. Energy Mater. 3 (2013) 505–512. doi:10.1002/aenm.201200713.

[12] C. Girotto, D. Moia, B.P. Rand, P. Heremans, High-performance organic solar cells with spray-coated hole-transport and active layers, Adv. Funct. Mater. 21 (2011) 64–72. doi:10.1002/adfm.201001562.

[13] Y. Zhang, J. Griffin, N.W. Scarratt, T. Wang, D.G. Lidzey, High efficiency arrays of polymer solar cells fabricated by spray-coating in air, Prog. Photovolt Res. Appl. 24 (2016) 275–282. doi:10.1002/pip.2665.

[14] Y. Zhang, N.W. Scarratt, T. Wang, D.G. Lidzey, Fabricating high performance conventional and inverted polymer solar cells by spray coating in air, Vacuum. 139 (2017) 154–158. doi:10.1016/j.vacuum.2016.09.017.

[15] N.W. Scarratt, J. Griffin, T. Wang, Y. Zhang, H. Yi, A. Iraqi, D.G. Lidzey, Polymer-based solar cells having an active area of 1.6 cm2 fabricated via spray coating, APL Mater. 3 (2015) 126108. doi:10.1063/1.4937553.

[16] K. Gilissen, J. Stryckers, J. Manca, W. Deferme, Towards fully spray coated organic light emitting devices, Proc. SPIE - Int. Soc. Opt. Eng. 9183 (2014) 918311. doi:10.1117/12.2060994.

[17] K. Gilissen, J. Stryckers, P. Verstappen, J. Drijkoningen, G.H.L. Heintges, L.

Lutsen, J. Manca, W. Maes, W. Deferme, Ultrasonic spray coating as deposition technique for the light-emitting layer in polymer LEDs, Org. Electron. Physics, Mater. Appl. 20 (2015) 31–35. doi:10.1016/j.orgel.2015.01.015.

[18] M. Eslamian, Spray-on Thin Film PV Solar Cells: Advances, Potentials and Challenges, Coatings. 4 (2014) 60–84. doi:10.3390/coatings4010060.

[19] J.E. Bishop, D.K. Mohamad, M. Wong-Stringer, A. Smith, D.G. Lidzey, Spray-cast multilayer perovskite solar cells with an active-area of 1.5 cm2, Sci. Rep. 7 (2017) 7962. doi:10.1038/s41598-017-08642-2.

[20] A.T. Barrows, A.J. Pearson, C.K. Kwak, A.D.F. Dunbar, A.R. Buckley, D.G. Lidzey, Efficient planar heterojunction mixed-halide perovskite solar cells deposited via spray-deposition, Energy Environ. Sci. 7 (2014) 2944–2950. doi:10.1039/C4EE01546K.

[21] H.H. Fong, A. Papadimitratos, G.G. Malliaras, Nondispersive hole transport in a polyfluorene copolymer with a mobility of 0.01 cm 2V -1s -1, Appl. Phys. Lett. 89 (2006) 87–90. doi:10.1063/1.2369545.

[22] H.H. Fong, A. Papadimitratos, J. Hwang, A. Kahn, G.G. Malliaras, Hole injection in a model fluorene-triarylamine copolymer, Adv. Funct. Mater. 19 (2009) 304–310. doi:10.1002/adfm.200800738.

[23] B.M. Redecker, D.D.C. Bradley, M. Inbasekaran, W.W. Wu, E.P. Woo, High Mobility Hole Transport Fluorene- Triarylamine Copolymers, Adv. Funct. Mater. 11 (1999) 241–246. doi:10.1002/(SICI)1521-4095(199903)11:3<241::AID-ADMA241>3.0.CO;2-J.

[24] T. Chiba, Y.J. Pu, M. Hirasawa, A. Masuhara, H. Sasabe, J. Kido, Solution-processed inorganic-organic hybrid electron injection layer for polymer light-emitting devices, ACS Appl. Mater. Interfaces. 4 (2012) 6104–6108. doi:10.1021/am301732m.

[25] Y. Chen, Y. Xia, G.M. Smith, H. Sun, D. Yang, D. Ma, Y. Li, W. Huang, D.L. Carroll, Solution-processable hole-generation layer and electron-transporting layer: Towards high-performance, alternating-current-driven, field-induced

polymer electroluminescent devices, Adv. Funct. Mater. 24 (2014) 2677–2688. doi:10.1002/adfm.201303242.

[26] S.A. Choulis, V. Choong, M.K. Mathai, F. So, S.A. Choulis, V. Choong, M.K. Mathai, F. So, The effect of interfacial layer on the performance of organic light-emitting diodes The effect of interfacial layer on the performance of organic light-emitting diodes, 113503 (2005) 2003–2006. doi:10.1063/1.2042635.

[27] S.-R. Tseng, S.-Y. Li, H.-F. Meng, Y.-H. Yu, C.-M. Yang, H.-H. Liao, S.-F. Horng, C.-S. Hsu, Deep blue light-emitting diode based on high molecular weight poly(9,9-dioctylfluorene) with high efficiency and color stability, Org. Electron. 9 (2008) 279–284. doi:10.1016/j.orgel.2007.11.003.

[28] S.-R. Tseng, S.Y. Li, H.F. Meng, Y.H. Yu, C.M. Yang, H.H. Liao, S.F. Horng, C.S. Hsu, High-efficiency blue multilayer polymer light-emitting diode based on poly(9,9-dioctylfluorene), J. Appl. Phys. 101 (2007) 1–4. doi:10.1063/1.2721830.

[29] J. Wang, N. Wang, Y. Jin, J. Si, Z.K. Tan, H. Du, L. Cheng, X. Dai, S. Bai, H. He, Z. Ye, M.L. Lai, R.H. Friend, W. Huang, Interfacial control toward efficient and low-voltage perovskite light-emitting diodes, Adv. Mater. 27 (2015) 2311–2316. doi:10.1002/adma.201405217.

[30] M. Abkowitz, J.S. Facci, J. Rehm, Direct evaluation of contact injection efficiency into small molecule based transport layers: Influence of extrinsic factors, J. Appl. Phys. 83 (1998) 2670–2676. doi:10.1063/1.367030.

[31] A. Ioannidis, J.S. Facci, M.A. Abkowitz, Evolution in the charge injection efficiency of evaporated Au contacts on a molecularly doped polymer, J. Appl. Phys. 84 (1998) 1439–1444. doi:10.1063/1.368179.

[32] Y. Shen, A.R. Hosseini, M.H. Wong, G.G. Malliaras, How to make ohmic contacts to organic semiconductors, ChemPhysChem. 5 (2004) 16–25. doi:10.1002/cphc.200300942.

[33] N.F. Mott, R.W. Gurney, Electronic processes in ionic crystals, Clarendon Press, Oxford, 1940. http://cds.cern.ch/record/2144379.

[34] E.H. Sondheimer, The mean free path of electrons in metals, Adv. Phys. 1 (1952) 1–42.

[35] T.-Y. Chu, O.-K. Song, Hole mobility of N,N′-bis(naphthalen-1-yl)-N,N′-bis(phenyl) benzidine investigated by using space-charge-limited currents, Appl. Phys. Lett. 90 (2007) 203512. doi:10.1063/1.2741055.

[36] M. Giulianini, E.R. Waclawik, J.M. Bell, N. Motta, Current-voltage characteristics of poly(3-hexylthiophene) diodes at room temperature, Appl. Phys. Lett. 94 (2009) 3–6. doi:10.1063/1.3086882.

[37] O.G. Reid, K. Munechika, D.S. Ginger, Space Charge Limited Current Measurements on Conjugated Polymer Films using Conductive Atomic Force Microscopy 2008, Nano Lett. 8 (2008) 1602–1609.

[38] A. Pitarch, K. Meerholz, D. Hertel, Effect of dopant concentration on charge transport in crosslinkable polymers, Phys. Status Solidi Basic Res. 245 (2008) 814–819. doi:10.1002/pssb.200743457.

[39] A.R. Buckley, Analysing space charge limited currents in organic light emitting diodes, Synth. Met. 160 (2010) 540–543. doi:10.1016/j.synthmet.2009.11.027.

[40] P. Blom, M. de Jong, M. van Munster, Electric-field and temperature dependence of the hole mobility in poly(p-phenylene vinylene), Phys. Rev. B - Condens. Matter Mater. Phys. 55 (1997) R656–R659. doi:10.1103/PhysRevB.55.R656.

[41] A. Buckley, D. Pickup, C. Yates, Y. Zhao, D. Lidzey, Hole injection in tri-arylamine containing polyfluorene co-polymer devices with molybdenum oxide contacts, J. Appl. Phys. 109 (2011) 1–7. doi:10.1063/1.3562184.

[42] H. Jia, S. Gowrisanker, G.K. Pant, R.M. Wallace, B.E. Gnade, Effect of poly (3-hexylthiophene) film thickness on organic thin film transistor properties, J. Vac. Sci. Technol. A Vacuum, Surfaces, Film. 24 (2006) 1228–1232. doi:10.1116/1.2202858.

[43] T.Y. Chu, O.K. Song, Apparent thickness dependence of mobility in organic thin films analyzed by Gaussian disorder model, J. Appl. Phys. 104 (2008). doi:10.1063/1.2959825.

[44] H. Xu, W.-J. Zhai, C. Tang, S.-Y. Qiu, R.-L. Liu, Z. Rong, Z.-Q. Pang, B. Jiang, J. Xiao, C. Zhong, B.-X. Mi, Q.-L. Fan, W. Huang, Thickness Dependence of Carrier Mobility and the Interface Trap Free Energy Investigated by Impedance Spectroscopy in Organic Semiconductors, J. Phys. Chem. C. 120 (2016) 17184–17189. doi:10.1021/acs.jpcc.6b03964.

[45] Y. Shen, M.W. Klein, D.B. Jacobs, J. Campbell Scott, G.G. Malliaras, Mobility-dependent charge injection into an organic semiconductor, Phys. Rev. Lett. 86 (2001) 3867–3870. doi:10.1103/PhysRevLett.86.3867.

[46] T. Wang, A.J. Pearson, A.D.F. Dunbar, P.A. Staniec, D.C. Watters, D. Coles, H. Yi, A. Iraqi, D.G. Lidzey, R.A.L. Jones, Competition between substrate-mediated π - π stacking and surface-mediated Tg depression in ultrathin conjugated polymer films, Eur. Phys. J. E. 35 (2012) 2–7. doi:10.1140/epje/i2012-12129-3.

[47] D. Liu, R. Osuna Orozco, T. Wang, Deviations of the glass transition temperature in amorphous conjugated polymer thin films, Phys. Rev. E. 88 (2013) 022601. doi:10.1103/PhysRevE.88.022601.

[48] R. Noriega, J. Rivnay, K. Vandewal, F.P. V Koch, N. Stingelin, P. Smith, M.F. Toney, A. Salleo, A general relationship between disorder, aggregation and charge transport in conjugated polymers, Nat. Mater. 12 (2013) 1038–1044. doi:10.1038/nmat3722.

[49] M.A. Baldo, S.R. Forrest, Interface-limited injection in amorphous organic semiconductors, Phys. Rev. B - Condens. Matter Mater. Phys. 64 (2001) 1–17. doi:10.1103/PhysRevB.64.085201.

[50] J.L. Keddie, R.A.L. Jones, R.A. Cory, Size-Dependent Depression of the Glass Transition Temperature in Polymer Films, Europhys. Lett. 27 (1994) 59–64. doi:10.1209/0295-5075/27/1/011.

[51] M.J. Harding, D. Poplavskyy, V.E. Choong, F. So, A.J. Campbell, Variations in hole injection due to fast and slow interfacial traps in polymer light-emitting diodes with interlayers, Adv. Funct. Mater. 20 (2010) 119–130. doi:10.1002/adfm.200900352.

# Chapter 7

# Ultrasonic Spray Cast Polymer OLEDs

## 7.1: Introduction

Organic light-emitting diodes (OLEDs) have the potential to be the next generation of solid-state lighting, screens and flexible displays.[1–3] OLEDs can be produced via solution processing which holds great potential in terms of increasing fabrication scale, speed and reducing cost. In order for solution processed OLEDs to realise their potential in bringing cost savings to high output OLED fabrication it is necessary to demonstrate their viability with scalable, industrially applicable deposition techniques. Ultrasonic spray coating, a promising roll-to-roll compatible deposition technique has previously been employed for the fabrication of polymer solar cells,[4–8] small molecule OLEDs [9–11] and for the deposition of the emissive layer of a polymer OLED.[12] In this chapter ultrasonic spray coating is used to deposit thin polymer films for the hole-injection layer (HIL), emissive layer (EML) and electron-injection layer (EIL) in separate polymer OLEDs. Furthermore white-light-emitting polymer OLEDs are fabricated in which the HIL and EML are sequentially spray cast, which to my knowledge of the literature is the first example of a multilayer ultrasonic spray cast polymer OLED, which are comparable in performance to spin cast references. In addition promising initial attempts are made to fabricate a large-area multilayer ultrasonic spray cast polymer OLEDs.

## 7.2: Spray Cast Hole-Injection Layer

PEDOT:PSS is a highly versatile material which has been used for a wide range of applications from work function modification to an anti-static coating.[13,14] The good electrical conductivity, high optical transparency and low thermal conductivity

of PEDOT:PSS has led to it becoming a commonly used material in optoelectronic devices.[13–15] The material properties, comparative low cost and ability to process from solution has led PEDOT:PSS to be used as a transparent electrode or hole-transporting layer in OLEDs, photovoltaics and transistors.[13–15] In lab-scale devices PEDOT:PSS is typically deposited via spin coating from an aqueous solution to form a hole-injection or -transport layer. The high surface tension of the PEDOT:PSS solution, which can be demonstrated by measuring the contact angle Figure 7.1), is not an issue when depositing using spin coating as the large shear forces acting on the wet film spread it uniformly across the substrate.

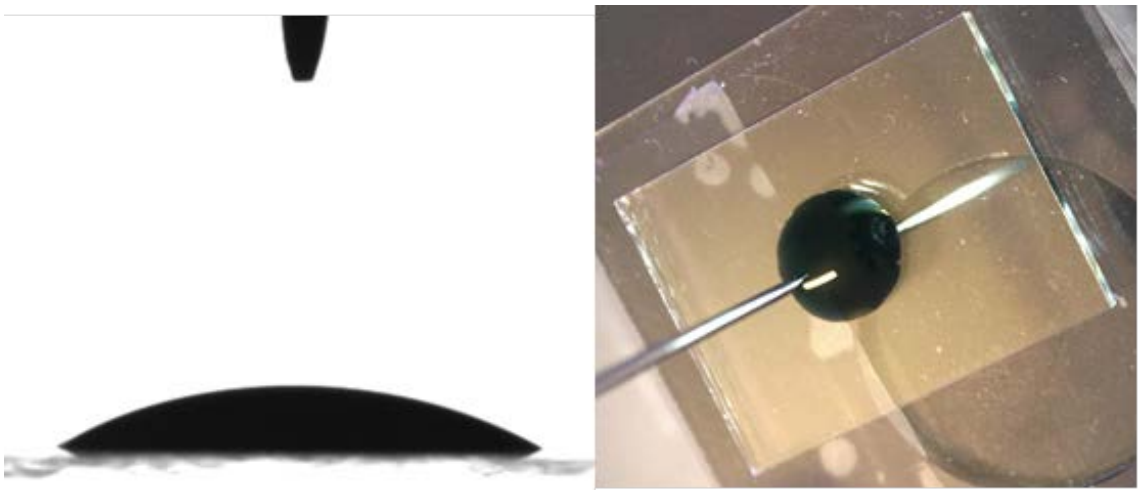

*Figure 7. 1: a) A contact angle image of PEDOT:PSS on an ITO substrate taken 5 seconds after deposition at 20 °C. The droplet of PEDOT:PSS settled to have a contact angle of 31°. b) An image from above of the same droplet of PEDOT:PSS, small black droplet in the centre of the image, on an ITO substrate taken 5 seconds after deposition (the large ring below the substrate is the linkam stage below the substrate).*

However, the reliance of the spreading and merging of multiple droplets to form a uniform wet film in the absence of such shear forces when spray coating presents an issue with such a high surface tension solution. To counter this problem when depositing PEDOT:PSS via spray coating researchers have investigated a range of solvent blends and additives to fabricate uniform thin films. Initial attempts to deposit PEDOT:PSS as a hole-transporting layer via airbrush and ultrasonic spray coating were promising but there were still issues with non-uniformity.[5,16–18]

Tait et al. built on the work in the field and used a blend of PEDOT:PSS, deionised water (DI), Isopropyl Alcohol (IPA) and Ethylene Glycol (EG) to deposit high conductivity PEDOT:PSS electrodes via ultrasonic spray coating for organic solar cells.[19] The films were deposited using a multi-pass technique which can cause a reduction uniformity and performance of polymer films, also the films were submerged in EG for 30 minutes post-deposition to increase conductivity, a potential issue for high throughput.[5,20] Scarratt et al. using a 1:8:1 blend of (PEDOT:PSS) : IPA : EG sprayed single pass large-area uniform films for the hole-transport layer in an organic solar cell. In this section I base my work on the ink formulation introduced by Scarratt et al. to deposit a uniform spray cast PEDOT:PSS film as the hole-injection layer in an OLED.[7]

As seen in Figure 7.1 the high surface tension of PEDOT:PSS is shown by a high contact angle (31°) and the inability to spread over the entire ITO substrate. IPA is known to have a low surface tension (23 mN $m^{-1}$ at 20 °C in comparison water = 72.8 mN $m^{-1}$) as such the addition of IPA to the ink will decrease the surface tension, helping the solution to spread across the ITO substrate. Figure 7.2 shows how with the addition of IPA a single droplet spreads across the substrate (300 $mm^2$) and the tensiometer struggles to accurately measure the small contact angle less than 1 s after initial deposition.

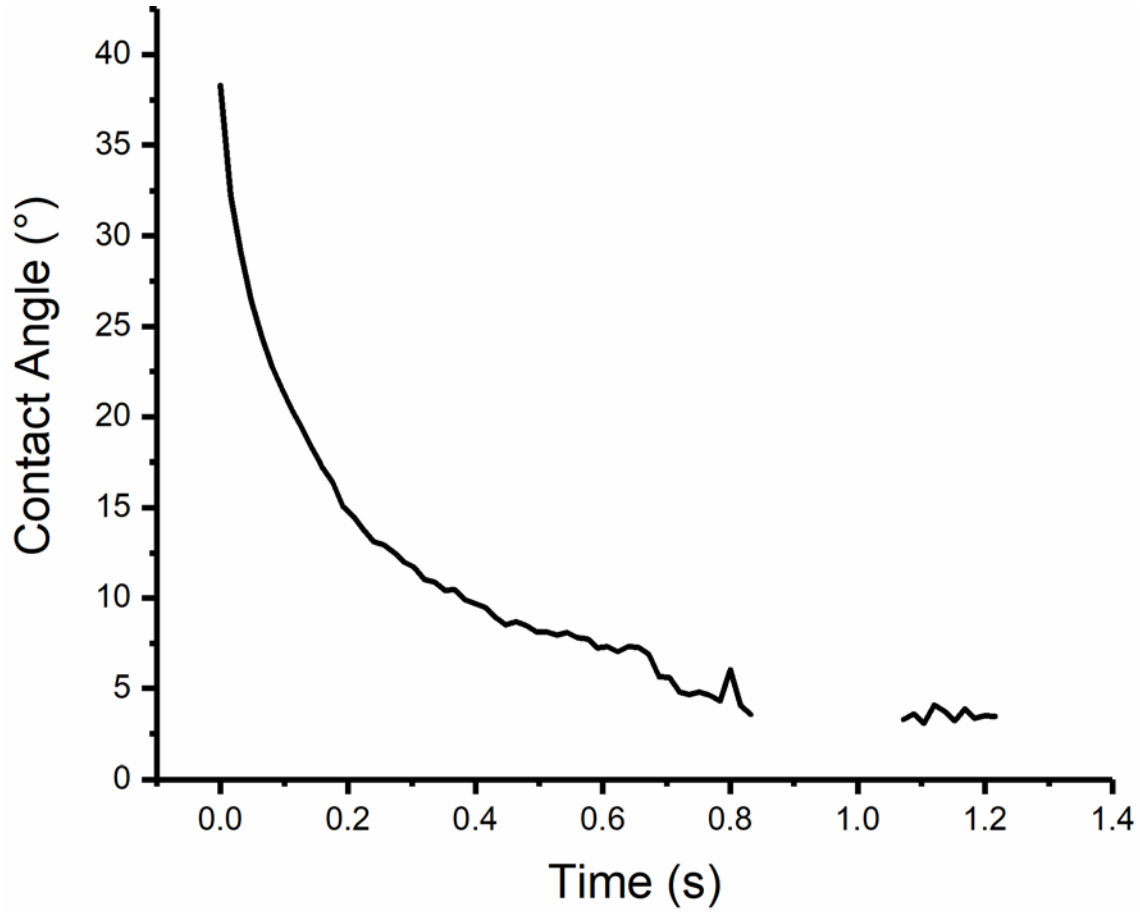


*Figure 7. 2: Contact angle measurement of a droplet of PEDOT:PSS ink with the ratio 2:7 (PEDOT:PSS to IPA) on an ITO substrate at 20 °C.*

As discussed in by others in the field the addition of IPA to PEDOT:PSS whilst improving the wetting of the ink after the low boiling point IPA evaporates there is a thin film of water containing PEDOT:PSS, this solution can partially de-wet before drying causing holes in the final film.[5]

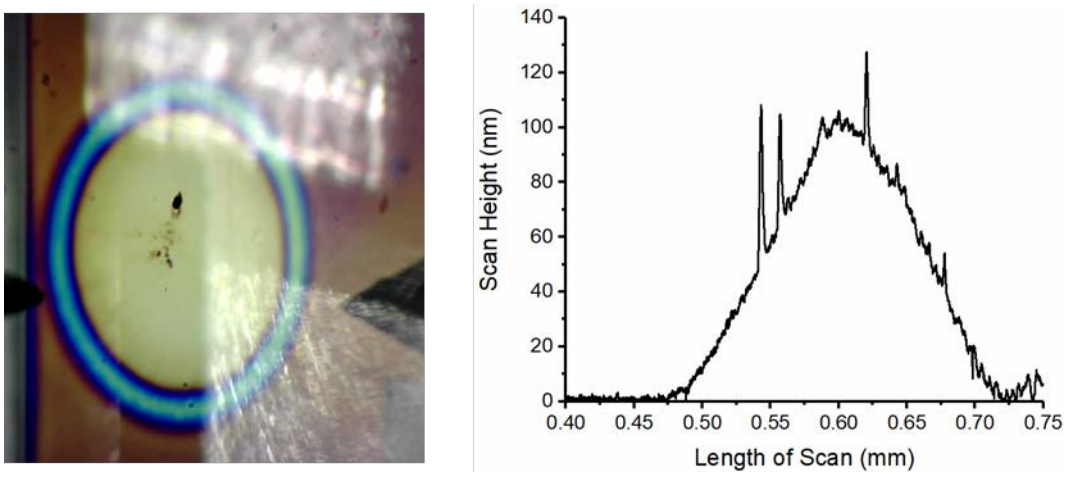


*Figure 7. 3: a) An image through a 10 times objective lens of an area of a spray cast PEDOT:PSS film demonstrating the reticulation of the film. b) A dektak line scan from the centre of the reticulated area, in which the PEDOT:PSS has entirely dewetted, across the thick outer ring.*

In order to limit the reticulation and increase the processing window a small volume of Ethylene Glycol is added to the mixture to form a tertiary blend of PEDOT:PSS, IPA, EG in the ratio 2:7:1.

| Solvent | Boiling point (°C) | Surface tension at 20 °C (mN $m^{-1}$) |
|---|---|---|
| **Water** | 100 | 72.8 |
| **IPA** | 82.6 | 23 |
| **EG** | 197 | 47.7 |

*Table 7. 1: The key parameters of the solvents used in the 2:7:1 PEDOT:PSS ink.*

As shown in Table 7.1 EG has a significantly higher boiling point than water and IPA as such once a droplet of the ink has spread the IPA rapidly evaporates leaving a thin film of PEDOT:PSS in a mixture of water and EG. The lower surface tension of EG compared to water stops the solution from dewetting as readily allowing a time window in which the substrate can be transferred to a high temperature hotplate (140 °C). Once transferred to a high temperature hotplate the remaining water then EG quickly evaporates leaving a dry uniform film of PEDOT:PSS.

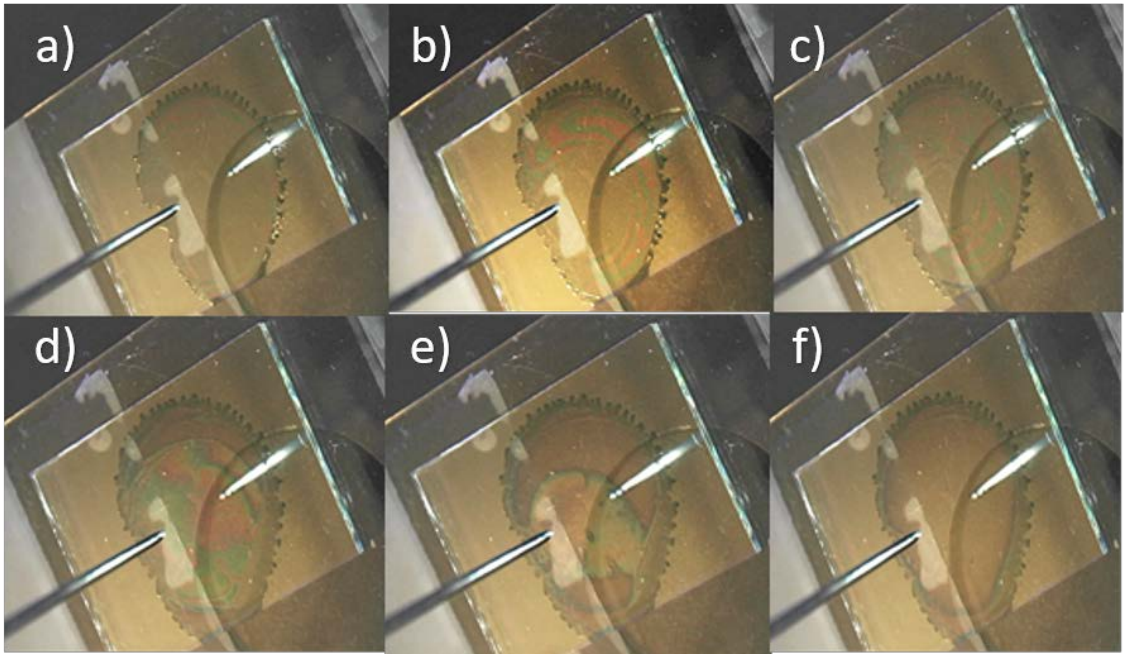


*Figure 7. 4: Images from a) through to f) showing the drying stages of the 2:7:1 PEDOT:PSS ink on and ITO substrate held at 20 °C. a) shows a droplet of solution which has spread across the substrate and the IPA component of the ink has evaporated, b) and c) show the drying front as the water component of the ink evaporates. Later the high boiling point ethylene glycol evaporates in d) and e) leaving the dry PEDOT:PSS film in f).*

Figure 7.4 shows the drying process of the 2:7:1 PEDOT:PSS ink when held at a constant temperature (20 °C). In the first image (a) the droplet has spread and the IPA has evaporated. In the second and third images (b and c) a drying front encroaches towards the centre of the substrate as the water evaporates. As further time passes in the fourth and fifth images (d and e) you can see the EG drying front and a dry PEDOT:PSS films in the final image (f).

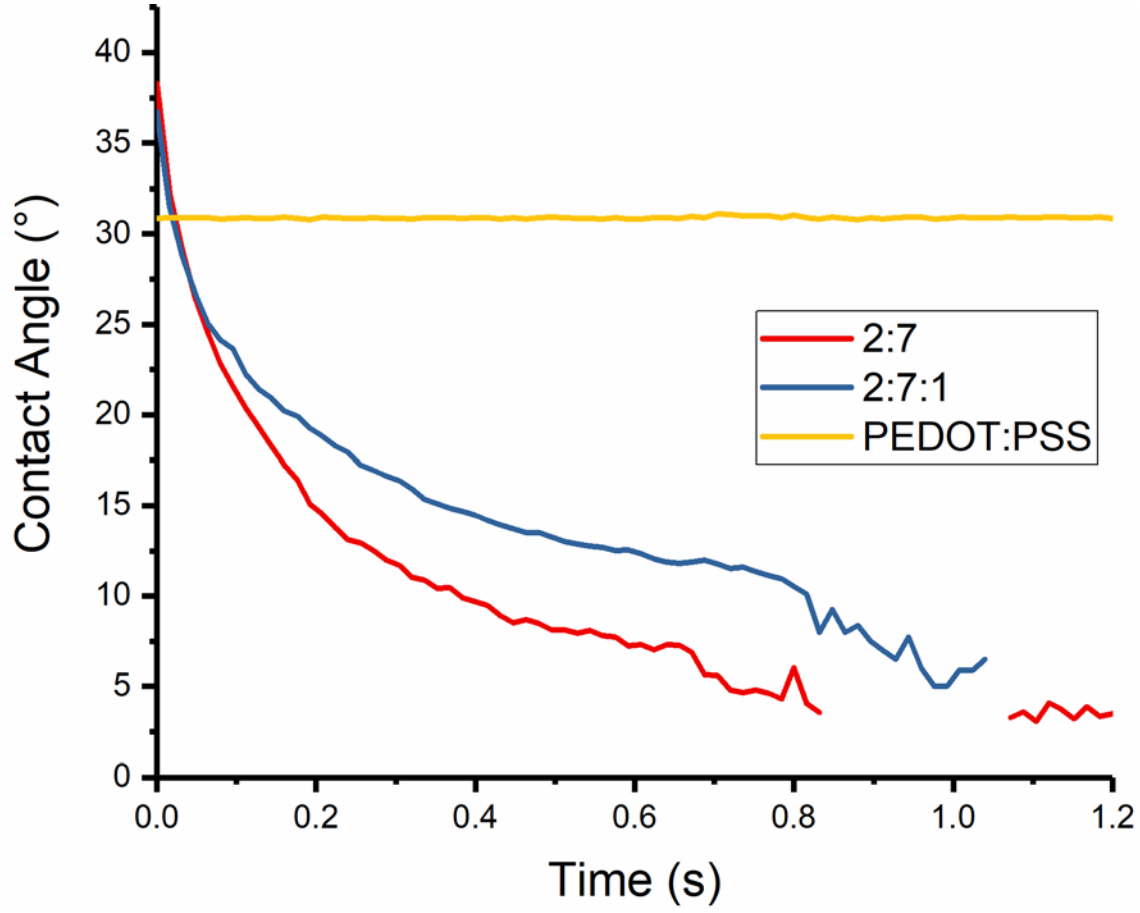


*Figure 7. 5: A graph comparing the wetting of the different PEDOT:PSS inks (PEDOT:PSS as purchased, 2:7 PEDOT:PSS to IPA and 2:7:1 PEDOT:PSS to IPA to EG) to ITO by comparing the contact angle overtime.*

Figure 7.5 demonstrates the contact angle of a drop of PEDOT:PSS on ITO, the drop after settling on the substrate doesn't spread, displaying poor wetting with a high contact angle (31°). The addition of IPA to PEDOT:PSS causes the drop to spread well as it settles on the surface due to the lower surface tension of the solution leading to a much lower contact angle, so low the system struggles to measure it around a second after the drop landed on the substrate. Although the addition of EG increases the surface tension of the ink, as demonstrated by the higher contact angle when compared to the PEDOT:PSS/IPA blend yet it still wets very well to the substrate.

### 7.2.1: Optimisation of Spray Coating Parameters

PEDOT:PSS films were deposited via spray coating from a 2:7:1 PEDOT:PSS, IPA, EG ink. The spray coater base plate temperature (20 °C), fluid flow pressure (50 mbar)

and shaping gas pressure (30 psi) were all kept constant whilst the head pass speed and height were varied to produce a range of thickness and to optimise film uniformity. The process of transferring the wet PEDOT:PSS film to a high temperature hotplate (140 °C) prior to annealing the films at 120 °C for 10 minutes is probed by varying the time the substrate is left on the initial hotplate. Figure 7.6 shows images of spray cast films deposited at a range of head pass speeds from 10 – 70 mm $s^{-1}$ whilst the height was kept constant at 30 mm.

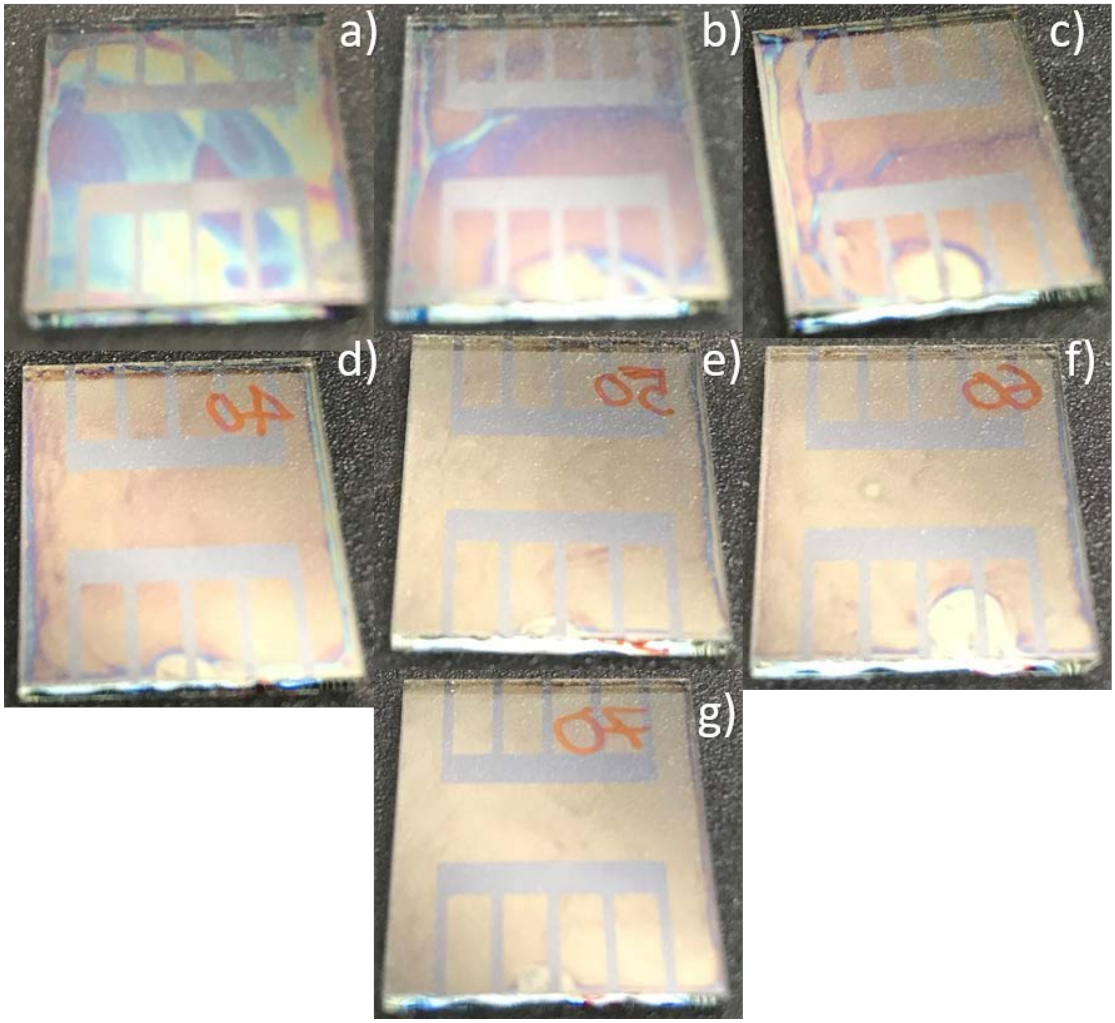


*Figure 7. 6: Images showing the varying film uniformity of PEDOT:PSS deposited via spray coating at a fixed height 30 mm and at a head pass speeds a) 10, b) 20, c) 30, d) 40, e) 50, f) 60 and g) 70 mm $s^{-1}$. The gap on the edge on most of the films is due to material being removed by the tweezers when transferring the wet film to the high temperature hotplate.*

The films deposited at spray speeds from 10 – 20 mm $s^{-1}$ have large variations in thickness across the substrate, varying from 83 – 154 nm for 10 mm $s^{-1}$ and 54 – 90 nm for the film sprayed at 20 mm $s^{-1}$. The large volume of solution deposited under these spray parameters leads to non-uniformity as when the IPA has evaporated and as the substrate is transferred to the high temperature hotplate the wet film can flow. Secondly, the drying time of the wet film is increased due to the large volume of solution on the substrate as such effects like pooling or even dewetting can occur. The film sprayed at 30 mm $s^{-1}$ has large areas which are uniform but still has an area in the central region in which slight pooling has occurred, the thickness of this film varied from 38 – 50 nm. The pooling seen in this film could be reduced by decreasing the transfer time to the high temperature hotplate or by a slight reduction in volume deposited. The film sprayed at 40 mm $s^{-1}$ is highly uniform across the surface of the substrate which the thickness varying from 30 – 33 nm. Figure 7.7 shows a dektak surface map scan of this film which has a low root-mean-square (rms) roughness of 2.14 nm.

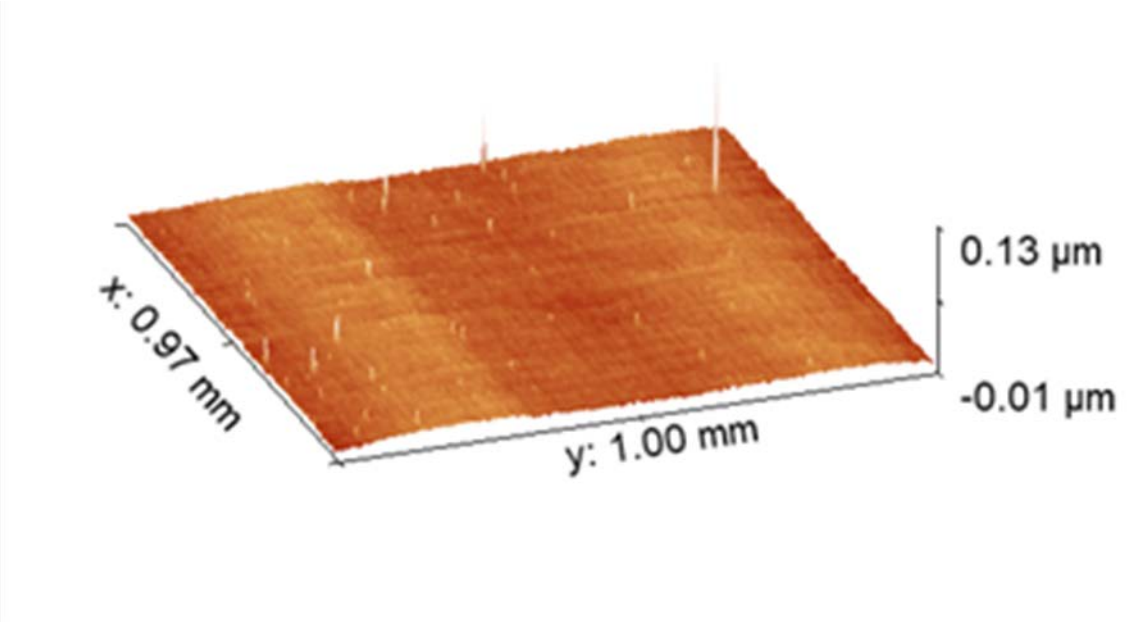


*Figure 7. 7: A 0.97 by 1 mm dektak surface map scan of a PEDOT:PSS deposited with a spray pass speed of 40 mm $s^{-1}$ at a height 30 mm. The film has an rms roughness of 2.14 nm. The large spikes seen in the image are artefacts/noise recorded during the measurement and are not real features of the film.*

The films sprayed from 50 – 70 mm $s^{-1}$ may look relatively uniform but they have increasing amounts of mottling and coffee stains as deposition speed increases due to the low volume of solution deposited not allowing the initial wet film to spread and level prior to the evaporation of the IPA. This non-uniformity is reflected in the variation in thickness of the film sprayed at 70 mm $s^{-1}$, the thickness varies ± 17 % from the average thickness compared to ± less than 5 % for the film sprayed at 40 mm $s^{-1}$. Further to this point in the film sprayed at 60 mm $s^{-1}$ there is a hole where the film has not completely formed before the initial drying step.

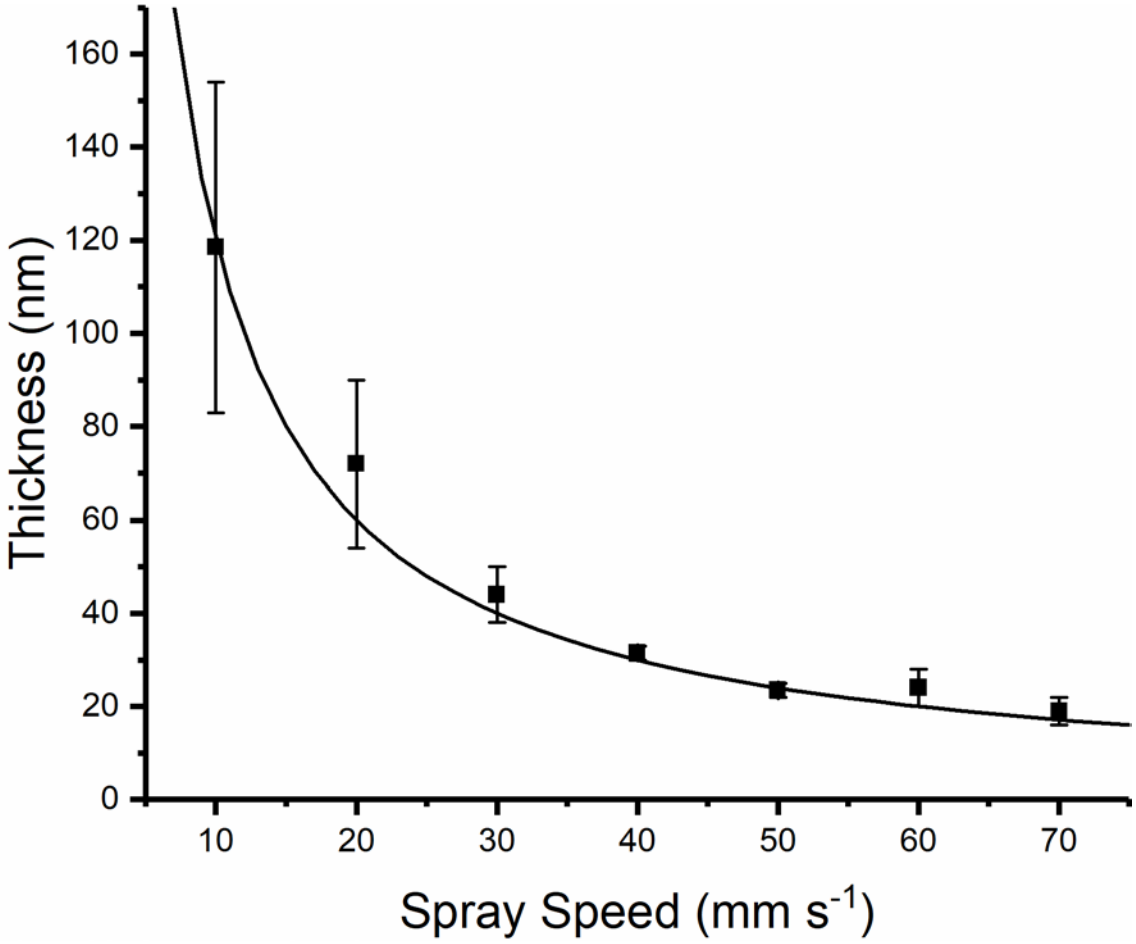


*Figure 7. 8: A graph of the thickness of PEDOT:PSS films as a function of the deposited spray speed. The height was fixed at 30 mm, the base plate temperature was fixed at 20 °C.*

The thickness as a function of spray speed from 10 – 70 mm $s^{-1}$ is plotted in Figure 7.8, a line is fitted to the data and shows that the thickness of PEDOT:PSS is inversely proportional to spray speed.

Figure 7.9 shows images of spray cast films deposited at a range of head pass heights from 10 – 70 mm whilst the speed was kept constant at 40 mm $s^{-1}$.

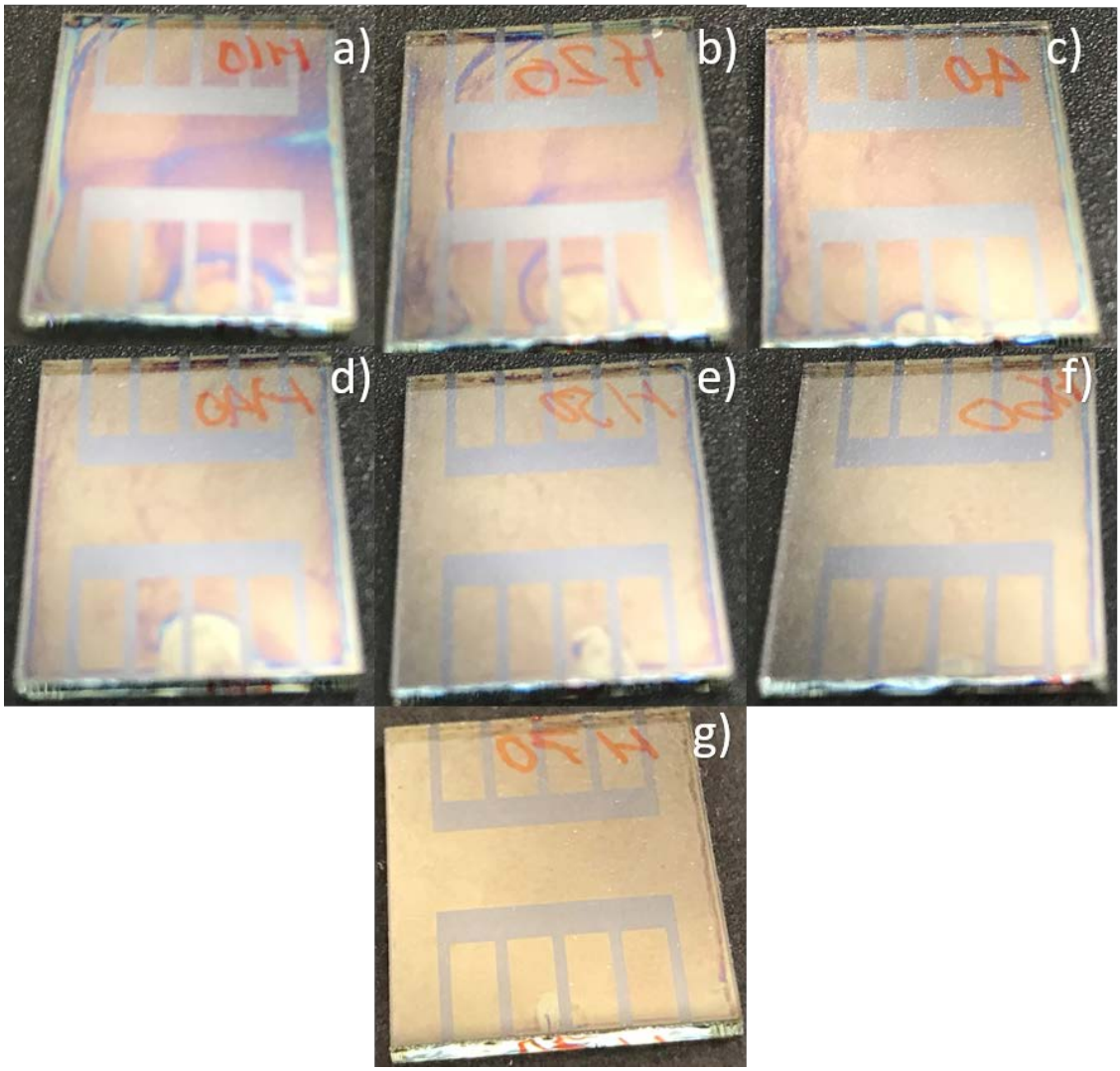


*Figure 7. 9: Images showing the varying film uniformity of PEDOT:PSS deposited via spray coating at a fixed pass speed 40 mm $s^{-1}$ and at head pass heights of a) 10, b) 20, c) 30, d) 40, e) 50, f) 60 and g) 70 mm. The gap on the edge on some of the films is due to material being removed by the tweezers when transferring the wet film to the high temperature hotplate.*

The films deposited at spray heights from 10 – 20 mm have large variations in thickness across the substrate, varying from 50 – 123 nm for 10 mm and 33 – 71 nm for the film sprayed at 20 mm. Similarly to the low pass speeds described above the large volume of solution deposited under these spray parameters leads to non-uniformity as when the IPA has evaporated and as the substrate is transferred to the high temperature hotplate the wet film can flow. Secondly, the drying time of the wet film is increased due to the large volume of solution on the substrate as such effects like pooling or even dewetting can occur. The film sprayed at a pass height of 30 mm was discussed in the previous section and is highly uniform (30 – 33 nm).

The films sprayed at 40 – 70 mm pass height have mottling and coffee stains as due to the low volume of solution deposited not allowing the initial wet film to spread and level prior to the evaporation of the IPA. Figure 7.10 plots the thickness variation of the PEDOT:PSS as the spray pass height increases from 10 – 70 mm. There seems to be a narrow processing window for this PEDOT:PSS ink to form uniform films when varying height compared to varying speed, with only films cast at a height of 30 mm having a thickness variation less than ± 20 % of the average film thickness in this experiment.

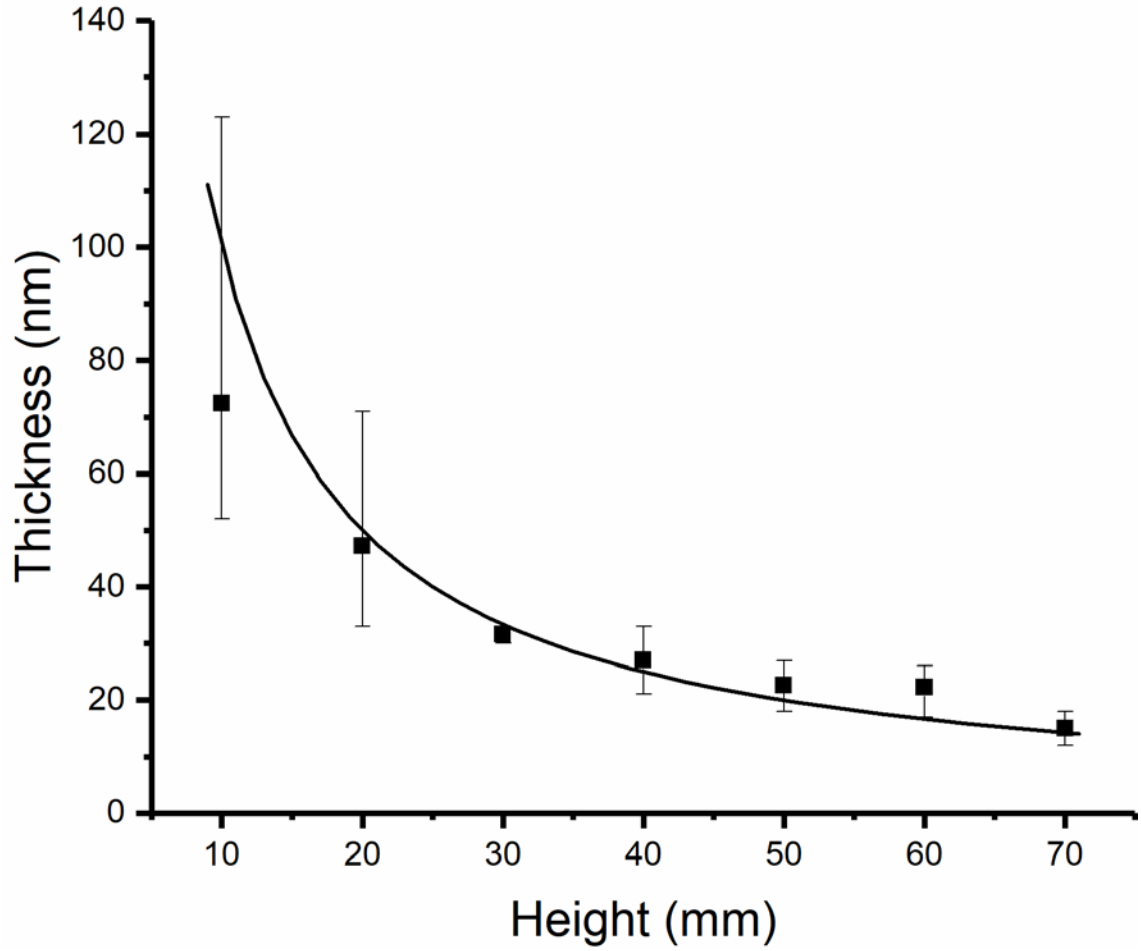


*Figure 7. 10: A graph of the thickness of PEDOT:PSS films as a function of the deposited spray pass height. The spray pass speed was fixed at 40 mm $s^{-1}$, the base plate temperature was fixed at 20 °C. A line is fitted showing that there is an inverse relationship between thickness and spray height.*

To further probe the sensitivity of the 2:7:1 PEDOT:PSS ink spray coating process three films were sprayed with identical parameters (H = 30 mm, S = 40 mm $s^{-1}$, T = 20 °C, fluid flow pressure = 50 mbar) but left for different periods of time before transferring from the low temperature hotplate to the high temperature hotplate.

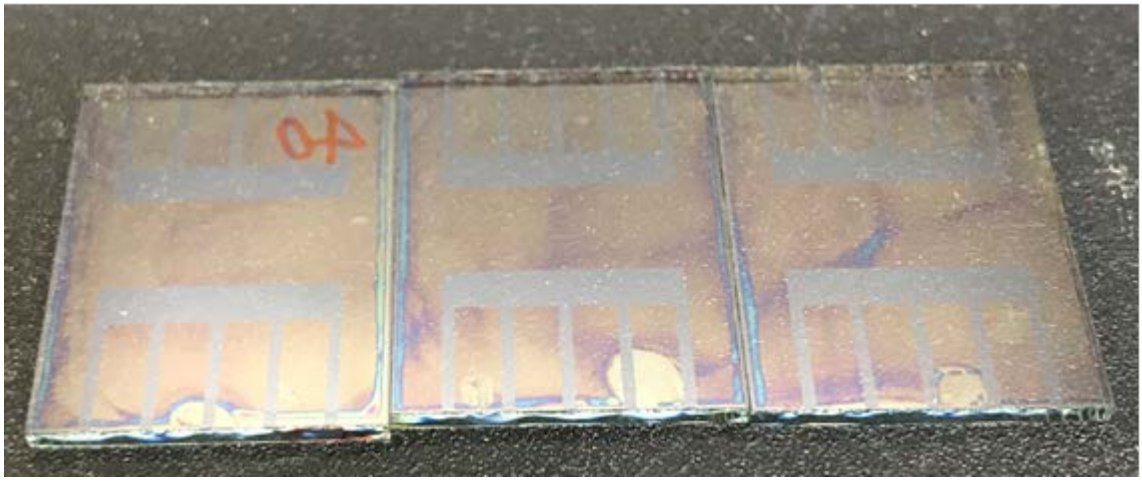

*Figure 7. 11: Image of three films of spray-cast PEDOT:PSS with varying wait times prior to transferring from the base plate hotplate to the high temperature hotplate. LHS wait time = 0 s, centre = 3 s, RHS = 5 s.*

The left-most film in Figure 7.11 was transferred from the low temperature hotplate immediately after the spraying process finished, when the spray head had returned to the parked position. The central film was left for 3 s and the right-most film was left for 5 s. The thickness across the left-most film varies from 30-33 nm, the central film varies from 30 – 40 nm and the right-most film from 30 – 55 nm. The addition of ethylene glycol to the PEDOT:PSS ink aids in the formation of uniform films but it is highly time sensitive due to the high surface tension of the water content remaining in the ink. Although the left-most film is removed from the spray coater and placed on a high temperature hotplate as fast as possible there are still delays in this manual process. The spray coater takes 1 – 2 s after passing over the substrate to park the head and allow the doors to be unlocked and the transferring process takes in the region of 3 s. In a fully industrial process the substrate would be on a moving track or stage that would make the transferring process far quicker and more controlled than in this work, improving the repeatability and control of surface morphology.

### 7.2.2: Spray Cast PEDOT:PSS Devices

The device architecture and fabrication used in this chapter is described in Chapter 3. Based on the process and optimisation discussed in the prior section the

PEDOT:PSS was deposited from a 2:7:1 ink of PEDOT:PSS to IPA to EG, at a pass speed of 32 mm $s^{-1}$ and height of 30 mm. These parameters were chosen to in order to match the thickness of the spray cast films with the reference spin cast films of 40 ± 3 nm. The active layer was spin cast from a 12 mg $ml^{-1}$ p-Xylene solution to achieve an active layer thickness of 65 ± 3 nm. The devices were completed by evaporating a 3 nm lithium fluoride (LiF) electron-injection layer and a 100 nm Aluminium electrode via thermal evaporation under high vacuum prior to encapsulation using a glass slide and UV curable epoxy.

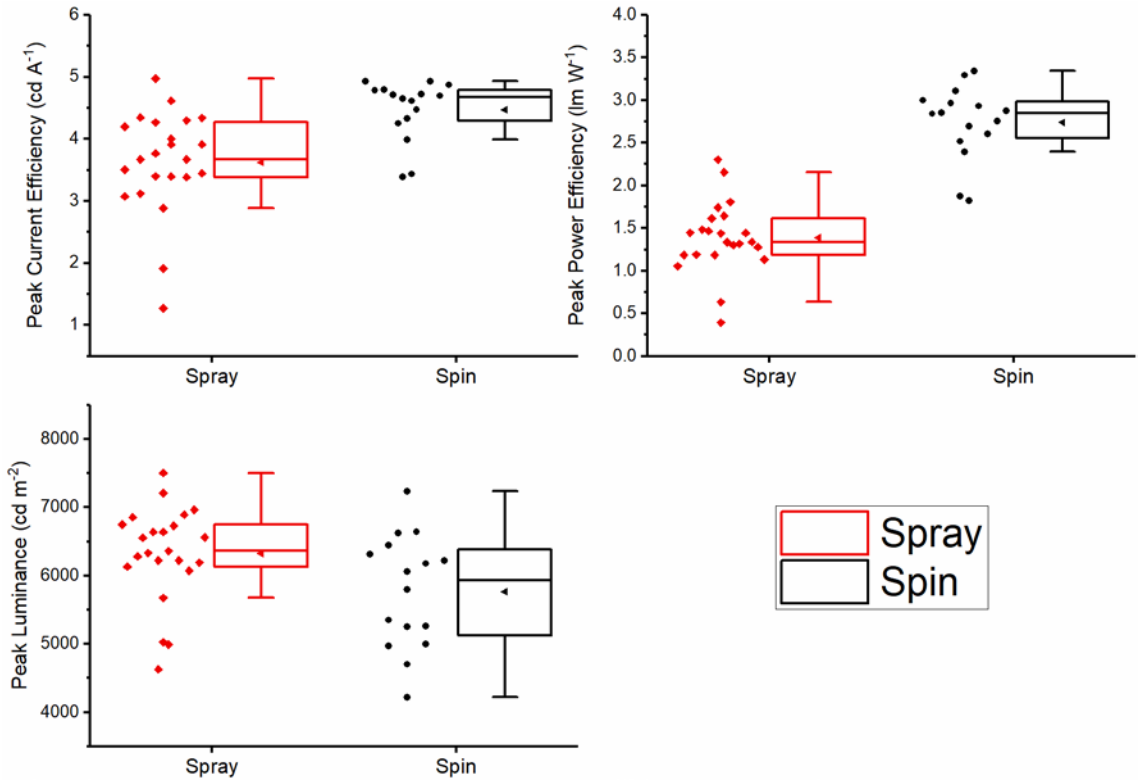


*Figure 7. 12: Box charts comparing the key device testing metrics; a) peak current efficiency, b) peak power efficiency, c) Peak luminance for devices with spin cast and spray cast PEDOT:PSS.*

Figure 7.12 compares the performance of devices with spray cast and spin cast PEDOT:PSS. The mean current and power efficiencies of the spray cast devices, 3.63 cd $A^{-1}$ and 1.39 Lm $W^{-1}$, are lower than the metrics for spin cast devices 4.47 cd $A^{-1}$ and 2.74 Lm $W^{-1}$. Whereas the mean peak luminance of the devices deposited by the two techniques are similar with 6325 cd $m^{-2}$ for spray cast devices slightly higher

than 5766 cd $m^{-2}$ for spin cast devices. The decrease in efficiency metrics can be explained by the addition of EG in the spray cast PEDOT:PSS ink. Studies have shown that the addition of EG to PEDOT:PSS causes a change of conformation of the PEDOT:PSS chains this increases the charge carrier mobility and thus conductivity of the film.[21,22] Typically an increase in conductivity would be beneficial for device performance but the increase in lateral conductivity combined with the device architecture causes a negative contribution to the current from outside of the defined pixel area. Figure 7.13 shows a cross section of the device stack, the pixel area is defined by the region in which there is a full device stack, where the evaporated to electrode overlaps the central ITO pad on the substrate (between red lines).

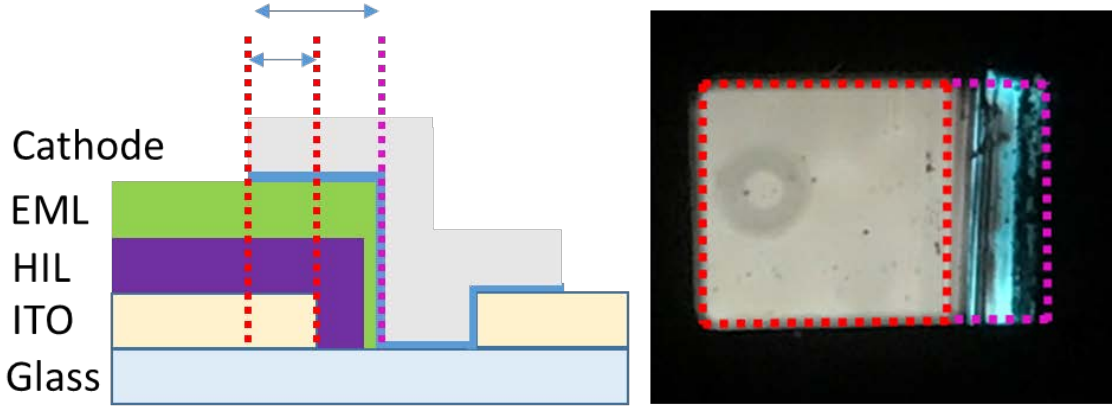


*Figure 7. 13: a) A schematic cross section of the device stack. The device area is defined by the overlap of all layers (between the red lines). Between the left-most line and the purple line shows the area in which all layers are present except for the ITO bottom contact. b) A top down view of a pixel with spray-cast PEDOT:PSS showing the defined pixel area (red lines) and the contribution from outside the typical pixel area (purple lines).*

The increased lateral conductivity of the spray cast PEDOT:PSS leads to the pixel area extending beyond the ITO pad to anywhere the PEDOT:PSS hasn't been fully removed in the swabbing process (red line to purple line). The effect of this lateral current leakage in the spray-cast devices is most obvious in the low voltage regime, just as the device is turning on, this contributes to the large difference in peak power

efficiency. Increasing the applied voltage increases the electric field between the electrodes within the device and the vertical current in the defined pixel area begins to dominate as such the luminance and efficiencies of the spin and spray-cast devices are very similar at high voltages. Figure 7.14 shows the data from a spray cast pixel in which the swab was close to the edge of the ITO compared to a typical spin cast pixel, all the metrics are very similar above 7 V.

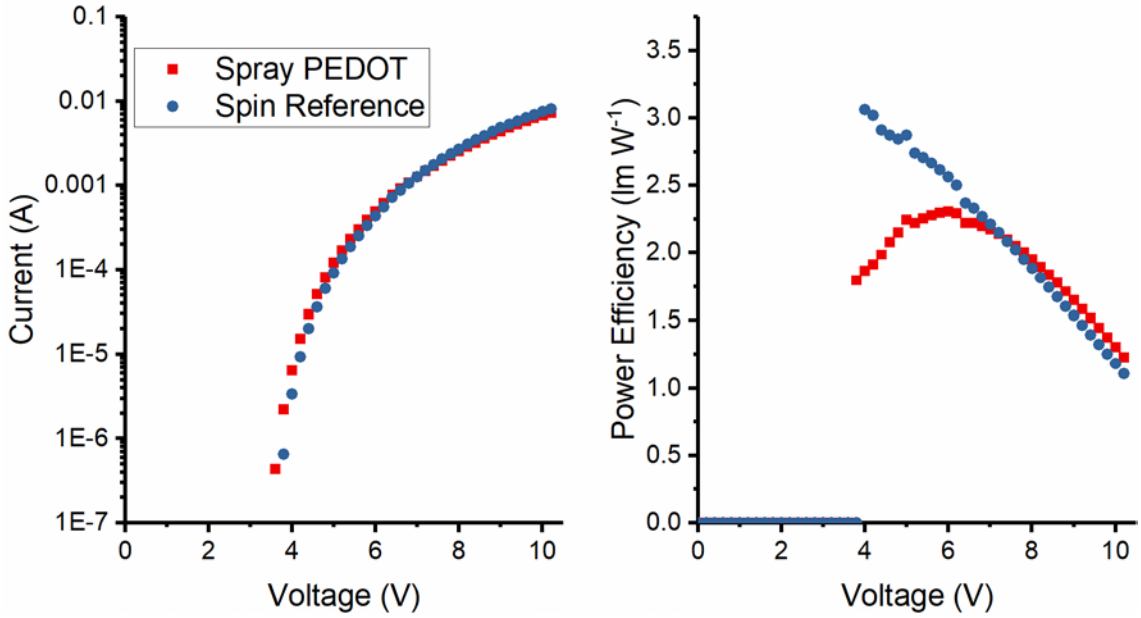


*Figure 7. 14: a) The current against voltage for a spray cast pixel with very closely swabbed PEDOT:PSS layer compared to a spin cast reference. b) The power efficiency against voltage for a spray cast pixel with closely swabbed PEDOT:PSS layer compared to a spin cast reference.*

Figure 7. 14 demonstrates that if the devices with spray cast PEDOT:PSS could be patterned with greater precision, so that only the area where the complete stack remains is the pixel, then the spray cast and spin cast device performance would be equivalent. Laser ablation of layers is a potential high-speed scalable route to increased patterning precision.

## 7.3: Spray Cast Emissive Layer

In this section the ultrasonic spray coating technique is used as an alternate solution deposition technique for the light-emitting layer of a polymer light-emitting diode

(PLED). Devices are processed in ambient conditions and a comparison is made between spin and spray cast devices. Uniform films are achieved by probing different solvents, concentrations and spray coating parameters. White-light-emitting PLEDs are fabricated with an average peak current efficiency of 4.93 cd $A^{-1}$, 90% of the value of the spin cast reference devices.

Devices in this section were fabricated using pre-patterned 8 pixel ITO substrates with a sheet resistance of 20 Ω $square^{-1}$ and an rms roughness of 1.8 nm (determined by AFM) purchased from Ossila Ltd. The ITO substrates were cleaned following the protocol laid out in Chapter 3. Al 4083 grade PEDOT:PSS was purchased from Ossila Ltd and was filtered using a 0.45 µm PVDF mircodisc filter prior to spin coating at 5000 rpm to yield a 40 ± 3 nm film. The PEDOT:PSS films were annealed on a hotplate, in air at 120 °C for 15 mins and then cooled to room temperature prior to deposition of further layers. The white-light-emitting polymer (LEP) was spray cast from a number of solvents under different spray parameters which will be discussed in detail later in this section. The spin coated reference devices were cast in ambient conditions from a 12 mg $ml^{-1}$ p-Xylene solution at a number of different spin speeds to obtain a range of thicknesses.

The layers over the ITO contacts were swabbed using p-Xylene to pattern the device and the films were annealed at 100 °C for 10 minutes to remove any residual solvent. A bilayer top electrode of 3 nm Lithium fluoride (LiF) and 100 nm Aluminium was thermally evaporated at a vacuum pressure of $4x10^{-6}$ mbar through a mask to define a pixel area of 4 $mm^2$. After the deposition of the top electrode the devices were encapsulated in an inert atmosphere (<1 ppm H2O and <1 ppm O2) using UV-curable epoxy and a glass slide. External electrical connection to the devices were gained via push-fit Ossila testing board, spring loaded gold pins make contact to the ITO pad and ITO fingers.

Initial attempts were made to spray coat the emissive polymer from commonly used solvent p-Xylene. Although individual pixels could have good efficiency and brightness there were large variations in these metrics from pixel-to-pixel across a device. The device performance is very sensitive to the thickness of the emissive

layer as such non-uniformity in the films cast from p-Xylene caused poor pixel-to-pixel repeatability.

The development of the multi-component PEDOT:PSS spray coating ink in Section 7.1 demonstrated the importance of the solvent properties as well as spray parameters when depositing films via spray coating. The addition of low boiling IPA to aid wetting of the suspension of PEDOT:PSS in water, the high boiling point EG to slow down the reticulation of the solution after the IPA evaporates. Based on this knowledge and after probing the solubility of the LEP in a range of potential solvents chloroform and mesitylene were found to have promising properties to use as a blend for depositing the LEP. Table 7.2 shows some of the solvent properties of chloroform, mesitylene and water for reference.

| Solvent | Surface Tension (mN $m^{-1}$) | Viscosity (mPa s) | Boiling Point (°C) |
|---|---|---|---|
| **Water** | 72.8 | 1.002 | 100 |
| **Chloroform** | 27.1 | 0.563 | 61 |
| **Mesitylene** | 28.84 | 0.727 | 164.7 |

*Table 7. 2: Compares the solvent parameters of chloroform, mesitylene and water. The surface tension and viscosity are measured at 20 °C.*

The low surface tension and low viscosity suggests chloroform is an ideal solvent for wetting and spreading across a substrate when deposited via spray coating. However, with such a low boiling point if used as a single solvent for spray coating the chloroform may evaporate before the droplets merge and form a wet film as such the processing window for chloroform is too narrow to use on its own.

Mesitylene has a similar surface tension to chloroform but a significantly higher viscosity and boiling point. This suggests if sprayed as a single solvent at a similar temperature in which chloroform could spread before evaporating then the vastly longer drying time of mesitylene would likely lead to pooling and non-uniform dry films.

If used in a blend where the majority of the volume is Chloroform with the very low viscosity and low surface tension will allow the solution to wet well and spread

across the substrate prior to the rapid evaporation of chloroform. This will leave a concentrated “gel” of the LEP in mesitylene, the low surface tension will limit any reticulation issues seen after the IPA evaporates when spraying a two part PEDOT:PSS blend. The high concentration of the remaining solution will limit its flow but with the high boiling point the solution will have a long drying time if the base plate temperature is kept low which could allow some levelling prior to evaporation leaving a uniform dry film.

The LEP was dissolved in solvent blends of chloroform and mesitylene at volume ratios from 60:40 to 90:10 (chloroform: mesitylene). Initially the solutions were spray cast at the same base plate temperature (25 °C), concentration (4 mg $ml^{-1}$) and same range of pass heights and speeds to probe film quality. On a macroscopic scale the films formed from and 80:20 volume blend ratio appeared to be highly uniform, films sprayed from blends with 90 % Chloroform formed coffee rings due to the rapid evaporation of the chloroform not allowing the induvial droplets to form a wet film. Films sprayed from blends with 40 % Mesitylene formed uniform wet films but the low base plate temperature the drying time was too long and the wet film pooled. Figure 7. 15 shows films of the WEP spray cast from 4, 5 and 6 mg $ml^{-1}$ solutions with the solvent blend 80:20 (Chloroform : Mesitylene) to vary the thickness of the dry films.

*Figure 7. 15: Picture of films of spray cast LEP from 80:20 solvent blend Chloroform to Mesitylene. The films were deposited at a base plate temperature of 25 °C, pass speed 50 mm $s^{-1}$, pass height 40 mm, fluid pressure 40 mbar and solution concentration of 4, 5 and 6 mg $ml^{-1}$ from left to right. The central film was scratched in order to measure the thickness.*

Although the films sprayed from a solvent blend appeared uniform macroscopically when viewed under 10 times magnification it could be seen the films were made up of many small regions with thicknesses varying by up to 45 nm.

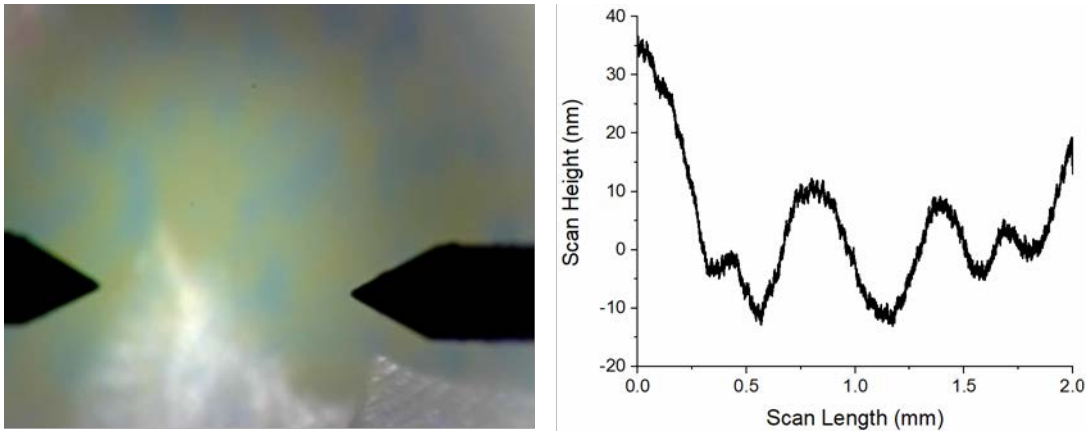


*Figure 7. 16:a) The mottled spray cast blend film pictured through the 10 times optical zoom camera on the dektak XT. b) A 2 mm line scan of the surface pictured.*

Devices were fabricated to observe the effect of the non-uniformity on the device metrics and compared with spin cast reference devices.

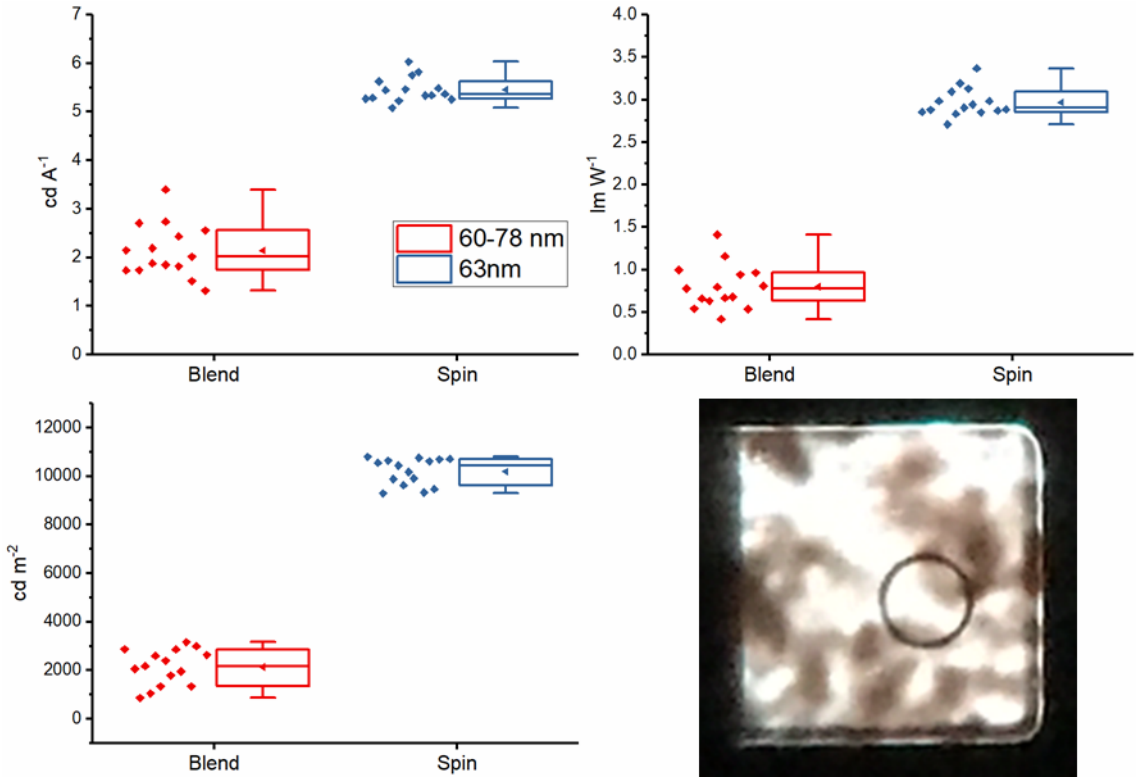


*Figure 7. 17: The key device performance metrics a) peak current efficiency, b) peak power efficiency and c) peak luminance of devices sprayed from 4 mg ml$^{-1}$ 80:20 solvent blend chloroform to mesitylene (60-78 nm) compared with spin cast devices with similar emissive layer thickness (63 ± 3 nm). d) A picture of the emission from a pixel of the spray cast device.*

The mean peak current efficiency of the spray cast blend was 2.14 cd A$^{-1}$ less than half the mean of the spin cast reference 5.45 cd A$^{-1}$. Similarly the mean power efficiency and mean peak luminance of the spray cast blend were less than a third of the spin cast references, 0.80 Lm W$^{-1}$ compared to 2.97 Lm W$^{-1}$ and 2139 cd m$^2$ compared to 10189 cd m$^2$. The image of the emission of a spray cast blend pixel is shown in Figure 7. 17, the non-uniformity of the thickness of the emissive layer is reflected in the thicker regions being much dimmer than the thinner areas.

The non-uniform electroluminescence (EL) from the spray cast blends, despite appearing to be macroscopically uniform, led to a return to spraying from a single

solvent. As discussed earlier the low boiling point of chloroform made it unsuitable for use as a lone solvent for spray coating however the low surface tension of mesitylene suggests it would make a good solvent if the drying time could be controlled. After probing different concentrations, base plate temperatures and spray parameters uniform films of the LEP were spray cast from a 6 mg $ml^{-1}$ solution in mesitylene when cast onto substrates held at 45 °C. Figure 7. 18 shows films cast at under these conditions with spray height 40 mm, fluid pressure 40 mbar and spray speeds 140 mm $s^{-1}$ (films labelled H) and 130 mm $s^{-1}$ (film labelled G). Macroscopically these films appear to be highly uniform but there is still a slight thickness gradient at the edge of the substrate, this could be improved by shortening the drying time fractionally by increasing the base plate temperature by a small amount. The slight pooling is restricted to the right hand side and bottom right corner of the films this suggests there may have been a small tilt to the spray coater base plate causing a flow of the wet film, by correcting this tilt the thicker edges could be removed.

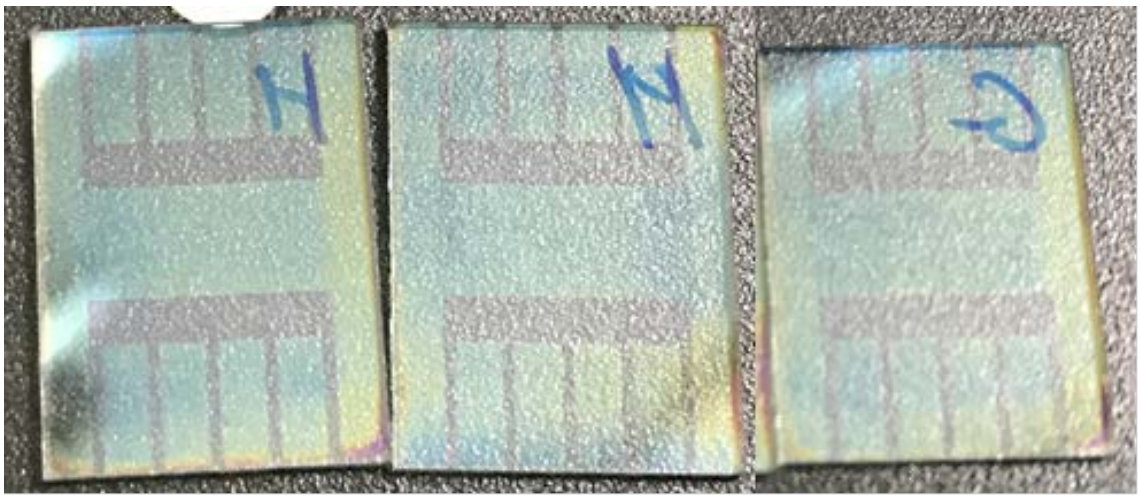


*Figure 7. 18: Films of the LEP deposited via ultrasonic spray coating from 6 mg $ml^{-1}$ mesitylene solution. The films labelled H were spray cast at 140 mm $s^{-1}$ and are measured to be 52 ± 3 nm. The film labelled G was spray cast at 130 mm $s^{-1}$ and is measured to be 65 ± 3 nm.*

The thicknesses of the layers cast at pass speed 130 mm $s^{-1}$ were measured across the substrate to be within a few nm, 65 ± 3 nm, of the optimal spin cast references,

63 nm, as such these films and subsequently the devices fabricated using these films are used to compare between spin coating and ultrasonic spray coating. 1 $mm^2$ surface maps scans of films deposited by spin coating and ultrasonic spray coating were taken using a Bruker DektakXT surface profilometer as shown in Figure 7.19. The root-mean-square (rms) roughness of the spray cast film was calculated from the map scan using Gwydion to be 1.33 nm almost identical to the rms roughness of the spin cast map scan 1.39 nm, demonstrating the high uniformity of the spray cast device.

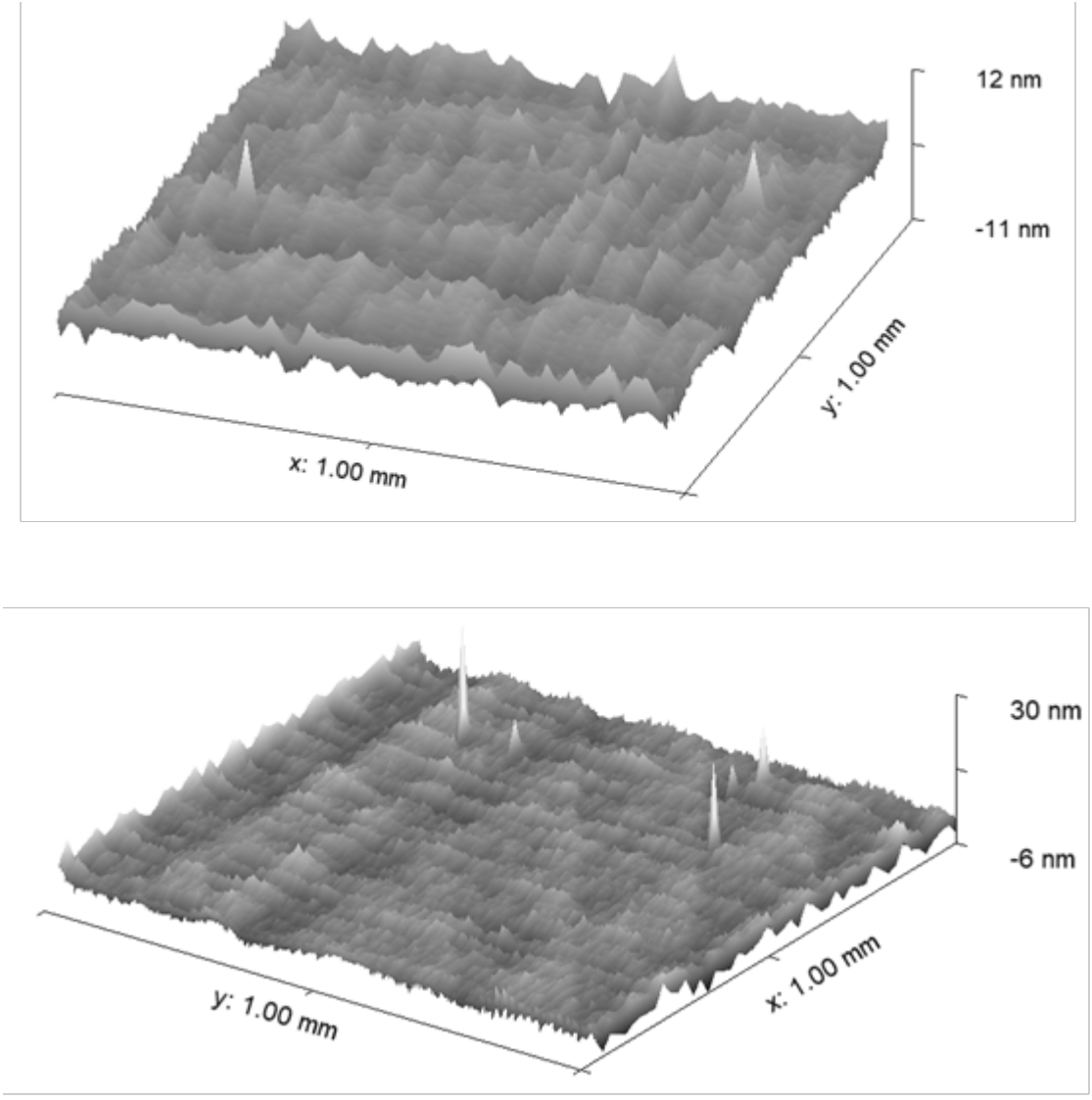


*Figure 7. 19:a) A 1 $mm^2$ dektak map scan of spin cast LEP on PEDOT:PSS. b) A 1 $mm^2$ dektak map scan of spray cast LEP on PEDOT:PSS.*

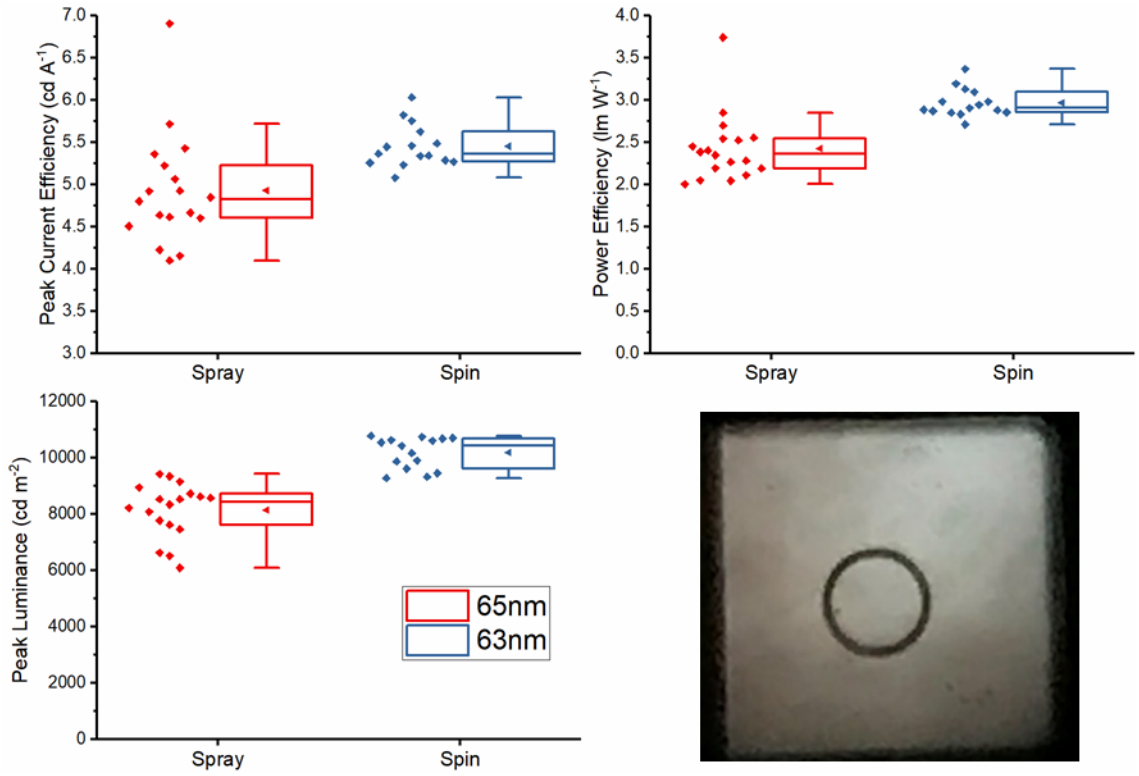


*Figure 7. 20: The key device performance metrics a) peak current efficiency, b) peak power efficiency and c) peak luminance of devices sprayed from 6 mg ml$^{-1}$ Mesitylene (65 ± 3 nm) compared with spin cast devices with 63 ± 3 nm emissive layer thickness. d) A picture of the emission from a pixel of the spray cast device.*

The mean peak current efficiency for the spray cast devices was 4.93 cd A$^{-1}$, 90 % of the value of the spin cast references 5.45 cd A$^{-1}$. The mean peak power efficiency of the spray cast devices was 2.42 Lm W$^{-1}$, 82 % of the spin cast references 2.97 Lm W$^{-1}$. The mean peak luminance of the spray cast devices was 8149 cd m$^{-2}$, 80 % of the reference spin cast value 10189 cd m$^{-2}$. In comparison Gilissen et al. fabricated devices with the emissive layer polymer (Merck Super Yellow) spray cast and achieved, with a champion device, a value for power efficiency 81 % of the spin cast reference (9.71 Lm W$^{-1}$ to 12 Lm W$^{-1}$).[12] Although the mean value of power efficiency for a spray cast device presented in this section is lower than that of the champion device fabricated by Gilissen et al. (2.42 Lm W$^{-1}$ to 9.71 Lm W$^{-1}$), by comparing the device performance of the two bodies of work with respect to their spin cast references any difference in the inherent performance of the materials used can be removed and it can be seen that the mean spray cast device in this

section performed equivalently to the champion spray cast device of Gilissen et al. (both 82 % of the performance of the spin cast reference). It can be seen from the boxplots in Figure 7.20 that the spread of values for the spray cast metrics is slightly larger than the spread in the spin cast data, the spread can be quantified by comparing the standard deviation (SD) of the spin cast and spray cast data. The SD of the mean peak current efficiency for spray cast devices is 0.66 cd $A^{-1}$ and 0.26 cd $A^{-1}$ for spin cast devices. The SD of the mean peak power efficiency for spray cast devices is 0.4 Lm $W^{-1}$ and 0.17 Lm $W^{-1}$ for spin cast devices. The SD of the mean peak luminance for spray cast devices is 968 cd $m^2$ and 557 cd $m^2$ for spin cast devices. The small difference in device performance and increase in SD between spin and spray cast devices is due to the small thickness variations measured across the active area of the spray cast devices and slight device to device variation.

## 7.4: Spray Cast Electron-Injection Layer

In this section the ultrasonic spray coating technique is used as an alternate solution deposition technique for the electron-injection layer of a polymer light-emitting diode (PLED). Typically electron-injection layers are deposited via high vacuum thermal evaporation but as shown in Chapter 4 polyethylenimine-ethoxylated (PEIE) is a potential solution-processed alternative. Devices are processed in ambient conditions and a comparison is made between spin and spray cast devices. The very thin, ~ 3 nm, and uniform films of PEIE required for optimal device performance prove to be very challenging to deposit via ultrasonic spray coating.

Devices in this section were fabricated using pre-patterned 8 pixel ITO substrates with a sheet resistance of 20 Ω $square^{-1}$ and an rms roughness of 1.8 nm (determined by AFM) purchased from Ossila Ltd. The ITO substrates were cleaned following the protocol laid out in Chapter 3. Al 4083 grade PEDOT:PSS was purchased from Ossila Ltd and was filtered using a 0.45 µm PVDF mircodisc filter prior to spin coating at 5000 rpm to yield a 40 ± 3 nm film. The PEDOT:PSS films were annealed on a hotplate, in air at 120 °C for 15 mins and then cooled to room temperature prior to deposition of further layers. The white-light-emitting polymer (LEP) was spin coated in ambient conditions from a 12 mg $ml^{-1}$ p-Xylene solution at 2400 rpm. The

reference electron injection layers were spin cast from 0.04 wt.% PEIE solution in IPA at 5000 rpm to form films 2.7 ± 0.1 nm.

The layers over the ITO contacts were swabbed using IPA, p-Xylene and deionised water to pattern the device and the films were annealed at 100 °C for 10 minutes to remove any residual solvent. A top electrode of 100 nm Aluminium was thermally evaporated at a vacuum pressure of $4x10^{-6}$ mbar through a mask to define a pixel area of 4 $mm^2$. After the deposition of the top electrode the devices were encapsulated in an inert atmosphere (<1 ppm $H_2O$ and <1 ppm $O_2$) using UV-curable epoxy and a glass slide. External electrical connection to the devices were gained via push-fit Ossila testing board, spring loaded gold pins make contact to the ITO pad and ITO fingers.

PEIE was sprayed from a range of concentrations with the best device results obtained with a solution diluted in a volume ratio 1:2, spin cast solution (0.04 wt.%) to IPA. Due to the low boiling point and volatility of the IPA the base plate temperature was chosen to be 20 °C, Figure 7.21 shows the key metrics from devices with PEIE spray cast with spray height 40 mm, fluid pressure 50 mbar and spray speeds 50-150 mm $s^{-1}$.

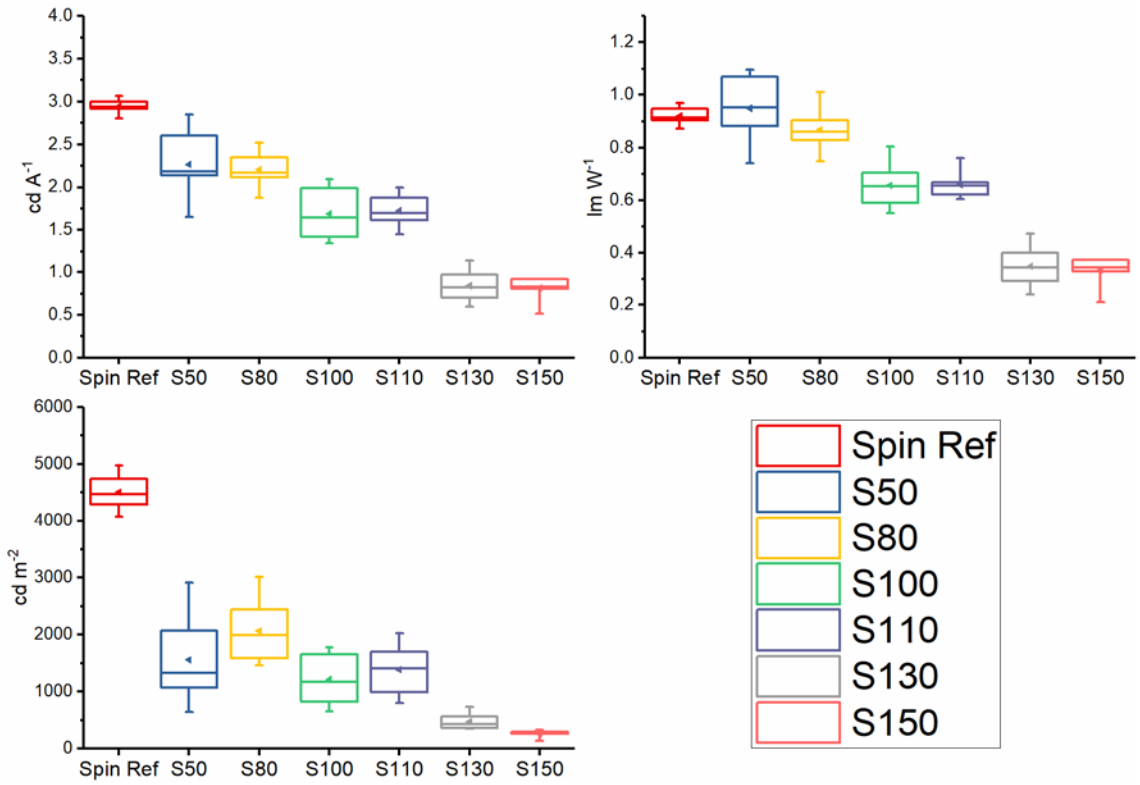


*Figure 7. 21: The key device performance metrics a) peak current efficiency, b) peak power efficiency and c) peak luminance of devices with spray cast EIL PEIE deposited at a range of spray speeds from 50-150 mm $s^{-1}$ compared with spin cast reference devices.*

The devices with PEIE sprayed at 50 and 80 mm $s^{-1}$ have the highest spray cast metrics 2.27 cd $A^{-1}$ to 2.21 cd $A^{-1}$, 0.95 Lm $W^{-1}$ to 0.87 Lm $W^{-1}$ and 1561 cd $m^{-2}$ to 2065 cd $m^{-2}$ respectively. The SD of the mean peak current efficiency for spray speed 80 mm $s^{-1}$ is 0.20 cd $A^{-1}$ and 0.42 cd $A^{-1}$ for devices cast at 50 mm $s^{-1}$. The SD of the mean peak power efficiency for spray speed 80 mm $s^{-1}$ 0.08 Lm $W^{-1}$ and 0.13 Lm $W^{-1}$ for devices cast at 50 mm $s^{-1}$. The SD of the mean peak luminance for spray speed 80 mm $s^{-1}$ is 548 cd $m^2$ and 811 cd $m^2$ for devices cast at 50 mm $s^{-1}$. As shown the devices sprayed at 80 mm $s^{-1}$ have a lower standard deviation than those sprayed at 50 mm $s^{-1}$ as such these devices were chosen for comparison with spin cast devices.

Although having similar power efficiency to the mean spin cast references, 0.87 Lm $W^{-1}$ to 0.92 Lm $W^{-1}$, the mean peak current efficiency, 2.21 cd $A^{-1}$ to 2.95 cd $A^{-1}$, and

mean peak luminance, 2065 cd $m^{-2}$ to 4508 cd $m^{-2}$, of the spray cast films are significantly lower than the spin cast references.

The difference in metrics between spin and spray cast PEIE devices can begin to be understood when observing images of the electroluminescence from the spray cast pixels as shown in Figure 7.22.

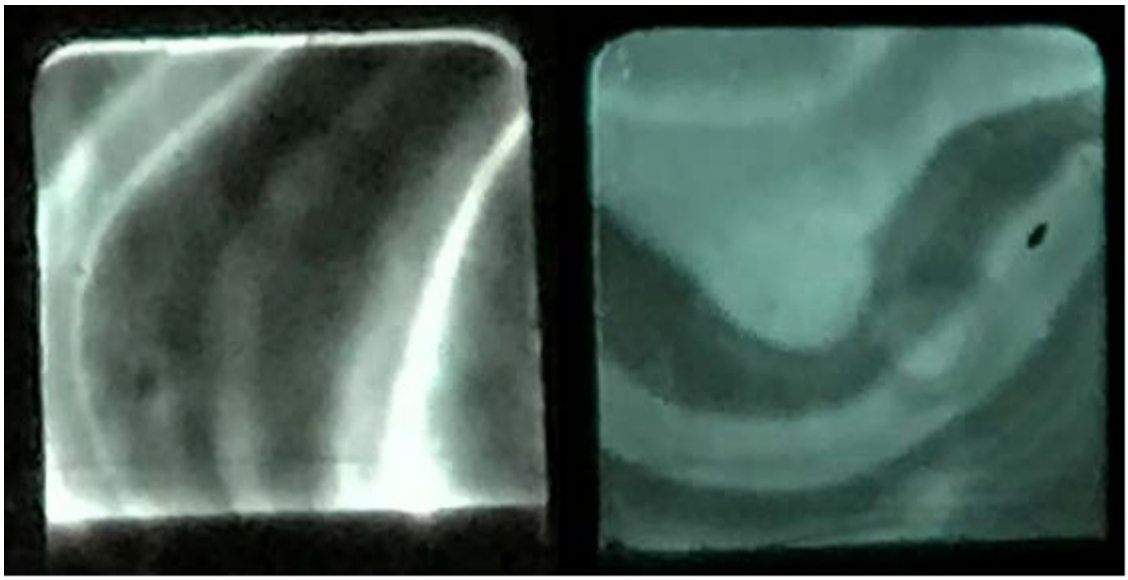

*Figure 7. 22: Image of the electroluminescence just above the turn-on voltage from two pixels of devices in which the EIL is spray cast.*

The emission from the devices with spray cast EIL is highly non-uniform across devices as well as within pixels. As discussed in Chapter 4 the device performance metrics are very sensitive to PEIE thickness, with only a very narrow thickness window for high device performance and with the optimum thickness being 2.7 ± 0.1 nm, even a variation of a few nanometres can drastically effect the device metrics. As all the other layers in the device are identical to the spin cast reference, of uniform thickness and the emission from the spin cast EIL is uniform then the variation in emission is due to thickness variations in the spray cast PEIE layer.

Attempts to characterise films of PEIE deposited via spray coating proved to be challenging. The PEIE solution and subsequent dry film are clear and colourless as such when spraying onto a substrate it can be seen that the solution wets to the substrate but little else can be observed as such no optimisation of the spray

parameters can be based on the drying of the wet film or the uniformity of the dry film. Thickness measurements of spray cast PEIE layers were immeasurable using the dektak as the layers were too thin and, unlike the spin cast PEIE layers, ellipsometry was unable to accurately measure the thickness of the layers likely due to the variation in thickness of the very thin layers.

Devices with spray cast PEIE have been fabricated with reasonable performance metrics compared to spin cast references but with non-uniform electroluminescence due to thickness variation across the devices. Improving the uniformity of spray cast PEIE films and thus fabricating devices of comparable performance to spin cast references proved to be exceptionally challenging due to the inability to characterise the transparent, colourless PEIE layers and optimise the spraying parameters accordingly during the fabrication process.

## 7.5: Multilayer Spray Cast OLED

In the previous sections of this chapter devices have been fabricated in which a single layer, either the hole-injection or emissive layer, has been deposited via ultrasonic spray coating whilst the other layer has been deposited via spin coating. To truly demonstrate the R2R potential for fabricating polymer OLEDs via ultrasonic spray coating both layers must be spray cast sequentially. PEDOT:PSS and the LEP are deposited as described in Sections 7.2 and 7.3 respectively, PEIE is spin cast as the electron-injection layer as described in Chapter 4. Devices with two layers spray-cast have a mean power efficiency of 71 % of the fully spin cast references, as shown below in Figure 7.23. Based on literature searches this is the first multilayer ultrasonic spray cast polymer OLED.

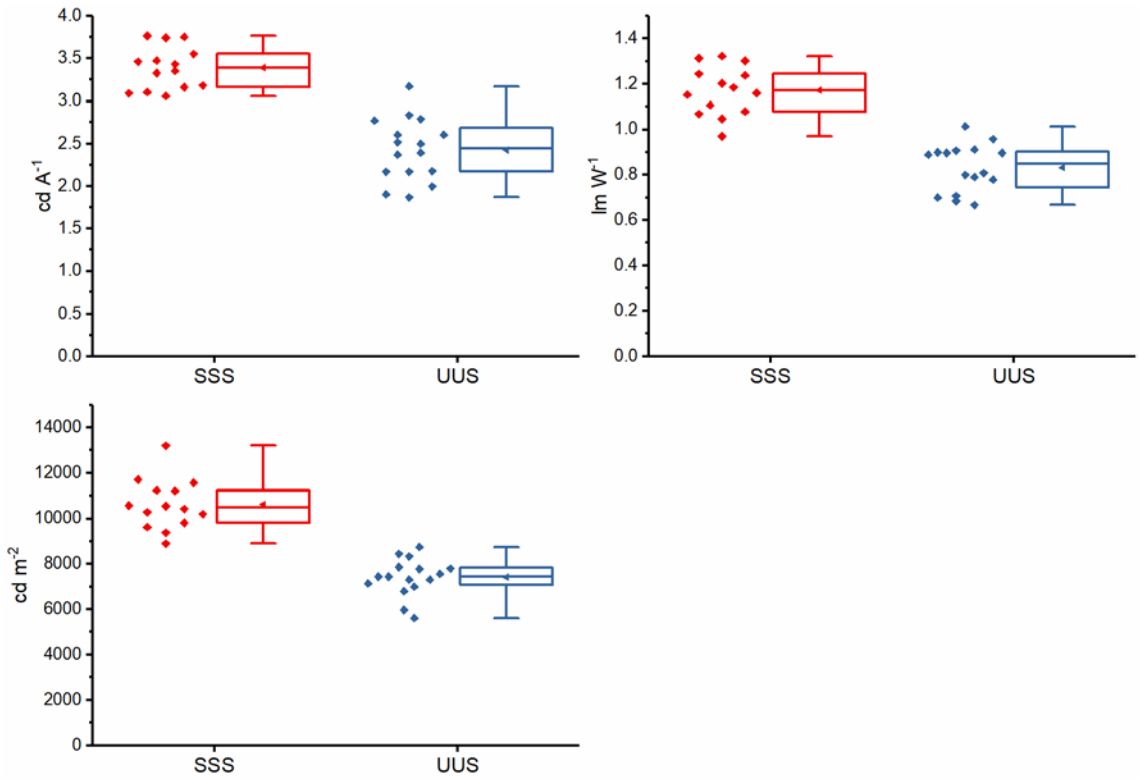


*Figure 7. 23: The key device performance metrics a) peak current efficiency, b) peak power efficiency and c) peak luminance of devices with spray cast PEDOT:PSS, LEP and spin cast PEIE (UUS) compared with fully spin cast reference devices (SSS).*

The mean peak current efficiency for the spray cast devices was 2.43 cd $A^{-1}$, 72 % of the value of the spin cast references 3.39 cd $A^{-1}$. The mean peak power efficiency of the spray cast devices was 0.83 Lm $W^{-1}$, 71 % of the spin cast references 1.17 Lm $W^{-1}$. The mean peak luminance of the spray cast devices was 7409 cd $m^{-2}$, 70% of the reference spin cast value 10626 cd $m^{-2}$.

The SD of the mean peak current efficiency for spray cast devices is 0.37 cd $A^{-1}$ and 0.25 cd $A^{-1}$ for spin cast devices. The SD of the mean peak power efficiency for spin and spray cast devices is 0.11 Lm $W^{-1}$. The SD of the mean peak luminance for spray cast devices is 824 cd $m^{-2}$ and 1106 cd $m^{-2}$ for spin cast devices.

The similar SD between spin and spray cast devices across the performance metrics suggests good uniformity across the multilayer spray cast devices and good device to device repeatability. The decrease in performance metrics from spin cast to multilayer spray cast devices is attributed to slight thickness differences of the spray

cast layers and the negative affect of the off pixel contribution due to the increase in conductivity of the spray cast PEDOT:PSS, as discussed in Section 7.2.2.

*Figure 7. 24: Images of electroluminescence from two multilayer spray cast polymer OLEDs.*

To characterise the difference between spin cast and spray cast devices further, laser-beam-induced current (LBIC) mapping has been used to probe the uniformity of layers of the full device stack via measuring the spatial homogeneity of the photocurrent. A 405 nm focussed laser spot was raster scanned across the surface of devices with a step size of 50 μm with the photocurrent recorded using a lock-in amplifier, the LBIC set up is described in more detail in Chapter 3. This is shown initially in Figure 7.25 where LBIC images across an entire fully spin cast and multilayer spray cast device are compared.

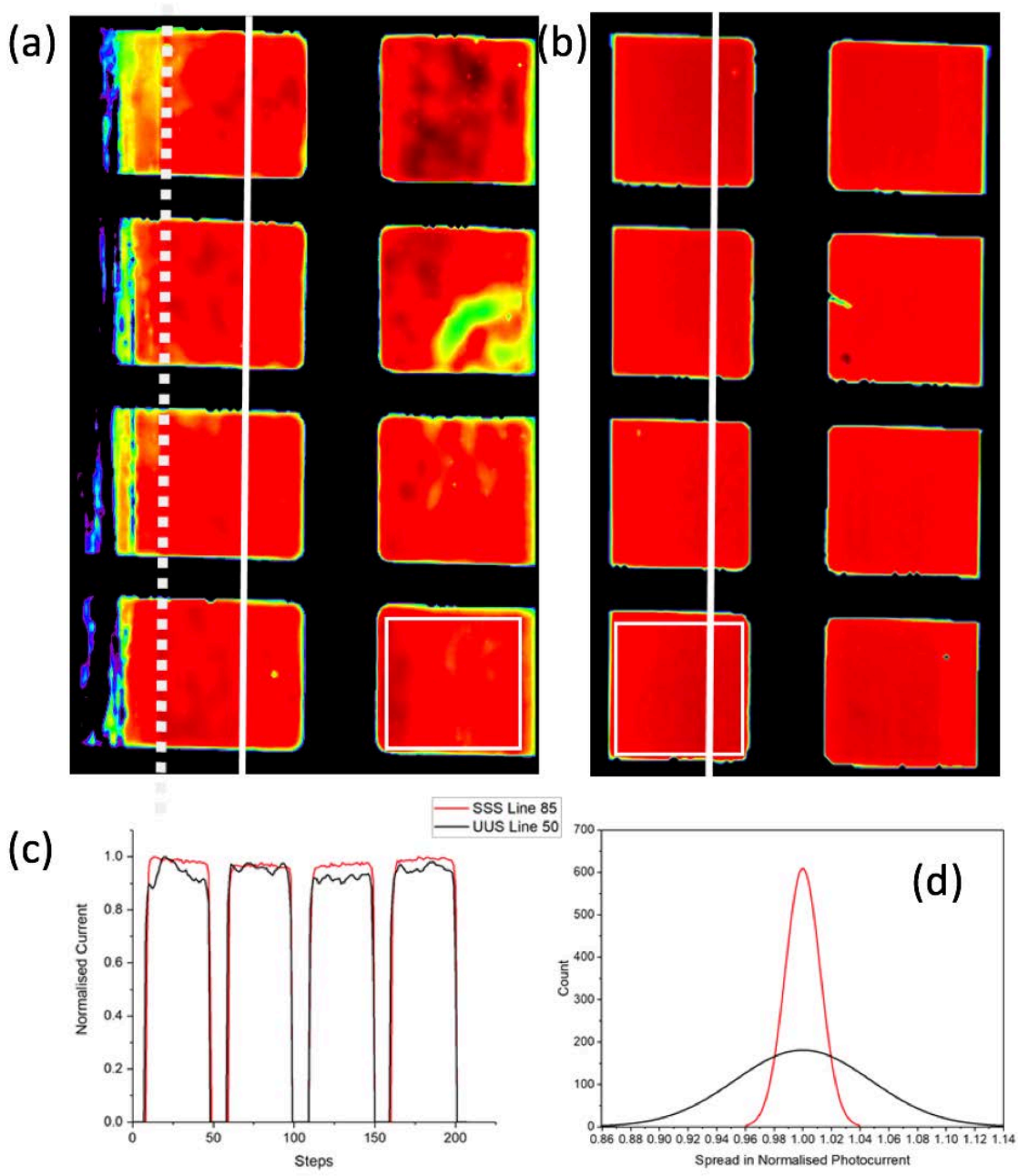


*Figure 7. 25: Comparing the uniformity of spin cast and multilayer spray cast polymer OLEDs by LBIC: Large-area images across the full array of pixels on a device of a multilayer spray cast device (a) and fully spin cast device (b). The dashed white line on (a) indicates the edge of the ITO pad which the overlap with the evaporated top contact typically defines the pixel area as seen in (b). Line profiles from (a) and (b) are shown in (c) and the position from which they are taken is demonstrated with solid white lines on (a) and (b). A histogram of the photocurrent data from a typical multilayer spray*

*cast pixel and a fully spin cast pixel, shown by the white boxes on (a) and (b), is shown in (d).*

Part (a) shows a LBIC image taken across an entire multilayer spray cast device, part (b) shows a LBIC image taken across an entire spin cast device. The dashed white line on part (a) marks the edge of the ITO pad on the substrate, areas to the left of this contributing to the photocurrent show the large parasitic off pixel contribution caused by the increased conductivity of the spray cast PEDOT:PSS, in contrast no such contribution can be seen in part (b) due to the lower conductivity spin cast PEDOT:PSS. It is apparent that the photocurrent generated across both spin and spray cast devices is relatively uniform except for one spray cast pixel with a large defect. The line profiles extracted from parts (a) and (b) (solid white lines) are plotted in part (c) and show comparable fluctuations from the maximum normalised photocurrent of 5 % for the spin cast and 11 % for the spray cast device over centimetre length scales. Part (d) shows a histogram illustrating the spread in photocurrent from within a typical multiplayer spray cast pixel and a typical fully spin cast pixel, as defined by the white boxes on (a) and (b). The edges of the pixels are omitted from the histogram as there are thickness variations in the evaporated top electrode at the edges from the evaporation mask which can be seen in the LBIC but are not being investigated here. The normalised photocurrents from the spin and spray cast pixels are further normalised to the mean of each data set so the different distributions peak at the same point, 1, to more obviously demonstrate the spread in photocurrents for the all spin cast and multilayer spray cast pixels. (d) Shows there is a greater spread of photocurrents generated from within a spray cast pixel than a spin cast pixel, this can be quantified by the standard deviation of 0.012 for the spin cast pixel and 0.05 for the spray cast pixel. This increase in spread of photocurrent is due to slight thickness variations of the PEDOT:PSS and LEP layers.

The spray cast pixel in which there is an area of lower photocurrent generation (2$^{nd}$ pixel down from the top right of Figure 7.25a), this area is a region of thicker LEP likely caused by a thinner area of PEDOT:PSS in the layer below leading to a slight pooling effect when the LEP was spray cast onto this area of PEDOT:PSS. This area is quite distinct on the LBIC suggesting a large thickness variation and a significant

effect will be had on the spatial uniformity of the electroluminescence of that pixel. Figure 7.26 compares the LBIC image of the spray cast pixel with an area of pooling with a greyscale image of the electroluminescence from the same pixel.

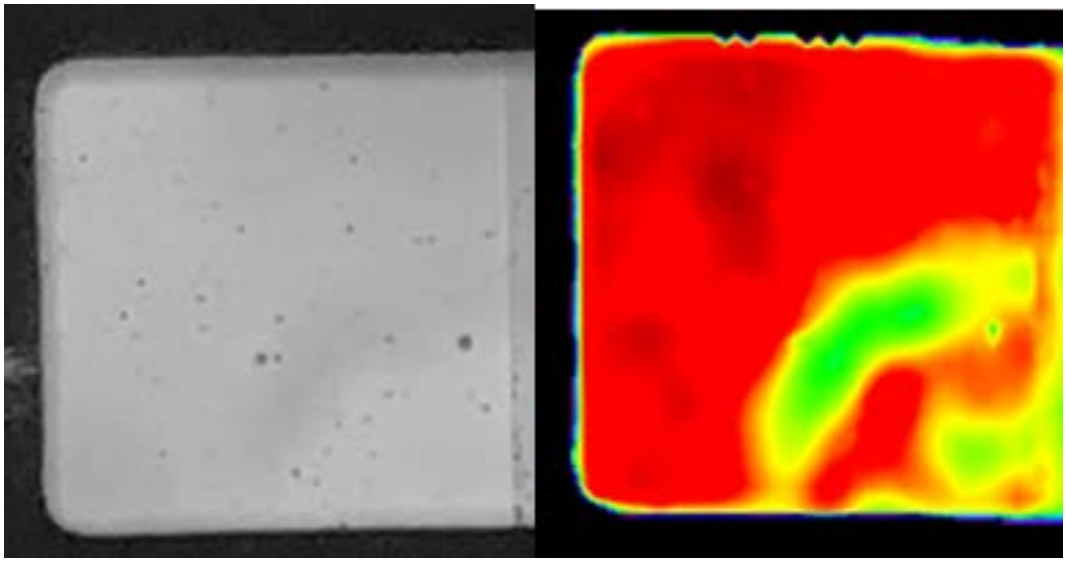

*Figure 7. 26: A greyscale image of the electroluminescence from a multilayer spray cast device (left). On the right is the LBIC image of the same pixel.*

The greyscale image of the electroluminescence was converted into a matrix of intensities allowing for a quantitative comparison between the brightest point and darkest point, a point within the pooling defect. The minimum intensity value from within the pixel from the electroluminescence image is 75 % of the intensity of the maximum intensity recorded. Whereas the minimum photocurrent value from the LBIC of the same pixel was 59 % of the maximum. As such what appears to be a large thickness difference in an LBIC image actually has a significantly lesser effect on the electroluminescence.

### 7.5.1: Large-Area Devices

In the previous section of this chapter the sequential deposition of PEDOT:PSS and the LEP via ultrasonic spray coating on standard 8 pixel substrates was achieved with comparable performance to fully spin cast devices. To demonstrate the scalability of the spray coating process an initial attempt was made to fabricate large-area devices with PEDOT:PSS and the LEP deposited via ultrasonic spray coating. Although initial device performance metrics were disappointing the high

yield is promising and if more time was available with slight optimisation of the spray parameters the metrics could be vastly improved.

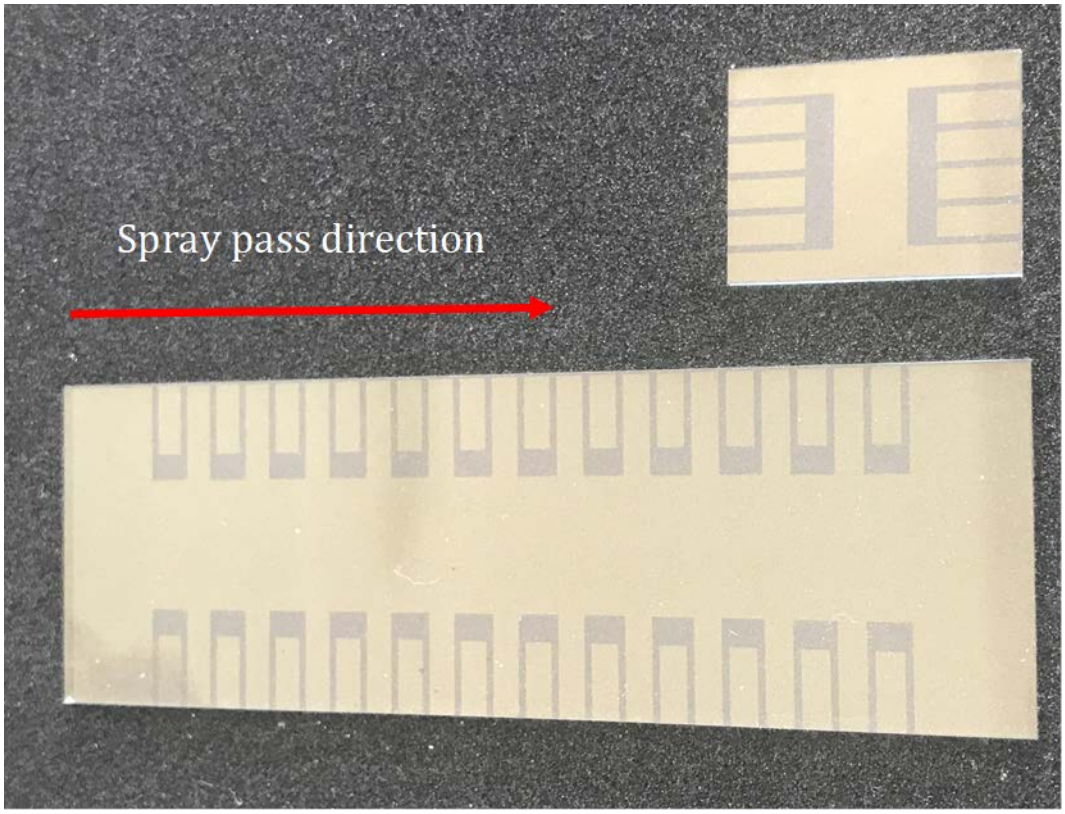


*Figure 7. 27: An image of the standard 8 pixel substrate next to the 24 pixel large area substrate. The direction in which the substrates were coated via ultrasonic spray coating is shown.*

Figure 7.27 shows the standard 8 pixel ITO substrate used throughout this chapter next to the large-area substrate used in this section. The standard 8 pixel substrate is 15 mm wide and 20 mm long whereas the large-area substrate is 25 mm wide and 75 mm long leading to an increase in the area that will be coated during the spraying process. The pixel area of the large-area substrate (9 $mm^2$) although over twice the size of the standard pixel (4 $mm^2$) it is not particularly large but the fact there are 4 times the number of pixels per substrate, 24, will give a large population for analysis of the spread of results and the yield.

| Architecture | Substrate dimensions (mm x mm) | Substrate area ($mm^2$) | Pixel area ($mm^2$) | Number of Pixels |
|---|---|---|---|---|
| **Standard substrate** | 15 x 20 | 300 | 4 | 8 |
| **Large area substrate** | 25 x 75 | 1875 | 9 | 24 |

*Table 7. 3: Descriptions of the architectures of the two substrate designs used in this subsection.*

The large-area substrates were prepared following the cleaning protocol as described in Chapter 3. The PEDOT:PSS was spray cast, as in Section 7.2.2, from a 2:7:1 ink of PEDOT:PSS to IPA to EG, at a pass speed of 32 mm $s^{-1}$, a pass height of 30 mm and a fluid pressure of 50 mbar but with an increase in spray path length to ensure coating of the longer substrate. The substrate was held at 20 °C during the spray deposition then rapidly transferred to a high temperature hotplate (140 °C) as described in Section 7.2.1. The emissive layer was spray cast from a 6 mg $ml^{-1}$ mesitylene solution onto substrates held at 45 °C, with a spray height of 40 mm, pass speed of 130 mm $s^{-1}$ and a fluid pressure of 40 mbar. After swabbing with p-Xylene and DI water to pattern the layers the devices were completed by evaporating a 3 nm LiF electron-injection layer and a 100 nm Aluminium electrode via thermal evaporation under high vacuum prior to encapsulation using a glass slide and UV-curable epoxy.

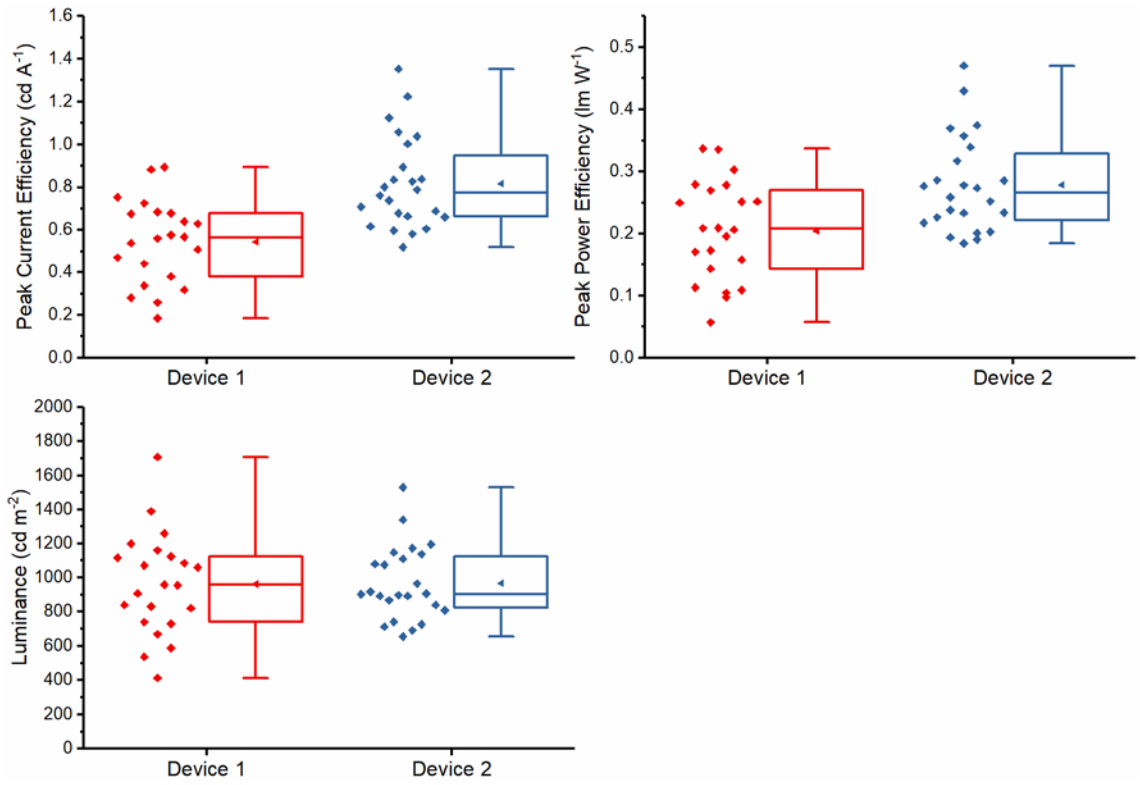


*Figure 7. 28: The key device performance metrics a) peak current efficiency, b) peak power efficiency and c) peak luminance of two large are devices with spray cast PEDOT:PSS, LEP and evaporated LiF as the electron-injection layer.*

It can be seen when comparing the results in Figure 7.28 and 7.23 that the key performance metrics were much lower than the results for two layers spray cast on the standard 8 pixel substrate. The mean peak current efficiency was 0.55 cd $A^{-1}$ for device 1 and 0.82 cd $A^{-1}$ for device 2, the mean peak power efficiency was 0.20 Lm $W^{-1}$ for device 1 and 0.28 Lm $W^{-1}$ for device 2 and the mean peak luminance was 962 cd $m^{-2}$ for device 1 and 967 cd $m^{-2}$. It has been shown in literature that as device area is scaled up the layout of the substrate becomes more important as increasing the length charges have to travel through ITO increases the series resistance of the device.[23–25] The 24 pixel large area substrate is designed to minimise this affect with the testing board connected to the ITO pad either side of each pixel, as such an increase in series resistance does not account for the large decrease in performance from standard to large-area devices. Figure 7.29 shows an image of spray cast PEDOT:PSS on a large-area substrate, sequentially spray cast PEDOT:PSSS and LEP

on a large-area substrate and electroluminescence from a large-area pixel with both layers spray cast.

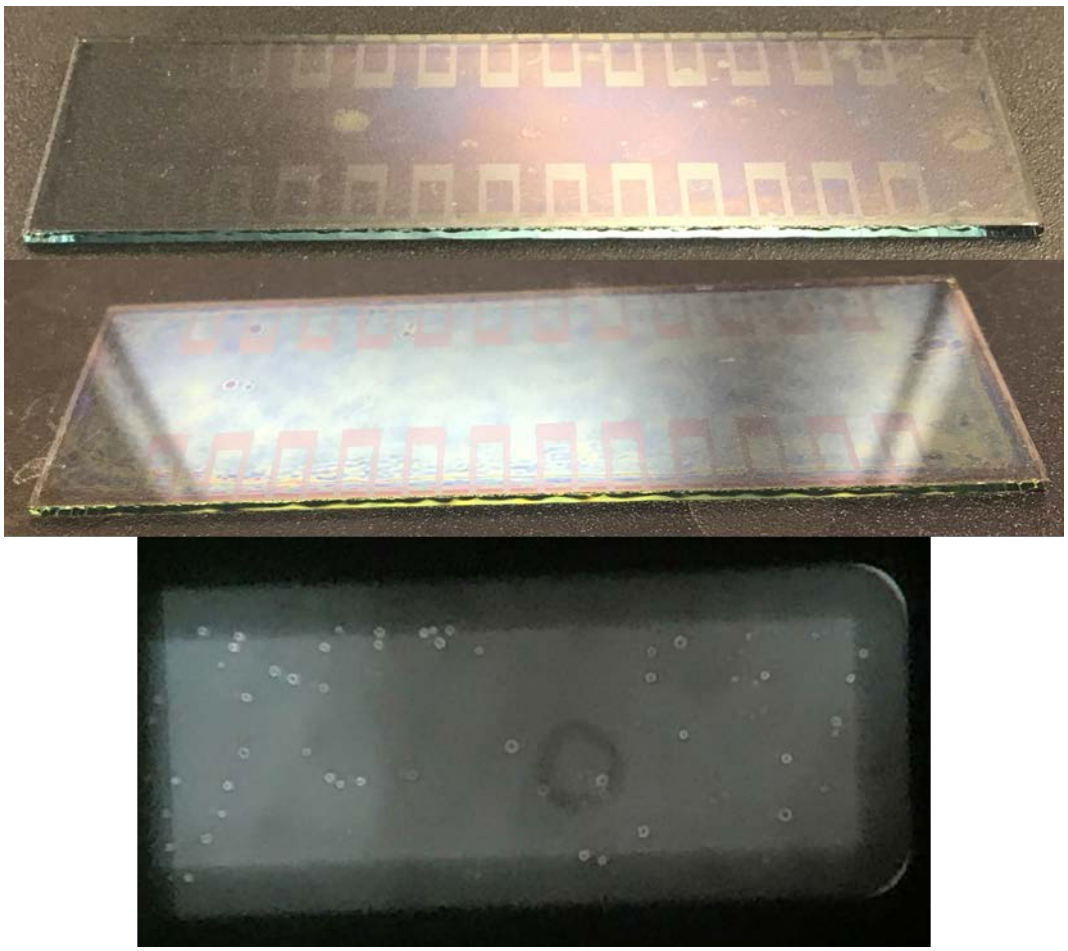

*Figure 7. 29: (Top) Image of spray cast PEDOT:PSS on the large-area substrate. (Middle) Image of large-area substrate coated with spray cast PEDOT:PSS and spray cast LEP. (Bottom) Image of the electroluminescence from a large-area pixel with two layers spray cast.*

It can be seen there are thickness variations and many areas in which the spray cast PEDOT:PSS has reticulated on deposition on the large-area substrate resulting in holes in the film, the spray cast LEP conforms to the non-uniform PEDOT:PSS surface leading to variations in thickness in the emissive layer. The emission from the pixel shows many small areas in which the PEDOT:PSS has reticulated as well as emission from outside of the defined pixel area (narrow brighter region) due to the high conductivity of the spray cast PEDOT:PSS ink as discussed in Section 7.2. Further to

this, the areas in which the PEDOT:PSS has entirely dewet from the substrate will be filled with pools of the polymer spray cast on top, thinning the LEP layer across the rest of the substrate contributing to the decrease in device performance.

It was discovered post-fabrication that an old batch of ethylene glycol (EG) had been used in the PEDOT:PSS ink preparation, this batch of EG was well past its shelf life and as such was likely to have degraded significantly changing the material properties thus not preventing the PEDOT:PSS wet film from dewetting the large-area substrate. The poor quality and non-uniformity of the PEDOT:PSS and as such the subsequently deposited emissive layer led to the poor device metrics. If more time was available the fabrication of these devices could have been repeated with new EG, with slight tuning of the spray parameters to ensure optimal emissive layer thickness across the larger substrate then device performance could have been largely improved.

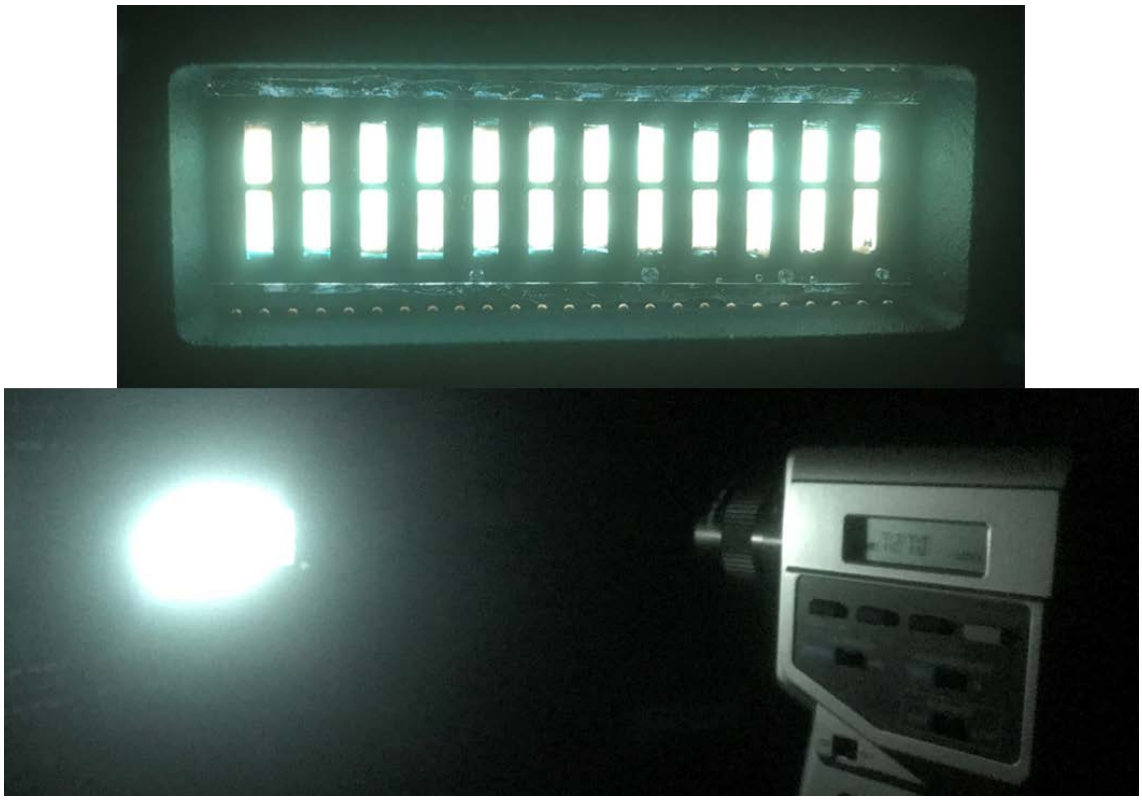

*Figure 7. 30: Image of the electroluminescence from a 24 pixel large area device (Device 2 from Fig 7.28) with PEDOT:PSS and the emissive layer polymer deposited via*

*ultrasonic spray coating, top a close up and bottom the device in the testing setup showing the luminance meter.*

In spite of the issues with the initial attempt to fabricate large-area devices via ultrasonic spray coating there are some positive results. The two devices fabricated had 48 potential pixels in total, 46 of these pixels worked, 1 pixel failed whilst being swept to 10 V and 1 pixel failed to turn on as such the yield was exceptionally high at 95.8 % even with the poor quality PEDOT:PSS layer. The high yield is promising for demonstrating the robust nature of spray coating as a scalable technology.

If this experiment could have been repeated with fresh EG in the PEDOT:PSS ink then I believe the high performance and small spread of the standard 8 pixel devices could have been replicated, this along with the very high yield already shown in large-area devices could have been a proof of concept for the use of ultrasonic spray coating as a scalable technique for the deposition of polymer OLEDs.

## 7.6: Conclusions

In Section 7.2 uniform PEDOT:PSS films, with an rms roughness of 2.14 nm, have been successfully deposited via ultrasonic spray coating. Films were spray cast from a solution of 2 parts PEDOT:PSS, 7 parts IPA and 1 part Ethylene glycol by volume, onto substrates held at 20 °C in a single pass then transferred to a high temperature hotplate (140 °C) to control the film morphology. OLEDs with spray cast PEDOT:PSS as the hole-injection layer have been demonstrated and have comparable luminance to spin cast references but the efficiency metrics are lower than the spin cast references. The addition of EG to the PEDOT:PSS ink increases the conductivity of the layer which leads to an extra current contribution from areas off the defined pixel area which aren't fully patterned, it has been demonstrated that if the devices are patterned more precisely the efficiency metrics of the spray cast PEDOT:PSS devices are comparable to the spin cast references.

In Section 7.3 highly uniform white-light-emitting polymer (LEP) films are successfully deposited using ultrasonic spray coating with an rms roughness of 1.33 nm, an equivalent roughness to spin cast films. After probing a variety of deposition

solvents and solvent blends, films were spray cast in a single pass from a 6 mg $ml^{-1}$ mesitylene solution onto substrates held at 45 °C, these films were incorporated into devices and compared with spin cast references. OLEDs with a spray cast emissive layer have a mean peak current efficiency, power efficiency and luminance of 90 %, 82 % and 80 % of the spin cast references respectively. Slight thickness variations are deemed to be the main difference between spin and spray cast devices. In comparison Gilissen et al. fabricated devices with the emissive layer polymer (Merck Super Yellow) spray cast and achieved, with a champion device, a value for power efficiency 81% of the spin cast reference.[12] The comparable device performance between spin and spray cast devices, narrow spread of metrics and high yield demonstrate the potential for the use of the roll-to-roll compatible technique of ultrasonic spray coating for the deposition of the emissive layer in a polymer OLED.

In Section 7.4 thin films of Ethoxylated Polyethylenimine (PEIE) were spray cast from a solution of 0.013 wt. % PEIE in IPA onto substrates held at 20 °C in a single pass at a range of speeds from 50 – 150 mm $s^{-1}$. Devices were fabricated with spray cast PEIE films as the electron-injection layer, these devices had comparable efficiency metrics to the spin cast references but the mean peak luminance was less than 50 % of the reference. Device performance has been shown to be highly sensitive to PEIE thickness with the optimum thickness of 2.7 ± 0.1 nm and a very narrow thickness window for good device performance. Improving the uniformity of spray cast PEIE films and thus fabricating devices of comparable performance to spin cast references proved to be exceptionally challenging due to the inability to characterise the thin, transparent, colourless PEIE layers and optimise the spraying parameters accordingly during the fabrication process, this was reflected in the non-uniform electroluminescence of these devices. Further work needs to be done on optimising this material for spray coating as such it was not carried forward to the next section.

In Section 7.5 the work in Sections 7.2 and 7.3 was built upon and OLEDs were fabricated in which PEDOT:PSS and the white-light-emitting polymer were deposited sequentially via ultrasonic spray coating, after studying the literature as far as I am aware this is the first multilayer ultrasonic spray cast polymer OLED.

These multilayer spray cast OLEDs have a mean peak current efficiency, power efficiency and luminance of 72 %, 71 % and 70 % of the spin cast references respectively. The high performance and comparable spread to spin cast references demonstrates the potential for the use of the roll-to-roll compatible technique of ultrasonic spray coating for the deposition of multilayer polymer OLEDs.

Finally in Section 7.6 the techniques used in Section 7.5 were scaled up to fabricate large-area (1875 $mm^2$) 24 pixel multilayer spray cast polymer OLEDs. A degraded batch of ethylene glycol in the PEDOT:PSS blend ink led to non-uniformity and holes in the spray cast PEDOT:PSS films which resulted in poor device metrics. Despite the issues with the PEDOT:PSS layer remarkably the yield was 95.8 % of 48 pixels across two devices this demonstrates the feasibility and robustness of using ultrasonic spray coating to process over large areas. If time had allowed for this experiment to have been repeated with fresh ethylene glycol I believe films of a similar uniformity to those cast on the standard 8 pixel substrate could have been replicated and similar device metrics achieved. As such if the narrow spread and high performance metrics of the standard 8 pixel devices could be scaled to the large-area substrate coupled with the high yield already demonstrated would present a strong argument for the feasibility of the roll-to-roll compatible technique of ultrasonic spray coating to be used for the large-area fabrication of multilayer polymer OLEDs.

## 7.7: References


[1] B.W. D'Andrade, S.R. Forrest, White organic light-emitting devices for solid-state lighting, Adv. Mater. 16 (2004) 1585–1595. doi:10.1002/adma.200400684.

[2] L.L.. Hung, C.C.. Chen, Recent progress of molecular organic electroluminescent materials and devices, Mater. Sci. Eng. R Reports. 39 (2002) 143–222. doi:10.1016/S0927-796X(02)00093-1.

[3] S. Logothetidis, Flexible organic electronic devices: Materials, process and applications, Mater. Sci. Eng. B Solid-State Mater. Adv. Technol. 152 (2008) 96–104. doi:10.1016/j.mseb.2008.06.009.

[4] K.X. Steirer, M.O. Reese, B.L. Rupert, N. Kopidakis, D.C. Olson, R.T. Collins, D.S. Ginley, Ultrasonic spray deposition for production of organic solar cells, Sol. Energy Mater. Sol. Cells. 93 (2009) 447–453. doi:10.1016/j.solmat.2008.10.026.

[5] C. Girotto, D. Moia, B.P. Rand, P. Heremans, High-performance organic solar cells with spray-coated hole-transport and active layers, Adv. Funct. Mater. 21 (2011) 64–72. doi:10.1002/adfm.201001562.

[6] T. Wang, N.W. Scarratt, H. Yi, A.D.F. Dunbar, A.J. Pearson, D.C. Watters, T.S. Glen, A.C. Brook, J. Kingsley, A.R. Buckley, M.W.A. Skoda, A.M. Donald, R.A.L. Jones, A. Iraqi, D.G. Lidzey, Fabricating high performance, donor-acceptor copolymer solar cells by spray-coating in air, Adv. Energy Mater. 3 (2013) 505–512. doi:10.1002/aenm.201200713.

[7] N.W. Scarratt, J. Griffin, T. Wang, Y. Zhang, H. Yi, A. Iraqi, D.G. Lidzey, Polymer-based solar cells having an active area of 1.6 cm2 fabricated via spray coating, APL Mater. 3 (2015) 126108. doi:10.1063/1.4937553.

[8] Y. Zhang, N.W. Scarratt, T. Wang, D.G. Lidzey, Fabricating high performance conventional and inverted polymer solar cells by spray coating in air, Vacuum. 139 (2017) 154–158. doi:10.1016/j.vacuum.2016.09.017.

[9] L. Yang, F. Cai, Y. Yan, J. Li, D. Liu, A.J. Pearson, T. Wang, Conjugated Small Molecule for Efficient Hole Transport in High-Performance p-i-n Type Perovskite Solar Cells, Adv. Funct. Mater. 27 (2017) 1–10. doi:10.1002/adfm.201702613.

[10] S. Liu, X. Zhang, M. Yin, H. Feng, J. Zhang, L. Zhang, W. Xie, Coffee-Ring-Free Ultrasonic Spray Coating Single-Emission Layers for White Organic Light-Emitting Devices and Their Energy-Transfer Mechanism, ACS Appl. Energy Mater. 1 (2018) 103–112. doi:10.1021/acsaem.7b00011.

[11] S. Liu, X. Zhang, L. Zhang, W. Xie, Ultrasonic spray coating polymer and small molecular organic film for organic light-emitting devices, Sci. Rep. 6 (2016) 1–10. doi:10.1038/srep37042.

[12] K. Gilissen, J. Stryckers, P. Verstappen, J. Drijkoningen, G.H.L. Heintges, L. Lutsen, J. Manca, W. Maes, W. Deferme, Ultrasonic spray coating as deposition technique for the light-emitting layer in polymer LEDs, Org. Electron. Physics, Mater. Appl. 20 (2015) 31–35. doi:10.1016/j.orgel.2015.01.015.

[13] A. Elschner, S. Kirchmeyer, W. Lovenich, U. Merker, PEDOT: principles and applications of an intrinsically conductive polymer, CRC Press, 2010.

[14] I. Perepichka, D. Perepichka, Handbook of Thiophene-Based Materials: Applications in Organic Electronics and Photonics, 2 Volume Set, John Wiley & Sons, 2009.

[15] S.G. Bucella, A. Luzio, E. Gann, L. Thomsen, C.R. McNeill, G. Pace, A. Perinot, Z. Chen, A. Facchetti, M. Caironi, Macroscopic and high-throughput printing of aligned nanostructured polymer semiconductors for MHz large-area electronics, Nat. Commun. 6 (2015) 1–10. doi:10.1038/ncomms9394.

[16] C.N. Hoth, R. Steim, P. Schilinsky, S.A. Choulis, S.F. Tedde, O. Hayden, C.J. Brabec, Topographical and morphological aspects of spray coated organic photovoltaics, Org. Electron. Physics, Mater. Appl. 10 (2009) 587–593. doi:10.1016/j.orgel.2009.02.010.

[17] K.X. Steirer, J.J. Berry, M.O. Reese, M.F.A.M. van Hest, A. Miedaner, M.W. Liberatore, R.T. Collins, D.S. Ginley, Ultrasonically sprayed and inkjet printed thin film electrodes for organic solar cells, Thin Solid Films. 517 (2009) 2781–2786. doi:10.1016/j.tsf.2008.10.124.

[18] S.I. Na, B.K. Yu, S.S. Kim, D. Vak, T.S. Kim, J.S. Yeo, D.Y. Kim, Fully spray-coated ITO-free organic solar cells for low-cost power generation, Sol. Energy Mater. Sol. Cells. 94 (2010) 1333–1337. doi:10.1016/j.solmat.2010.01.003.

[19] J.G. Tait, B.J. Worfolk, S.A. Maloney, T.C. Hauger, A.L. Elias, J.M. Buriak, K.D. Harris, Spray coated high-conductivity PEDOT:PSS transparent electrodes for stretchable and mechanically-robust organic solar cells, Sol. Energy Mater. Sol. Cells. 110 (2013) 98–106. doi:10.1016/j.solmat.2012.09.005.

[20] C. Girotto, B.P. Rand, J. Genoe, P. Heremans, Exploring spray coating as a

deposition technique for the fabrication of solution-processed solar cells, Sol. Energy Mater. Sol. Cells. 93 (2009) 454–458. doi:10.1016/j.solmat.2008.11.052.

[21] B.D. Martin, N. Nikolov, S.K. Pollack, A. Saprigin, R. Shashidhar, F. Zhang, P.A. Heiney, Hydroxylated secondary dopants for surface resistance enhancement in transparent poly(3,4-ethylenedioxythiophene)-poly(styrenesulfonate) thin films, Synth. Met. 142 (2004) 187–193. doi:10.1016/j.synthmet.2003.09.005.

[22] J. Ouyang, C.-W. Chu, F.-C. Chen, Q. Xu, Y. Yang, High-Conductivity Poly(3,4-ethylenedioxythiophene):Poly(styrene sulfonate) Film and Its Application in Polymer Optoelectronic Devices, Adv. Funct. Mater. 15 (2005) 203–208. doi:10.1002/adfm.200400016.

[23] S. Choi, W.J. Potscavage, B. Kippelen, Area-scaling of organic solar cells, J. Appl. Phys. 106 (2009). doi:10.1063/1.3211850.

[24] A. Armin, M. Hambsch, P. Wolfer, H. Jin, J. Li, Z. Shi, P.L. Burn, P. Meredith, Efficient, Large Area, and Thick Junction Polymer Solar Cells with Balanced Mobilities and Low Defect Densities, Adv. Energy Mater. 5 (2015) 1401221. doi:10.1002/aenm.201401221.

[25] J.E. Bishop, D.K. Mohamad, M. Wong-Stringer, A. Smith, D.G. Lidzey, Spray-cast multilayer perovskite solar cells with an active-area of 1.5 cm2, Sci. Rep. 7 (2017) 7962. doi:10.1038/s41598-017-08642-2.

# Chapter 8

# Conclusions and Future Work

Whilst many advances have been made in the field of organic light-emitting diodes (OLEDs) with efficient, white-emitting, solution-processed devices achieved there is still a great deal of progress required towards the commercialisation of OLEDs for lighting and displays. A major barrier for the commercial use of OLEDs is the cost, as the current fabrication techniques typically used on a lab scale are slow, expensive and can only coat small-areas. In order to reduce the cost of fabricating OLEDs a large-area, roll-to-roll compatible deposition technique is required that can sequentially deposit the uniform thin films of an OLED structure. This thesis investigates the use of the large-area, roll-to-roll compatible deposition technique of ultrasonic spray coating for the fabrication of polymeric organic light-emitting diodes.

In Chapter 4, caesium carbonate, 8-hydroxy-quinolinato lithium and polyethylenimine-ethoxylated (PEIE) were investigated as solution-processed electron-injection layers (EILs) for white-emissive polymer LEDs. The EILs were deposited via spin coating at a range of different thicknesses to optimise device performance, the effect of ambient processing on device performance was also investigated to probe the compatibility of these materials with a large-area ambient coating technique such as ultrasonic spray coating. It is found that under ambient processing conditions PEIE performed best with mean peak metrics of 3.18 cd $A^{-1}$, 1.14 Lm $W^{-1}$, and 10690 cd $m^{-2}$.

Chapter 5 described the physics behind the key stages of depositing a thin film via ultrasonic spray coating; the formation of droplets of a solution, transferring the droplets onto the substrate, the spreading and merging of droplets to form a

continuous wet film and the evaporation of the solvent to form a dry thin film. Thin films of poly[(9,9-dioctylfluorenyl-2,7-diyl)-co-(4,4'(N-(4-sec-butylphenyl))) (TFB) were cast via ultrasonic spray coating using a range of different deposition parameters and the morphology is characterised in order to demonstrate the parameter space and the optimisation process required to deposit uniform thin films. Issues with the USI Prism Ultra-coat 300 system were raised and how they are managed was discussed in order to maintain a good level of repeatability from device-to-device and run-to-run.

In Chapter 6, the influence of thin film processing technique and surface roughness on the electrical performance of unipolar polymer devices was studied. The injection efficiency of holes into films of poly[(9,9-dioctylfluorenyl-2,7-diyl)-co-(4,4'(N-(4-sec-butylphenyl))) diphenylamine], cast by ultrasonic spray coating was compared with those cast by spin coating. It was shown via statistical analysis, across a range of thicknesses typical of those used in OLEDs, that there is no intrinsic difference in the injection efficiency between ultrasonic spray coating and spin coating. This reinforces the applicability of spray coating as a potential route to high volume manufacturing of OLED based technology. The importance of controlling the roughness of films was also demonstrated and a threshold of 10 nm average roughness was determined, below which the effect of roughness on injection efficiency is negligible. As such a process window for achieving comparable spin and spray cast hole injection performance is wide with spray cast films with Ra < 10 nm being easily achieved by control of drying time through solvent choice, substrate temperature, formulation concentration and pass speed.

In Chapter 7, uniform PEDOT:PSS films, with a root-mean-square (rms) roughness of 2.14 nm, were successfully deposited via ultrasonic spray coating. OLEDs with spray cast PEDOT:PSS as the hole-injection layer were demonstrated and have comparable luminance to spin cast references but the efficiency metrics were lower than the spin cast references. The lower efficiencies were due to additives to the spray cast ink increasing the conductivity of the layer leading to off pixel current contributions, it is demonstrated that if the devices are patterned more precisely the

efficiency metrics of the spray cast PEDOT:PSS devices were comparable to the spin cast references.

Highly uniform white-light-emitting polymer (LEP) films are successfully deposited via ultrasonic spray coating with a rms roughness of 1.33 nm, an equivalent roughness to spin cast films. These films were incorporated into devices and compared with spin cast references. OLEDs with a spray cast emissive layer have a mean peak current efficiency, power efficiency and luminance of 90 %, 82 % and 80 % of the spin cast references respectively. In comparison Gilissen et al. fabricated devices with the emissive layer polymer (Merck Super Yellow) spray cast and achieved, with a champion device, a value for power efficiency 81% of the spin cast reference.[1] The comparable device performance between spin and spray cast devices, narrow spread of metrics and high yield demonstrate the potential for the use of the roll-to-roll compatible technique of ultrasonic spray coating for the deposition of the emissive layer in a polymer OLED.

Devices were fabricated with spray cast polyethylenimine-ethoxylated (PEIE) films as the electron-injection layer, these devices had comparable efficiency metrics to the spin cast references but the mean peak luminance was less than 50 % of the reference. Device performance was shown in Chapter 4 to be highly sensitive to PEIE thickness with the optimum thickness 2.7 ± 0.1 nm and a very narrow thickness window for good device performance. Improving the uniformity of spray cast PEIE films and thus fabricating devices of comparable performance to spin cast references proved to be exceptionally challenging due to the inability to characterise the thin, transparent, colourless PEIE layers and optimise the spraying parameters accordingly during the fabrication process, this was reflected in the non-uniform electroluminescence of these devices.

OLEDs were then fabricated in which PEDOT:PSS and the white-light-emitting polymer were deposited sequentially via ultrasonic spray coating, after studying the literature as far as I am aware this is the first multilayer ultrasonic spray cast polymer OLED. The multilayer spray cast OLEDs had a mean peak current efficiency, power efficiency and luminance of 72 %, 71 % and 70 % of the spin cast references respectively. The high performance and comparable spread to spin cast references

demonstrates the potential for the use of the roll-to-roll compatible technique of ultrasonic spray-coating for the deposition of multilayer polymer OLEDs.

Attempts were then made to scale up to fabricate large-area (1875 $mm^2$) 24 pixel multilayer spray cast polymer OLEDs. A degraded batch of ethylene glycol used in the PEDOT:PSS blend ink caused non-uniformity and holes in the spray-cast PEDOT:PSS films which resulted in poor devices metrics. Despite the issues with the PEDOT:PSS layer remarkably the yield was 95.8 % of 48 pixels across two devices this demonstrates the feasibility and robustness of using ultrasonic spray coating to process over large areas.

## 8.1: Future Work

To further build on the work in Chapter 4 either phase diagrams produced by atomic force microscopy in tapping mode or kelvin probe force microscopy could be used to confirm if the EIL films cast from dilute solutions form incomplete films. An extension of the work in Chapter 4 would be to further investigate solution-processed 8-hydroxy-quinolinato lithium (Liq) as other have successfully achieved high performance devices using Liq and it is more stable in ambient than caesium carbonate ($Cs_2CO_3$).[2] This would involve purchasing higher purity source of material and investigating a wider range of deposition parameters.

Chapter 5 could be developed further by demonstrating the effect of depositing the same polymer in a range of different solvents. It would be of interest to broaden the optimisation guide and processing window to other polymers, soluble small molecules and solution-processable inorganic materials such nanoparticle suspensions.

The work in Chapter 6 could be replicated with an electron-transporting polymer in an electron-only device structure to investigate if the conclusions match those of spray cast hole-transporting polymers and confirm the processing window demonstrated.

In Chapter 7 uniform thin layers of PEIE proved challenging to deposit and characterise, it could be possible to use kelvin probe force microscopy coupled with

spin cast reference films to optimise thickness and uniformity of such films. An alternate route would be to investigate other solution-processed electron-injection layers which have a larger optimum thickness and greater thickness tolerance. If this involved moving away from organic materials it has been shown that combining zinc oxide nanoparticles and Liq in solution can be spin cast to form an effective electron-injection layer with a thickness ~10 nm.[2] Also it has been shown that by combining Liq with pyridine- containing polymers that the solution-processed electron-injection layer can be increased to a thickness of 16 nm whilst limiting the increase in driving voltages and decrease in EQE typically associated with a thicker Liq layer.[3]

To progress with the work spraying the emissive layer in Chapter 7, higher performing emissive polymers could be used to replicate this work in order to increase the device metrics and thus the impact.

In the unlikely case the issues with spraying PEDOT:PSS ink over large areas, as seen towards the end of Chapter 7, continued with fresh ethylene glycol then the PEDOT:PSS the ink could be adapted to include a very small proportion of high molecular weight polyethylene glycol, as introduced by Griffin et al., which has been shown to further limit reticulation when spray coating PEDOT:PSS.[4] I have successfully replicated this work during my PhD on 8 pixel substrates but batch-to-batch repeatability was an issue due to the small volumes of solution fabricated and the very small volume of PEG added, but for larger scale processing or for high-throughput larger volumes of ink would be required and as such this issue would be resolved.

The next step beyond large-area devices fabricated by ultrasonic spray coating would be to fabricate devices of a similar scale on flexible substrates as progress is made towards a roll-to-roll process.

## 8.2: References

[1] K. Gilissen, J. Stryckers, P. Verstappen, J. Drijkoningen, G.H.L. Heintges, L. Lutsen, J. Manca, W. Maes, W. Deferme, Ultrasonic spray coating as deposition technique for the light-emitting layer in polymer LEDs, Org. Electron. Physics, Mater. Appl. 20 (2015) 31–35. doi:10.1016/j.orgel.2015.01.015.

[2] T. Chiba, Y.J. Pu, M. Hirasawa, A. Masuhara, H. Sasabe, J. Kido, Solution-processed inorganic-organic hybrid electron injection layer for polymer light-emitting devices, ACS Appl. Mater. Interfaces. 4 (2012) 6104–6108. doi:10.1021/am301732m.

[3] T. Chiba, Y.J. Pu, S. Takahashi, H. Sasabe, J. Kido, Lithium Phenolate Complexes with a Pyridine-Containing Polymer for Solution-Processable Electron Injection Layers in PLEDs, Adv. Funct. Mater. 24 (2014) 6038–6045. doi:10.1002/adfm.201401060.

[4] J. Griffin, A.J. Ryan, D.G. Lidzey, Solution modification of PEDOT:PSS inks for ultrasonic spray coating, Org. Electron. Physics, Mater. Appl. 41 (2017) 245–250. doi:10.1016/j.orgel.2016.11.011.